DESARROLLO DE NUEVOS MATERIALES PARA EL TRATAMIENTO DE AGUAS RESIDUALES Y LA PRODUCCIÓN DE HIDRÓGENO MEDIANTE FOTOCATÁLISIS

Sandra Yurani Toledo Camacho

Sandra Yurani Toledo Camacho

Development of new materials for hydrogen generation and wastewater treatment by photocatalysis

Doctoral Thesis

Supervised by:

Dr. Francisco Medina Cabello

Dr. Sandra Contreras Iglesias

Chemical Engineering Department

UNIVERSITAT ROVIRA i VIRGILI

Tarragona (Spain)

2019

UNIVERSITAT ROVIRA i VIRGILI

DEPARTMENT OF CHEMICAL ENGINEERING
ESCOLA TÈCNICA SUPERIOR D'ENGINYERIA QUÍMICA
Av. Països Catalans, 26, 43007, Tarragona (Spain)
Tel. +34 977 55 96 03 / 04 Fax +34 977 55 96 21
e-mail: secdeq@etseq.urv.es
http://www.etseq.urv.es/DEQ/

Dr. Francisco Medina Cabello and Dr. Sandra Contreras Iglesias

CERTIFY:

That the present study, entitled "Development of new materials for the hydrogen generation and wastewater treatment by photocatalysis " presented by Sandra Yurani Toledo Camacho to award the degree of Doctor, has been carried out under our supervision at the Chemical Engineering Department of this university, and it fulfils all the requirements to be eligible for the European Doctorate Award.

Tarragona, 29 of May 2019

Doctoral Thesis Supervisors

Dr. Francisco Medina CabelloDr. Sandra Contreras Iglesias

ACKNOWLEDGMENTS

First of all I would like to thank my supervisors Dr. Francisco Medina Cabello and Dr. Sandra Contreras Iglesias, for giving me the opportunity to develop my PhD in the Catàlisi Heterogèni (CATHETER) Group at the Universitat Rovira i Virgili (URV). I really appreciate their support, guidance and patience along these years. I know it has not been easy. Thank you very much.

I also would like to thank the Spanish Ministry of Economy and Competitiveness (MINECO) fellowship for the financing support (Project CTQ2012-37039-C02-02), both for Ph.D. fellowship and mobility grant to The Netherland for 90 days, and to the Red FOTOCAT (Project CTM2015-71054-REDT) for mobility financing support to the Solar Platform Plant (PSA) in Almería (Spain).

I must say a doctoral thesis is not an one-person work. It involves the effort of many other people that in different ways has contributed to this work, so I would express my gratitude to all them.

From scientific collaborations, special thanks to Dr. Fernando Juan Beltran Novillo, Dr. Ana Rey Barroso and Dr. María Dolores Hernández-Alonso from the Department of Chemical Engineering and Physical Chemistry, University of Extremadura (Badajoz) for the supply of the catalytic supports used in this thesis. Dr. Jordi Llorca from the Institut de Tèchniques Energètiques (Barcelona) for the HRTEM and XPS analysis, and to the Dr. José R. Galán-Mascarós and Dr. Franziska S. Hegner from the Photomagnetic materials and bioinorganic models for energy applications group, Institut Català d'Investigació Química (ICIQ) (Tarragona) for their kind collaboration in diffuse reflectance UV-Vis analysis tests. Dr. Manuel Ignacio Maldonado Rubio from the Plataforma Solar de Almería (PSA) - CIEMAT (Tabernas) for his open scientific support in my short stay in the PSA.

I would also like to thank Dr. Guido Mul, who supervised my work and stay at PhotoCatalysis Synthesis (PCS) group, in the University of Twente, The Netherland, and all the member of this group who were open and really kind to me during my stay. A special thank to Lidy Harryvan, Dr. Kai Han, Devin O'Neill and Dr. Kasper Wenderich.

From the Universitat Rovira i Virgili, I am very grateful to Sandra Ramos Garcia, Vanessa Torné Fernández and Susana Dominguez Zaragoza, CATHETER group without them would not be the same, thank you very much for your different kind of support and help, I really appreciate it. Thank also to Núria Juanpere Mitjana from the ETSEQ department.

I am also grateful to all the member of the CATHETER group, whom I shared many experiences during these years of my Ph.D. studies and helped me in different ways, Dr. Mayra García Álvarez, Dr. Ana

Antolín, Dr. Llorenç Gavilà, Dr. Anton Ivanov Dafinov, Dr. Jesús Sueiras Romero and Abel Toscano, and the technician Ana Belén Montero Cabrera. To my "CATHETERIAN" friends Hande Demir, Dr. Silvia Jimenez Herrera, Raiana Tomazini, Dr. Margarita Jimenez Tototzintle and Richard Ahorse, also for all of you a big thank for all your emotional and scientific support in my ups and downs during my research.

I want to thank as well Dr. Daniel Salavera and Dr. Juan Prieto because I learnt a lot from our friendship, thank for doing the lunch time easier in hard days.

Gracias también, por supuesto, a mis mejores amigos en Colombia de toda la vida y de todo el mundo. Los quiero mucho y sin ese soporte vital que han sido ustedes mis amigos, éste camino cuesta arriba no hubiera sido tan ameno, gracias, Fabiola Patricia Jaimes García, José Miguel Berrio Sánchez, Laura Nataly Vargas Ramírez, Jhonis Javier Pérez Bravo, Anny Katherine Lozano Valdés y Julián Eduardo Sánchez Velandia.

A mi mejor amigo en Tarragona, Sergio Cobo, muchas gracias por tu amistad y todo el apoyo que me has brindado desde que nos conocimos, y al Equipo Màster del CN Tàrraco por su inigualable buen ambiente y energía. Yo no sería la misma de no haber conocido a este grupo tan maravilloso en el que puedo gozar de paz y amor por el mar.

Mi más sincero agradecimiento en todo este proceso se lo debo a una persona que ha estado en las buenas y en las no tan buenas de mi vida en Tarragona. Arturo Ordoñez García, te agradezco mucho todo el soporte que me has brindado y me sigues brindando, tanto profesional como personal. Tú haces parte de los cimientos de la persona que decido ser ahora, me has ayudado a crecer con tus palabras de aliento, con el tiempo que me dedicaste y con la gran experiencia que ha sido estar a tú lado. Gracias Arturo.

Y por supuesto, debo extender mi más profundo agradecimiento a mi familia, mami Francy Isabel Camacho Becerra, Diógenes Lobo Celis, a mi hermanito Juan Pablo Lobo Camacho y a mi querida hermana melliza (o alma gemela como ella dice) Marla Katherine Toledo Camacho. También a mi padre Bob Dwight Toledo Santamaría. Con ustedes empecé esta gran aventura hacia el viejo continente y acá estoy, culminando una etapa más de esta gran competición que es la vida. Estoy inmensamente agradecida con ustedes, siempre han estado ahí para ayudarme a levantar en los momentos difíciles, sus pequeños consejos se hicieron grandes con la distancia. Gracias querida Familia.
Gracias familia Tarraconense. Gracias familia URV.

Index

Figure Index

Table Index

Summary

The unlimited supply of solar energy presents the challenge of developing materials and processes capable of absorbing and transforming this sort of energy into new fuels for our wasteful energy lifestyle. Since Fujishima and Honda, in 1972, the photocatalytic hydrogen production on semiconducting materials, as titanium dioxide, has been not only a potential technology to achieve these challenges, but also an environmentally friendly alternative to fossil fuels.

On this regard, the interest toward hydrogen settles on its high efficient energy conversion, its three times higher capacity of storing energy than natural gas, its simple conversion to other kind of energy and its friendly combustion that only produces water. Although non-conventional methods for hydrogen production are not mature enough, still expensive and present low efficiencies, currently prevails a motivation for investigating new technologies (or work on those that already exist) to make hydrogen become the fuel of the future. In this sense, this thesis is based on the development of new materials for hydrogen generation and wastewater treatment by photocatalysis.

Firstly, the thesis introduces the state of the art related to the energy situation background, where it is presented the fossil fuel crisis and is commented in more details the main features, advantages and drawbacks of the renewable energy sources (wind power, hydro power, oceans power, geothermal power and solar power).

Later, the thesis focuses on the properties that make hydrogen an interesting energy carrier and describes the different hydrogen generation methods. These methods are explained according to the hydrogen source, for instance, hydrogen from fossil fuel (steam-methane reforming, partial oxidation of methane, auto-thermal reforming and coal gasification), hydrogen from water (water electrolysis, water splitting by photocatalysis, water thermolysis and thermo-chemical splitting of water) and hydrogen from biomass (thermo-chemical conversion of biomass, biofuel reforming and algae).

The state of the art related to the heterogeneous photocatalysis describes the fundamental of photocatalysis, the photocatalytic hydrogen generation and the photocatalytic semiconductor materials. It is talked in deeper detail the limiting steps in the photocatalytic processes, like the light absorption and the photogenerated electron-holes recombination, and later are exposed the alternatives offered by many researchers. On this latter regard, there is an extensive number of studies that have worked on titanium dioxide, without any modification, for the photocatalytic hydrogen generation and many others, attempting to overcome its limited light absorption from different points of view. These possible outcomes are given from the perspective of the photocatalytic reforming and also by using co-catalysts such as non-metal doping, noble metal loading, or transition metal oxides and metal sulfides deposition, either by doping or simply loading the titanium dioxide surface.

After all these considerations is understood the need to study new catalytic materials that improve the efficiencies toward hydrogen by means of photocatalytic processes driven by visible and solar light, in addition to the hydrogen generation by the photoreforming of different organic compounds.

Therefore, in this thesis are mainly studied catalysts based on palladium, titanium dioxide and tungsten trioxide ($Pd/TiO_2(-WO_3)$), but also studied catalysts based on platinum, titanium dioxide and tungsten trioxide ($Pt/TiO_2(-WO_3)$), as well as a short study is performed on catalysts based on palladium, P25 (commercial titanium dioxide) and cupper (Pd/P25-Cu). The hydrogen generation is carried out from water-methanol (or glycerol in some cases) mixtures and from some municipal wastewater. For better understanding and organization, in this thesis, the catalysts previously commented were classified in five groups: (i) w-$Pd/TiO_2(-WO_3)$ - CATHETER Lab, (ii) m-$Pd/TiO_2(-WO_3)$ - CATHETER Lab, (iii) m-$Pd/TiO_2(-WO_3)$ - PCS Lab, (iv) m-$Pt/TiO_2(-WO_3)$ - PCS Lab and (v) Pd/TiO_2-Cu - CATHETER Lab catalysts.

Moving on to the methodology, concerning the photocatalytic limiting step related the poor absorption on bare-titanium dioxide, in this thesis two catalytic supports supplied by the Department of Chemical Engineering and Physical Chemistry, University of Extremadura, Spain, are explored. These catalytic supports consist on (i) nanotubes of titanium dioxide plus tungsten trioxide nanoparticles (NT-WO_3 (4.5 wt.%)) and (ii) commercial titanium dioxide (P25) plus tungsten trioxide nanoparticles (P25-WO_3 (4.1 wt.%)). On the other hand, respect to the photocatalytic limiting step related to the high electron-hole recombination on bare-titanium dioxide, within this thesis the photodeposition of palladium was widely studied. Moreover, it is also explored the photodeposition of platinum and the deposition of cupper on titanium dioxide.

In order to see the differences between the catalyst features and their effect on the photocatalytic hydrogen generation, the following characterization techniques were used: Inductively Coupled Plasma (ICP-OES), Total Surface Area (BET), X-ray Diffraction power (XRD), High Resolution Transmission Electron Microscopy (HR-TEM), Scanning Transmission Electron Microscopy (STEM) and Diffuse Reflectance UV-Vis. For the photocatalytic hydrogen tests, four experimental set-up were used: (i) Simulated Solar Light (SSL-system), (ii) UVA light (UVA-system), (iii) Pilot Plant Scale (PPS-system) and (iv) Small Scale (SS-system) system. The analytical procedures include gas chromatography (GC) for the hydrogen detection and quantification, total organic carbon (TOC) measurement to see the degradation of organic compounds and actinometry tests to measure the number of photons absorbed by the reaction system for the hydrogen generation.

In general words, it was possible to develop new catalytic materials for hydrogen generation by photocatalysis. Moreover, the TOC removal on this kind of materials was not good enough.
With regard to the Pd photodeposition study it was found that the hydrogen evolution is quite influenced by the metal photodeposition conditions on any of the three catalytic supports studied: NT-WO_3, P25-WO_3 and P25. Some of the photodeposition conditions studied were the catalyst (1000 - 4000 ppm) and

methanol concentration (0 - 20 vol.%), metal amount (0.1 - 2 wt.%) and metal nature (Pd and Pt) in the photodeposition solution. The catalysts containing 0.25 wt.% of metal (either platinum or palladium), presented the highest hydrogen evolution.

The hydrogen evolution was seen to be also affected by the reaction conditions such as the catalyst (86 -1000 ppm) and sacrificial agent concentration (0 - 50 vol.%), the sacrificial agent nature (methanol, glycerol and real wastewater), pH (12, natural and 2) and the water matrix (tap or milliQ water)

Resumen

La posibilidad de obtener un suministro de energía ilimitado del sol, nos presenta el reto de desarrollar materiales y procesos capaces de absorber y transformar esta forma de energía en nuevos combustibles para poder soportar nuestro estilo actual de vida intensivo en consumo de energía. Desde Fujishima y Honda, 1972, la producción fotocatalítica de hidrógeno sobre materiales semiconductores, como el dióxido de titanio, ha sido no sólo un tecnología potencial para lograr estos retos, sino que también se presenta como una alternativa más amigable con el medio ambiente que los combustibles fósiles.

Sobre este aspecto, el interés en el hidrógeno recae en su conversión de energía de alta eficiencia, su capacidad para almacenar tres veces más la energía almacenada en un mismo volumen de gas natural, su simple conversión a otras formas de energía y su combustión amigable con el medio ambiente porque sólo produce agua al ser quemado. Hay que decir que aunque los métodos no convencionales para la producción de hidrógeno no son lo suficientemente maduros y siguen siendo aún costosos y presentan bajas eficiencias, actualmente aún prevalece una motivación sobre la investigación de nuevas tecnologías (o trabajar sobre las ya existentes) para hacer del hidrógeno el combustible del futuro.

Con este marco, esta tesis está basada en la investigación y desarrollo de nuevos materiales para la generación de hidrógeno y el tratamiento de aguas residuales mediante la fotocatálisis. En primer lugar, esta tesis hace un recorrido sobre los antecedentes de la situación energética mundial, donde se habla sobre la crisis de los combustibles fósiles y se comenta con mayor detalle las principales características, ventajas y desventajas de las fuentes de energía renovables (energía eólica, energía hidroeléctrica, energía del océano, energía geotérmica y energía solar).

Más adelante, en el marco teórico se habla más específicamente sobre las propiedades que hacen al hidrógeno un interesante portador de energía, y se describen también los diferentes métodos de producción de hidrógeno, explicados de acuerdo a la fuente de hidrógeno. Por ejemplo, se puede obtener hidrógeno de los combustibles fósiles (reformado de vapor, oxidación parcial de metano, reformado auto-térmico y gasificación de carbón), hidrógeno a partir de agua (electrólisis del agua, *water splitting* por fotocatálisis, termólisis del agua y *water splitting* por procesos termo-químicos) e hidrógeno de la biomasa (conversión termo-química de biomasa, reformado de biocombustibles y a partir de algas).

En el estado del arte de la fotocatálisis heterogénea se describen los fundamentos de la fotocatálisis, la generación fotocatalítica de hidrógeno y los materiales semiconductores fotocatalíticos. Se habla con

más profundidad de las etapas limitantes en los procesos fotocatalíticos, como la pobre absorción de luz y la recombinación de las cargas fotogeneradas electrón-hueco, y se exponen más adelante las alternativas dadas por diferentes investigadores. Sobre éstas limitaciones, hay un amplio número de estudios que han trabajado sobre el dióxido de titanio, sin modificación alguna para la generación fotocatalítica de hidrógeno y muchos otros, sobre su mejora para resolver su limitada absorción de luz, desde diferentes puntos de
vista. Éstas posibles soluciones están dadas desde la perspectiva del reformado fotocatalítico y también por medio del uso de co-catalizadores como no-metales o metales nobles, depositar óxidos de metales de transición o sulfatos metálicos, ya sea dopando o simplemente cargando la superficie del dióxido de titanio.

Después de todas estas consideraciones, se puede entender la necesidad de estudiar nuevos materiales catalíticos que mejoren las eficiencias hacia el hidrógeno por medio de procesos fotocatalíticos impulsados por luz visible y solar, además de generar hidrógeno por medio del fotoreformado de diferentes compuestos orgánicos y el análisis del grado de degradación de éstos compuestos orgánicos.

Por lo tanto, en esta tesis se han estudiado principalmente catalizadores basados en paladio, dióxido de titanio y trióxido de wolframio ($Pd/TiO_2(-WO_3)$), pero también catalizadores basados en platino, dióxido de titanio y trióxido de wolframio ($Pt/TiO_2(-WO_3)$), así como un estudio más corto sobre catalizadores basados en paladio, P25 (el dióxido de titanio comercial más conocido) y cobre (Pd/P25-Cu). La generación de hidrógeno sobre estos materiales ha sido llevada a cabo a partir de mezclas agua-metanol (o glicerol en algunos casos) y también se han usado aguas residuales municipales. Para un mejor entendimiento y organización, en ésta tesis, los catalizadores previamente comentados han sido clasificados en cinco grupos: (i) w-$Pd/TiO_2(-WO_3)$ - CATHETER Lab, (ii) m-$Pd/TiO_2(-WO_3)$ - CATHETER Lab, (iii) m-$Pd/TiO_2(-WO_3)$ - PCS Lab, (iv) m-$Pt/TiO_2(-WO_3)$ - PCS Lab y (v) Pd/TiO_2-Cu - CATHETER Lab.

Pasando a la metodología, respecto a la etapa fotocatalítica limitante relacionada con la pobre absorción del dióxido de titanio puro, en ésta tesis se exploran dos soportes catalíticos suministrados por el Departamento de Ingeniería Química y Química Física de la Universidad de Extremadura, España. Estos soportes consisten en: (i) nanotubos de óxido de titanio más nanopartículas de trióxido de wolframio ($NT\text{-}WO_3$ (4.5 wt.%)) y (ii) dióxido de titanio comercial más nanopartículas de trióxido de wolframio ($P25\text{-}WO_3$ (4.1 wt.%)). Por otra parte, respecto a la etapa fotocatalítica limitante relacionada con la alta recombinación de los pares electrón-hueco sobre el dióxido de titanio puro, en ésta tesis se estudia ampliamente la fotodeposición de paladio, pero también se explora la fotodeposición de platino o la deposición de cobre sobre el dióxido de titanio.

Con el fin de ver las diferencias entre los características de los catalizadores y su efecto en la generación fotocatalítica de hidrógeno, las siguientes técnicas de caracterización han sido usadas en

esta tesis: Plasma de Acoplamiento inductivo (ICP-OES), Área superficial total (BET), Difracción de Rayos X (XRD), Microscopía Electrónica de Transmisión de Alta Resolución (HR-TEM), Microscopía Electrónica de Transmisión con unidad de Barrido (STEM) y la Reflectancia Difusa UV-Vis. Para las pruebas fotocatalíticas de hidrógeno se usaron cuatro sistemas de reacción distintos: (i) luz solar simulada (*SSL-system*), (ii) luz UVA (*UVA-system*), (iii) planta a escala piloto (*PPS-system*) y (iv) sistema de reacción a escala pequeña (*SS-system*). El procedimiento analítico incluye cromatografía de gases (GC) para la detección y cuantificación de hidrógeno, medición del carbón orgánico total (TOC) para ver la degradación de los compuestos orgánicos y, prueba de actinometría para medir el número de fotones absorbidos por el sistema de reacción para la producción de hidrógeno.

En términos generales, fue posible desarrollar estos nuevos materiales catalíticos para la generación de hidrógeno mediante la fotocatálisis, pero la eliminación TOC sobre estos materiales no fue buena. Lo más probable es que sea debido a su sensibilidad a envenenamiento por acumulación de sub-productos en su superficie. Respecto al estudio de la fotodeposición del paladio, se encontró que la evolución de hidrógeno está bastante influenciada por las condiciones a las cuales se realizó la fotodeposición del metal sobre cualquiera de los tres soportes catalíticos estudiados: NT-WO_3, P25-WO_3 y P25. Algunas de las condiciones de fotodeposición estudiadas fueron: la concentración de catalizador (1000 - 4000 ppm), la concentración de metanol (0 - 20 vol.%), la cantidad de metal (0.1 - 2 wt.%) y la naturaleza del metal (Pd y Pt) en la solución de fotodeposición. En su mayoría, los catalizadores que contienen 0.25 wt.% de metal (ya sea paladio o platino) presentaron mayor evolución de hidrógeno.

Se observó que la evolución de hidrógeno también estuvo influenciada por las condiciones de reacción, tales como la concentración de catalizador (86 - 1000 ppm) y del agente de sacrificio (0 - 50 vol.%), la naturaleza del agente de sacrificio (metanol, glicerol, agua residual municipal), pH (12, natural y 2) y la matriz de agua (de grifo o pura).

Resum

La possibilitat d'obtenir un subministrament d'energia il·limitat del sol, ens presenta el repte de desenvolupar materials i processos capaços d'absorbir i transformar aquesta forma d'energia en nous combustibles per poder suportar el nostre estil actual de vida intensiu en consum d'energia. Des de Fujishima i Honda, 1972, la producció fotocatalítica d'hidrogen sobre materials semiconductors, com el diòxid de titani, ha sorgit no només un tecnologia potencial per aconseguir aquests reptes, sinó que també es presenta com una alternativa més amigable amb el medi ambient que els combustibles fòssils.

Sobre aquest aspecte, l'interès en l'hidrogen recau en la seva conversió d'energia d'alta eficiència, la seva capacitat per emmagatzemar tres vegades més l'energia emmagatzemada en un mateix volum de gas natural, la seva simple conversió a altres formes d'energia i la seva combustió amigable amb el medi ambient perquè només produeix aigua en ser cremat. Cal dir que encara que els mètodes no convencionals per a la producció d'hidrogen no són prou madurs i segueixen sent encara costosos i presenten baixes eficiències, actualment encara preval una motivació sobre la investigació de noves tecnologies (o treballar sobre les ja existents) per fer l'hidrogen el combustible del futur.

Amb aquest marc, aquesta tesi està basada en la investigació i desenvolupament de nous materials per a la generació d'hidrogen i el tractament d'aigües residuals mitjançant la fotocatàlisi.
En primer lloc, aquesta tesi fa un recorregut sobre els antecedents de la situació energètica mundial, on es parla sobre la crisi dels combustibles fòssils i es comenta amb més detall les principals característiques, avantatges i desavantatges de les fonts d'energia renovables (energia eòlica, energia hidroelèctrica, energia de l'oceà, energia geotèrmica i energia solar).

Més endavant, en el marc teòric es parla més específicament sobre les propietats que fan a l'hidrogen un interessant portador d'energia, i es descriuen també els diferents mètodes de producció d'hidrogen, explicats d'acord amb la font d'hidrogen. Per exemple, es pot obtenir hidrogen dels combustibles fòssils (reformat de vapor, oxidació parcial de metà, reformat auto-tèrmic i gasificació de carbó), hidrogen a partir d'aigua (electròlisi de l'aigua, water splitting per fotocatàlisi, termòlisi de l'aigua i water splitting per processos termo-químics) i hidrogen de la biomassa (conversió termo-química de biomassa, reformat de biocombustibles i a partir d'algues).

En l'estat de l'art de la fotocatàlisi heterogènia es descriuen els fonaments de la fotocatàlisi, la generació fotocatalítica d'hidrogen i els materials semiconductors fotocatalítics. Es parla amb més profunditat de les etapes limitants en els processos fotocatalítics, com la pobra absorció de llum i la recombinació de les càrregues fotogenerades electró-forat, i s'exposen més endavant les alternatives donades per diferents investigadors. Sobre aquestes limitacions, hi ha un ampli nombre d'estudis que han treballat sobre el diòxid de titani, sense cap modificació per a la generació fotocatalítica d'hidrogen i molts altres, sobre la seva

millora per resoldre la seva limitada absorció de llum, des de diferents punts de vista. Aquestes possibles solucions estan donades des de la perspectiva del reformat fotocatalític i també per mitjà de l'ús de co-catalitzadors com no-metalls o metalls nobles, dipositar òxids de metalls de transició o sulfats metàl·lics, ja sigui dopant o simplement carregant la superfície del diòxid de titani.

Després de totes aquestes consideracions, es pot entendre la necessitat d'estudiar nous materials catalítics que millorin les eficiències cap l'hidrogen per mitjà de processos fotocatalítics impulsats per llum visible i solar, a més de generar hidrogen per mitjà del fotoreformat de diferents compostos orgànics.

Per tant, en aquesta tesi s'han estudiat principalment catalitzadors basats en pal·ladi, diòxid de titani i triòxid de wolframi ($Pd/TiO_2(-WO_3)$), però també catalitzadors basats en platí, diòxid de titani i triòxid de wolframi ($Pt/TiO_2(-WO_3)$, així com un estudi més curt sobre catalitzadors basats en pal·ladi, P25 (el diòxid de titani comercial més conegut) i coure (Pd/P25-Cu). La generació d'hidrogen sobre aquests materials ha estat portada a terme a partir de mescles aigua-metanol (o glicerol en alguns casos) i també s'han fet servir aigües residuals municipals. Per a un millor enteniment i organització, en aquesta tesi, els catalitzadors prèviament comentats han estat classificats en cinc grups: (i) $w\text{-}Pd/TiO_2(-WO_3)$ - CATHETER Lab, (ii) $m\text{-}Pd/TiO_2(-WO_3)$ - CATHETER Lab, (iii) $m\text{-}Pd/TiO_2(-WO_3)$ - PCS Lab, (iv) $m\text{-}Pt/TiO_2(-WO_3)$ - PCS Lab i (v) Pd/TiO_2-Cu - CATHETER Lab.

Passant a la metodologia, respecte a l'etapa fotocatalítica limitant relacionada amb la pobra absorció del diòxid de titani pur, en aquesta tesi s'exploren dos suports catalítics subministrats pel Departament d'Enginyeria Química i Química Física de la Universitat d'Extremadura, Espanya. Aquests suports consisteixen en: (i) nanotubs d'òxid de titani més nanoparticules de triòxid de wolframi ($NT\text{-}WO_3$ (4.5 wt.%)) i (ii) diòxid de titani comercial més nanopartícules de triòxid de wolframi ($P25\text{-}WO_3$ (4.1 wt.%)). D'altra banda, pel que fa a l'etapa fotocatalítica limitant relacionada amb l'alta recombinació dels parells electró-forat sobre el diòxid de titani pur, en aquesta tesi s'estudia àmpliament la fotodeposició de pal·ladi, però també s'explora la fotodeposició de platí o la deposició de coure sobre el diòxid de titani.

Per tal de veure les diferències entre els característiques dels catalitzadors i el seu efecte en la generació fotocatalítica d'hidrogen, les següents tècniques de caracterització han estat usades en aquesta tesi: Plasma d'Acoblament inductiu (ICP-OES), Àrea superficial total (BET), Difracció de Raigs X (XRD), Microscòpia Electrònica de Transmissió d'alta resolució (HR-TEM), Microscòpia Electrònica de Transmissió amb unitat de Rastreig (STEM) i la Reflectància Difusa UV-Vis. Per a les proves fotocatalítiques d'hidrogen es van usar quatre sistemes de reacció diferents: (i) amb llum solar simulada (SSL-system), (ii) amb llum UVA (UVA-system), (iii) planta a escala pilot (PPS-system) i (iv) sistema de reacció a escala petita (SS-system). El procediment analític inclou cromatografia de gasos (GC) per a la detecció i quantificació d'hidrogen, mesura del carbó orgànic total (TOC) per veure la degradació dels compostos orgànics i, prova d'actinometria per mesurar el nombre de fotons absorbits pel sistema de

reacció per a la producció d'hidrogen.

En termes generals, va ser possible desenvolupar aquests nous materials catalítics per a la generació d'hidrogen mitjançant la fotocatàlisi, però l'eliminació de TOC sobre aquests materials no va ser bona. El més probable és que sigui a causa de la seva sensibilitat a enverinament per acumulació de sub-productes en la seva superfície. Respecte a l'estudi de la fotodeposició del pal·ladi, es va trobar que l'evolució d'hidrogen està bastant influenciada per les condicions a les quals es va realitzar la fotodeposición del metall sobre qualsevol dels tres suports catalítics estudiats: NT-WO_3, P25-WO_3 i P25. Algunes de les condicions de fotodeposició estudiades van ser: la concentració de catalitzador (1000 - 4000 ppm), la concentració de metanol (0 - 20 vol.%), la quantitat de metall (0.1 - 2 wt.%) i la naturalesa del metall (Pd i Pt) en la solució de fotodeposició. En la seva majoria, els catalitzadors que contenen 0.25 wt.% de metall (ja sigui pal·ladi o platí) van presentar una major evolució d'hidrogen.

Es va observar que l'evolució d'hidrogen també es va veure influenciada per les condicions de reacció, com ara la concentració de catalitzador (86 - 1000 ppm) i de l'agent de sacrifici (0 - 50 vol.%), La naturalesa de l'agent de sacrifici (metanol , glicerol, aigua residual municipal), pH (12, natural i 2) i la matriu d'aigua (d'aixeta o pura).

CHAPTER 1

Introduction: Energy situation background

1. ENERGY SITUATION BACKGROUND

1.1. Fossil fuel crisis

Our planet provides us with primary energy from its own natural resources in two different ways: fuel and energy flow. In the first group the energy is stored discretely inside matter whereas the second group corresponds to energy associated to the movement, for instance: sun shining, water or wind flowing and Earth's internal heat.

The primary energy can be direct usable (like the wind, solar and hydraulic energy) or indirectly usable (like oil, natural gas or coal). This primary energy requires a physical or chemical transformation to be used, therefore, in the case of fuels like coal, petroleum, natural gas or uranium, their transformation is by burning them. This transformation gives rise to the secondary energies like electricity or gasoline.

Unlike the energy flow, which comes from renewable energy source and in most of the cases its conversion represents low carbon dioxide (CO_2) release, the fossil fuel on the other hand, take thousands of years to regenerate. Consequently fossil fuel are depleted every time they are used, and additionally, they release more greenhouses gases such CO_2, methane (CH_4) and nitrous oxides species (NO_x) [1][2].

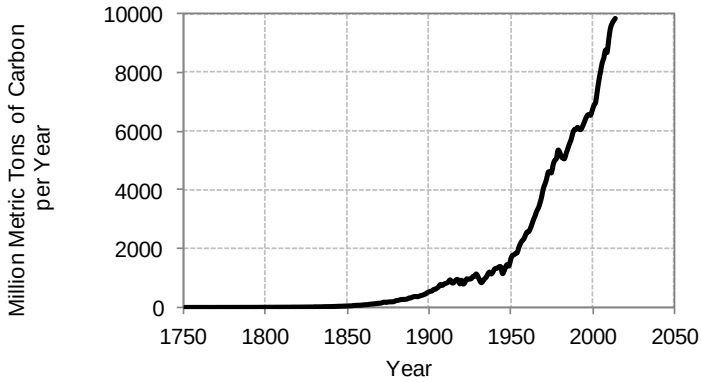

Source: Boden, T. A., G. Marland, and R. J. Andres. 2015. Global, Regional, and National Fossil-Fuel CO2 Emissions. Carbon Dioxide Information Analysis Center, Oak Ridge National Laboratory, U.S, Department of Energy, Oak Ridge, Tenn., U.S.A.
doi: 10.3334/CDIAC/00001_V2015

Figure 1.1. Annual Global Fossil Fuel CO_2 emission [3]

Since the Industrial Revolution in the middle 18th century, the massive changes in human activities have demanded progressively more fuel. It means that the time of the replacement of the hand labour and the animal or human muscle energy for steam engines represented the beginning of a new era of machines and locomotives. This new era of machines and locomotives, hand in hand with the expanding trade, has catapulted the Industrial Revolution not only toward the development of more machinery, new inventions and more manufacturing and transportation productivity but also it catapulted the mankind toward a culture highly demanding of manufactured product and energy. All in all, the Industrial Revolution traduced in environmental terms has been the beginning of an excessive greenhouse gases release.

Accordingly to the Carbon Dioxide Information analysis Centre (CDIAC) [3], 400 billion metric tons of

CO_2 have been released to the atmosphere since 1751, which 200 billion correspond only since the late 1980s. Figure 1.1 shows the CO_2 emission trend since the beginning of the Industrial Revolution (1751) up to 2014. The estimations were done taking into account the individual contributions from gas, liquids and solids fuel plus the contribution of the cement production and gas flaring.

It is important to highlight that in the period between 1750 and 1950, the percentage of increase in CO_2 emission (based on the total CO_2 emissions up to 2014: 9855 million metric tons of carbon per year), was 16.5 %, whereas only in the last 65 years there have been released 83.5 %, it means 5 times the CO_2 emitted in two centuries. These CO_2 emissions have made its concentration in the atmosphere increase from 280 part per million (ppm) up to 403 ppm in 2016 [2][3].

Different climate scientists agree on the fact that most of these emissions corresponds to anthropogenic CO_2 emissions, which have caused the Earth's global warming observed in the average temperature increase of around 0.8°C since 1885 [4]. However, the global warming has not been caused only by CO_2 emissions. Compounds such as CH_4, NO_x and water vapor [5] have been also released into the atmosphere by processes related mostly to human activities like agriculture, deforestation, chemical productions, use of fertilizer, decomposition of wastes in landfills, meat production (in ruminant digestion), biomass and fossil fuel burnt as well.

Under equilibrated concentration levels of the compounds above in the atmosphere, they absorb the heat radiated from the Earth and this process warms the Earth's surface to a life-supporting average of 15 °C. When CO_2, CH_4, NO_x and water vapour are present at high concentration levels, they block the Earth's heat from escaping toward the space. Consequently, this heat is stored in the Earth (mostly in oceans and atmosphere), increasing in a long-term Earth's surface temperature.

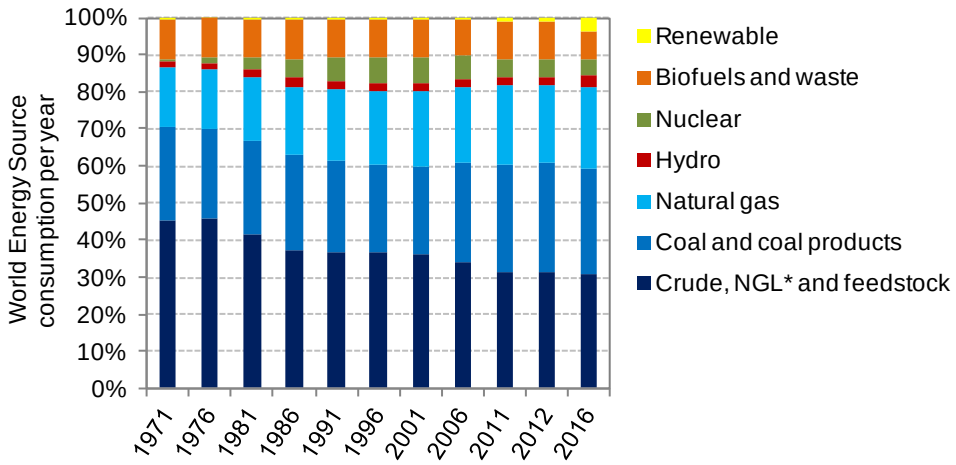

Data Source: J. Hanania, J. Jenden, J. Donev, Fuel vs flow - Energy Education, Energy Publ. 2015). http://energyeducation.ca/encyclopedia/Fuel_vs_flow (accessed February 10, 2018).

Figure 1.2. Percentages of World Energy Source consumption per year [1]

Accordingly to the trends of the world energy source consumption in the last 47 years, reported by the International Energy Agency (IEA) [1] (Figure 1.2), despite the slight growth of non-fossil energy consumption, fossil fuels have been the primary energy mostly exploited, hoarding in average the 85 % of the world energy consumption since 1971 up to 2016.

Figure 1.3 shows the primary energy consumption in 2016 reported by the BP Statistical Review of World Energy [6]. The percentage calculation is on the basis of 13276.3 million tonnes of oil equivalent of primary energy consumption for the year 2016. From this figure, it is confirmed that 85.52 % corresponded to fossil fuel (33.28 % oil, 24.13 % natural gas and 28.11 % coal), whereas Nuclear Energy corresponds to 4.46 %, hydroelectricity to 6.86 % and renewable only reached 3.16 % .

Despite the previous pollution problems related to the fossil fuel burning, its higher conversion yields and less energy losses in the conversion into secondary energy of fuel compared to flow energies, make them still more attractive to supply our energy demand.

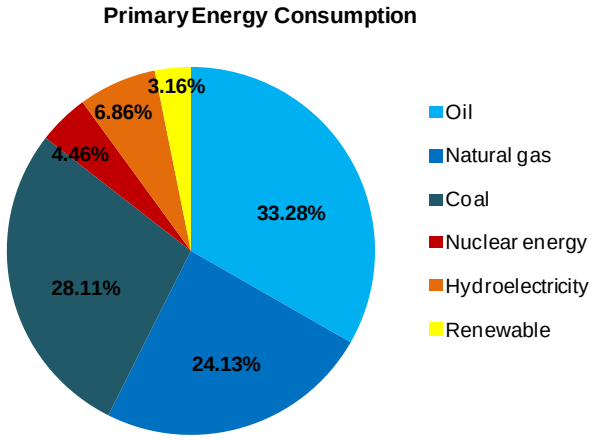

Data Source: B. Dudley, S. Dale, BP Statistical Review of World Energy. June 2017, (2017) 49. http://www.bp.com.

Figure 1.3. Primary Energy consumption. Percentages based on the 13276.3 million tonnes of oil equivalent of primary energy consumption [6]

Moreover, in order to avoid more dangerous climate change and continue with our current wasteful energy lifestyle, it is necessary to decline the use of fossil fuels and develop technologies based on renewable energy, which represents a kind of energy extraction more environmentally feasible. On this regards, next, it is described briefly the basic principle, some advantages and disadvantages of the renewable energy source.

1.2. Renewable energy source

As it was mentioned above, primary energy is classified in two ways: fuel and energy flow. Although both of them are natural resources, in renewal terms, the first group is called non-renewable resources due to its very long renewal time so its use contributes to a progressively depletion. Otherwise, energy flow like wind, hydro, oceans, solar and geothermal energy, are called renewable energy source because they are always available and naturally resupply in very short time. This fact makes them accessible to use them again and again.

1.2.1. Wind power [7]

The wind power is the conversion of the wind movement (kinetic energy) into electricity or mechanical energy by using wind turbine or windmills, respectively. Figure 1.4 shows some of the main parts of a wind turbine. Therefore, in the wind turbine, the conversion of the primary energy into secondary occurs basically when the wind force makes spin a three (or two) bladed rotor in a vertical (or horizontal) plane. The spinning movement of the rotor is transferred through a main shaft toward a generator, where the electricity is generated.

Before and during the installation of wind turbines, there is contamination produced due to their construction and besides related to transportation to the wind farm. But once the wind turbine is installed, the energy output does not emit greenhouse gases, and no air pollution or acid rain is produced. As wind is a free natural source, operational costs of wind turbines could be close to zero and its price can be independent from fossil fuel trade.

Accordingly to the World Energy Council, the world wind power generation capacity reached at 435 GW in 2015, whose global wind power generation resulted in 950 TWh. At the end of this, Spain was the fourth country in the world in terms of wind power generation with 4.47 Mtoe per year (megatonne of oil equivalent per year) [8]. In 2017, the energy produced by wind power in Spain was 47886 GWh, according to the Wind Business Association (AEE for its acronyms in Spanish). It converted the wind power in Spain, in the second technology most used, covering 18.4 % of the electrical demand in 2017. As an important data, the use of this wind power avoided the emissions of 28 MTon of CO_2 [9].

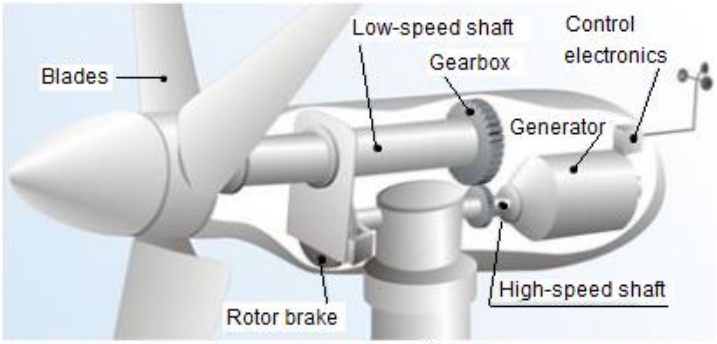

Source: O. Gökhan Eğilmez, Gürsel A. Süer,Özgüner, World ' s largest Science , Technology & Medicine Open Access book publisher:, Des. Control Appl. Mechatron. Syst. Eng. (2012) 135–152. doi:10.5772/67458.

Figure 1.4. Basic principle of a wind turbine [10]

Now, although the environmental and energy advantages offered by this kind of technology cannot be denied, there are detractors of wind power, who proclaims different disadvantages, such as killing thousands of birds by hitting them with the propeller. However, other disadvantages can be stated such as:

- **Unsteady electricity generation:**

Wind is caused by irregular heating of the atmosphere due to the sun. As it is a natural resources that cannot be controlled by man, the output energy is intermittent. To overcome this limitation, wind turbine are often used in parallel with other energy sources (hybrid systems) [7].

- **Expensive wind turbines:**

Although wind turbines are mega structures and their installation require manufacture and transportation costs, the rapid growth and technological advances have gone down the production cost of wind power plant [7].

- **Large areas for wind farms:**

Wind farms use 4 - 20 hectares of land per megawatts generated (ha/MW), but every wind turbine occupies only 0.43 ha/MW, which means that, in between, the area can be harnessed for agriculture, pasture for livestock or walking routes.

- **Visual contamination:**

Wind turbines are huge towers that can reach 140 m in height, that are often placed on high places to trap efficiently the power contained in the wind (power output increases cubically with wind speed). These mega structures impact the beauty of the countryside, either because they are considered as a visual pollution or because they are a nice sample of technology advancement.

- **Noisy pollution:**

The propeller spinning movement and its effect of flickering shadow represent a problem more related to the coexistence with neighbourhood.

1.2.2. Hydropower

Hydropower refers to the conversion of the kinetic energy held in water flowing into electricity. This transformation from primary energy into secondary is similar to the wind turbines, but instead of wind energy, in this case water energy is used.

Basically, in hydro power plants (Figure 1.5), the potential energy contained in stored body water or upstream river causes the spinning motion in turbine blades. This mechanical rotation energy is transferred from the turbine through a main shift up to a generator, where electricity is produced. Unlike wind power, where the wind flows naturally through wind farms, in hydropower, the water is stored in dam (man-made reservoirs) and driven through channel called penstocks down the turbine. These dams elevate the river's water level creating a falling water, whose hydraulic head is the potential energy contained in the stored body water. Despite electricity can be obtained from regular river flow, these "run-of-river systems" work only for residence electricity, meanwhile dams increase water flow and efficiencies for large-scale electricity generation.

Hydropower is considered as a renewable energy source due to the use of water and because the water cycle ensures the continuity of river, lakes and streams flow. Moreover, hydropower plants are not

completely free from CO_2 release due to the main contamination produced during their construction. But once the hydroelectric plant is built, the electricity produced is clean and does not emit greenhouse gases.

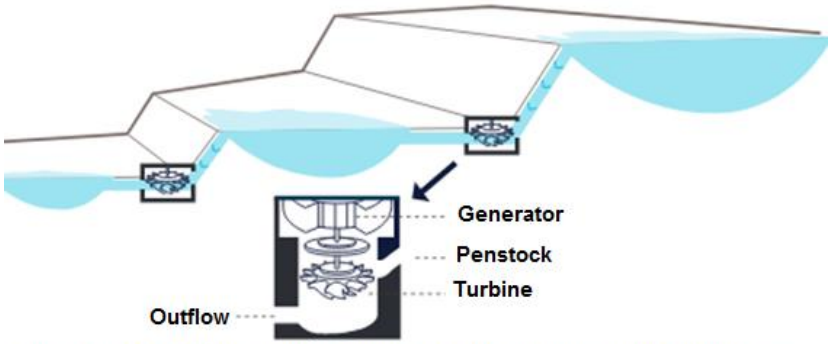

Source: Statkraft, Hydropower, (2009). https://www.statkraft.com/globalassets/old-contains-the-old-folder-structure/documents/hydropower-09-eng_tcm9-4572.pdf (accessed February 28, 2018).

Figure 1.5. Basic principle of a hydroelectric plant [11]

Initial costs for dams construction are considerably high, however, as water is not affected by fossil fuels trade, the electricity output does not depend on market volatilities and maintenance cost are usually low. Regarding efficiencies, there are some losses related to frictions forces in channels and turbine and, resistance wire in electricity transportation. Even though, due to the mechanical energy of water is high quality energy, its efficiency conversion into electricity is higher than 90 % [12], which make it interesting on one side.

Respect to environmental and social aspects, hydropower presents very important drawback, mainly because huge dam are built on rivers. It alters the natural flow of rivers or lake, modifying ecosystems or blocks the migratory fish course. Additionally, water reservoirs mean to flood large areas around rivers, it creates a social effect due to the local communities' displacement. Also, sudden floods, drought or high emissions of CO_2 and CH_4 due to the rotten plant underwater could make this technology no attractive for local people around hydropower plants.

Accordingly to the IEA, since 1971, the world electricity generation from hydropower plants has increased 1204.6 TWh up to 3888.3 TWh in 2015. The BP Statistical Review of World Energy, 2017, reported for 2016, China was the largest producer of hydroelectricity, 263.1 million tonnes oil equivalent, and meanwhile countries such as Canada, Brazil, US, Russia, Norway produced 87.8, 86.9, 59.2, 42.2 and 32.4 million tonnes oil equivalent, respectively. For Spain, this hydroelectricity production reached 8.1 million tonnes oil equivalents.

1.2.3. Oceans power

The energy contained in the oceans is another kind of hydropower whose energy source is based on the oceans movement produced from natural energy flows like wind. Although it exists six kind of oceans energy, i) ocean wave, ii) tidal current, iii) tidal range, iv) ocean current, v) ocean thermal energy and vi) salinity gradient, only the two firsts are most advanced in researching [13]. Due to waves are generated

by the constant wind blowing near the surface of the sea and tide by natural gravitational forces between moon and sun, these two phenomena are classified as renewable energy sources.

Concerning the energy stored in **ocean waves**, it is caught from the surface waves of pressure fluctuations below the surface of the sea. The waves energy devices are regularly installed near shore or offshore at surface level of water. Then, there are basically four applications for oceans waves energy capturing: terminator device, attenuators, point absorber and overtopping devices. For further information about their operational fundaments, we suggest next literature [14][15].

Tidal power on the other hand, is caused by the constant rotational movement of the Earth and the moon, which creates daily, a periodic and vast movement of the oceanic water. This periodic movement of rising and falling sea is harnessed to produce electricity.

Similar to hydroelectric plants, the electricity coming from natural water flow is created by turbines. But unlike hydropower in dam, where water flows in one forward direction, in tidal power the water flows in and out the turbines, hence, tidal generator is designed to work in whatever direction the rotor blades is turning. It adds cost to the equipment. For tidal energy capturing, there are two type of tidal energy systems: tidal barrage and tidal stream. For more detailed information on operational fundaments of tidal systems, check next literature [16][17].

In general words, the regularity of oceans waves and tide allows ocean power be more predictable [16] compared to wind or solar power. On the other hand, although the ocean energy is renewable, its energy capturing facilities are not environmentally friendly due to the activities related in manufacturing, operation, maintenance and decommissioning of the oceans power facilities.

One important drawbacks of this technology is related to the alterations of the natural sea environment, where benthic communities can be affected by factor such as changes in the flow patterns, wave structures or sediments. Other disadvantages such as physical interactions between animals and tidal turbines, acoustic impact (noise disruption, vibrations) and energy removal on physical system can create adverse effects and negative impact on floral and faunal species. Electromagnetic fields by subsea cables, disruption of the biota and habitats, competitions for space and most likely pollution due to wave or tidal structures or sediments are drawback as well, of these technologies [13][18].

1.2.4. Geothermal power

Geothermal energy is the thermal energy that comes from within the Earth. This heat is produced continuously, therefore, geothermal energy is a renewable energy source.

The inner core of the Earth is solid iron and its temperature is higher that the sun's surface temperature. Next outer core is magma (molten rock). Mantle and crust are next layers, where mantle is a combination between magma and rock, and the crust is the outermost layer of Earth. This outer layer is broken into tectonic plates and the magma comes near the Earth's surface and there is when volcanoes occur [19][20].

Nowadays, geothermal power represents an economic challenge in the development of technologies related to the distribution of geothermal resources. Firstly, as the geothermal resources are not evenly distributed on Earth, which is a natural fact, updated surveys to locate those geothermal goals are required. Concerning the design of geothermal power plant and the core drilling more detailed studies have to be carried out on the geological and geothermal features of the locality: permeability of the rock in the vicinity of the geothermal resource, intensity and abundance of the surface hydrothermal systems. Additionally, geophysical surveys are required as well: aeromagnetic studies and remote infrared spectral techniques.

The geothermal power conversion is basically the conversion of thermal energy contained in geothermal fluid into mechanical energy, and this latter into electrical energy through a generator. Since the last 30 years up to now, most of the geothermal power plant use steam turbines, whose dry steam is generated by single or double flash (1.5 GW) using organic Rankine cycles (ORC) [19]. For more information about geothermal energy, we suggest next literature [19][21] and about efficiencies of geothermal plants [22].

1.2.5. Solar power

Solar power is the harnessing of solar energy to produce other type of energy directly usable, such as electricity or thermal energy. The main interest on this natural source is due to the sun is the most plentiful energy source on Earth. Daily, the Earth absorbs 120 petawatts of solar energy. This energy is quite enough to supply energy demands for above 20 years [23].

Numerous researchers have investigated solar power for many applications: solar thermoelectric cooling technologies [24], solar energy for water desalination technologies [24], solar powered aircraft [25], solar water pumping systems [26], solar drying applications [27], solar thermal applications [28] and solar cookers [29], etc. At large scale, there are four techniques to concentrate the sun's energy: (i) Linear Fresnel reflector (IFR), (ii) Parabolic trough, (iii) Central receiver and (iv) Parabolic dish. Figure 1.6 shows the configuration of these concentrated solar power (CSP).

The basic principle of CSP consists in concentrate large area of solar radiation onto smaller area through mirrors or lenses. This concentrated energy is converted into heat and transferred to a fluid (air, water or oil) and later, this energy is transformed into electric power [23][30]. The configuration and location of the mirror gives rise to the different techniques commented above. For instance, in **IFR** systems (Figure 1.6 (a)), a series of flat or slightly curved mirror are settled in parallel in a linear configuration. The mirrors reflect the sunlight onto a linear receiver tube, which contain fluid that is heated due to the light incoming. This heat produce electrical energy by means of a steam generation.

The temperature reached with this arrangement is 390 °C and its annual efficiency (solar to electricity) is 13 % with a capacity between 10 - 200 MW [23][31]. IFR system uses reflectors cheaper than parabolic trough systems [30].

Parabolic trough system (Figure 1.6 (b)) is also a linear concentrator that uses parabolic trough sunlight collectors. Unlike IFR system, where the tube is located above the mirrors, in parabolic trough the receiver tube is placed along the focal line of the parabolic reflectors [31]. Among all four configurations, this is the most mature CSP technology. It produces heat at 350 - 550 °C and its capacity is between 10 - 300 MW with an efficiency that ranged between 11 - 16 % [30][31].

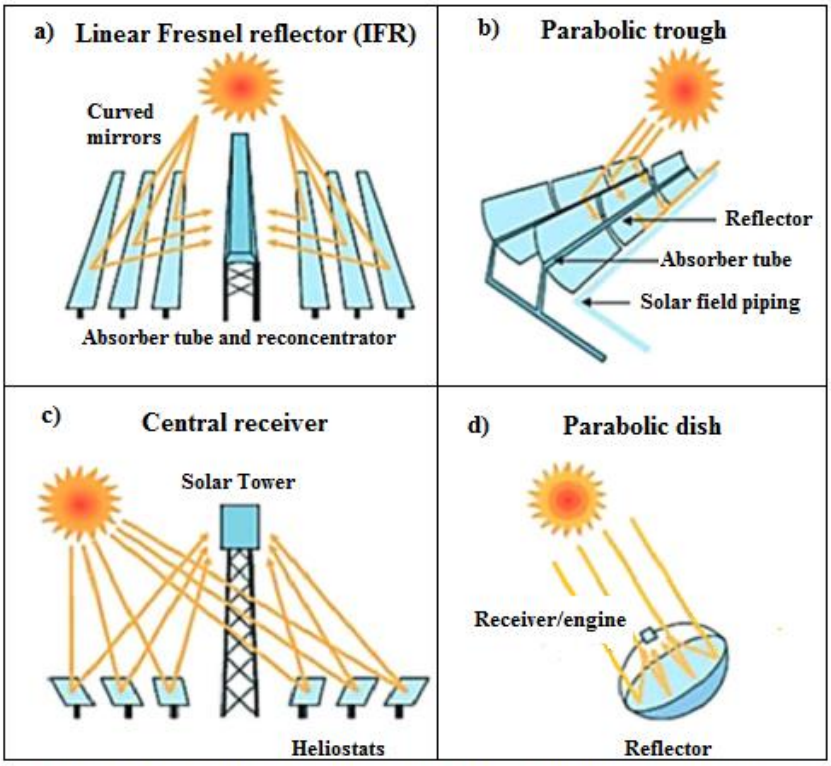

Source: J. Khan, M.H. Arsalan, Solar power technologies for sustainable electricity generation - A review, Renew. Sustain. Energy Rev. 55 (2016) 414–425. doi:10.1016/j.rser.2015.10.135.

Figure 1.6. Concentrated solar power (CSP) [23]

In a **central receiver** system (Figure 1.6 (c)), a set of flat mirrors (heliostats), which turns in the direction of the sun, reflects the solar radiation toward a solar tower. In this latter, also called central receiver, the concentrated radiation heats a fluid , which can be a molten salt to generate steam and later produce electricity [23]. Although this technique is still in pilot commercial projects, increases the annual efficiency up to a 20 % with a capacity of 10 - 200 MW.

Parabolic dish system (Figure 1.6 (d)) shows the highest annual efficiency among the four CSP technologies (12 - 25 %) though it presents high cost and the heat transfer section needs an important number of equipments [23]. The configuration of this technology consists in a parabolic dish mirror where the incoming solar rays are reflected toward a receiver. The concentrated solar light in the receiver is converted to thermal energy and also electrical energy [30].

1.3. Hydrogen as energy carrier

Hydrogen (H_2) is one of the simplest material in the universe with the smallest molecular structure. Although it is one of the most abundant substances, on Earth hydrogen is only available bonded to other compounds, mostly to carbon and oxygen. The latter converts H_2 in an indirect energy source, which means that, to make use of its large chemical energy, it is necessary to utilise other energy source [32][33].

The main interest toward the H_2 settle on its calorific power, which is around three times the energy contained in the same amount of natural gas (143 vs. 53.6 MJ/kg, respectively) [32] . Additionally, this interest lays on the high efficient energy conversion of H_2, which means that it is easily converted to other kind of energy. Also, the higher Higher Flammability Level (HFL) and Lower Flammability Level (LFL) than most of the conventional fossil fuels make H_2 a very potential energy carrier fuel. Also, H_2 is a friendly energy carrier as its combustion only produces water, which helps to mitigate climate change [34][35][36]. As a fuel, H_2 can be used in systems such as internal combustion engines, turbines, heaters and also fuel cells, which covers sector of the economy such as transportation, power, buildings and industry. Therefore, the replacement of fossil fuel devices by H_2 systems would be not only good to reduce greenhouse gases emissions, but also to increase lifespan of those systems [37].

Regard to the H_2 flammability levels, the big gap between LFL and HFL allows to produce combustion engines or turbines able to work under softer conditions. For instance functional car engines under low pressure conditions such as high altitudes or low temperature conditions in winter [32]. Table 1 shows properties of the most common fuels. H_2 presents the highest octane number, which measures the anti-knock capacity of a fuel under compression conditions inside the combustion chamber of an engine. At high pressures, the fuel temperature increases and if this temperature exceeds the auto ignitions level of the fuel, the fuel suffers the combustion. Therefore, the higher the fuel octane number, the higher the motor efficiency.

Table 1. Properties of some common fuels [32]

Fuel	Energy per kilogram (MJ/kg)	Flammable range (%)	Octane number
Hydrogen	143	4-75	> 130
Methanol	-	6 -36.5	-
Methane	55.6	5.2-15	125
Propane	49.6	2.2-9-6	105
Gasoline	46.4	1-7.6	87
Diesel	45.4	0.6 -5.5	30

Taking into account all the advantages of H_2 as a clean and efficient fuel, it is possible to expect it as the "future fuel", but in order to replace fossil fuel by H_2, it needs to be produced in comparable scale, costs and efficiencies as fossil fuel generation. Therefore, as H_2 is only available bonded to other compounds and not as a pure gas in the nature, it is really important to investigate on "green" H_2 resources and the development of technologies through which, H_2 can be obtained at industrial scale and the technologies itself, are efficient and environmentally friendly.

1.4. H_2 generation methods

H_2, as one of the most abundant component in the universe (75 %), cannot be directly usable as it is not present naturally as a pure substance. Therefore, to harness the large amount of energy contained inside its structure, firstly, it is necessary to (i) "extract" H_2 from its different sources and obtain it as pure as possible and (ii) harvest it. Both steps are big challenge if we consider the premise of H_2 as a green and clean fuel. Nowadays, H_2 is obtained by different methods, being most of the H_2 generation still based on non-renewable sources. For instance, around 50 % of the global H_2 generation is from steam methane reforming (SMR), 30 % from oil reforming, 18 % coal gasification and only 3.9 % from water electrolysis and 0.1 % from other sources such as renewable feedstock like biomass [35].

Figure 1.7, summarizes the different H_2 sources, from where, different methods are applied to obtain H_2. For example H_2 generation by photosynthesis in algae, steam reforming, partial oxidation (POX) or auto-thermal reforming (ATR) of natural gas, biogas and oil, gasification of coal, alcohols reforming from gas or biomass, power from water electrolysis using renewable energy sources and biomass pyrolysis [38]. In the literature the H_2 generation method is commonly classified by its energy source. Table 2 shows this categorization.

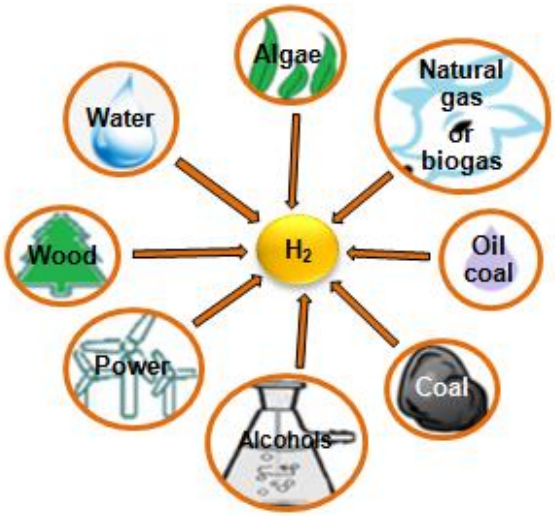

Figure 1.7. Hydrogen sources adapted from [38]

1.4.1. Hydrogen from fossil Fuel

From fossil fuel, H_2 can be obtained from natural gas, coal oil and coal. Regarding the method utilized to extract H_2 from these materials, there are four main methods: (i) SMR, (ii) POX and (iii) ATR and (iv) gasification [32][35][38].

- **SMR (Steam Methane Reforming)**

It is the most popular and economical method to obtain H_2 in large scales [39][40]. It carries out an endothermic conversion between methane and vapor into H_2 and carbon monoxide (CO). The required heat comes from feed-gas methane combustion and the CO produced can further react with water to produce CO_2. Although SMR has high greenhouse gas emissions, it works under relatively soft conditions: 700 - 850°C and 3 - 25 bar and it presents high hydrogen efficiencies.

- **POX (Partial Oxidation of Methane)**

Although the overall reaction is exothermic, which allows more compacted systems, intermediary reactions require high temperatures. The POX used pure oxygen feed, whose requirement adds costs and complexity to the process due to oxygen separation units. This method also produces byproducts such as CO and CO_2.

- **ATR (Auto-Thermal Reforming)**

It is a combination of SMR and POX methods. It emits CO and CO_2 as well, but its operational conditions are milder than POX. ATR and POX methods presents lower efficiencies than SMR.

- **Coal gasification**

Coal gasification carries an endothermic carbon conversion to CO and H_2 through the partial oxidation of carbon in solid state with steam and O_2. Although this method is commercially mature and it is technically a practical option for H_2 generation at industrial scale, it shows environmental and economical drawbacks. The reaction requires high temperature and pressure and the reactor itself is more complex and more expensive than the ones used in the natural gas conversion. As coal has high content of carbon, large amounts of greenhouse gases are released, such as CO and CO_2. The latter comes from further water-gas shift reaction, which transforms CO into CO_2. [32][35][38].

Table 2. H_2 generation methods

H_2 Source	Energy Source	Method
Fossil fuel: Natural gas, coal oil and Coal	Electricity Thermal	SMR, POX and ATR Gasification
Water	Electricity Thermal Chemical Photonic	Electrolysis Thermolysis Thermo-chemical
Biomass: Lignocellulosic matter, biofuels, algaes, bacteria	Thermal Chemical Bio-chemical photonic	Pyrolisis Gasification thermo-chemical Biofuels reforming Dark fermentation Photo-fermentation

1.4.2.H_2 from water

- **Water electrolysis**

The water electrolysis is the conversion of water into H_2 and O_2 using electrical energy in an electrolysis cell. Basically, in an electrolysis cell there are two compartments separated by a membrane. A power supply is connected between two electrolyzers: an anode and a cathode. The electricity forces water molecules to decomposed into O_2, ions of hydrogen (H^+) and electrons ($\bar{e}$). Therefore, $\bar{e}$ flow from the anode toward the cathode and the H^+ ions flow toward the cathode compartment through a membrane. This latter keeps separated both compartments and avoid gases diffusion [41]. On the other side, in the cathode compartment, electrons react with the H^+ ions, producing a gas of H_2.

The medium, where the cathode and anode reactions happen, is the electrolyser. The most common and mature electrolyser technology is the **KOH dissolution**, an alkaline electrolyser (20 - 30 percent in weight, wt.%) whose operational temperature and pressure are lower than 100 °C [41] and no more than 25 bar [38], respectively. Differently to the liquid electrolyte, polymer membranes (PEM) and solid oxide (SOE) are also used.

PEM electrolyser does not require a liquid electrolyte, which can benefit toward more compact and simpler system than alkaline electrolyser. Its turndown ratio is higher than alkaline dissolution as with PEM electrolyser it is possible to operate under some hundreds of bar. Moreover, the acidic PEM shows short lifetime, is expensive and still present low efficiencies [38][42].

SOE electrolyser is based on high-temperature electrolysis where the water splitting occurs at 1000 °C, which helps to reduce the power supply to the electrolysis cell and increase the efficiencies as at these high temperatures the reaction is more reversible. The main drawback of this kind of technology is related to materials that can support thermo-mechanical stress [38]. This technology can be classified as a hybrid technology that combines ***electrical and thermal energy*** to produces H_2.

Concerning the electrode materials or electro-catalysts, the water electrolysis research is focused on two objectives: (i) develop electrode materials with high electro-catalytic power and (ii) reduce the power supply to the electrolysis cell. The investigation on electrode materials is focused on increasing the active surface area, which is possible making electrodes more porous [41], but it implies an increase in cost and also increasing the electro-catalytic power for the H_2 evolution.

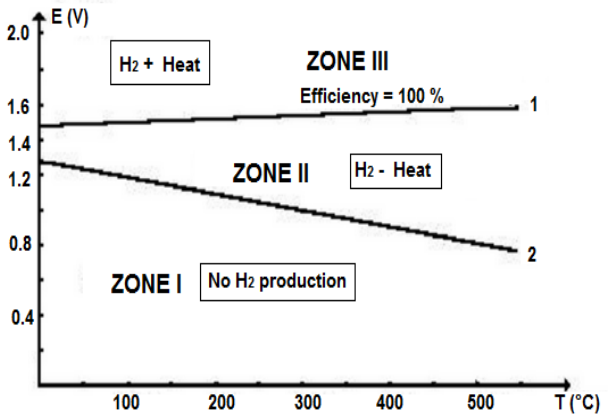

Source: J.C. García, Producción de hidrógeno mediante electrolizadores. Estado del arte de la tecnología. - Ingeniería Química, Prod. Hidrógeno Median. Electrolizadores. Estado Del Arte La Tecnol. (2012). http://www.ingenieriaquimica.net/articulos/302-produccion-de-hidrogeno-mediante-electrolizadores-estado-del-arte-de-la-tecnologia-electrolizadore (accessed March 8, 2018).

Figure 1.8. Potential vs. Temperature for H_2 generation by electrolysis [41]

With respect to the power supply, it is necessary to apply a minimum potential to make the electrolysis possible. In Figure 1.8, this potential is represented by the line 2, and below this value (zone I), the electrolysis does not happen, even at high temperature. In the zone II, additional to the power supply, heat is also required to produce H_2. It means, in the zone II, the electrolysis reaction is endothermic.

The zone II can be classified as a hybrid form of energy, which combines ***electrical and thermal energy*** to produce H_2 [35]. Above line 1, the H_2 generation by water electrolysis is exothermic, which means that the electrical energy supply is used to produce H_2, but additionally, heat is produced as well [41]. In the last case, line 1 represents a thermo-neutral potential where the efficiency of the electrolysis cell is 1. Therefore, the higher is the potential above line 1, the efficiency decreases, and the lower is the potential in the zone II, the efficiency increases up to 1.2, which is the ideal value, that is possible only under reversible conditions.

Considering all the information presented, although the H_2 produced from water electrolysis is absolutely clean if the power supply comes from a renewable energy source, this technology is still expensive, presents low system efficiency and required electrical power expenses. Besides, as some electrolyser are highly sensitive to water purity, a desalinization and demineralization is needed, affecting operation and maintenance costs [35].

- **Water splitting by photocatalysis**

The water splitting is the conversion of water into H_2 and O_2 by using semiconductors materials and light. Since 1972, when Fujishima and Honda found out the H_2 and O_2 evolution on a titanium dioxide (TiO_2) electrode irradiated under ultraviolet light (UV) [43], the photocatalytic water splitting has been a promising technology to generate a kind of clean fuel, H_2.

The basic principle of this reaction consists in the excitation of electrons located in the valence band (VB) of a semiconductor material by using photonic energy. When this energy is transferred to the electrons, they "jump" to the conduction band (CB), from where, further reactions go on and H_2 is involved.

Although this reaction seems to be a potential solution to overcome problems related to the depletion of fossil fuels and the pollution related to their use, the water splitting still presents low efficiencies. There are three general causes for these low efficiencies towards H_2 in photocatalytic processes: (i) a reverse reaction between H_2 and O_2; (ii) photogenerated electron-hole recombination (e^--h^+), and (iii) a limited capacity in light absorption. In chapter 2, section 2.2 more detailed information about this topic is presented.

- **Water thermolysis**

The water thermolysis is a reversible process that implies the conversion of water into H_2 and O_2 in one step, using only thermal energy. This technology needs, as minimum, temperatures of 2500 K (under 1 bar) to obtain a minimum grade of dissociation of the water (4%). At 3000 K and 1 bar, the grade of dissociation reaches a 64 % [35][44]. These lower dissociation percentages are due to the recombination of the species involved in the reaction, such as H_2, O_2, hydroxyl ions and atomic hydrogen.

To avoid this recombination, the reaction should be stopped by instant cooling (in the order of milliseconds (ms) or by H_2 separation at high temperature inside the reactor. For the first option, product gas quenching is added to the reactor [35][45]. The main drawback of this technology is the high operational temperatures and the kind of energy source used.

In order to make this technology "green", renewable energy sources are being investigated to reach up to these high temperatures. One example is the solar water thermolysis, which involves the use of concentrated solar energy for the thermal decomposition of water to generate hydrogen [44]. This method is a hybrid technology that combines ***thermal and solar energy*** to obtain hydrogen. It is still under development.

- **Thermo-chemical splitting of water**

Under the same principle of the water thermolysis, thermochemical water consists in splitting water into H_2 and O_2 by using heat and several chemical reactions shown below. In this case, the chemical energy is used to reduce the thermal energy requirement [35][37], which compared to the water thermolysis, the operational temperature of this method is relatively low (600 - 1200 K). This method is a hybrid technology because combine ***thermal and chemical energy***.

(1) $H_2SO_{4(ac)}$+ Q (300-500)°C→$H_2O_{(g)}$+$SO_{3(g)}$ (Thermal decomposition)
The product gases are separated and $SO_{3(g)}$ heated up to temperature of next reaction

(2) $SO_{3(g)}$+Q (800-900)°C→½$O_{2(g)}$+$SO_{2(g)}$ (Thermal decomposition)
$SO_{2(g)}$ is separated from O_2.

(3) $SO_{2(g)}$ + $I_{2(g)}$+2$H_2O_{(l)}$→2$HI_{(g)}$+$H_2SO_{4(ac)}$ Exothermic reaction
(4) 2$HI_{(g)}$ + Q (425-450)°C →$H_{2(g)}$+$I_{2(g)}$ (Thermal decomposition)

The thermo chemical splitting of water is considered as a clean and sustainable method for H_2 generation, as it shows low electrical energy demands and the reagents are recycled for thermochemical cycles. Compared to the water thermolysis, this technology does not need O_2-H_2 separation and though this method entails robust materials and high volumes, materials are low cost and the technology is reliable [35].

1.4.3. H_2 from biomass

The biomass is one of the most abundant renewable energy source in the nature. It is defined as the renewable organic matter derived from vegetal or animal nature and also, the material coming from the natural or artificial conversion of vegetal and animal matter. Therefore, biomass can be a product derived from agricultural, forestry and energy crops waste, wastes from forest and agro-food industries, urban waste and livestock waste [46][47][48].

Biomass, as a primary energy source, has its energy stored inside its matter, similar to fossil fuel, therefore, the transformation of its primary energy into secondary, in some cases is also similar to fossil fuel. Although the combustion of biomass is one of the most common way to obtain thermal or electrical energy, its high moisture content make this conversion low efficient, with high requirements of energy and investment due to the drying process [46].

Regards to the H_2 generation, the biomass conversion methods can be classified as thermo-chemical and reforming.

- **Thermo-chemical conversion of biomass**

It consists in the biomass treatment at relatively high temperatures, which could produce solid, liquid or gaseous products depending on the temperature [47]. Although energy extraction from biomass by thermal-chemical conversion can be done by burning, pyrolysis and gasification, only the two latter are considered promising technologies for commercialization of H_2 generation from biomass [38].

Briefly**, burning** wood is the most common and direct form to obtain energy from biomass. The disposable energy after burning varied in functions of its nature, for instance, 8 MJ/kg from the combustion of green wood and 20 MJ/kg from dry plant matter [48]. Similar to fossil fuel, when biomass is combined with O_2 in a high temperature environment, CO_2 and water vapor is generated. But, unlike fossil fuel combustion, burning biomass is a cleaner and an efficient combustion if the right amount of fuel and O_2 are mixed at the right temperature during the right time [49]. Furthermore, biomass is renewable, so its supply is insured for the future, what does not happen with fossil fuels.

Pyrolysis is the chemical decomposition of biomass under 400 - 500 °C and deaerated conditions (without O_2) [47][50]. H_2 is produced from pyroligneous oils, which are produced from the pyrolysis of lignocellulosic biomass [48]. The lignocellulosic biomass refers to plant biomass that is composed of cellulose, hemicellulose, and lignin, for instance: wood, agricultural residues such as corn, straw or municipal solid waste like kitchen waste.

In general, the type of products from the pyrolysis depend on the nature of the biomass and its transformation conditions, and can be gases such as H_2, CO and CO_2 and hydrocarbons, liquid fuels or carbonaceous waste. The coal gas is widely obtained from pyrolysis, which is a mixture of H_2 (around 50%), CO and CO_2 [50].

Gasification consists in the incomplete combustion, where its temperatures are between 700 - 1500 °C and O_2 fraction is between 10 - 50 %. The gaseous proportion of the gaseous final product is a mixture of CO, CO_2, CH_4 and H_2. The content of H_2 in the final gas varies depending on the reactions conditions, [50]. Also, according to the temperature under which the gasification is carried on, the process is called either as auto-thermal or thermal, therefore under auto-thermal conditions, the heat is provided from the incomplete combustion in the gasifier [35].

- **Biofuel reforming**

Biofuel is defined as any fuel whose energy is obtained through the conversion of CO_2 into organic compounds that can be found in living organisms [51]. In other words, biofuel is any hydrocarbon fuel produced from biomass in a short period time. Although the latter makes biofuels a renewable energy source, not all biofuels are completely cataloged as green energy. This is because some of them release

greenhouse gases, but these greenhouse gases are more related to the energy invested to produce biofuels crops and converting the feedstock into biofuels before any energy is obtained [51]. Liquid or gaseous biofuels such as ethanol, biodiesel, methanol or biobutanol can replace fossil fuels mainly by two factors: cost and availability [51]. On one side, in the case of fossil fuels, their availability is limited until they run out. Then, in the future, the fewer the fossil fuels stockpile are, the more complex is its extraction from the ground, which would add important cost to this sort of fuel. On the other side, a third factor represent a drawback for biofuels: food supply competition [52].

This latter factor is related to the use of land for "biofuel crops". Due to biofuels are produced from biomass, biomass crops are required to produce the necessary feedstock for biofuels production. As our current and most likely future involves increasing energy and food demand far out-pace the earth ability for land, which might make an economy based absolutely on biofuels not feasible in these terms. These limitations have encouraged researchers to find alternatives to overcome the biofuels feedstock: oils, sugars, starches, lignocellulosic compounds, and waste and residues [53][54].

Regard to the H_2 generation, bioethanol and glycerol seems to be two strong alternatives as feedstock. Both of them can be found either as a waste or a by-product in some processes related to biomass transformation. On one hand, bioethanol production is possible from the bagasse of the sugarcane, which is the lignocellulosic residue after the sucrose extraction [54]. The steam-reforming process (ESR) "extract" the H_2 from the ethanol and water stoichiometrically as follows [55]:

$$CH_3CH_2OH + 3H_2O \rightarrow 6H_2 + 2CO_2 \Delta H° = 173.4 \text{ kJ/mol}$$

These ESR requires three mol of water per mol of ethanol. Although this reaction is endothermic, comparing the ethanol reforming with other hydrocarbons such as methane, the extraction of 1 mol of H_2 from ethanol requires only 32.22kJ/mol instead of 72.82 kJ/mol from methane. On the other hand, glycerol is a by-product of the biodiesel production and represents *ca.* 10% of the products obtained. The crude glycerol coming from biodiesel production contains overload amount of alcohol, and also some inorganic salt and soap. Hence, so as to it can be used as a feedstock, major purification or refining is required [55].

Different studies on uses for glycerol have highlighted the H_2 production or synthesis gas by the glycerol reforming [55][56]. Mainly, because the glycerol reforming would not need many changes in the existing industrial processes for H_2 [39]. The global reaction of ESR to extract H_2 from glycerol is:

$$C_3H_8O_3 + 3H_2O \rightarrow 7H_2 + 3CO_2 \Delta H° = 128 \text{ kJ/mol}$$

The molar ratio of H_2 and glycerol is 7:1, which make this reforming reaction attractive. Additionally, the water-gas shift reaction entails extra H_2 generation.
The main drawback of this reaction is its energy requirement for vaporization of the reaction mixture, which reduces yields. For more details about bioethanol and glycerol reforming for H_2 generation, we refer to next literature [39][55][56].

- **Algaes**

Algaes are aquatic organisms that belong to the kingdom Protista, whose size range from microscopy unicellular up to multicellulars organisms that conform larger colonies. They make one of the greatest contributions of O_2 to the world.

Since the Second World War, the use of algae has evolved from the consumption to overcome dietary protein deficiency up to a potential feedstock for biofuels production [57]. As the primary producers in any ecosystem, algaes utilize the solar light to fix atmospheric CO_2 and transform it into organic compounds.

As the algaes growth rate can be improved by additions of micronutrients and aeration, their supply does not depend on seasonal variations. Therefore, compared with other biomass based feedstock, algaes seem to be a prospective raw material for biofuels production [57][58]. Concerning fuels production, the biological H_2 generation is possible through dark fermentation and photo-fermentation [59].

Dark fermentation is the conversion of biochemical energy contained in organic materials to other kind of energy without using light [35] and in the absence of water and O_2 [58]. Fermentative microorganisms hydrolyze complex organic matter to monomers, converting heavy molecules into lighter molecules such as organic acid and alcohols. In this reaction, H_2 is also generated [58].

Carbon feedstock for dark fermentation can be any organic compounds coming from waste. Compared to the photo-fermentation, in industrial scale, the bioreactor used in dark fermentation is cheaper and the control system simpler as well, therefore, the operational cost are diminish [35][59]. As drawbacks, in dark fermentation the H_2 efficiencies are relatively low and the final gas mixture product contains CO_2, which has to be separated and treated to avoid environmental pollution.

Photo-fermentation, on the other hand, is the conversion of biochemical energy stored in organic matter to H_2 and CO_2 by action of photosynthetic bacteria that use solar light as an energy source [58][59]. Similar to dark fermentation, in photo-fermentation processes, different kind of organic waste can be used as substrates.

There are mainly four species of Purple Non-Sulfur (PNS) bacteria through which, H_2 production is performed in photo-fermentation: *Rhodobacter sphaeroides* [60], *Rhodopseudomonas palustris* [61] and *Rhodobacter capsulatus* [62]. These bacteria produce H_2 from conversion of fatty acids to smaller gas molecules containing carbon, for instance CO_2 under anaerobic or anoxic conditions. The bacteria use the nitrogenase enzyme to catalyze the nitrogen fixation, so the molecular nitrogen is reduced to ammonia and H_2 is generated [59]. This may represent a disadvantage due to the fact that the feedstock requires a pretreatment to enrich it with nitrogen.

There are also some other H_2 generation technologies that are still under investigation for implementations and future commercialization [37]:

- Super adiabatic decomposition of hydrogen sulfide
- Sorption enhanced reaction process (SERP)
- Photo electrochemical H_2 production
- Biological H_2 from fuel gases and H_2O
- Two-phase photo biological algal H_2 production
- H_2 generation from Glucose-6-Phosphate

CHAPTER 2

State of the art: Heterogeneous Photocatalysis

2. HETEROGENEOUS PHOTOCATALYSIS

The term "heterogeneous photocatalysis" is used to describe chemical reactions or processes that involve a solid catalyst (in most of the cases) in a "fluid phase" (liquid or gas phase), and light energy to activate the catalyst.

The heterogeneous photocatalysis encompasses different kind of chemical reactions, like oxidation, dehydrogenation, hydrogen transfer, pollutant removal, etc. [63]. In environmental applications, the heterogeneous photocatalysis has been widely used as air or water purification method, which has made it to be considered as a new "Advanced Oxidation Process" (AOPs) [64]. Next sections describe the principles of the photocatalytic reactions, main processes and catalytic materials involved on heterogeneous photocatalyst.

2.1. Fundamentals of photocatalysis

The heterogeneous catalysts are also called surface catalysts because the chemical reaction occurs in its surface, therefore, all the catalytic steps are related to the catalyst surface. Next are the basic steps on a conventional catalytic material [64][65]:

(i) Transfer of the reactants from the fluid phase towards the catalyst surface
(ii) Adsorption of the reactants on the catalyst surface
(iii) Reaction on the catalyst surface
(iv) Desorption of products
(v) Transfer of the products from the catalyst surface towards the fluid phase

For heterogeneous photocatalytic reactions, the reaction on the catalyst surface (step iii) happens as follows:

a) Incident photons absorption
b) Electrons (e^-) and holes (h^+) excitation (also called photogenerated charges)
c) Photogenerated charges migration

Figure 2.1 shows this photocatalytic mechanism, where the photons absorption (step a) occurs only if the photons incoming to the catalytic surface has an equal or higher energy than the band bag (E_g) of the catalyst. When photons with enough energy ($h\nu \geq E_g$) "crash" in the valence band (VB), they photo-excite the electrons located in the VB, which "jump" to the conduction band (CB), leaving in the VB positive holes (step b). Then, electrons and positive holes migrate towards the catalyst surface (steps c), where they could participate in further reactions [63][66][67].

Regarding the further reaction of the photogenerated charges, the final products depend on the initial materials present in the reactor, both in the liquid and gaseous phase. For instance, if the reaction is carried out only in water, steps c2, c3, and c4 tend to take place (**photocatalytic water splitting**)

[66][68][69]. On the other hand, if organic compounds are present under aerated conditions, steps c1, c3 (low probability) and c4 happen (**photocatalytic organic degradation**) [66][70][71]. But if the organic compounds are under deaerated conditions steps c1, c3 (high probability) and c4 take place (**photoreforming**) [72][73][74].

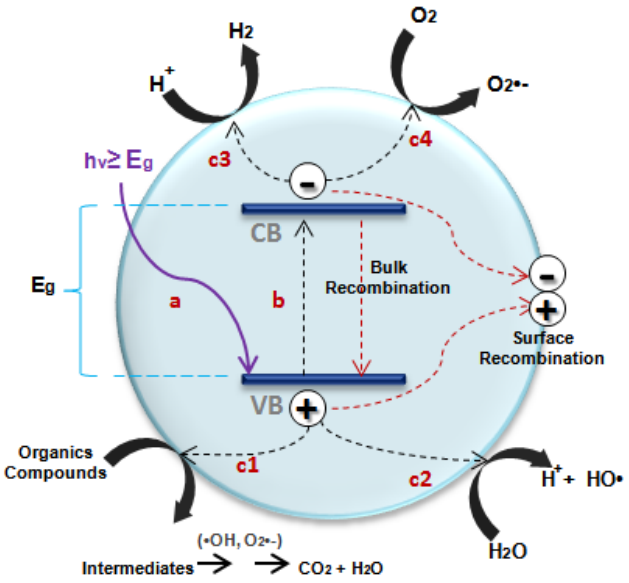

Figure 2.1. Scheme of the photocatalytic mechanism. Source: own elaboration

Another pathway that the photogenerated charges can take, is their backward reaction, either by bulk recombination, which is when electrons from the CB go back to the VB (straight and dotted red line in Figure 2.1), or by surface recombination, where electrons and holes recombine back after migration in the catalyst surface (curves and dotted red lines in Figure 2.1), releasing energy under the light or heat form [63]. Concerning the photocatalytic organic degradation (next section covers the photocatalytic water splitting and reforming in more detail), it is carried out under aerated conditions, where, either the reactor is open to the atmosphere or enriched by bubbling with O_2 or air [67][70][75][76]. Since 1977, titanium dioxide (TiO_2) has been widely investigated in environmental remediation [75][76][77][78][79] due to its photo response under UV light (rutile phase up to 413 nm [79] and anatase up to 387 nm [80]), low cost and toxicity, and thermally and chemically stable [66][79].

Different authors [63][67][79] describe the basic mechanism of photocatalytic organic compound degradation on TiO_2 as it is shown in Figure 2.2. UV irradiation ($\lambda < 400$ nm) on TiO_2 photo-excites electron-hole pairs (e^-/h^+) (Eq. 2.1.1), which leave the VB and the CB with a positive and negative charge, respectively. As it was explained in Figure 2.1, the photogenerated charges might recombine (Eq. 2.1.2), releasing energy, or migrate toward the catalyst surface where they participate in reduction-oxidation (redox) reactions with adsorbed compounds (oxidation reactions in the VB and reduction reactions in the CB).

$$TiO_2 + h_\nu \rightarrow h^+_{VB} + e^-_{CB} \quad (2.1.1)$$

$$h^+_{VB} + e^-_{CB} \rightarrow energy \quad (2.1.2)$$

Before going in more detail about the redox reactions, we want to explain briefly two useful concepts related to the initial materials present in the reactor that subsequently react with the photogenerated charges. They are electrons donors and acceptors. Regarding the electron donors, they are those compounds/chemical species which give their electrons to react with the photogenerated h^+ located in the VB of the catalytic materials. Other "nicknames" to the electron donors are hole scavengers and sacrificial agents [67][70][81]. In this thesis, we use these three names to refer to molecules or chemical species which "trap" holes in the VB. On the other side, the electron acceptors are those compounds/chemical species which accept the electrons located in the CB of the catalytic materials.

Concerning the oxidation reactions in the VB, Patsoura et al. [67][82] said the photogenerated h^+ might act directly or indirectly in the formation of hydroxyl radicals ($^{\bullet}OH$) by the oxidation of water adsorbed on the catalysts surface. Pelaez et al. [66] explained that the h^+ oxidize the hydroxide ions (OH^-) or water to produce $^{\bullet}OH$ radicals (Eq. 2.1.3 and 2.1.4, respectively). Badawy et al. [83] on the other hand, reported the reaction between H_2O and h^+ in the VB to form superoxide ($O_2^{-\bullet}$) and hydroxyl radicals (2.1.5). As $^{\bullet}OH$ radicals are powerful oxidizing agents, and might be also the h_{VB}^+, they are involved in the partial or total oxidation of organic compounds, as it was shown in Figure 2.1, step c1, with the evolution of intermediary products or final products such as CO_2 and H_2O (Eq. 2.1.5 and 2.1.6).

$$OH^- + h_{VB}^+ \rightarrow \bullet OH \quad (2.1.3)$$

$$H_2O + h_{VB}^+ \rightarrow \bullet OH + H^+ \quad (2.1.4)$$

$$2H_2O + 2h_{VB}^+ \rightarrow \bullet OH + O_2^{\bullet -} \quad (2.1.5)$$

$$Organic\ Compounds + h_{VB}^+ \rightarrow Intermediates \quad (2.1.6)$$

$$Organic\ Compounds/Intermediates + \bullet OH \rightarrow CO_2 + H_2O \quad (2.1.7)$$

On the other hand, in the conduction band, as the degradation of organic compounds requires aerated conditions, which means presence of molecular oxygen (O_2), O_2 is absorbed on the electron sites of the TiO_2 surface.

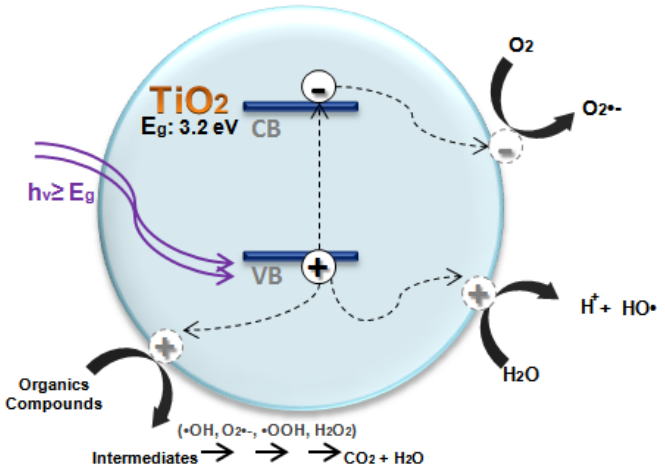

Figure 2.2. Scheme of the photocatalytic degradation of organic compounds. Source: own elaboration

This O_2 traps e^- to form $O_2^{\bullet-}$ radicals (Eq. 2.1.8), which in turns, react with protons (H^+) to produced hydroperoxyl radicals ($HO_2^\bullet$) [66][67][79][82] (Eq. 2.1.9).

$$O_2 + e_{CB}^- \rightarrow O_2^{\bullet-} \quad (2.1.8)$$

$$O_2^{\bullet-} + H^+ \rightarrow HO_2^\bullet \quad (2.1.9)$$

$$Organic\ Compounds/Intermediates + O_2^{\bullet-} \rightarrow CO_2 + H_2O \quad (2.1.10)$$

$$Organic\ Compounds/Intermediates + HO_2^\bullet \rightarrow CO_2 + H_2O \quad (2.1.11)$$

$$HO_2^\bullet + e_{CB}^- \rightarrow HO_2^- \quad (2.1.12)$$

$$HO_2^- + H^+ \rightarrow H_2O_2 \quad (2.1.13)$$

$$HO_2^\bullet + HO_2^\bullet \rightarrow H_2O_2 + O_2 \quad (2.1.14)$$

$$HO_2^\bullet + H^+ + e_{CB}^- \rightarrow (H_2O_2)_S \leftrightarrow H_2O_2 \quad (2.1.15)$$

The products of these two reactions (Eq. 2.1.8 and 2.1.9) are also potent oxidizing agents, therefore they degrade the organic compounds or pollutants toward intermediates or CO_2 and H_2O (mineralization). Some reaction systems are arranged with a constant flow of H_2O_2, which has a remarkable capacity to generate •OH radicals [79].

Romão [81] explained the formation of H_2O_2 by the e^- trapping by $HO_2^\bullet$ radicals (Eq. 2.1.12 and 2.1.13) as a pathway to avoid the recombination and hence to improve the rate in degradation of organic compounds. On the other hand, Pelaez et al. [66] suggested the formation of H_2O_2 by the reaction between two $HO_2^\bullet$ radicals (2.1.14). H_2O_2 - $(H_2O_2)_S$ in solution) might be also produced by the reaction of $HO_2^\bullet$ radicals with protons and e^- (2.1.15)

2.2. Photocatalytic hydrogen generation

Next two sections "*Photocatalytic Water Splitting*" and "*Photocatalytic reforming*" check out briefly, the fundamental concepts of the H_2 generation from the water splitting and the photocatalytic reforming on TiO_2, without going in detail on the literature review about the photocatalytic materials used in every process. More detail about different materials is presented in section 2.3 "*Photocatalytic semiconductors materials*".

2.2.1. Photocatalytic Water Splitting

The photocatalytic water splitting consists in the split or oxidation of H_2O into H_2 and O_2 on a catalytic material activated by light energy. Therefore, in the same way as it was explained in section 2.1 and Figure 2.1, the photo-activation of the catalyst consists basically on 3 steps: a) Incident photons absorption, b) e^- and h^+ excitation and c) migration of the photogenerated charges (in this case c2, c3 and/or c4).

Although in the water splitting is possible to obtain O_2 and H_2 [68], there are many studies more focused on the H_2 generation due to its property as energy carrier [68][72][84]. Then, the photocatalytic water splitting for H_2 generation, unlike the photo-degradation of organic compounds, is carried out under

deaerated conditions (in absence of O_2) in order to promote favorably, the H_2 evolution (step c3 in Figure 2.1) [67][85][86][87][88][89]. Therefore, in this case the reactor is closed to the atmosphere and before the irradiation, is commonly bubbled the liquid phase with an inert gas such as He, Ar or N_2 to take the oxygen out. Another difference with photo-degradation systems is the absence of additional hole scavengers such as the organic compounds.

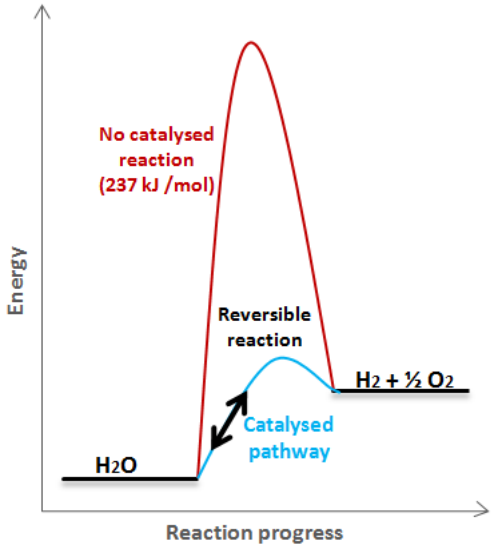

Figure 2.3. Energetic scheme: catalysed and non-catalysed pathway for water splitting [88]

As water is stable at the earth's surface, water splitting is an uphill reaction with positive change in Gibbs free energy ($\Delta G° = 237$ kJ / mol) [90] (Figure 2.3). So, in order to provide this thermodynamic energy with light energy, photons of around 500 nm wavelength are required [88].

Figure 2.4 shows the fundamental principle of the photocatalytic water splitting, where water is reduced in the CB by photogenerated electrons and oxidized in the VB by photogenerated holes [90]. So, regard to the **(i) energetic band positions**, the bottom level of the CB must be more negative than the redox potential of water to generate H_2 (0 eV vs. NHE at pH 0) and the top level of the VB must be more positive than the redox potential of water to produce O_2 (1.23 eV vs. NHE) [91][92]. Therefore, **(ii) the band gap of the semiconductor materials should be, as minimum, higher than 1.23 eV**, which is the theoretical dissociation energy of water [93]. 1.23 eV corresponds to a wavelength of ca. 1000 nm [94].

When it is talked about band-gap of a photocatalytic material, it is also understood that this band-gap energy is the minimum energetic requirement for photons incoming. Which additionally to the bang-gap energy, the photons require to have a higher energy than 1.23 eV in order to overcome the energetic barrier involved in the charge-transfer process between the water and photocatalytic material [94].

Although a band-gap of 1.23 eV seems possible to absorb easily the entire spectra of visible radiation, unfortunately the energetic positions for CB and VB commented above are not enough to satisfy an effective water splitting. Some other fundamental requirements related to semiconductor material are **(iii) long term stability under photo-corrosive conditions**, **(iv) e^-/h^+ lifetime enough long** and **(v) a band**

gap lower than 3.4 eV. The latter has to do with the catalytic activation under solar radiation [94].

About methods to make the e^-/h^+ lifetime longer and reduce the recombination probability, there are two approaches: addition of sacrificial agents (more details in section "*Photocatalytic reforming*") and creating active sites on the surface photocatalysts to separate the photogenerated charges (e^-/h^+) (more details in section 2.3) [90].

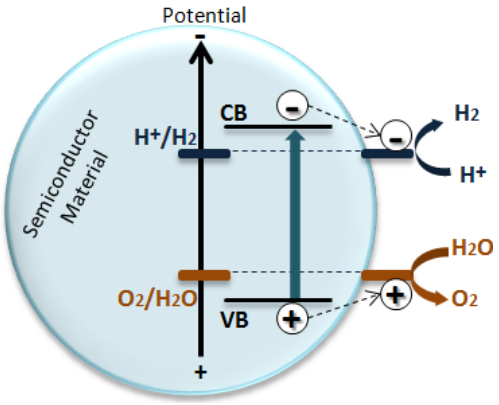

Figure 2.4. Energetic positions of CB and VB for photocatalytic water splitting. Source: own elaboration adapted from [90][94].

2.2.2. Photocatalytic reforming

The photocatalytic reforming is the photodecomposition and mineralization of organic compounds under anaerobic conditions (absence of O_2), where the water plays the role of the oxidant [95]. This reaction takes place at room temperature and it is widely attractive because it utilises solar light to activate the catalyst [96].

Nowadays, the most common route for H_2 generation is by thermochemical process or steam reforming processes of fossil fuels as natural gas [39][55]. However, both of them are endothermic reactions and produce environmental pollutions because of greenhouse gases releasing. These facts, as it was explained in the previous chapter, have made pressure on the research world to find more environmentally fuel for future generations.

Unlike the steam reforming from fossil fuels, which require high temperatures (1000 °C) and pressures (25 bar) [96], photoreforming occurs at much milder conditions (near to ambient conditions). Eq. 2.2.1 and 2.2.2 show the H_2 generation from natural gas by steam reforming [36]:

$$CH_{4(g)} + H_2O_{(g)} \rightarrow CO_{(g)} + 3H_{2(g)} \quad (2.2.1)$$

$$CO_{(g)} + H_2O_{(g)} \rightarrow CO_{2(g)} + H_{2(g)} \quad (2.2.2)$$

On the other hand, the fundamental principle of the H_2 generation by the photoreforming of organic compounds, which are partially or totally degraded, can be explained similar to section 2.1 (Figure 2.1). It is: under radiation ($h_v \geq Eg$) (step a), photogenerated e^- and h^+ are produced in the BC and VB (step b) of the photocatalyst. Then, they migrate for further reactions toward the catalytic surface (in this case c1, probably c2 and c3 steps).

Similar to the photocatalytic water splitting, in order to promote the H_2 evolution instead of O_2 on the catalyst surface, the photoreforming is also carried out under anaerobic conditions. Consequently, the photoreactor is closed to the atmosphere as well, and before irradiation, the liquid solution is bubbled with a noble gas to take air out [88][89][96].

Additionally, unlike the photocatalytic water splitting, where there are not additional hole scavengers, in the photoreforming reaction, of course, hole scavengers are required. This is essentially, one of the two approaches commented above in the previous section "*Photocatalytic Water Splitting*" to make the e^-/h^+ lifetime longer and reduce the recombination probability: addition of sacrificial agents. Therefore, one of the main limitation of the photocatalytic water splitting toward its application as a large-scale process to produce H_2 is its low efficiency, which is mainly due to recombination of the photogenerated charges (e^-/h^+) [67][83][97][98]. Hence, in order to suppress the e^-/h^+ recombination and promote their separation, which is the same if we say "*make the e^-/h^+ lifetime longer*", different sacrificial agents have been used.

Basically, the sacrificial agents are electron donors that reduce the photogenerated h^+, being themselves oxidized. In the literature can be found many surveys about the photocatalytic H_2 generation on different photocatalytic materials (see more detail about photocatalytic materials in section 2.3) using different sacrificial agents such as alcohols [33][67][99][100][101][102], organic acids [33][67][97][99][100][103], aldehydes [67][88], alkanes [67], amines [88][97][98], sugars [101][104], biomass [105][106], inorganic compounds [107], dyes [81][82][108] and real wastewater [33][83][103].

Concerning the fundamental mechanism for the H_2 generation by photoreforming reactions, it depends strongly, not only on the nature of the sacrificial agent, but also on the nature of the photocatalytic material. Therefore, in spite of the fact that diverse reaction mechanisms have been proposed, nowadays this reaction pathway is not still clear, even though the fact that significant efforts have been done for a better understanding.

On this regard, Patsoura et al. [67] have reported that in the case of the H_2 photogeneration on TiO_2 under unaerated conditions, oxygen is barely formed. But likely, some O_2 remaining adsorbed on the surface of TiO_2 may react further to form peroxotitanate complexes and H_2O_2 in solution. On the holes side, they might oxidize the TiO_2 surface, being the TiO_2 itself, an electron donor. In this study [67] about Pt/TiO_2 materials, the authors suggested the addition of sacrificial agents as a way to delay the deactivation of the catalyst. Hence, organic compounds "cleans up" the catalyst surface by removing the photogenerated oxygen/oxidants. They proposed the reaction mechanism as a reforming of organic compounds at room temperature as follows:

$$C_xH_yO_z + (2x - z)H_2O + h_{\nu(\geq Eg)} \xrightarrow{Pt/TiO_2} xCO_2 + (2x - z + (y/2))H_2 \qquad (2.2.3)$$

At low concentrations of sacrificial agents, they reported the complete mineralization of the organic compound after around 1200 min of irradiation [67]. In some others surveys, this same pathway has

been proposed [33][109]. On the other hand, Bahruji et al. [96] explained this process as the general mechanism shown in Eqs. (2.2.4) - (2.2.6). Eq. 2.2.4 consists in the oxidation of water molecules by photogenerated h^+ in the VB to produce •OH radicals, which attack the organic compound by abstracting an alpha hydrogen and form $•RCH_2$-OH radicals (Eq. 2.2.5) and $•RCH_2$-OH radicals that are later oxidized toward aldehydes (Eq. 2.2.6). Bahruji et al. reported the H_2 production from the photoreforming of different alcohols, where primary and secondary alcohols showed similar H_2 rates but not tertiary.

$$TiO_2 + h_\nu \rightarrow h^+_{VB} + e^-_{CB} \quad \text{(Eq. 2.1.1)}$$

$$h^+_{VB} + e^-_{CB} \rightarrow energy \quad \text{(Eq. 2.1.2)}$$

$$H_2O + h^+_{VB} \rightarrow • OH + H^+ \quad (2.2.4)$$

$$Organic\ Compounds + • OH \rightarrow • RCH_2OH + H_2O \quad (2.2.5)$$

$$• RCH_2OH + O_2 \rightarrow RCHO + HO_2^• \quad (2.2.6)$$

$$CH_{3(a)} + H_{(a)} \rightarrow CH_{4(g)} \quad (2.2.7)$$

$$CH_{3(a)} + 2H_2O_{(a)} \rightarrow CO_2 + {}^7/_2 H_{2(g)} \quad (2.2.8)$$

From most of the alcohols they studied, the main gas phase products were H_2 and CO_2. In some cases, methane (CH_4) and other longer chain alkanes. Concerning the alkanes formation, there could be a competing reactions for methyl groups where either H^+ ions react with methyl groups (Eq. 2.2.7) or methyl groups react with water to be photoreformed toward CO_2 and H_2 (Eq. 2.2.8).

All in all, they proposed **four general rules to find out the photoreforming products of alcohols: (i)** there must be a hydrogen atom in the α-position (respect to the oxygen containing group) in the alcohol molecule; **(ii)** primary alcohols undergo decarbonylation toward CO_2 and H_2, plus an alkane (except methanol); **(iii)** methylene groups between alcohols are completely oxidised to CO_2 and **(iv)** the dominant pathway for methyl groups formed in the photoreforming is the recombination with H^+ toward their alkanes (Eq. 2.2.7).

Strataki et al. [110] presented a more specific mechanism for the photocatalytic H_2 production from alcohol-water mixtures. They explained that H^+ ions are generated in the reaction between h^+ in the VB and sacrificial agents (water-alcohol mixtures). Therefore, the H^+ might come from both, water (Eqs. 2.2.4 or Eq. 2.2.9) and alcohol (Eq. 2.2.10). Then, those H^+ ions are reduced in metal sites by photogenerated e^- in the CB to produce H_2 (Eq. 2.2.11).

$$2h^+_{VB} + H_2O \rightarrow 2H^+ + {}^1/_2 O_2 \quad (2.2.9)$$

$$2h^+_{VB} + ROH \rightarrow 2H^+ + RCHO \quad (2.2.10)$$

$$2e^-_{CB} + 2H^+ \rightarrow H_2 \quad (2.2.11)$$

Regarding the Eq. 2.2.9, previously it was said about "remaining O_2" in the solution, even, after purging the system with a noble gas. This equation might explain the presence of O_2, which following the Eq. 2.2.6, O_2 could promote the formation of powerful oxidizing agents, as it was explained in the previous

section (Eqs. 2.1.7 and 2.1.8). Accordingly to Strataki, et al., Eqs. 2.2.7 and 2.2.8 may explain the generation of H^+ cations from water and alcohol oxidations. Husin et al. [111] depicted a similar mechanism (Eq. 2.2.9 - Eq. 2.2.11) to form H_2 with a general reaction pathway like Eq. 2.2.3.

$$4h_{VB}^{+} + CH_3OH \rightarrow 4H^+ + CO_{(g)} \quad (2.2.12)$$

$$CH_3OH \rightarrow H_2CO + H_{2(g)} \quad (2.2.13)$$

$$H_2CO + H_2O \rightarrow H_2CO_2 + H_{2(g)} \quad (2.2.14)$$

Romão et al. [81], on the other hand, proposed a reaction mechanism where methanol intervene to donate H^+ protons which are oxidized either toward CO (Eq. 2.2.12) or CO_2. The final formation of CO_2 is a longer pathway from the alcohol with intermediary products such as formaldehyde (Eq. 2.2.13) and formic acid (Eq. 2.2.14) to produce also H_2 (on the metallic co-catalysts) by reduction of H^+ protons for photogenerated e^- in the CB. Concerning the photocatalytic H_2 generation using short chain carboxylic acids as sacrificial agents, after the formation of the photogenerated charges (e^-/h^+), Zhang et al. [100] proposed as firsts step the adsorption of dissociated species of the organic acid on the catalyst surface (Eq. 2.2.15). Later, the e^- transfer to H^+ (e^- acceptors) to produce H_2 (Eq. 2.2.11). On the other side, h^+ react with $RCOO^-$ species to form CO_2 (Eq. 2.2.16)

$$RCOOH_{(a)} \rightarrow H^+ + RCOO^- \quad (2.2.15)$$

$$2h_{VB}^{+} + RCOO^- \rightarrow H^+ + CO_2 \quad (2.2.16)$$

$$h_{VB}^{+} + OH^- \rightarrow \bullet OH \quad (\text{Eq. } 2.1.3)$$

$$\bullet OH + RCOO^- \rightarrow \bullet COO^- + H_2O \quad (2.2.17)$$

$$\bullet COO^- + H^+ \rightarrow CO_2 + {}^1/_2\ H_2 \quad (2.2.18)$$

Accordingly to Zhanget al. [100], the generation of •OH radicals could also come from reaction between h^+ and hydroxyl groups on the catalyst surface (Eq. 2.1.3), which consequently oxidize $RCOO^-$ species to $^{\bullet}COO^-$ species (Eq. 2.2.17) and from the oxidation of these latter species with H^+ ions, H_2 is produced (Eq. 2.2.18). All in all, although most of the surveys commented above propose relatively different reactions pathways for the photocatalytic H_2 generation from aqueous solution of organic compounds, up to this point we can summary the following ideas:

Photogenerated h^+:

- Oxidize organic compound or water to produce H^+ protons (Eqs. 2.2.4, 2.2.9, 2.2.10, 2.2.12, probably 2.2.15, and 2.2.16)
- In absence of O_2, they could promote the formation of •OH radicals (Eqs. 2.1.3, 2.1.5, 2.2.4 and probably 2.2.13 as well), which help in the partial (Eqs. 2.2.5, 2.2.12, probably 2.2.13, and 2.2.17,) or total degradation of organic compounds (Eqs. 2.2.8, 2.2.16 and 2.2.18).

Photogenerated e^-:

- Reduce H^+ protons to produce H_2 (Eq. 2.2.11)

Additionally, the general understanding of the photocatalytic materials is that most of them are commonly composed by a metallic part (co-catalyst) on a semiconductor (SC) catalytic support. Of course there are many other variants, as it is shown in more details in next section, but in this line, the most popular considerations is that oxidation reactions happen on the SC surface while reduction reactions occur on the metallic surface.

However, in contrast of these general ideas commented above, there are some surveys [88][96][112][113][114] (most of them related to M. Bowker) where they consider the alcohol oxidation on the metal surface. For instance, in the works of Bowker et al. [88] and [113] related to the description of the reaction mechanism of the H_2 generation from the photo-reforming of organic compounds, they explained the role of the metal in the catalysts as it is shown in the next reaction pathway (Eqs. 2.2.19 - 2.2.22) and Figure 2.5 as well. From a previous work [112], where they performed the reaction between methanol and pure Pd at 300 K and observed the H_2 generation with a fast deactivation of the catalyst, they assumed a saturation of the metal surface due to the CO production, strongly adsorbed on it.

Then, in the work [113], where Bowker et al. studied the metal-support interface in the photocatalytic reforming of methanol on Pd/TiO_2, authors conclude the same when in experiments under dark conditions, no plateau was observed but when the system was illuminated, the H_2 evolution reached a plateau.

$$CH_3OH_{(a)} + Pd_s \rightarrow CO_a + H_2 \quad (2.2.19)$$

$$TiO_2 + h_\nu \rightarrow Ti^{3+} + O^- + O^{2-} \quad (2.2.20)$$

$$CO_a + O^- \rightarrow CO_2 + Pd_s + V_o^- \quad (2.2.21)$$

$$V_o^- + Ti^{3+} + O^{2-} + H_2O \rightarrow TiO_2 + H_2 \quad (2.2.22)$$

Figure 2.5 (adapted from ref. [88]) presents this mechanism proposed. Under dark conditions, step 1 shows the adsorption of methanol on Pd surface (Eq. 2.2.19), where the methanol is decarbonylated and dehydrogenated to produce CO strongly adsorbed on the metal and H_2. The adsorbed CO poisons the Pd surface, then, the H_2 evolution decays. Then, when the catalyst is irradiated (step 2) (Eq. 2.2.20), a highly electrophilic hole (O^-) attacks the CO adsorbed to produce CO_2 (step 3). This attack releases a site (V_O^-) on the metal surface for further adsorption of methanol molecules (Eq. 2.2.21) and an anion vacancy (V_O^{2-}) in the SC material. Bowker et al. proposed these last vacancies to be filled by water molecules, where it is dissociated to produce an additional mol of H_2.

In the work of Bahruji, et al [96], they also commented the decarbonylation and dehydrogenation of organic compounds on Pd to produce CO_2 and H_2. But, in the case of experiments performed on TiO_2 in absence of Pd, they explained that the alcohol reforming proceeded by dehydration of the alcohol, therefore, CO and H_2O were formed. Regard to the reforming rate, they explained it was independent of the kind of alcohol due to accordingly to the model presented in Eqs. (2.2.19) - (2.2.22), this rate depended on the rate of CO removal. About the removal of CO_2 from the Pd surface, authors supposed

it happen by mean a kind of active oxygen state which could be present in oxidizing agents, such as •OH radicals or H_2O_2, but it is not clear for them. Along this section, it has observed that organic compounds, in most of the cases alcohols, are widely studied as sacrificial agents in photocatalytic processes for H_2 production. Figure 2.6 could explain the reason why they are good as sacrificial agents. Organic compounds present lower oxidation potentials than water, which allows, in the photoreforming of organic compounds, a more efficient e^-/h^+ pair separation, preventing their recombination [109]. This less energy demanding process makes the photoreforming a more attractive option for H_2 generation than the water splitting. Besides, this process offers the opportunity to produce energy form waste, like wastewater.

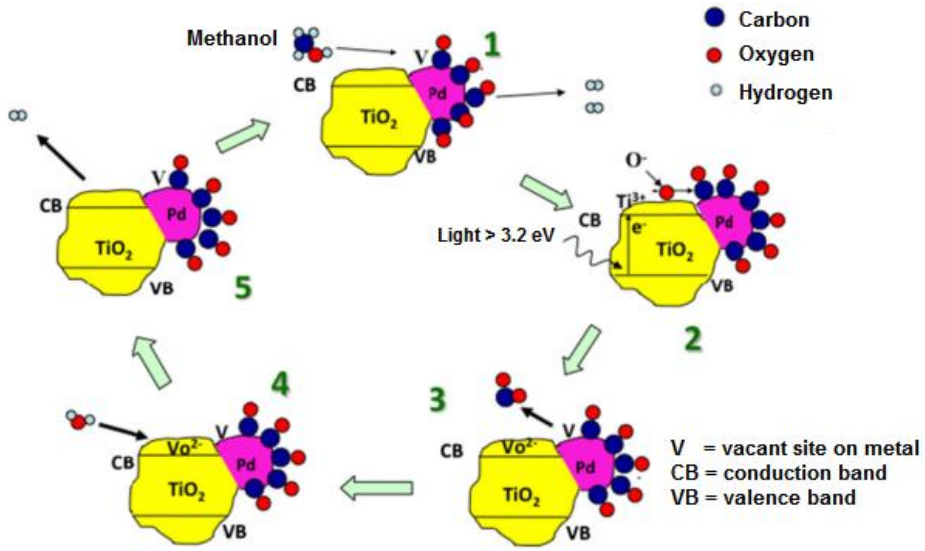

Figure 2.5. Catalytic cycle proposed by Bowker et al. [88][113]

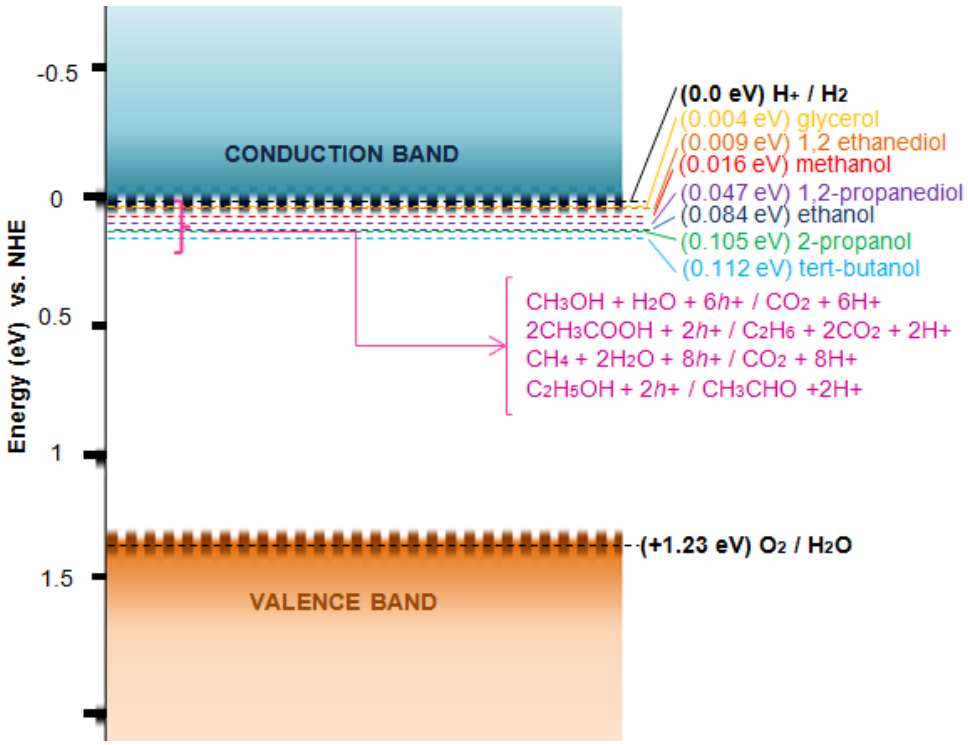

Figure 2.6. Oxidation potential of several organic compound and their position with respect to redox potentials of water splitting. Source: own elaboration adapted from [109][115].

2.3. Photocatalytic semiconductor materials

In section 2.1 was presented that photocatalysis describes the chemical reactions where catalytic materials are activated by light energy and also that these catalysts are commonly semiconductor materials, but, why semiconductor materials? The simplest answer could be that is because naturally this kind of materials are easily activated by light energy. However, the semiconductor nature is not the absolute requirement for a material to be an efficient photocatalyst. They also have to own specific parameters that are more related to two basic steps of photocatalytic reactions: (i) e^-/h^+ photoexcitation and (ii) e^-/h^+ migration.

The first parameter is an **appropriate band-gap structure** which is related to: (i) the e^-/h^+ photoexcitation. Appropriate, in terms of the semiconductor materials application, means a not very wide or not too narrow band-gap for the photocatalytic water splitting and mostly to the photoreforming of organic compounds to produce H_2. Where a not very wide band-gap ensures a higher photons absorption in the visible light range and a not too narrow band-gap avoids (or reduce) the e^-/h^+ recombination. Nevertheless, two other terms should be included to this first parameter: **appropriate CB** and **VB positions**. Next are the theoretical values for this first parameter:

(a) Minimum band-gap higher than 1.23 eV [93], which is the theoretical dissociation energy of water. Christoforidis et al. [109] stated that in practice this value rises to 2.0–2.4 eV.
(b) Maximum band-gap lower than 3.4 eV, which is related to the catalytic activation under solar radiation [94][115].
(c) Bottom level of the CB must be more negative than the redox potential of water to produce H_2 (0 eV vs. NHE at pH 0) [91][92] for the water splitting or redox potential of H^+ cations that could come from organic compounds [89], so that e^- are able to participate as reduction agents in further reactions [109] such as Eq. 2.2.11.
(d) Top level of the VB must be more positive than the redox potential of water to produce O_2 (1.23 eV vs. NHE) [91][92] for the water splitting or the redox potential of mostly of the organic compound, so that h^+ are able to participate as oxidation agent in reactions related to the organic photoreforming [109] such as Eq. 2.2.4, 2.2.9, 2.2.10, 2.2.12 and 2.2.16. See Figure 2.7 where it is shown a graphical description of these 4 items.

Figure 2.7 shows the band-gap structure of different SC materials that have been investigated as photocatalysts, either for the water splitting or the photoreforming of organic compounds [94][95][105][109][115][116][117]. It can be observed in Figure 2.7 that there are some semiconductor materials which do not meet some of the theoretical values commented above in items a, b, c and d. For instance, taking into account only the item (a), Silicon (Si) owns a lower band-gap value (1.1 eV) than the required. Even, counting the value of Christoforidis et al. [109] of 2.0–2.4 eV, GaAs, CdSe, MoS_2, Cu_2O and GaP neither meet that condition. This narrow band-gap leads to high probabilities of e^-/h^+ recombination.

On the other side, materials such as ZrO_2, SnO_2 and ZnS exceed the maximum band-gap (item b), which in their bared form, make them not appropriated for photocatalytic application under solar light irradiation and low efficient, as they require photons highly energetic to be activated and because the UV region corresponds only to around 3-5 % [66][72][109] of the total solar energy.

Concerning the items (c) and (d), some other catalysts do not meet the conditions of appropriate CB and VB positions for the water splitting or the photoreforming of organic compounds. For instance, the bottom level of the CB of materials such as SnO_2, WO_3 and Fe_2O_3 is more positive than the potential required to reduce H^+ cations. It means the photogenerated e^- on these materials are not energetically able to reduce H^+ cations. As a result, the H_2 generation from water, or even from some organic compounds, hardly ever occurs.

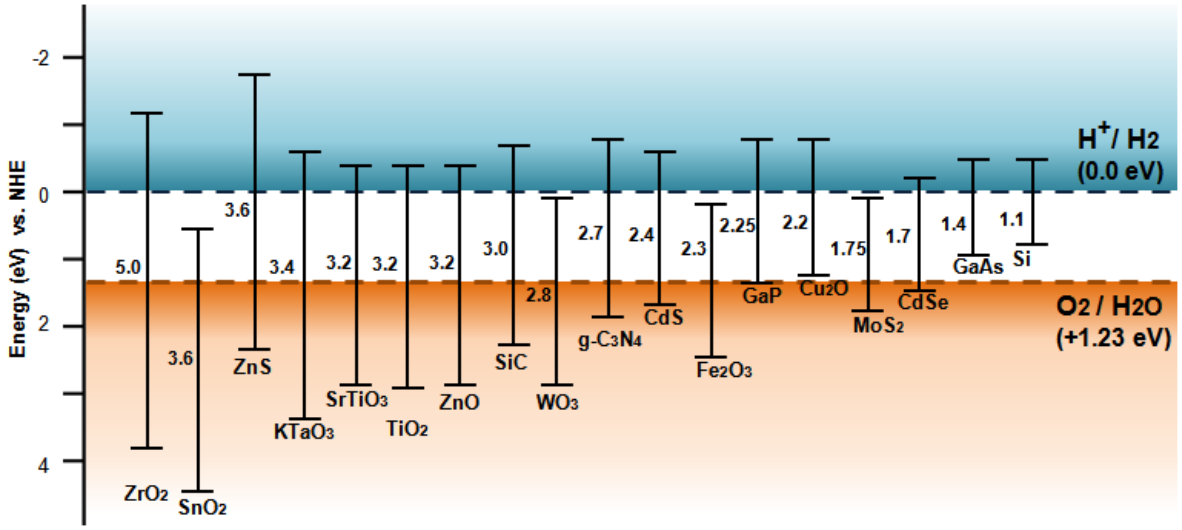

Figure 2.7. Band-bap structure of different photocatalytic materials. Source: own elaboration adapted from [94][95][105][109][115][116][117]

Now, concerning ii) the e^-/h^+ migration step, this step is much more related to the methods to make the e^-/h^+ lifetime longer and reduce the recombination probability. Previously was commented these methods were the addition of sacrificial agents and the creating active sites on the surface photocatalysts to separate the photogenerated charges (e^-/h^+). The first method was already explained in section 2.2.2. Concerning the creation of active sites, explained in more details in next section, is related to the addition of co-catalysts that works as "e^- pump", improving the separation of the e^-/h^+ pair.

2.3.1. Co-catalyst materials

Co-catalyst materials are additional compounds on a catalyst that lead to an important improvement in the activity of the catalyst. Commonly, co-catalysts are present in very low concentration and by themselves, they are weak catalysts, but in combination with some other catalysts, they promote a higher activity of the catalyst [117][118]. For photocatalytic materials, this activity enhancement is related, again, to the e^-/h^+ pair photoexcitation (at the beginning of section 2.3 was defined the parameter appropriate band-gap structure), and the e^-/h^+ migration. In the case of e^-/h^+ photoexcitation, co-catalysts are used to obtain a higher solar light absorption by narrowing the catalyst band-gap,

meanwhile the diminution of the e^-/h^+ recombination is also enhanced by the improvement of the e^-/h^+ separation (previously was commented the addition of sacrificial agents to improve the e^-/h^+ separation by trapping photogenerated h^+). Although co-catalysts can act as either h^+ or e^- scavenger, in the specific case of the photocatalytic H_2 generation, most of the investigated co-catalysts works as e^- trapping, which act by "pumping" the photogenerated e^- from the CB of the photocatalyst toward their own surface. Then, e^- react with H^+ protons adsorbed on the co-catalyst surface to produce H_2. This pumping of e^- increases the lifetime of the photogenerated e^-/h^+ pair, which is thought to enhance the H_2 evolution. But nevertheless, regarding co-catalysts for h^+ scavenging, instead of using co-catalytic materials as h^+ scavenger, sacrificial agents such as organic compounds seems a more attractive technique, as was commented in section 2.2.2, due to the possibility of using wastewater as a source of organic species .

Even though, since Fujishima and Honda [43] in 1972, TiO_2 has been largely used as catalytic support of different co-catalysts. So that, the acceptable good photocatalytic properties of TiO_2 (long-term chemical stability against photo-corrosion, non-toxic nature, cheap and relatively narrow electronic band-gap, and extensive literature review) [81][89][109][115], make it an interesting catalytic support. Next the different co-catalysts of varied nature that have been incorporated to TiO_2:

- **Non-metal doping (N, F, C and S)**

Several studies have explained that when elements like carbon (C), fluorine (F), sulphur (S) and nitrogen (N) are doping co-catalysts, they change lattice parameters of TiO_2, narrowing the band-gap of TiO_2 [66][119]. Pelaez et al. [66] said N seems to be the most promising element in the development of visible light active titania, as N is easily incorporated in the TiO_2 structure, because N and O have a similar atomic size, small ionization energy and high stability. Kampus et al. [119] stated that N substitutes O in lattice sites or interstitial lattice sites forming Ti-N bond. This fact gives a best visible light absorption to the TiO_2, likely due to a decrease in the band-gap energy, because the mixture of 2p states of N and p states of O could move the VB. Regard to F-doping, though it does not shift the TiO_2 band-gap, it does change the surface acidity and it seems to promote the charge separation (F^- and Ti^{4+} form Ti^{3+}).

- **Noble metal loading (Ru, Rh, Pd, Ag, Pt and Au)**

Noble metals have been described to work like pump of photogenerated e^-, where the they are pumped from the CB of the semiconductor toward the noble metal surface, favouring a faster e^- flux to the catalyst surface, retarding their recombination with photogenerated h^+ [67][120][121].

- **Transition metal oxides (V-, Mn-, Fe-, Co-, Ni-, Cu-, Zn-, Zr-, Nb-, Mo-, Ta-, W- oxide)**

Some studies have demonstrated that transition metals such us cobalt (Co), iron (Fe), chromium (Cr) and vanadium (V) can wide the absorption light of TiO_2 toward the visible range, then, enhancing its photocatalytic activity [66][72]. In general, for transition metal, including also some noble metals such as platinum (Pt), ruthenium (Ru) and gold (Au), their incorporation in the titania lattice could form new energy levels between the VB and CB, therefore, the band-gap is narrowed and the light absorption is shifted toward the visible range [66].

- **Metal oxides (Ga-, Ge-, In-, Sn- and Sb- oxides)**

These metal oxides have shown to be effective in the photocatalytic water splitting when they are loaded as co-catalysts. As they can make possible a faster transport of e^- from the photocatalyst surface toward the H^+ protons adsorbed on themselves, the photogenerated charges are efficiently separated, reducing the e^-/h^+ pair recombination [90]. Although, unlike the transition metal oxides, these metal oxides do not absorb in the visible range due to their band-gap values are higher than 3.6 eV [36].

- **Metal sulfides (CdS, ZnS, Bi_2S_3)**

These compounds are considered as promising materials to develop high efficient photocatalysts due to their high visible light response [122], and coupled composites of these materials increase considerably the photocatalytic activity by decreasing the recombination rate. Besides, multilayer catalysts based on CdS and ZnS have shown the capacity, not only to produce H_2 but also, to degrade organic pollutants [66][99][106][107].

All in all, the strategies above propose the heterojunction between catalysts and co-catalysts as an internal electric field [116] that allows to obtain photocatalytic materials with a narrower band gap and a faster migration of photogenerated charges.

Specifically in the photocatalytic H_2 generation by reforming of organic compounds, noble metals, such as Pt, Ag, Au or Pd are commonly used as co-catalysts due to their capacity of H^+ protons reduction. In the case of water oxidation, metal oxides such as CoO_x, IrO_2 and RuO_2 are used as co-catalysts [117]. Concerning the incorporation of co-catalysts, it can be performed by loading or doping methods, where loading is referred to the surface incorporation of nanoparticles and doping to the introduction of new atoms into the chemical structure of photocatalysts [117].

2.3.2. Co-catalyst deposition methods

Final characteristics of solid catalysts depend on their preparation, then, with an appropriate deposition method, co-catalysts can lead to higher activity. Therefore, it is important to choose the adequate synthesis steps of the catalysts as well as the co-catalysts precursors in order to obtain a catalyst highly active for the specific purpose of the work. Concerning the preparation steps, experimental parameters such as the concentration of solids in solution, stirring conditions, temperature, pressure, sequence and duration of every step, may influence positive or negatively on the catalytic activity [123].

In the literature can be found studies where co-catalysts of diverse nature are synthesized on catalytic supports: impregnation methods [89][119][120][124][125], chemical reduction [126][127], sputtering [86], deposition-precipitation [72][107][125][126][128], co-precipitation [39][129], sol-gel method [130], electrodeposition [126][131]. This thesis is mostly focused on the photodeposition method for the synthesis of metal/semiconductors (M/SC) materials.

- **Photodeposition method**

The photodeposition method is based on the absorption of light energy to produce active sites on a SC catalyst for the co-catalysts deposition on the SC surface. It is one of the simplest methods to deposit metals on SC materials because photodeposition does not require hard conditions of temperature or pressure, electric potential or complex step processing [117][132]. On the contrary, its most basic set up consists only in the irradiation of an aqueous solution containing the SC and the co-catalyst precursor.

Photodeposition can be performed by two ways: oxidative photodeposition and reductive photodeposition[117].

Figure 2.8 (a) (also Eq. 2.3.2.1) describes the reductive photodeposition of a metallic nanoparticle, where the process is similar to the explanation already given in section 2.1, about the fundamentals of photocatalysis. The SC is irradiated and photons with energy higher than the band-gap of the SC are absorbed (**absorption of incident photons**). This photonic energy is transferred to an e^- from the VB that jumps toward the CB, leaving a h^+ in the VB (**e^-/h^+ excitation**). The e^- migrates toward the SC surface, where it reacts in the reduction reaction of a metal ($M^+ + e^- \rightarrow M^0$) (**migration of photogenerated charges**). In this photodeposition method, as well as in any of the photocatalytic reactions, the e^-/h^+ recombination is a possible cause for low photodeposition rates.

Therefore, aimed to overcome this awkward, some researchers have added sacrificial agents to the photodeposition solution [78][117][122][125][132][133]. Sacrificial agents trap h^+, in that way more e^- are available for the metal reduction reaction.

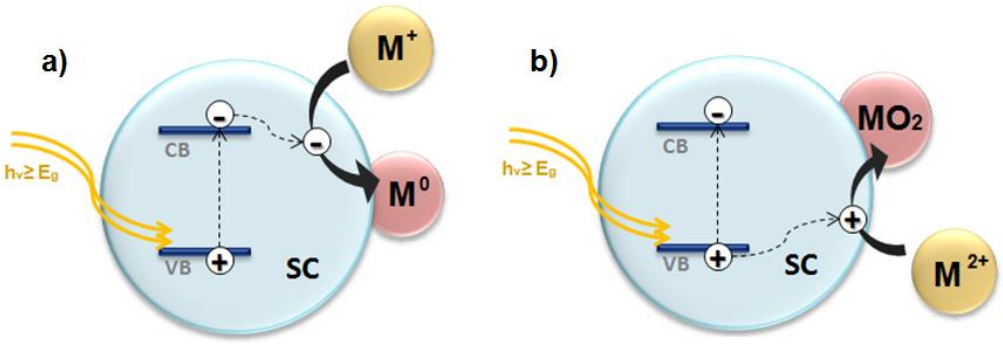

Figure 2.8. Photodeposition method mechanism. **a)** Reductive photodeposition and **b)** Oxidative photodeposition. Source: own elaboration adapted from [132]

Under aerated conditions, reactions between e^- and O_2 are possible in the CB, as it was explained in Figure 2.1, step c4 (section 2.1). Then, in order to reduce the probabilities of this reaction, the photodeposition solution is purged, before the irradiation, by bubbling with an inert gas, N_2 or Ar, to take oxygen out [117][132]. Some studies have also changed the pH of the photodeposition solution [78][134][135].

$$M^{2+}{}_{(aq)} + 2e^- \rightarrow M_{(deposited)} \qquad (2.3.2.1)$$

$$M^{2+}{}_{(aq)} + 2h^+ + 2H_2O \rightarrow MO_{2\,(deposited)} + 4H^+ \qquad (2.3.2.2)$$

On the other hand, Figure 2.8 (b) (also Eq. 2.3.2.2) describes the oxidative photodeposition, where a metal oxide (MO_2) is formed and deposited on the SC surface. In this photodeposition type, unlike the reductive one, the metal reacts with the photogenerated h^+ in the VB, and e^- trapping methods has have to be implemented to reduce the e^-/h^+ recombination.

Lee et al. [132] suggested several conditions to be met by the photoreactor set up and SC material to facilitate the photodeposition method. (i) Photon energy of the light higher than the band-gap of the SC; (ii) reduction potential of the metal ion more positive that the CB level of the SC; (iii) efficient e^-/h^+ separation and (iv) SC has to be an efficient template for active sites for metal or oxide metal deposition and own a large surface area.

Further details about photodeposition method can be found in the literature [117][132][133][136].

CHAPTER 3

Aim and thesis outline

3. AIM AND THESIS OUTLINE

Considering the evolution of our habits toward a society highly energy demanding, either because of real needs for energy or simply due to a non-efficient use, look for alternative energy sources to fossil fuel is becoming little by little an increasing area of interest in the researching field.

As it was already commented in **chapter 1**, the fossil fuel crisis (reserves depletion, global warming and pollution) has encouraged many countries to invest more and more on renewable energy developments. And though nowadays the fossil fuel burning is still the most attractive way to obtain energy, the growing awareness of the general and scientific society, for the earth future and next generation lifestyle, has encouraged many researcher to pay much more attention to the renewable energy topic, which seems to be our unique outcome to solve two current main problems: energy supply and environment pollution.

In **chapter 2**, the state of the art of the heterogeneous photocatalysis was presented. Here was explained the most basic fundamentals of the photocatalytic processes carried out for the hydrogen generation on photocatalytic semiconductor materials, either by water splitting or by photocatalytic reforming. Regarding this latter topic, chapter 2 counts with a compilation of reaction mechanisms proposed by different researchers for hydrogen generation from organic compounds of diverse nature, where the most widely studied catalysts are based on TiO_2. In addition, it was explained the four parameters to consider efficient material for hydrogen generation by the photocatalytic reforming: minimum ban-gap, maximum band-gap, bottom level of the conduction band and top level of the valence band, and later, the attempts by many researchers with regards to these four parameters. Most of the strategies have included the deposition of co-catalysts such as non-metal doping, noble metal loading, transition metal oxides, metal oxides and metal sulphides deposition. The co-catalysts above mentioned, can be deposited by different methods, which were briefly explained at the end of chapter 2, and we focused on the photodeposition method. The photodeposition was chosen as deposition method in this thesis due to the possibility of using the solar light since the catalyst synthesis.

After all these considerations, by the present thesis, we mainly aim at:

"Developing new materials for hydrogen generation and wastewater treatment by photocatalysis"

To achieve this general objective, next are the specific objectives established for the development of this thesis:

- To study and develop new catalytic materials that improve the efficiencies toward hydrogen by means of photocatalytic processes driven by visible and solar light
- Photocatalytic hydrogen generation using the photoreforming of different organic compounds, either with synthetic or real wastewater.

To analyze the degradation degree of the organic compound used for photocatalytic hydrogen generation.

Firstly, it was carried out a literature review about photocatalytic materials and their efficiencies toward the H_2 generation and their capacity to degrade organic compounds under different types of irradiation. In this initial review, we found the TiO_2 material as the widest studied catalyst for these two purposes. Then, among all kind of modification or attempts to improve the TiO_2 light absorption, we found interesting and simple the use of WO_3 species as a co-catalyst of TiO_2 to narrow its band-gap, or in other words, to improve the absorption of light . This type of catalysts, TiO_2-WO_3, were found to be widely studied for the wastewater treatment by photocatalytic processes [75][79][137][138][139][140], but not many publication were found for their application in the photocatalytic hydrogen generation [141]. From this point, the literature review moved on to the use of noble metal as co-catalysts as an alternative extensively studied to improve the H_2 efficiencies in photocatalytic processes [34][142].

In **chapter 4**, the experimental section is presented. Firstly, the TiO_2-WO_3 support synthesis, which was carried out by the Department of Chemical Engineering and Physical Chemistry, University of Extremadura, Spain [75]. In order to achieve the first specific objective, in this thesis we focused on the metal photodeposition conditions, therefore the metal photodeposition was performed in water (w-Pd/TiO_2(-WO_3) catalysts) and in methanol (m-Pd/TiO_2(-WO_3) catalysts). Among other photodeposition parameters, the catalytic support and methanol concentration, and source of irradiation in the photodeposition solution were also studied.

To see the differences in the catalyst features when these photodeposition parameters were modified, a wide catalysts characterization was performed: ICP-OES, total surface area (BET), XRD, HR-TEM, XPS and Diffuse Reflectance UV-Vis. Chapter 4 also provides the operational fundamentals of each technique commented above and the respective conditions used for their characterization. Similar information is given for the analytical procedures related to the hydrogen detection (GC), TOC determination, actinometry and ATR-FTIR experiments. At last, the four hydrogen generation experimental set-ups used in this thesis were presented.

Results are reported in **Chapter 5**. The characterization results for most of the catalysts studied in this thesis are explained firstly, so as to understand the differences that can be observed in the hydrogen generation results. Due to the wide number of catalysts used in this thesis, we classified the catalysts as next: w-Pd/TiO_2(-WO_3) - CATHETER Lab, m-Pd/TiO_2(-WO_3) - CATHETER Lab, m-Pd/TiO_2(-WO_3) - PCS Lab, m-Pt/TiO_2(-WO_3) - PCS Lab. In chapter 5, the detailed information about the label of every group is given. In addition, although this thesis was more focused on Pd/TiO_2(-WO_3) catalysts, we wanted to study the effect of Pt or Cu on the hydrogen generation as well, hence, some characterization and hydrogen results are also given about Pt/TiO_2(-WO_3) - PCS Lab and Pd/P25-Cu - CATHETER Lab catalysts. Results comparison with the available literature is also provided, taking into account the quantum yield, whose calculation is explained as well.

Finally, **Chapter 6** provides some conclusion of the work done, as well as suggestions for further future studies and **Chapter 7** the publications derived from the thesis.

CHAPTER 4

Experimental Section

4. METHODOLOGY

4.1. Materials

4.1.1. NT-WO_3 and P25-WO_3 supports

The supports of P25-WO_3 and nanotubes of titania (NT) containing WO_3 (NT-WO_3) were supplied by the Department of Chemical Engineering and Physical Chemistry, University of Extremadura, Spain [75]. Concerning the preparation of the NT we refer some papers for more details [143][144].

The starting material for both supports, P25-WO_3 and NT-WO_3 was Aeroxide TiO_2 P25 (anatase/rutile 80/20, 21 nm crystal size). Briefly, NTs were prepared from following this procedure: 1 g of P25 plus 70 ml of NaOH (10 M) was stirred for 30 minutes. Then, the mixture was treated at 130 °C for 48 h in a Teflon-lined autoclave. After the thermal treatment the mixture was stirred again for 30 minutes. The powders were recovered by centrifugation and the obtained powders were washed several times with diluted HCl and dried at 100 °C overnight. Then, the samples were calcined in air atmosphere (350 °C) for 3 h.

WO_3 nanoparticles were deposited over P25 and NT by precipitation of H_2WO_4 solution with ammonia, where an aqueous solution of ammonia was added drop by drop to a mixture of 0.216 g of H_2WO_4 plus 100 ml of ultrapure water. To this solution was added 5 g of P25 or NT under continuous stirring and stirred for 30 minutes more. Then, the mixture was acidified to pH 4 with 0.5 M HCl. In order to avoid the aggregation of WO_X species and their precipitation, 10 ml of 0.1 M of an aqueous solution was added to the mixture above and stirred for 1 h at 40 °C. The powders were recovered by filtration, dried (100 °C, 2 h) and calcined in air atmosphere for 2 h at 420 °C.

4.1.2. Photodeposited Pd- and Pt-catalysts

For the **catalysts prepared in the CATHETER Lab (- CATHETER Lab catalysts)**,Titanium (IV) oxide, Aeroxide P25 (Acros Organics) (XRD analysis: 87.6 % anatase and 12.4 % rutile; 16.9 - 30 nm primary particle size) and Titanium dioxide, TiO_2 - anatase (Probus) (XRD analysis: 88.3 % anatase and 11.6 % rutile; 53.4 - 85 nm primary particle size) were used as support for the Pd/P25 and Pd/TiO_2-anatase catalysts, respectively. Tungstic acid (H_2WO_4) (Aldrich, 99 %) was used as the starting material for WO_3 synthesis. Palladium (II) Chloride ($PdCl_2$, Johnson Matthey, metal purity 59.66 %) diluted in hydrocloric acid (HCl) 37 % (Analytical reagent from Fisher) was used for Pd incorporation on these supports. Cupric (II) nitrate trihydrate ($CuN_2O_6.3H_2O$, Sigma Aldrich, metal purity 98 - 100%).

For the **photocatalytic tests in CATHETER Lab**, two kind of water were used for the water-methanol mixtures: tap water (conductivity < 907.6 µS/cm, Cl^- = 0.001 mg/L, total organic carbon (TOC): 3.93 mg/L, inorganic carbon (IC): 45.29 mg/L, pH 7.83) and milliQ water (conductivity < 0.06 µS/cm, mg/L, TOC: 2.14 mg/L, IC: 6.42 mg/L, pH 6.42). Methanol was supplied by Sigma Aldrich (99.8 % purity).

For the **catalysts prepared in the Photocatalytic Synthesis Lab (- PCS Lab catalysts)**, Evonik TiO_2 P25 from Evonik Industries was used as precursor of P25 in Pt/P25 and Pd/P25 catalysts. Hexachloroplatinic (IV) acid hydrate (H_2PtCl_6, Sigma-Aldrich) diluted in pure water and $PdCl_2$ (Sigma-Aldrich, metal purity 60 %) diluted in HCl were used for Pt and Pd incorporation, respectively, on P25, NT-WO_3 and P25-WO_3 supports. For the photocatalytic tests, methanol and glycerol were of analytical grade purchased at Sigma-Aldrich.

For the **photocatalytic tests in the PSA pilot plant,** the methanol and glycerol were of analytical grade and purchased from Sigma-Aldrich. High purity N_2 (99.9992 %) was used to purge out the air from inside the reactor and a commercial gas mixture of 1000 ppmv of H_2/N_2 was used for GC calibration. Distilled water from PSA distillation plant (conductivity < 10 µS/cm, SO_4^{2-}=0.5 mg/L, Cl^- = 0.7 - 0.8 mg/L, dissolved organic carbon (DOC) < 0.5 mg/L) was used to prepare the aqueous solutions of methanol or glycerol. Municipal wastewater from the Sewage Treatment Plant of Almeria (Spain) were also used as source of sacrificial agents.

4.2. Preparation of Pd/TiO_2(-WO_3) - CATHETER Lab catalysts

Regarding the preparation of the catalysts of the type Pd/TiO_2(-WO_3), two groups are differentiated: (i) Catalysts prepared in water and (ii) Catalysts prepared in methanol. In these two groups we refer to the Pd photodeposition solution which was either only in water or in a water-methanol solution, respectively.

4.2.1. Pd Photodeposition in water: w-Pd/TiO_2(-WO_3) catalysts

For the Pd photodeposition in water (PD-w), 500 ml of pure water and a solution of $PdCl_2$ in diluted HCl plus water, containing a nominal amount of Pd (0.1, 0.25 or 0.5 wt.%), were added to a glass flask and stirred by some minutes. Then, the catalytic support (P25-WO_3, NT-WO_3, TiO_2-anatase, P25 or WO_3) was added under continuous stirring (the amount of catalyst was such that the support concentration was 2000 or 4000 ppm). Afterward, the system, under continuous stirring, was deaerated with Ar (50 ml/min) for around 1 hour (h). Then, after deaeration, the glass flask was closed hermetically and irradiated with a UV lamp (λ: 365 nm, 6 W) overnight (around 14 h). After irradiation, the solid particles were recovered by filtration, washed several times with distilled water and kept at room temperature until drying.

4.2.2. Pd Photodeposition in methanol: m-Pd/TiO_2(-WO_3) catalysts

The Pd photodeposition in methanol (PD-m) was performed following the same procedure for the PD-w, but instead of using pure water, a water-methanol solution was used. Therefore: 500 ml of a water-methanol solution (1, 5, 10 or 20 vol.% methanol) and a solution of $PdCl_2$ in diluted HCl plus water, containing a nominal amount of Pd (0.1, 0.25 or 0.5 wt.%), were added to a glass flask and stirred by some minutes. Then, the catalytic support (P25-WO_3, NT-WO_3, TiO_2-anatase, P25 or WO_3) was added under continuous stirring. In this case, different concentration of the supports in the photodeposition

solution were studied (800, 1000, 2000 or 4000 ppm). Afterward, the system, under continuous stirring, was deaerated with Ar (50 ml/min) for around 1 h. Then, after deaeration, the glass flask was closed hermetically and irradiated with a UV lamp (λ: 254-365 nm, 6 W) overnight (around 14 h). The solid particles were recovered by filtration, washed several times with distilled water and kept at room temperature until drying.

In this case the abbreviation is "AmB", where A corresponds to the concentration of the catalytic support in the photodeposition (PD) solution and mB to the concentration of methanol in the PD solution. Therefore, "4m10" for instance, corresponds to a catalyst where the Pd was photodeposited using a water-methanol solution of 10 vol.% and the concentration of the catalytic support in the photodeposition solution was 4000 ppm. Figure 4.1 shows some photos of the metal PD setup in CatHeter labs.

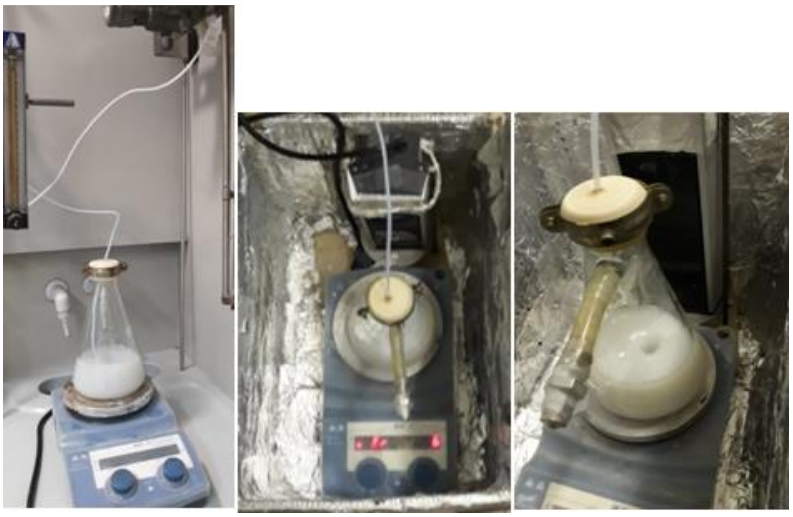

Figure 4.1. Metal photodeposition setup in CatHeter lab

4.2.3. Pd Wetness impregnation Pd/TiO_2(-WO_3) catalysts

Pd wetness impregnation (wi) was prepared as follows: 0.3 ml* of pure water and a specific quantity of $PdCl_2$, containing the nominal amount of Pd (0.25 wt.%) were stirred for 1 h. Afterwards, 1 g of P25 was added to the solution above and stirred for 3 h. Later, this solution was placed in the oven at 80 °C for 12 h to remove the remaining water and after triturating the solids in an agate mortar, the solids powder were reduced in a vertical tube furnace (Hobersal TR-2B, power 2 kW, 220 V, 50/60 Hz. Temperature ramp: 25 °C, 2 °C/min, 300 °C (2 h); carrier gas: H_2 with flow rate of 30 ml/min). *0.3 ml is the volume of water needed to fill the entire porosity of 1 g of the support P25. This volume was obtained from the physisorption analysis (BJH method).

4.3. Preparation of Pd/TiO_2(-WO_3) - PCS Lab catalysts

The Pd PD in the PCS Lab was performed as follows: in a quartz container (100 ml) was added an aqueous solution of methanol (10 or 20 vol.%) and the catalytic support (P25, NT-WO_3 or P25-WO_3) (3200 or 2000 ppm). Then, under continuous stirring, an aqueous solution of $PdCl_2$ in diluted HCl plus

water, containing the nominal amount of Pd (2 or 0.25 wt.%), was added to the mixture above. Afterwards, the system was deaerated with N_2 (0.15 ml/min) for 1 h and stirred under dark conditions inside a box reactor as described by Romão et al. [145]. Then, the quartz container was covered with a quartz plate and the reactor was irradiated with 7 UV lamps (λ_{max}: 368 nm, 18 W/lamp) for 4 h. The powders were recovered by centrifugation for 30 minutes (min) at 8500 revolution per minute (rpm), washed several times with distilled water and dried at 80 °C for 20 h.

For these catalysts prepared in the PCS Lab, the concentrations related to the catalytic support, methanol and amount of Pd in the photodeposition solution were calculated on the basis to have a final photodeposition solution volume of 62 ml. Regarding the abbreviation, it is similar to that commented in section 4.2.2., and for the catalysts prepared in the PCS Lab is possible to distinguish two abbreviations: 3.2m20 and 2m10; where 3.2m20 corresponds to a photodeposition solution containing a water-methanol solution (20 vol.% methanol) and 3200 ppm of catalytic support and 2m10 to a photodeposition solution containing a water-methanol solution (10 vol.% methanol) and 2000 ppm of catalytic supports.

4.4. Preparation of $Pt/TiO_2(-WO_3)$ - PCS Lab catalysts

The Pt PD in the PCS Lab was performed following the same procedure described in section 4.4., but instead Pd, Pt was photodeposited on three supports (P25, NT-WO_3 or P25-WO_3). Briefly: an aqueous solution of methanol in a quartz container is mixed with the catalytic support. Under continuous stirring, the aqueous solution of H_2PtCl_6 , containing the nominal amount of Pt was added to the mixture above (62 ml). Then, the system was deaerated with N_2 for 1 h under dark condition. After deaeration time, the quartz container was covered with a quartz plate and irradiated with 7 UV lamps (λ_{max}: 368 nm, 18 W/lamp) for 4 h. The solution with the photocatalytic powders was centrifuged for 30 min and then, washed several times with distilled water and dried at 80 °C.

Figure 4.2 shows a photo of the metal photodeposition setup in the PCS labs.

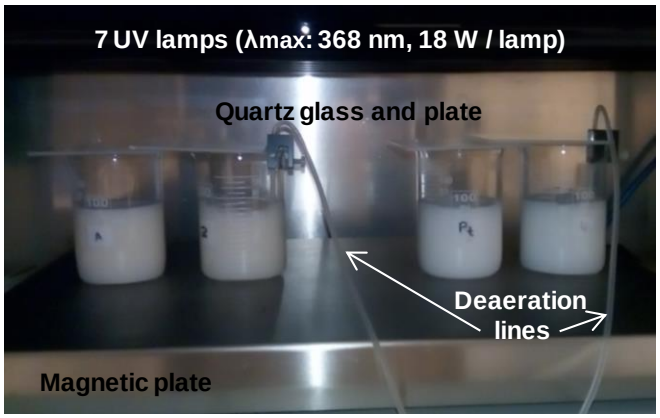

Figure 4.2. Metal photodeposition setup in PCS labs

4.5. Preparation of Pd/TiO_2-Cu - CATHETER Lab catalysts

For the catalysts of the type Pd/TiO_2-Cu, the cupper (Cu) was first deposited on P25 as follows: 0.3 ml of pure water and a specific quantity of $CuN_2O_6.3H_2O$, containing the nominal amount of Cu (0.5, 1 or 2 wt.%) were stirred for 1 h. Afterwards, 1 g of P25 was added to the solution above and stirred for 3 h. Later, this solution was placed in the oven at 80 °C for 12 h to remove the remaining water and after milling the solids in an agate mortar, the solids powder were calcined in a furnace (Hobersal HD-150. Max. Temperature: 1200 °C, air environment). The deposition of Pd on P25-Cu were performed by PD or wi following the protocol previously explained in sections 4.2.2 *" Pd Photodeposition in methanol..."* and 4.2.3 *" Pd Wetness impregnation...".*

4.6. Characterization techniques

In order to know the different characteristics (surface area, porous morphology in the case of porous materials, crystal size and structure, optical properties, surface chemical composition, as well as the co-catalysts content and the co-catalysts nanoparticles sizes) of the solid photocatalytic materials developed in this thesis, diverse characterization techniques have been used. In this section, these equipment are described together with a brief explanation of their principle of operation.

4.6.1. Inductively Coupled Plasma (ICP-OES) [146]

The palladium (Pd) content (wt.%) of the catalysts prepared in CATHETER labs was analysed by inductively coupled plasma with an optical emission spectrophotometer (ICP-OES, Spectro Arcos FHS-16). Total Pd content of the catalysts was determined by subtraction of the Pd content of the liquid sample before and after the metal deposition procedure.

The principle of operation of this analytical technique is based on the vaporization, atomization and excitation of a sample to measure the radiation intensity of the light emitted when the sample is not anymore excited (Figure 4.5 "*Light emission after cutting out excitation*"). In Figure 4.3 is shown the operational basic mechanism of the ICP-OES, which is mainly divided in four parts: auto sampler, nebuliser, ICP torch and detector. The instrumentation of this technique consists, firstly, in an auto sampler **(i)** that introduces the sample to a nebuliser **(ii)**. The sample, usually in liquid solution, is transported into the nebuliser by the Bernoulli effect(suction), where the sample is brought into the gas phase due to the high gas velocity in the nebuliser, splitting the liquid sample in very fine drops. From the nebuliser, the "vaporized sample" is conducted into the ICP torch by a gas flow, commonly Argon (Ar) **(iii)**.

Before continuing, let's first talk about the inductively plasma generation: Figure 4.4 shows a scheme of a characteristic source for a coupled plasma by induction that consists in three quartz concentric tubes, through which Ar flows (1 L/min). At the top of the quartz tubes, an induction coil (**(v)** in Figure 4.3) of radio frequency (radio frequency power **(iv)** in Figure 4.3) creates a circular electromagnetic field. A spark from Tesla coil causes the ionisation of the Ar gas, producing Ar cations (Ar^+) and electrons (e^-). In

the induction coil **(v)**, a magnetic field forces the ions and electrons, into the coil, to move in circular trajectories **(vi)**. The resistance of these ions and electrons to move with the circular magnetic field causes an intense heat, which produces the ohm heating of the plasma, then, occurring the plasma generation.

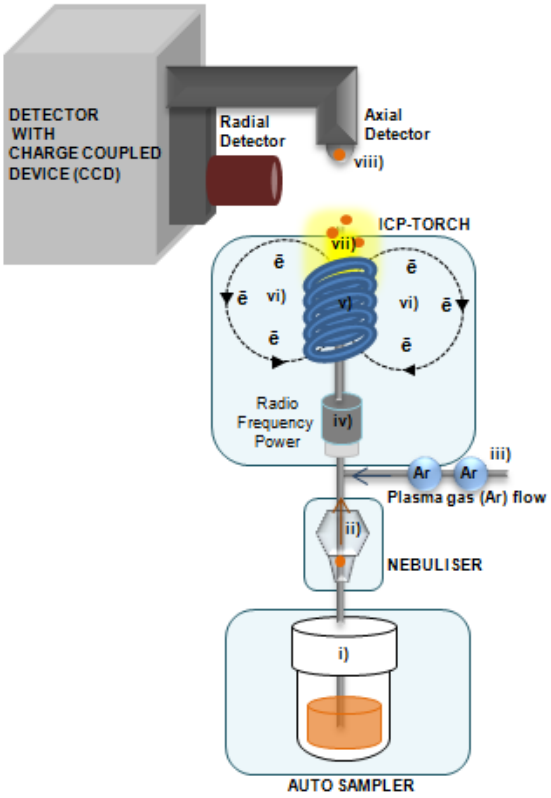

Figure 4.3. Operational fundamentals of ICP-OES. Source: own elaboration adapted from [146]

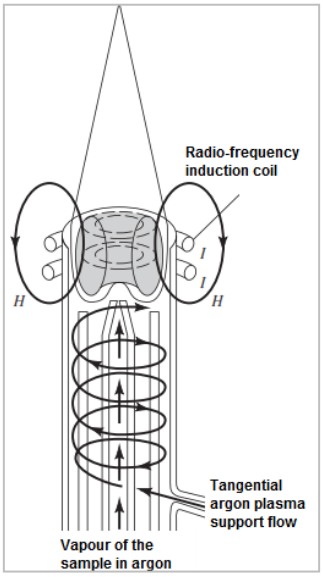

Figure 4.4. Characteristic source of ICP [146]

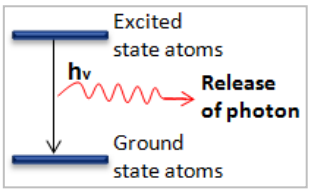

Figure 4.5. Light emission after cutting out excitation [146]

When the "vaporized sample" passes through the ICP torch, it is atomized and excited upon leaving flame **(vii)**. Without any additional excitation, atoms in excited state forms return rapidly to ground state forms, releasing photons **(viii)** at some specific wavelength that depends on the kind of metal is being analysed. The calibration was performed using different known concentration (from 5 to 20 ppm) of palladium prepared previously to the analysis.

4.6.2. Total Surface Area (BET) [147]

The surface area and pore volume of the photocatalytic materials were determined by nitrogen adsorption - desorption isotherms obtained at -196 °C using a Quadrasorb *SI* Models 4.0 using QuadraWin software (v. 5.0+newer). Before the sample analysis, materials were outgassed at 150 °C for 18 h under high vacuum (6 milliTorr) in the instrument pre-chamber to eliminate chemisorbed volatile species. The principle of operation of this analytical technique is based on the physical adsorption and desorption of a gas on and from a powdered solid sample, respectively, to measure different porous characteristic of the sample, such as the shape, volume and surface area of the pores.

Then, when a porous solid, inside a closed glass reactor chamber (Figure 4.6), is exposed to a gas under determined pressure and constant temperature, the solid begins to adsorb gas and it gains weight and the pressure inside the chamber diminishes. Consequently, depending on the porous characteristics of the sample, the profile of the amount of gas adsorbed in function of the relative pressure (P/Po: Po is the saturation pressure of nitrogen) shows different patterns. These patterns (adsorption isotherms curves), are observed in Figure 4.7, which are the most general classification, accordingly to the IUPAC recommendations:

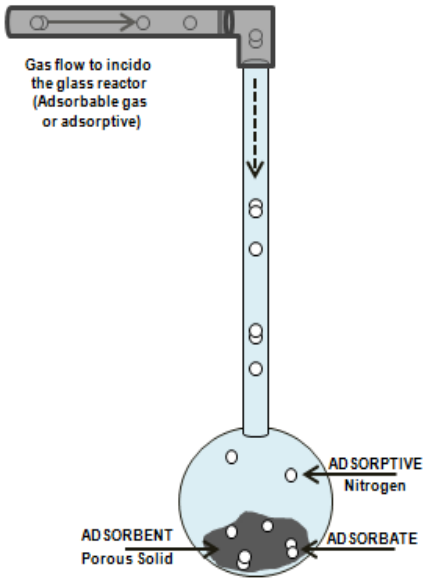

Figure 4.6. Adsorption-desorption chamber. Source: own elaboration

Type I: At very low P/Po, the amount of gas adsorbed increases sharply upon a saturation plateau in the amount of gas adsorbed. This initial high gas adsorption corresponds to a good adsorbent - adsorptive interaction in narrow micropores. As a result, the micropore is filled rapidly at low P/Po. This reversible isotherm curve is characteristic in microporous materials (pore diameter < 2 nm).

Type II: At low P/Po, the amount of gas adsorbed increases up to the point B, where the formation of the monomolecular layer finishes and the multilayer formation starts. This reversible isotherm is given by non-porous or macroporous solids.

Type III: The amount of gas adsorbed increases softly at low P/Po. It indicates a weak adsorbent - adsorbate interaction, even at relatively high P/Po. On this type of isotherms is not possible to observe the monolayer formation and the gas molecules are adsorbed as clusters around the most favourable sites on the solid surface. This type of isotherms may be characteristic of non-porous or mesoporous solids but they are hardly ever found.

Type IV: In these isotherms, is observable a different way for pores filling and emptying (adsorption and desorption line, respectively) process. This isotherm shows, at low P/Po, an increasing amount of gas adsorbed up to the point B (monomolecular layer formation) followed by the multilayer formation. When pressure continues increasing, the pore condensation takes place. Therefore, depending on the geometry of the pores, this condensation occurs at different and lower pressure than the pore evaporation. It leads to the creation of a hysteresis loops (Figure 4.8). Usually, wider hysteresis loops are referred to smaller pore internal radio. This type of isotherm is observed in mesoporous solids (pore diameter 2-50 nm).

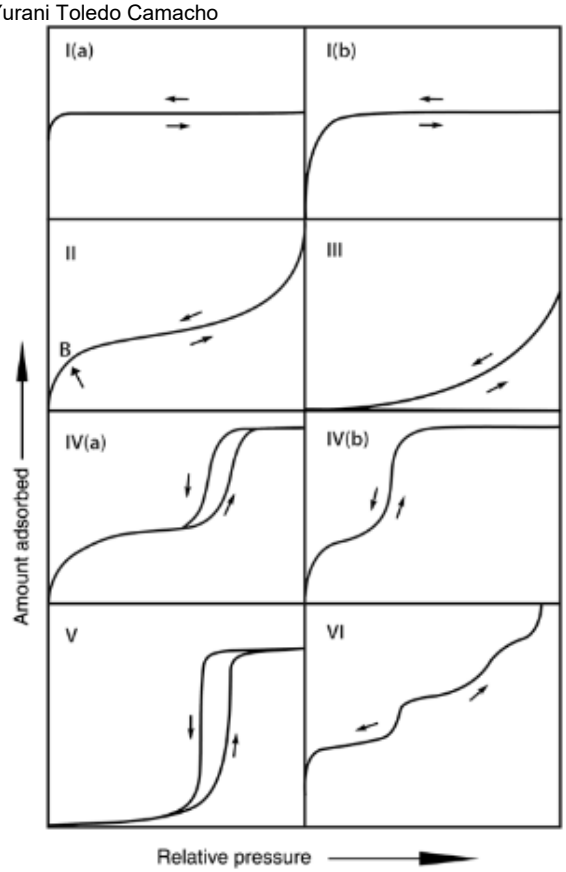

Figure 4.7. Isotherms classification according to the IUPAC [147]

Briefly, **type H1 loop** is observed in uniform mesoporous solids with narrow pore distribution, but also in networks of ink-bottle pores with similar width in the neck and body pore. Pore structure is open-close cylindrical pores. The **type H2 loop** is the most common hysteresis loop given in complex structure pores, where the sharply sloped desorption line corresponds to a pore blocking in some pore necks. The width neck distribution is larger than in type H1 loops. The **type H3 loop** appears in non-rigid aggregates of plate-like particles [147]. The desorption line indicates the presence of macropores filled partially in the pore condensation. The **type H4 loop** is related to the filling of micropores in micro-mesoporous solids. The **type H5 loop** is less common and it is characteristic of solids that contain open and partially blocked mesopores.

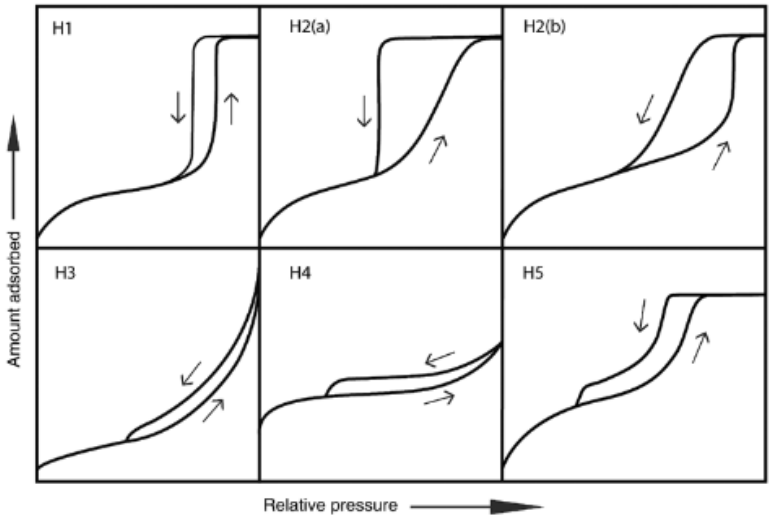

Figure 4.8. Hysteresis loop classification according to the IUPAC [147]

4.6.3. X-ray Diffraction powder (XRD) [146][148]

In **CATHETER Lab,** the X-Ray Diffraction (XRD) measurements for catalysts, whose Pd photodeposition was in water: w-Pd/TiO_2(-WO_3)(section 4.2.1.), were made by using a Siemens D5000 diffractometer (Bragg-Brentano parafocusing geometry and vertical θ-θ goniometer) fitted with a curved graphite diffracted -beam monochromator, incident and diffracted-beam Soller slits, a 0.06 ° receiving slit in

scintillation counter as a detector. The angular 2θ diffraction range was between 5 and 70 °. The data were collected with an angular step of 0.05 ° at 3 seconds per step and sample rotation. $Cu_{k\alpha}$ radiation was obtained from a copper X-ray tube operated at 40 kV and 30 mA. For the photocatalytic materials prepared in methanol: m-Pd/TiO_2(-WO_3) (section 4.2.2.), the crystalline phases were determined using a Bruker-AXS D8-Discover diffractometer with parallel incident beam (Göbel mirror) and vertical theta-theta (θ-θ) goniometer, XYZ motorized stage mounted on a Eularian cradle, diffracted-beam Soller Slits, a 0.2 ° receiving slit and a scintillation counter as a detector. The angular 2θ diffraction range was between 5 and 70 °. The data were collected with an angular step of 0.05 °at 3 seconds per step. $Cu_{k\alpha}$ radiation was obtained from a copper X-ray tube operated at 40 kV and 40 mA.

In PCS Lab, the XRD characterization was performed by using a Bruker D2 PHASER diffractometer. The angular 2θ diffraction range was between 20 - 70°. The data were collected with an angular step 0.05° at 0.5 seconds per step. $Cu_{k\alpha}$ radiation was obtained from a copper X-ray tube operated at 30 kV and 10 mA.

The XRD technique allows to identify qualitatively and quantitatively the compounds present in a crystalline sample, and besides, the order and spacing of atoms of the crystalline material. Basically, this technique consists in using a beam of X-ray which irradiate a fine powdered sample in an angle θ. When the X-ray beam passes through the fine sample, the X-ray beam is diffracted due to its interaction with the atoms of the sample.

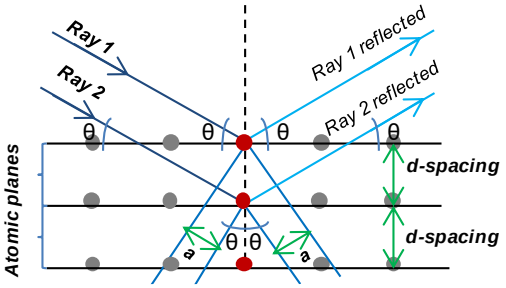

Figure 4.9. X-ray diffraction. Source: own elaboration adapted from [146]

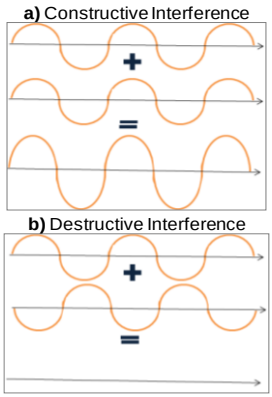

Figure 4.10. Wave interference. Source: own elaboration adapted from [146]

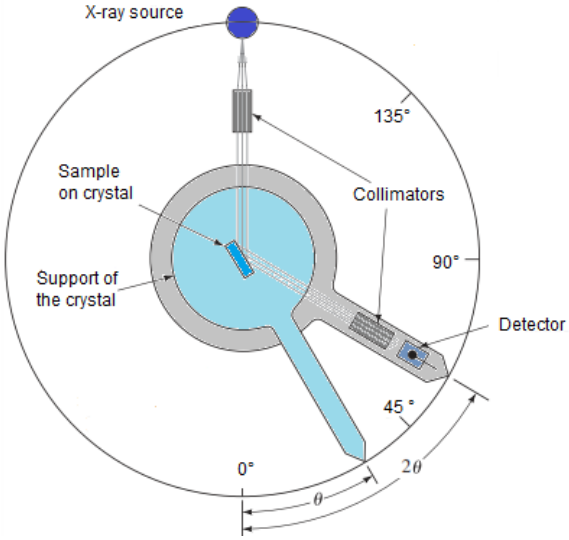

Figure 4.11. Operational fundaments of XRD [146]

Therefore, looking at Figure 4.9, when a monochromatic X-ray beam (**ray 1 and 2**) crashes on the surface of the crystal sample in an angle of θ, a portion of this beam is reflected out of the upper atomic

plane at the same angle of the incoming ray: θ (light blue line "**Ray 1 reflected**"). Another portion of the initial beam (Ray 2) penetrates up to the second layer of atoms, where again, a fraction is reflected ("**Ray 2 reflected**") at the angle θ, and another fraction of the initial beam get into next atomic plane inside and a fraction of it is reflected, and so on. The accumulative effect of those reflected rays produce a diffracted ray. However, as X-ray beam is a bundle of different waves that can interact with one another, constructive or destructive interferences can be produced (Figure 4.10) (a) constructive interference and (b) destructive interference), Consequently, not all the reflected beam produces a diffracted ray. In order to have a properly and detectable X-Ray diffracted, two requirements are necessary: (i) the distance between atomic plane (**d-spacing**) should be approximately the same to the wavelength of the X-ray (0.02 - 100 Å) and (ii) the dispersion centres in the sample, which is the atomic dispersion (red and grey points in Figure 4.9) should be distributed in a very regular pattern. Overall, the diffracted ray is composed by a large number of different rays, reflected at the same wavelength (λ) of the incident beam and in phase, which reinforce each other.

The **Bragg's Law** for XRD describes this set of conditions under next relation: **nλ=2d.sin Θ**, where "n" is the diffraction order and it has to be an integer number with sin Θ ≤ 1.
Figure 4.11 shows the operational fundaments of XRD, where the sample is previously ground up to fine particles in order to have: (i) random orientation and (ii) most of the atomic planes parallel to the surface. Then, by a scanning at different angles θ (0 to 90°) of the incident X-ray beam it most probable to find all the angles where diffraction occurs. Then, the XRD equipment consists in a **X-ray tube** to produce a X-ray monochromatic beam and a rotation system to produce angle from 0 to 90° between the X-ray source and the sample, and an **electronic detector** where is recorded the diffracted bean coming out the sample (counts/sec). The **goniometer** is the instrument used to rotate both X-ray tube and detector. The collimators diverge the initial X-ray beam coming from the X-ray tube or the X-ray diffracted into parallel beam.

4.6.4. High Resolution Transmission Electron Microscopy and Scanning Transmission Electron Microscopy (HRTEM and SEM) [146][149]

High resolution - transmission electron microscopy (HR-TEM) analysis were carried out with a JEOL 2010F instrument equipped with a field emission source. The point-to-point resolution was 0.19 nm and the resolution between lines was 0.14 nm.

For - **PCS Lab catalysts**, the microstructural characterization by HR-TEM was performed at 200 kV with a JEOL 2010F instrument equipped with a field emission source. The point-to-point resolution was 0.19 nm and the resolution between lines was 0.14 nm. Samples were dispersed in alcohol in an ultrasonic bath, and a drop of supernatant suspension was poured onto a holey carbon-coated grid. Unlike the optic microscopes, the operation principle of an electronic microscope consists in using a beam of electrons instead of a beam of visible light or photons to create and image of the sample, which is generated by the electrons reflected (or transmitted). Therefore, "**primary beam**" is called to those

electrons impacting on the solid surface and "**secondary beam**" to those electrons reflected or transmitted. Basically, the TEM equipment consists in a electron emission source, some electromagnetic lenses and an detector of electrons (see Figure 4.12). Commonly, for the electron emission source (or **electron gun**) is used a tungsten filament, which is heated to increase its atoms and electrons energy. When the electrons have enough energy to escape from their atoms, these free electrons are conducted toward the sample.

Figure 4.12 shows the different parts of the TEM equipment: illumination system, imaging system and viewing chamber. Then, the illumination system consists in a series of electromagnetic lenses (**condenser lenses**), where electric and magnetic fields make electrons diverge or converge in one point due to their interaction with these both fields. The collection angle is limited with an aperture (**condenser aperture**) and such aperture in the objective lens allows to control the resolution of the image formed by the lens. From the imaging system, once the electrons have impacted on the sample, only some of them pass through the sample and go toward the viewing chamber. The others electrons are dispersed. In the viewing chamber, electrons impact on a fluorescent screen and an image of the sample is built. The information collected by the fluorescent screen is transmitted toward a computer to assign artificial colours to the obtained image.

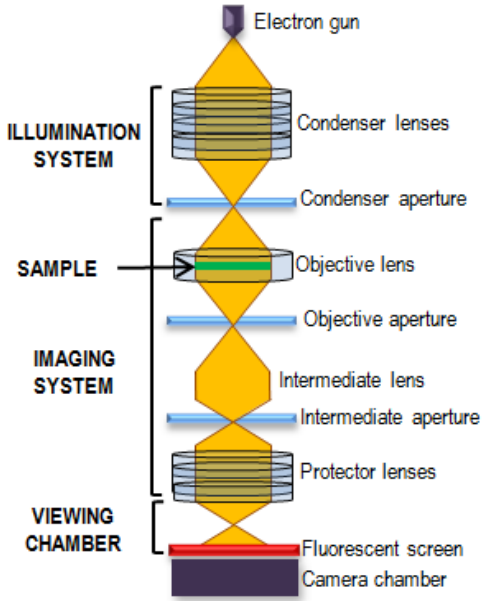

Figure 4.12. Operational fundaments of TEM. Source: own elaboration adapted from [150].

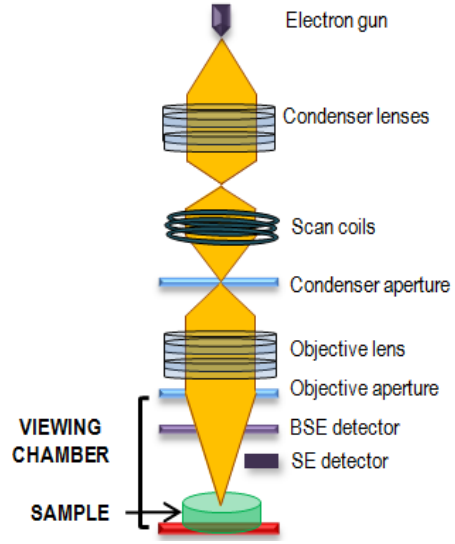

Figure 4.13. Operational fundaments of SEM. Source: own elaboration adapted from [150].

Taking into account that the internal characteristics of the sample might vary, the TEM image is seen as a picture in different tonalities of dark zone, where the darkest zones correspond to less electrons passing through the sample and arriving to the detector and the less dark zones correspond to more electrons going through the sample up to the detector. This is the reason why the sample preparation consist in a very thin film of sample (thickness < 200 nm). High amount of sample might blockage the pass of electron. This technique does not allow to extract information about the sample surface but there is a second techniques that do it: scanning electron microscopy (SEM). With this type of microscope is

possible to get information about the form or roughness of the sample [150]. Figure 4.13 shows the operational fundaments of SEM, where, unlike the TEM that illuminate the whole sample, the electron beam in SEM focuses on one point of the sample to scan it and later moving on to another point and so on upon scan all de sample.

SEM equipment consist in an **electron gun**, some **condenser lenses** and **condenser aperture** to make electrons diverge or converge, and to control the resolution of the image. The **scan coil** cause the electron beam to move in a rectangular way on the sample, which produce a horizontal scanning pattern on the whole sample. When electron impact the sample surface, the initial electron beam loss energy as a result of small energy transfer between the initial electron beam and some electrons from the sample, making the latter electrons escape from their atoms, becoming then, in secondary electrons (SE). These low energy electrons are detected in the **SE detector**. When secondary electrons leave the atom, the outer orbiting electron jump into the gap orbit left by the SE, releasing some energy: the backscattered electrons (BSE). They are detected in the BSE detector shown in Figure 4.13. The number of electrons detected depends on the variation of the sample surface, therefore, with the scanning of the whole solid surface is possible to see a magnified image of the tridimensional topography of the solid.

In terms of magnification and resolution, TEM has up to 50 million magnification level and a resolution of 0.5 angstroms (Å), whereas SEM reaches only up to 2 million level of magnification and 0.4 nm of resolution [151].

High-resolution transmission electron microcopy (HR-TEM) on the other hand, is a technique of high magnification that allow to study the crystal structures and lattice imperfection of nanomaterial at atomic resolution scale. This technique uses both, the transmitted and scattered beams to create and interference image and ensue in an interference pattern or "phase contrast". So, all the electrons coming out from the sample are combined at a point in the image plane [152].

4.6.5. X-ray Photoelectron Spectroscopy (XPS) [146]

The X-ray photoelectron spectroscopy (XPS) spectra for catalysts prepared in CATHETER Lab were acquired in a VG Escalab 200R electron spectrometer equipped with a hemispherical electron analyzer, operating in a constant pass energy mode, and a non-monochromatic Mg-*Kα* (*hν* = 1253.6 eV, 1 eV=1.603x10^{-19} J). X-ray source was operated at 10 mA and 1.2 kV. The angle of the incident photon beam was 45 ° with respect to the normal of the sample. The background pressure in the analysis chamber was kept below 7x10^{-9} mbar during data adquisition. The binding energy (BE C1s=284.9 eV) of adventitious C1 was used as reference. A Shirley background subtraction was applied and Gaussian-Lorentzian product functions were used to approximate the lines shapes of the fitting components.

On the other hand, for catalysts prepared in PCS Lab, the surface chemical characterization was done by X-ray Photoelectron Spectroscopy (XPS) on a SPECS system equipped with a XR50 source operating at 150 W and a Phoibos 150 MCD-9 detector. The pass energy of the hemispherical analyzer

was set at 25 eV and the energy step of high-resolution spectra was set at 0.1 eV. The pressure in the analysis chamber was always below 10^{-7} Pa, and binding energy (BE) values were referred to the C 1s peak at 284.9 eV. Data processing was performed with the CasaXPS software. Atomic fractions were calculated using peak areas normalized on the basis of acquisition parameters after background subtraction, experimental sensitivity factors and transmission factors provided by the manufacturer.

This analytical technique supplies information not only about atomic composition of the sample, but also about the structure and oxidation state of the compound under study and its operational fundaments consists in the X-ray irradiation of a surface solid sample. The energy of this beam is transferred to core-level electrons which are emitted with a specific energy and intensity. This energy and intensity is analysed to identify and determine the information commented above.

The equipment for XPS analysis consists in a X-ray source, port sample, analyser, detector and a signal processer. Figure 4.14 shows the typical configuration of X-ray photoelectron spectrometer. The solid sample is located in between the **X-ray source** (commonly Al Kα or Mg Kα) and the entrance slit of the spectrometer. The **sample** compartment, which is the analysis chamber, is under vacuum in order to avoid the beam attenuation and also to keep the sample surface clean from oxygen or water.

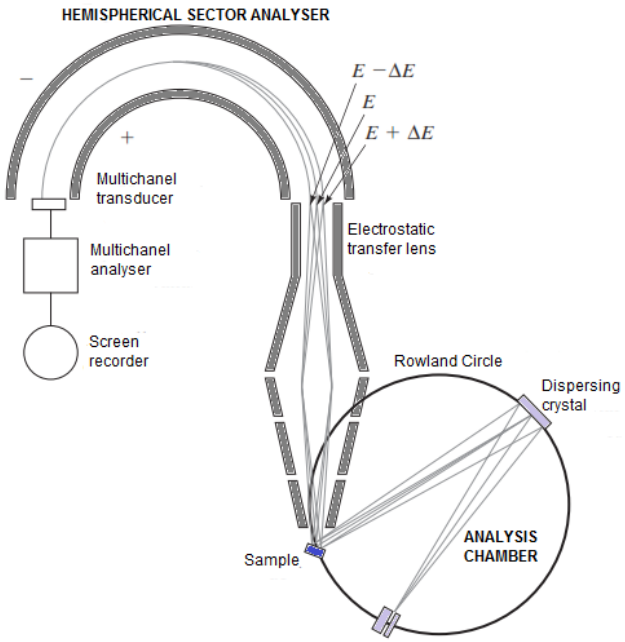

Figure 4.14. Operational fundament of XPS [146]

In the **analyser**, the emitted electrons are dispersed accordingly to their kinetic energy by **recollection lens**, which allow a wide recollection angle for better effectiveness. The emitted electron beam is deflected by the electrostatic field in the **hemispherical sector analyser** to follow a curved trajectory from the lens up to the **channel electron multiplier**. Aimed to focus electrons of different kinetic energies in the transducer and obtain a whole spectrum, the field is varied.

4.6.6. Diffuse Reflectance UV-Vis [153][154]

The band-gap values were determined by diffuse reflectance UV-Vis of solids, measured by a UV-2410 pc spectrometer with integrating Sphere attachment (SHIMADZU ISR-240), converting it into absorbance using the Kubelka -Munk function The optical band gap was determined by means of Tauc's plot for indirect semiconductors ([Photon energy*Absorbance]$^{1/2}$ versus the Photon energy) obtained from diffuse reflectance spectra. Barium sulphate ($BaSO_4$) was used as standard.

Reflection refers to the capacity of a body to reflect light, either **specularly**, which consist in the reflection of a ray at the same angle of the incident ray, or by diffuse reflection, which consists in the

other rays reflected at different angles of the incident ray. Figure 4.15 shows the diffuse and spectral reflection. When powdered samples are irradiated with a UV-Vis ray, due to diverse shapes of the powder particles, a fraction of this incident light beam is reflected in different directions and another fraction is refracted into the powder.

Inside the powder, the light is also scattered by internal reflection and emitted back into the air. This light reflected in different direction from the surface and from inside the powder sample is measured and observed in a diffuse reflected spectrum. Figure 4.16 shows the configuration for the measurement of diffuse reflection using an integrating sphere. The sample is placed in front of the incident light window and the light reflected from the sample is concentrated on the detector using a sphere with a barium sulphate-coated inside. This configuration avoids the specular reflection to be detected. The obtained value is a relative reflectance with respect to the reflectance of the reference standard white board (its value is 100%).

Figure 4.15. Diffuse and spectral reflection. Source: own elaboration adapted from [153][154]

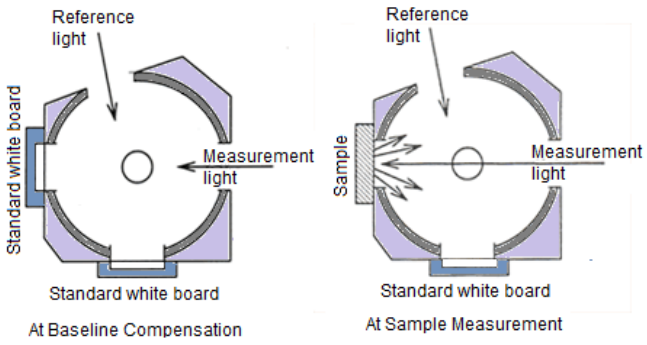

Figure 4.16. Operation fundaments of Diffuse Reflectance UV-Vis [155]

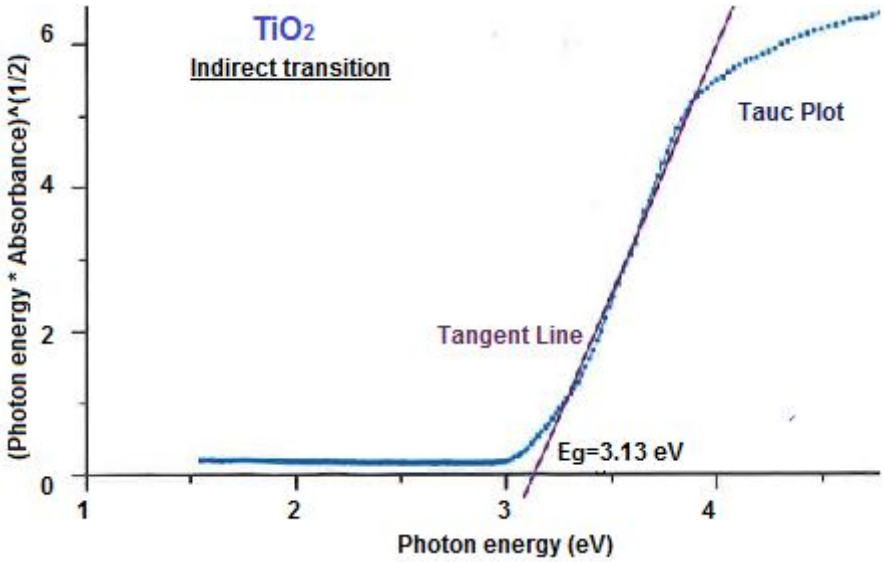

Figure 4.17. Tauc Plot for Band-gap determination [155]

Diffuse reflectance spectroscopy is widely used for determination of band gap in semiconductor materials. The **band-gap** is the difference in energy between the top conduction band filled with electrons and the bottom valence band empty of electrons. Therefore, band-gap is related to the electric

conductivity of materials. The most common theory to describe and analyse the diffuse reflectance spectra is by Kubelka-Munk function, which convert the diffuse reflectance spectrum into absorbance. The determination of band-gap was by the Tauc plot for Indirect transition (see Figure 4.17), that relates the photon energy (hν) and absorbance in the vertical axis $((h\nu * Absorbance)^{1/2})$ vs. hν (eV) in the abscissa axis. A drawn line, tangent to the point of inflection on the curve of Tauc plot and the hν value at the point of intersection of the tangent line and the abscissa axis is the band gap Eg value.

4.7. Analytical procedures

4.7.1. Gas Chromatography (GC) [146]

H_2 evolution was monitored by on-line gas chromatography (GC) (Shimadzu, GC-14B, Carbosieve SII 100/120, 3 m 1/8" SS column, TCD detector, gas carrier: Ar. Oven and detector temperatures: 60 °C and 150 °C, respectively) by injecting sample to the GC every 15 minutes for 3 h.

The operational basis of the gas chromatography (GC) is based in the separation of a gaseous sample in its components while it passes along a chromatographic column. The components are then, identified and determined by the difference in the coming out time from the column in a detector. Figure 4.18 shows a basic scheme of a gas chromatography. The **gas carrier** is used as a **mobile phase**, which has to be inert chemically. Although helium is the most common carrier gas in gas chromatography, argon, nitrogen and hydrogen are also used. This flow is controlled and regulated before entering in the GC equipment.

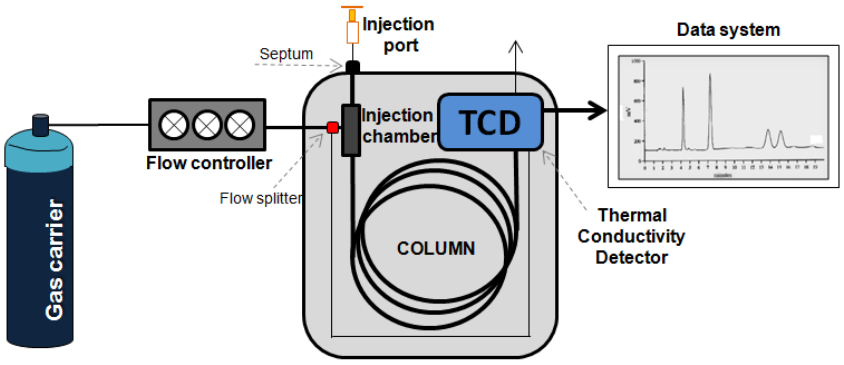

Figure 4.18. Gas Chromatographic system (GC). Source: own elaboration

Figure 4.19 shows the operational basis of the separation in a chromatographic column, which consists in a narrow tube filled with an inert solid finely distributed along the column. The fine solid layer keeps the stationary phase on its surface while the mobile phase carries the vaporized sample along the column.

When the sample (A+B+C) come into the column (t0), due to its interaction between the mobile and stationary phase, the components are distributed between both phases (t1). The constant introduction of new mobile phase, push the eluent (sample + mobile phase) to move forward and downward along the column, where components A, B and C advance at different medium velocities. The advance velocity of each component depends on the portion of time they reside on the mobile phase, which depend on how

strongly or weakly are retained the components, A, B and C, by stationary phase. From Figure 4.19, it is seen for instance, component C is more strongly retained by the stationary phase that B or A, and the same fact if is compared component B and C.

As a result of these differences in the velocity, the components are separated in bands or zones along the column and these bands elute from the column toward the detector (in this case it was a **Thermal Conductivity Detector TCD**) at different **retention time** (t3: A, t4: B and t5: C component).

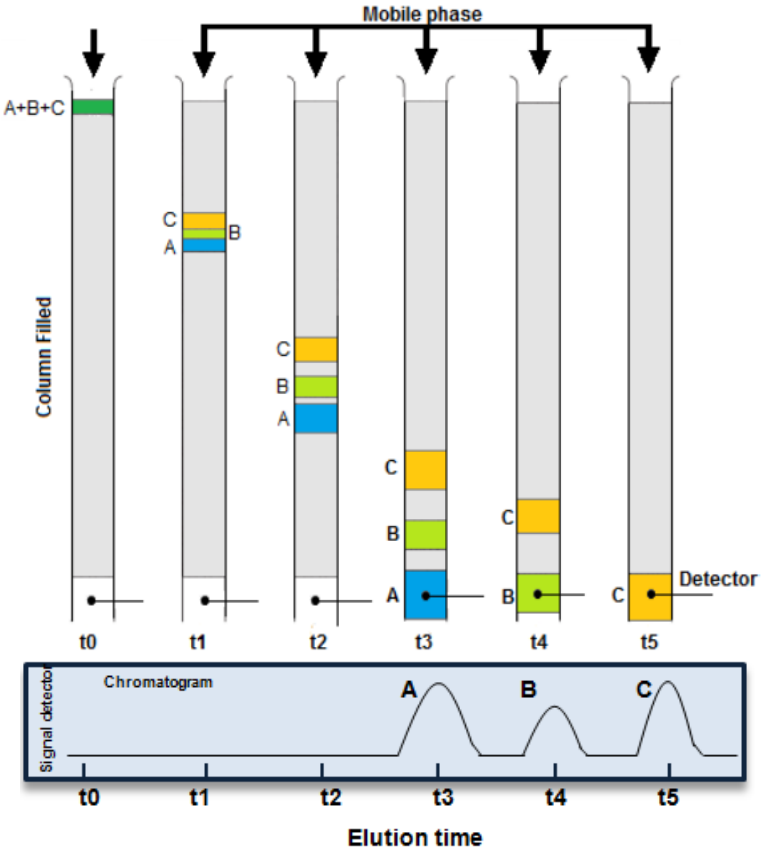

Figure 4.19. Operational fundament of a chromatographic column. Source: own elaboration adapted from [146]

4.7.2. Total Organic Carbon (TOC) [156][157][158]

The organic content was quantified as TOC by using a Total Organic Carbon analyzer: Shimadzu TOC-L CSH/CSN. The total organic carbon (TOC) is the total amount of carbon in an organic aqueous solution and it is commonly used to have an easy and direct measurement of the pollution level due to the organic matter. To the TOC value contribute substances with natural origin as amines, humic and fulvic acids, and urea, or synthetic materials from human activities such as pesticides, fertilizers and detergents. TOC analysis includes indication of water contamination by synthetic compounds, chemical characterization, degree of humification of wastes (in soil for instance), carbon cycling of soils and also the carbon in aquatic systems.

Basically, the TOC measurement is performed by converting all the kind of carbon from the sample into CO_2 and exist direct or indirect methods for it. In the direct method, the organic carbon (OC) can be

measured by two ways: (i) removing the inorganic carbon (IC) by mean an acid treatment before measuring the OC, or (ii) not removing the IC, then the content of OC is determined by a chemical oxidation. The indirect method consists in a mathematical subtraction of the inorganic compounds content (IC) from the total carbon (TC). In this second method, the IC content can be determined in the purging gas from acid treatment or by the decomposition after the OC elimination. In the case of the TC measurement, it is by the oxidation of all the carbon present in the sample. For more information about this technique, authors suggest next literature: [158].

4.7.3. Actinometry

The quantum yield of a photochemical process is determined by the relationship between the amount of the reactant material (or product generated) during the photoreaction, and the total amount of light absorbed by the system at a specific wavelength. Then, the chemical actinometry is a tool that allows determining the total amount of light absorbed by the reactant solution.

The actinometry used in this work has been the Parker's actinometry [159] based on the photochemical reduction of the Fe(III) from the ferrioxalate complex $[Fe(C_2O_4)_3]^{3-}$ to Fe(II). This reaction takes place with a quantum yield 1 - 1.2 mol.Einstein^{-1} between 250 - 450 nm [160]. Briefly, for this reaction was necessary to prepare three solutions: (i) an aqueous solution of **perchloric acid** ($HClO_4$) (**0.03 M**) at pH 2; (ii) an **oxalic acid (0.15 M)** solution in the buffer solution (i) (perchloric/ perchlorate); (iii) a **Fe(III) solution (0.15 M)** in the solution (i), which was purged with argon for 30 min before the photoreaction.
Fe(III) source was $Fe(ClO_4)_3.9H_2O$. The three solutions were then, added to the reactor in the proportion 80 % of solution (i), 10 % of solution (ii) and 10 % of solution (iii). In that way the final concentration of the actinometer solution $Fe(C_2O_4)_3^{3-}$ was 5.10^{-3} M.
The **Fe(II) concentration along time was followed by the *o*-phenanthroline method** [161], which is based on the formation of a coloured complex between the Fe(II) in solution and the 1,10-phenanthroline in acid medium acetic acid/acetate at pH 3 - 4. The coloured complex absorbance is measured at 510 nm. Then, the Fe(II) concentration was determined by the Beer's law, where in the absence of any species that absorb radiation at 510 nm, it is:

$$C_{Fe(II)}, M = \frac{(Abs_m - Abs_0)}{\varepsilon_{510\,nm}.C}.\frac{V_T}{V_m} \qquad (4.7.3.1)$$

where $C_{Fe(II)}$: Fe(II) molar concentration; Abs_0: absorbance of the blank; Abs_m: absorbance of the sample; ε_{510nm}: molar absorptivity or molar extinction coefficient of the complex *o*-phenanthroline-Fe(II) at 510 nm (11023 $M^{-1}.\,cm^{-1}$); c: optical path (1 cm); V_T: total volume (5.1 ml) and V_m: volume of the sample (3 ml). Then, the incident radiation intensity (I_0) determination was by means of the Eq. 4.7.3.2 as follows: in the absence of any other compound that could photoreact, the rate at which the ferrioxalate is photoreduced, or the same if we express it in terms of the rate at which Fe(II) is formed is:

$$\frac{-dC_{Fe(III)}}{dt} = \frac{dC_{Fe(II)}}{dt} = I_0.\Phi.(1 - \exp(-2.303 - L.\varepsilon_{510\,nm}.C_{act})) \qquad (4.7.3.2)$$

where I_0: Incident radiation intensity; ϕ: quantum yield at the wavelength of the radiation (1.2 mol·einstein^{-1}); L: effective radiation pass through the reactor; ε: molar extinction coefficient of the ferrioxalate (500 $M^{-1}\cdot cm^{-1}$ at 365 nm [162]); and C_{act} actinometer concentration. For values of the expression ($2{,}303\cdot L\cdot\varepsilon\cdot C_{act}$) higher than 2, which is the case under these experimental conditions, the Eq. 4.7.3.2 is simplified to Eq. 4.7.3.3. Then, as the representation of the Fe(II) concentration evolution vs. time is linear with a value slope of $I_0\cdot\phi$, where ϕ is known (1.2 mol·einstein^{-1}), is possible to obtain the Incident radiation intensity I_0:

$$\frac{-dC_{Fe(III)}}{dt} = \frac{dC_{Fe(II)}}{dt} = I_o \cdot \Phi \qquad (4.7.3.3)$$

$$C_{Fe(II)} = I_o \cdot \Phi.t \qquad (4.7.3.4)$$

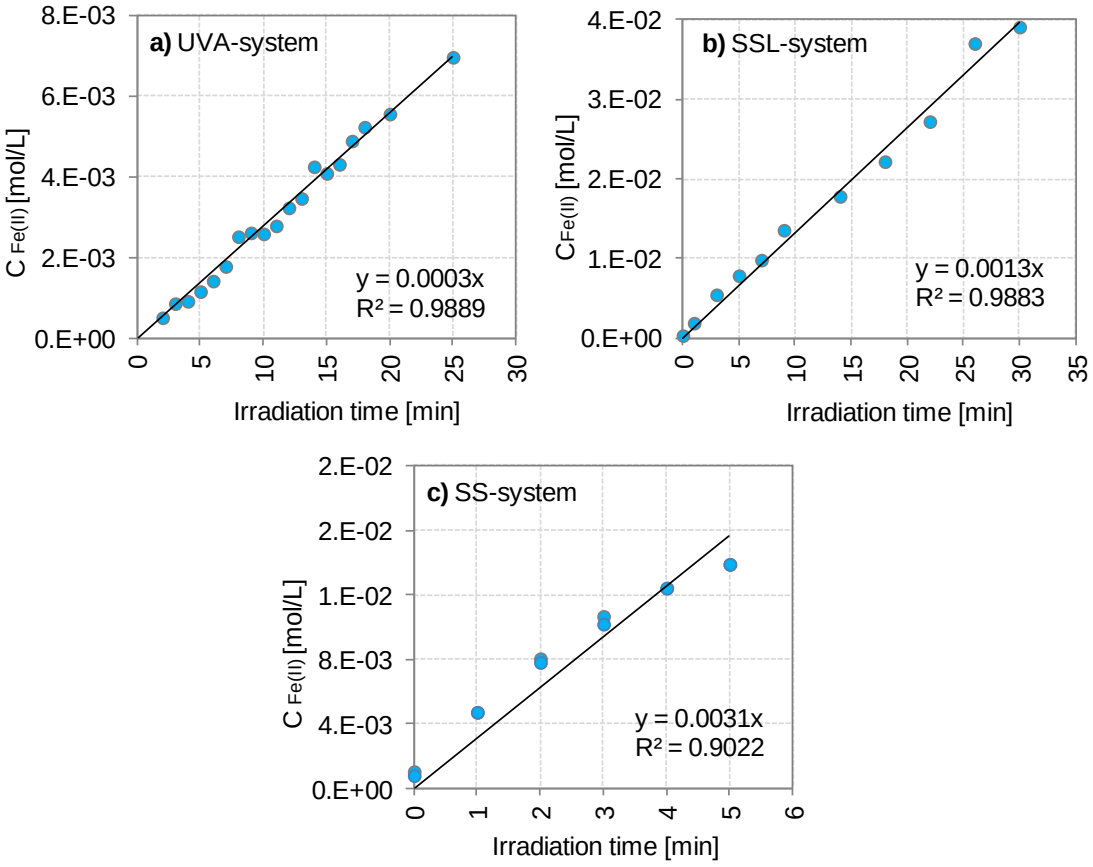

Figure 4.20. Determination of the Incident radiation intensity I_0

Figure 4.20 shows the determination of the incident radiation intensity for both UVA and solar box systems. Then, in the case of the UVA box, the slope 0.0003 is multiplied by the volume of the reactor (0.25 L) and divided by ϕ (1.2 mol·einstein^{-1}). For the solar box the slope is 0.0013 and the volume of the reactor 0.6 L. In thesis, the actinometry test was performed to three systems which are later explained in more details, but briefly they are: UVA (UVA-system), Solar Simulated Light (SSL-system) and Small Scale (SS-system). Therefore, for UVA-system, **$I_{0\ (250\text{-}450\ nm)}$ =8.33x10^{-5} Einstein/min**, **$I_{0\ (250\text{-}450\ nm)}$ =6.25x10^{-4} Einstein/min** for the SSL-system and **$I_{0\ (250\text{-}450\ nm)}$ =3.88x10^{-5} Einstein/min** for the SS-system.

4.8. H_2 generation experimental set-up

The photocatalytic H_2 tests were performed in four different systems: (i) Simulated solar light system (SSL-system), (ii) UVA light system (UVA-system), (iii) Pilot plant scale system (PPS-system) and (iv) small scale system (SS-system). The SSL-system and UVA-system both are located in the CATHETER labs, the PPS-system in the Solar Platform of Almeria (PSA) and the SS-system in the PCS labs.

4.8.1. Simulated Solar light System (SSL-system)

Figure 4.21 (a) shows a simplified diagram of the SSL-system. It consisted in a borosilicate reactor (750 ml) with a wider shape inside of a solar simulator chamber (SUNTEST CPS+) with a Xe lamp at the top of the chamber (300 - 800 nm; 250 W/m^2, $I_{250\text{-}450nm}$: 6.5x10^{-4} Einstein/min). See in picture 1 (a and b) the photography of the reactor for the SSL-system and the chamber.

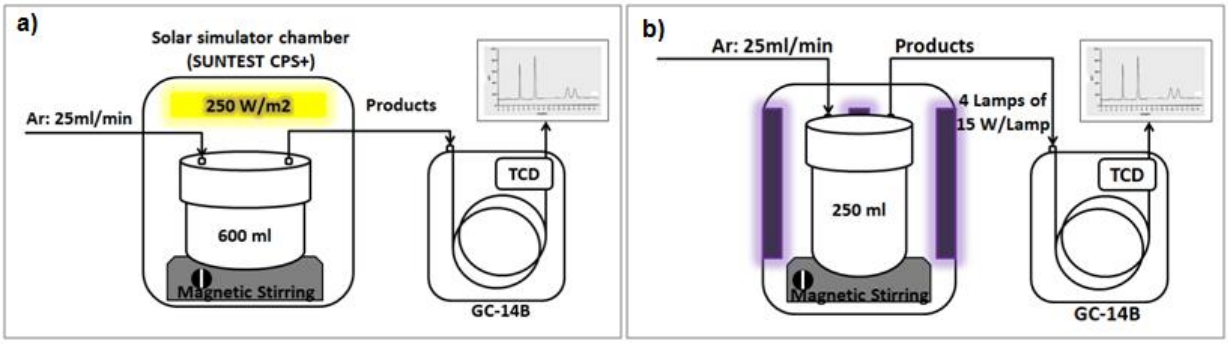

Figure 4.21. Experimental set up for photocatalytic H_2 generation. **a)** SSL-system diagram (λ: 300 - 800 nm; 250 W/m^2, $I_{250\text{-}450\ nm}$: 6.5x10^{-4} Einstein/min). **b)** UVA-system diagram (λ: 300 - 400 nm; 4 lamps of 15 W/lamp, $I_{250\text{-}450nm}$: 8.33x10^{-5} Einstein/min).

The reactor was provided with a gas inlet connected to a mass controller (Alicat scientific MC-50SCCM-D/5M) to keep constant the flow (25 ml/min) of the carrier gas through the system and the gas outlet was connected to a water trapping (to avoid damages in controller mass equipment in case of over pressure in the line forward). H_2 evolution was monitored by on-line gas chromatography (GC) (Shimadzu, GC-14B, Carbosieve SII 100/120, 3 m 1/8" SS column, TCD detector, gas carrier: Ar. Oven and detector temperatures: 60 °C and 150 °C, respectively) by injecting sample to the GC every 15 minutes for 3 h. The H_2 production reaction was performed without adjusting the pH and without control of temperature; this parameter oscillated between 25 - 40 °C during the experiment. A magnetic stirring was used to maintain the catalyst in suspension during the reaction time.

4.8.2. UVA light System (UVA-system)

Figure 4.21 (b) shows a simplified diagram of the UVA-system, which consisted on a vertical glass reactor (300 ml) placed inside a white methacrylate chamber equipped with four UVA lamps arranged in each one of the inner faces of the chamber (300 - 400 nm; 15 W/lamp, $I_{250\text{-}450nm}$: 8.3x10^{-5} Einstein/min). Picture 1(c) shows a photography of the reactor for the UVA-system inside the UV box. The reactor in the UVA-system was provided with the same gas inlet and outlet described above for SSL-. The mass

controller was set also at a constant flow of 25 ml/min to lead the carrier gas through the system (water trapping - reactor - GC). The H_2 production reaction was also performed without adjusting the pH and without control of temperature (without sensor for temperature measurement in this system).

Picture 1. (a) Reactor for SSL-system, **(b)** solar simulated chamber and **(c)** reactor for UVA-system and UV box

In a typical photocatalytic experiment, either in the SSL-system or UVA-system, the reactor was loaded with an aqueous solution of a sacrificial agent, methanol or glycerol, (5, 10, 25 or 50 vol.%), or a real wastewater, and the catalyst (500, 333, 167 or 83 ppm). Then, the reactor was placed inside the solar box or the UVA box, and the solution was bubbled with argon (50 ml/min) around 60 minutes to remove air inside the reactor. The reactor was under irradiation for 185 min and every 15 minutes a sample was automatically injected into the GC. Before and after the irradiation, a small liquid sample was withdrawn to perform pH and TOC measurement.

In the case of real wastewater, the reactor was loaded with the real wastewater plus the catalysts, and before and after the photocatalytic test, a liquid sample was also taken for pH and TOC measurement. Additionally, chlorine and conductivity measurement were made with an ISE Chloride electrode with a selective membrane: solid state $AgCl/Ag_2S$ (CRISON) and a CRISON 5061 conductivity cell, respectively. Gas samples were also automatically injected to the GC every 15 min for 185 min of irradiation.

4.8.3. Pilot Plant Scale System (PPS-system)

Figure 4.22 shows a simplified diagram of the PPS-system, which consisted of two sections: (i) **a closed stainless tank** of 27 L, provided with gas and liquid inlet and outlet, and a liquid sample port. A centrifugal pump (PanWorld NH-100PX) with a flow rate of 20 L/min was used to recirculate the aqueous solution from the tank to the tubes of the Compound Parabolic Collector (CPC), and (ii) the **CPC photoreactor** was composed of 16 Pyrex glass tubes (inner diameter 28.45 mm, outer diameter 32.0 mm, length1401 mm) mounted on a fixed platform tilted 37° (local latitude). The total area and volume irradiated were 2.1 m^2 and 14.25 L, respectively.

In a typical experiment, the catalyst (5 g) was sonicated in water for 15 minutes, then, the tank was loaded with 25 L of an aqueous solution (0.2, 0.37 or 5 vol.% of methanol or glycerol). The later solution

was circulated through the system (from the tank toward the CPC photoreactor and again to the tank) under dark conditions for 15 minutes and the tank was bubbled with N_2 for 10 minutes. After that, the CPC photoreactor was uncovered and left under solar irradiation around 6 h, and every 60 minutes a gas sample was manually injected to the gas micro-chromatograph (Agilent technologies 490, CP-MolSieve 5A column channel: 10 m with blackfush and retention time stability, TCD detector, carrier gas: N_2, injection and oven temperatures: 90°C and 50°C, respectively).

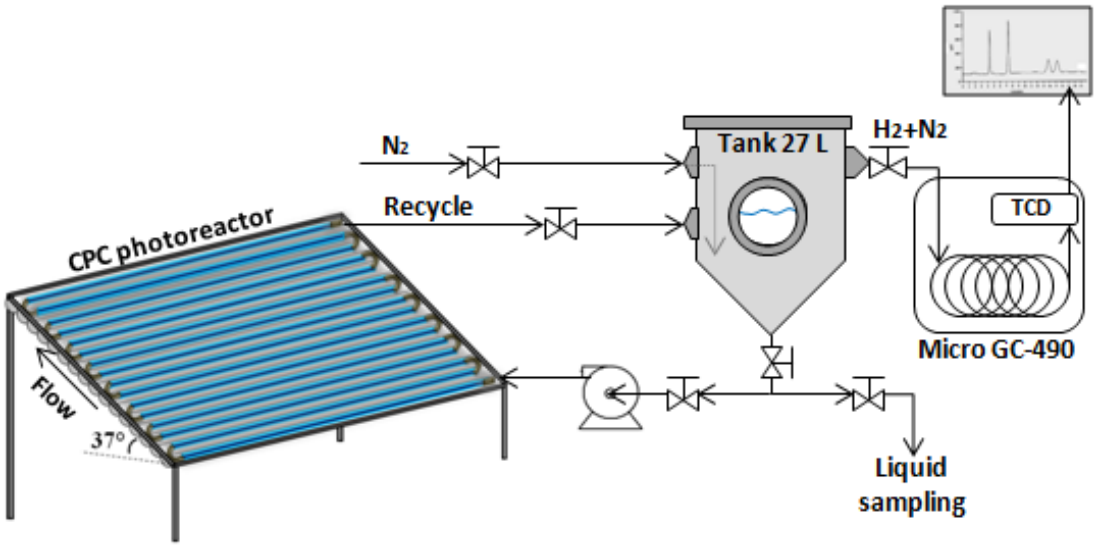

Figure 4.22. Experimental set up for photocatalytic H_2 generation in the PPS-system in the PSA.

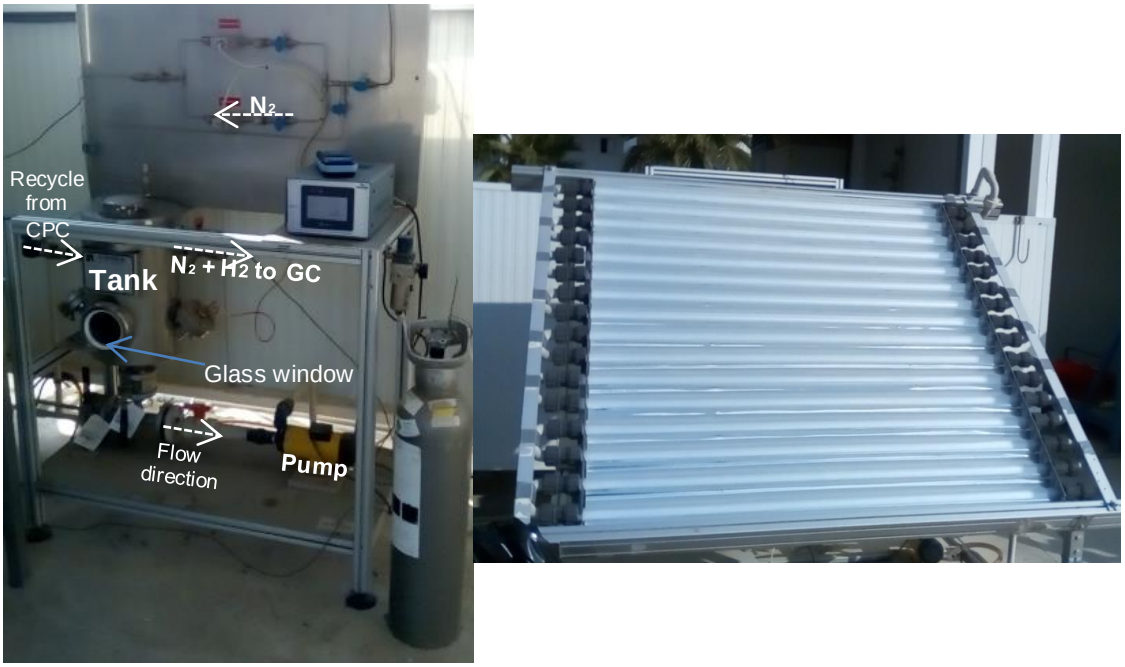

Picture 2. Pilot plant setup in the PSA

When solar radiation is used as an energy source it is necessary to take into account its lack of steadiness and the fact that it changes during the day or in one hour (depending on the time and weather of the day, or the year season). Therefore, in order to compare the H_2 production of experiments performed in different days, it is required to normalize the data by using Eq. (4.8.3.1):

$$Q_{UV,n} = Q_{UV,n-1} + \Delta t_n \overline{UV}_{G,n} \frac{A_i}{V_t} \qquad (4.8.3.1)$$

Where $Q_{UV,n}\ (kJ/L)$ is the solar UV energy accumulated per reactor volume unit along the experiment and it is used instead of the irradiation time to normalize the H_2 evolution. This irradiation is referred to the 300 - 400 nm wavelength range. $\Delta t_n\ (seg)$ is the experimental time for every gas sampling, $A_i\ (m^2)$ is the irradiated area of the CPC photoreactor, $V_t(L)$ is the volume of the solution loaded to the tank and $\overline{UV}_{G,n}\ (W/m^2)$ is the average solar UV radiation intensity measured by a radiometer (KIPP&ZONNEN, CUV3 model) in the period Δt_n.

The radiometer provided data every minute of the incident radiation corresponding to wavelengths below 400 nm. The approximate value of $Q_{UV,n}$on the experimental days of autumn in Almería (around 10 h to 16 h) is 30 - 35 kJ/L. Organic content was quantified as DOC by using a Shimadzu VCSH TOC analyzer. In the picture 2 is shown some photos of the experimental set up for H_2 generation in the in the PSA.

4.8.4. Small scale system (SS-system)

Figure 4.23 shows the simplified diagram of the SS-system in the PCS labs. The photocatalytic H_2 set up consisted in a small quartz reactor (reaction volume of 15 ml) inside a cylindrical batch stainless vessel (internal volume of 50 ml). Magnetic stirring was used to maintain the reaction solution continuously stirred during the reaction time. The light source was a 120 W high pressure mercury lamp from Dr. Gröbel UC-Electronik GmbH, with an spectral range from 280 - 700 nm, from which the light was introduced in the reactor through an optical fiber UV/Vis-Emission: ca. 8 W/cm^2. The optical fiber was introduced into the system through a small window (fused silica which allows 90% transmission) in the lid of the reactor.

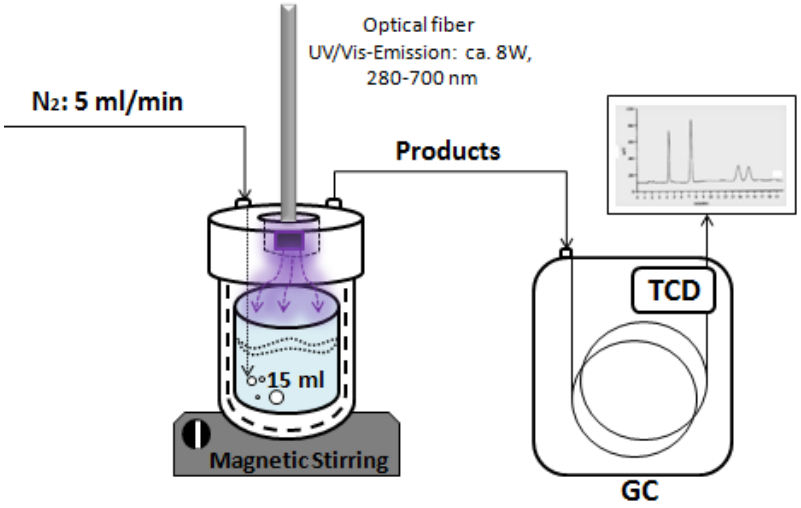

Figure 4.23. Experimental set up for photocatalytic H_2 generation in the SS-system in PCS Labs.
Irradiation: Optical fiber UV/Vis-Emission: ca. 8W/cm^2 (280-700 nm, $I_{250-450nm}$: 3.88x10^{-5} Einstein/min)

The reactor was provided with a gas inlet and outlet, where the gas inlet was connected to a mass flow controller (LabView interphase) to keep the mass flow of the gas carrier constant (N_2: 5 ml/min). The gas

outlet was connected on-line to a gas chromatograph (GC equipped with a Parabond Q column (10 m), TCD detector) to determine the H_2 concentration in the product gas. Similar to previous systems, in SS-system the H_2 production reaction was performed without adjusting the pH and without control of temperature. Picture 3 shows some photos of the experimental set up for H_2 generation in the in the PCS labs.

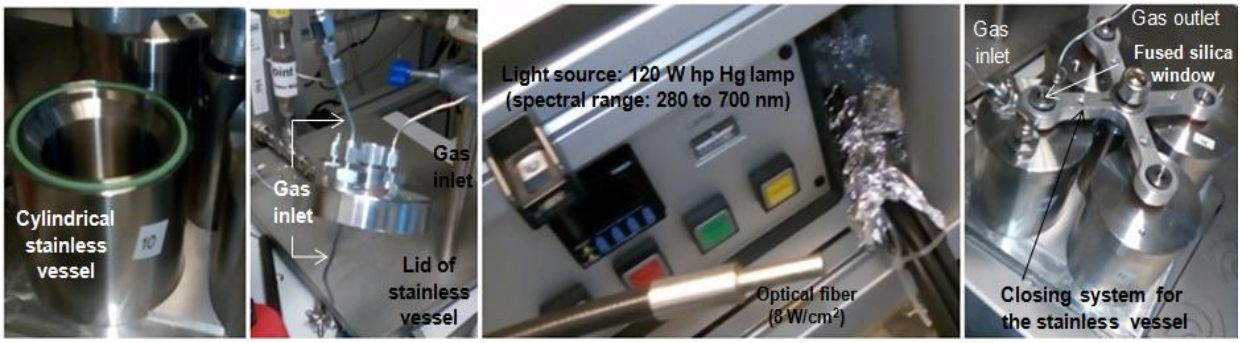

Picture 3. PCS Lab setup for photocatalytic H_2 generation

4.8.5. Attenuated Total Reflectance-Fourier Transform Infrared Spectroscopy [163][164]

A Harrick Scientific ATR-setup, including in the compartment a Bruker Vertex 70 spectrometer) was used to study the solid-liquid interface during the photocatalytic experiments.

FTIR is a technique for molecular characterization by means of the identification of the type of functional groups in the sample. This identification is facilitated by the type of chemical bond in the molecule, which vibrates at a frequency characteristic of that bond.

Additionally, as vibrational frequencies of most of the molecules correspond to the infrared frequency radiation, this characterization technique uses the mid-infrared range corresponding to 4000 - 400 cm^{-1}. Therefore, when the photons of infrared (IR) radiation are absorbed by a molecule, the chemical bonds oscillate at a higher level of energy; this molecular oscillation might be as stretching or bending vibrations. Then, according to the type of bond in the molecule the frequency of the IR radiation is absorbed, giving rise to a characteristic infrared spectrum that allows the determination of a functional group in the molecule.

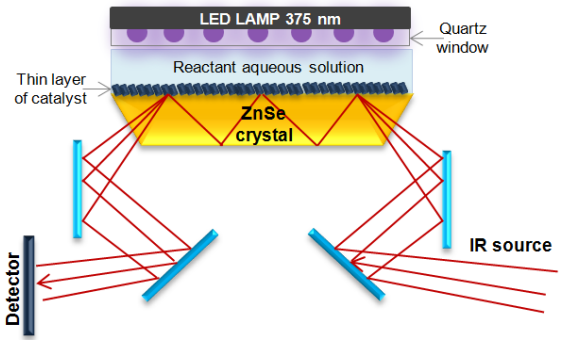

Figure 4.24. Operational fundaments of ATR-FTIR. Source: own elaboration adapted from [65]

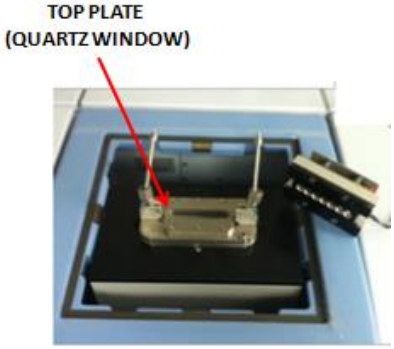

Picture 4. Setup for ATR-FTIR experiments [65]

Figure 4.24 shows the experimental setup for the in-situ ATR-FTIR spectroscopy experiments. A thin layer of catalyst with a pre-treatment was deposited on a ZnSe ATR crystal. The amount of catalyst corresponded to 1000 ppm in 2 ml of an aqueous solution of methanol (50 vol.%). The pre-treatment consisted in: firstly, a milliQ water solution with 1000 ppm of catalysts was treated for 30 min in a 35 kHz Elmasonic ultrasonic bath. Then, 1 ml of this solution was added dropwiseon the ATR crystal, and dried in a desiccator at room temperature in vacuum and dark conditions overnight.

Previously to photocatalytic experiment, a water-methanol (50 vol.%) solution was prepared and purged with argon for 30 min. Then, the deaerated solution was deposited on the thin film of catalyst. The crystal with the thin film catalyst was already mounted on a special configuration for ATR-FTIR tests (see picture 4). On top of the system was placed a 7 LED's lamp (365 nm) which was separated from the reactant aqueous solution by a top plate with a quartz window. Before irradiation, a spectrum of the system under dark conditions was recorded and used as background spectrum for activity measurement during the experiment. Every 1 minute a spectrum was measured from 500 - 4000 cm^{-1}, averaged from 64 scans with a resolution of 4 cm^{-1}.

CHAPTER 5

Results and Discussion

5. RESULTS AND DISCUSSION

In this section the results corresponding to the photocatalytic materials characterization, H_2 generation, H_2 generation comparison and literature comparison are discussed. Characterization and H_2 generation results are presented by groups of catalysts, which are:

- w-Pd/TiO_2(-WO_3) - CATHETER Lab catalysts
- m-Pd/TiO_2(-WO_3) - CATHETER Lab catalysts
- m-Pd/TiO_2(-WO_3) - PSC Lab catalysts
- m-Pt/TiO_2(-WO_3) - PSC Lab catalysts
- Pd/TiO_2-Cu - CATHETER Lab catalysts

5.1. Characterization Results

5.1.1. Inductively Coupled Plasma (ICP-OES) and X-Ray Fluorescence (XRF)

Some of the features of the characterization of photocatalytic materials based on Pd/TiO_2(-WO_3) prepared in CATHETER Lab are shown in Tables 3 and 4. Tables 5 and 6 show the same characterization but for those catalysts prepared in the PCS Lab, where catalysts containing Pd are presented in Table 5 and those containing Pt are shown in Table 6. Table 7 presents some characterization of catalysts containing Cu, Pd and TiO_2.

5.1.1.1. w-Pd/TiO_2(-WO_3) - CATHETER Lab catalysts

For catalysts listed in Table 3, the Pd was introduced by PD-w and the objective was to introduce a very low amount of Pd (around 0.01 wt %) in order to determine the effect of small amount of Pd particles on the H_2 generation. The NT, P25, pure anatase phase and the incorporation of WO_3 in these supports were also studied.

Table 3 shows the amount of Pd determined by ICP-OES of the different w-Pd/TiO_2(-WO_3), samples. Surface area (S_{BET}), pore volume (V_{PORE}) and band-gap energy (Eg) with the corresponding wavelength are also included.

Table 3. List of w-Pd/TiO_2(-WO_3) - CATHETER Lab catalysts and some of their features related to characterization of the solids

Catalyst	Weight % (ICP-OES)	Pd Particle size (nm) by TEM	S_{BET} (m^2g^{-1})	Total V_{PORE} (cm^3g^{-1})	E_g (eV)	λ (nm)
Pd/NT-WO_3-4w	0.013	< 2	94.13	0.3691	2.94	422
Pd/P25-WO_3-4w	0.011	< 2	58.02	0.3407	3.06	406
Pd/P25-4w	0.009	5 - 7	55.16	0.3960	3.08	403
Pd/TiO_2-anatase-4w	0.007	-	11.07	0.0856	3.11	399
NT-WO_3	-	-	104.64	0.3890	2.97	418
P25-WO_3	-	-	58.81	0.3690	3.08	403
P25	-	-	54.69	0.2635	3.10	399
TiO_2-anatase	-	-	9.81	0.0575	3.14	395

5.1.1.2. m-Pd/TiO_2(-WO_3) - CATHETER Lab catalysts

Table 4 shows the amount of Pd, determined by ICP-OES for m-Pd/TiO_2(-WO_3) samples. Palladium was introduced by PD. The objective was to study the influence of the metal deposition method on the photocatalytic H_2 evolution. Briefly, as a reminder, catalyst nomenclature includes metal, real Pd content, deposition method and the PD conditions. Below Table 4, the nomenclature is explained in more detail.

Table 4. List of m-Pd/TiO_2-WO_3 - CATHETER Lab catalysts and some of their features related to characterization of the solids

Catalyst	Nominal Pd (wt.%)	Measured Pd % (ICP-OES)	E_g (eV)	λ_{max} (nm)	Particle size (nm) by TEM	S_{BET} (m^2g^{-1})	Total V_{PORE} (cm^3g^{-1})
	0.5	0.35	-	-	-	104.06	0.40
Pd/NT-WO_3-2m10[a]	0.25	0.21	2.89	429	1, 4 -10	99.60	0.34
	0.1	0.1	2.94	422	2 - 3	101.57	0.37
	0.5	0.52	-	-	-	58.29	0.37
Pd/P25-WO_3-2m10	0.25	0.23	2.99	415	2, 6 - 8	55.39	0.35
	0.1	0.1	3.00	414	< 1	58.15	0.36
	0.5	0.51	3.00	414	4 - 12	56.64	0.41
Pd/P25-2m10	0.25	0.24	2.92	425	5 - 7	56.48	0.37
	0.1	0.09	2.94	422	< 2	55.56	0.42
Pd/P25-2m5[b]	0.25	0.25	2.96	419	-	56.32	0.41
Pd/P25-2m1[c]	0.25	0.23	2.98	416	3 - 15	54.70	0.43
Pd/P25-WO_3-2m1	0.25	0.23	2.98	416	2, 4- 10	59.87	0.35
Pd/NT-WO_3-4m10[d]	0.25	0.26	2.96	419	-	101.37	0.37
Pd/P25-WO_3-4m10	0.25	0.27	3.00	414	-	59.70	0.35
	0.5	0.47	2.97	418	4 - 12	56.68	0.44
Pd/P25-4m10	0.25	0.21	2.95	421	5 - 7	55.65	0.36
	0.1	0.1	2.98	416	< 2	54.86	0.43
Pd/NT-WO_3 -1m10[e]	0.25	0.15	2.94	422	-	100.47	0.33
Pd/NT-WO_3-4w[f]	0.25	0.012	2.94	422	< 2	94.13	0.37
Pd/P25-WO_3-4w	0.25	0.011	3.06	406	< 2	58.02	0.34
Pd /P25-4w	0.25	0.001	3.08	403	5 - 7	55.16	0.40
Pd/P25-wi[g]	0.25	0.25	2.98	416	5 - 15	53.11	0.40
NT-WO_3	-	-	2.97	418	-	104.64	0.39
P25-WO_3	-	-	3.08	403	-	58.81	0.37
P25	-	-	3.10	399	-	54.69	0.26
TiO_2-anatase	-	-	3.14	395	-	9.81	0.06

Pd photodeposition with:
[a] 2m10: 2000 ppm of catalyst in a mixture of water-methanol (10 vol.% methanol)
[b] 2m5: 2000 ppm of catalyst in a mixture of water-methanol (5 vol.% methanol)
[c] 2m1: 2000 ppm of catalyst in a mixture of water-methanol (1 vol.% methanol)
[d] 4m10: 4000 ppm of catalyst in a mixture of water-methanol (10 vol.% methanol)
[e] 1m10: 1000 ppm of catalyst in a mixture of water-methanol (10 vol.% methanol)
[f] 4w: 4000 ppm of catalyst in mlQ water
[g] wi: Wetness Impregnation

Comparing the Pd content, it is observed that for catalysts where Pd was deposited by PD-m methods, the Pd content is above 80 % of the nominal content, while in the PD-w methods, the real content of Pd was scarcely around 10 %. This fact reveals the importance of a sacrificial agent in the PD, which acts as h^+ scavenger and therefore, more photoexcited e^- are available to reduce the Pd^{+2} in solution to Pd^0 on the support surface, increasing the Pd content photodeposited. Regarding the effect of the Pd concentration during the photo-deposition process using different amount of supports (PD in 4000, 2000 and 1000 ppm of catalyst), no significant differences in the Pd content were observed.

5.1.1.3. m-Pd/TiO_2(-WO_3) - PCS Lab catalysts

For those catalysts prepared in the PCS Lab, Pd and Pt metal content (Table 5 and 6, respectively) were analyzed by X-Ray Fluorescence (XRF, Philips PW 1480).

Two different PD methods were used for catalyst preparation, named: 2m10 and 3.2m20, whose definition is given below Table 5. The influence of the Pd deposition method on the photocatalytic H_2 evolution was studied in Table 5, comparing the Pd PD preparation methods performed in the PCS group (called 3.2m20) and CATHETER group (2m10).

Table 4 shows the catalysts prepared in CATHETER Lab, whereas Tables 5 and 6 show the catalysts prepared in PCS Lab. Hence, it is possible to see in Table 5 that, for most of the catalysts, the Pd content is above 75 % of the nominal content, both for the lowest Pd content (0.25 wt.%). For the highest Pd content (2 wt.%), the deposition was 100 % of the nominal Pd.

Table 5. List of Pd/TiO_2(-WO_3) - PCS Lab catalysts and some of their features related to characterization of the solids

Catalyst	Nominal Pd (wt.%)	Measured Pd % (XRF)	E_g (eV)	λ_{max} (nm)	Particle size (nm) by TEM	S_{BET} (m^2g^{-1})	Total V_{PORE} (cm^3g^{-1})
Pd/P25 - 2m10[a]	0.25	0.25	3.03	409	-	16.48	0.47
	2	2.01	3.05	407	-	12.31	0.39
Pd/P25 - 3.2m20[b]	0.25	0.25	3.05	407	-	11.23	0.40
	2	-	2.87	432	-	-	-
Pd/NT-WO_3 - 2m10	0.25	0.19	3.06	406	0.5 - 1*	9.48	0.42
	2	-	2.88	430	2.0 ± 0.4	9.37	0.35
Pd/NT-WO_3 - 3.2m20	0.25	0.27	3.06	406	-	10.93	0.40
	2	-	2.94	423	-	-	-
Pd/P25-WO_3 - 2m10	0.25	0.25	2.85	436	-	9.25	0.38
	2	-	2.79	444	-	6.35	0.36
Pd/P25-WO_3 - 3.2m20	0.25	0.23	3.03	410	-	-	-
	2	-	2.86	434	-	9.17	0.39

Photodeposition method at:
[a] **2m10**: 2000 ppm of catalyst in a mixture of water-methanol (10 vol.% methanol)
[b] **3.2m20**: 3200 ppm of catalyst in a mixture of water-methanol (20 vol.% methanol
* Diameter of Pd nanoparticles ensembles

5.1.1.4. m-Pt/TiO_2(-WO_3) - PCS Lab catalysts

The objective in Table 6 was to study the influence of the metal nature and the Pt PD method on the photocatalytic H_2 evolution. These catalysts were compared to those containing Pd.
For catalysts containing Pt, the % in the metal deposition compared to the nominal seems lower than the catalysts containing Pd (see Table 5). For instance, for Pt(0.25 wt.%)/NT-WO_3 - 3.2m20, the real Pt content scarcely reached 52 % of the nominal amount, and for Pt(2 wt.%)/P25 - 2m10, this % deposition was 74.5%.

Table 6. List of Pt/TiO_2(-WO_3) -PCS Lab catalysts and some of their features related to characterization of the solids

Catalyst	Nominal Pd (wt.%)	Measured Pt % (XRF)	E_g (eV)	λ_{max} (nm)	Particle size (nm) by TEM	S_{BET} (m^2g^{-1})	Total V_{PORE} (cm^3g^{-1})
Pt/P25 - 2m10	0.25	0.18	3.04	408	0.5 *	26.70	0.81
	2	1.49	3.06	406	-	21.74	0.64
Pt/P25 - 3.2m20	0.25	0.15	3.06	405	-	14.68	0.49
	2	-	2.86	434	-	-	-
Pt/NT-WO_3 - 2m10	0.25	0.24	3.05	407	0.5 *	9.70	0.52
	2	-	2.84	437	-	9.56	0.40
Pt/NT-WO_3 - 3.2m20	0.25	0.13	3.06	405	-	10.67	0.46
	2	-	2.80	444	-	-	-
Pt/P25-WO_3 - 2m10	0.25	0.21	2.89	430	0.5 *	11.22	0.35
	2	-	2.82	440	2.9 ± 0.5	9.98	0.35
Pt/P25-WO_3 - 3.2m20	0.25	0.2	2.93	423	-	-	-
	2	-	2.80	443	-	-	-

*Diameter of Pt nanoparticles ensembles

5.1.1.5. Pd/TiO_2-Cu - CATHETER Lab catalysts

Table 7 shows some of the features of characterization of photocatalytic materials containing copper (Cu). For this type of catalysts, Cu was deposited first by wi, and then, Pd was introduced by PD or by wi as it is detailed below in Table 7.

The objective was to introduce different amount of Cu (2, 1, 0.5 and 0.1 wt %) in order to determine the effect of the insertion of this additional element, on the already studied Pd/P25 catalysts, on the H_2 generation (see Table 7).

Table 7. List of Pd/P25-Cu - CATHETER Lab catalysts and some of their features related to characterization of the solids

Catalyst	Synthesis Method	Nominal Pd (wt.%)	Measured Pd % (ICP-OES)	E_g (eV)	λ_{max} (nm)	S_{BET} (m^2g^{-1})	Total V_{PORE} (cm^3g^{-1})
Pd/P25-Cu(1 wt.%)	**Cu:** wi + C350[a] **Pd:** PD 2m10[b]	0.25	0.14	2.97	418	12.23	0.36
Pd/P25-Cu(0.5 wt.%)		0.25	0.12	2.88	430	8.39	0.39
Pd/P25-Cu(0.5 wt.%)		0.1	0.07	2.95	421	7.97	0.37
Pd/P25-Cu(0.1 wt.%)		0.1	0.03	2.92	425	8.80	0.40
Pd/P25-Cu(0.5 wt.%)	**Cu:** wi sC[c] **Pd:** PD 2m10	0.1	0.07	2.89	429	6.68	0.37
Pd/P25-Cu(0.1 wt.%)		0.1	0.06	2.89	429	9.67	0.37
Pd/P25-Cu(0.5 wt.%)	**Cu:** wi + C350 **Pd:** wi + R300[d]	0.25	0.25	2.89	429	5.49	0.34
Pd/P25-Cu(1 wt.%)		0.25	0.25	2.95	421	10.85	0.41
Pd/P25-Cu(0.5 wt.%)		0.1	0.1	2.85	435	6.78	0.42
P25-Cu(2 wt.%)	**Cu:** wi + C350	-	-	2.93	423	12.41	0.38
P25-Cu(1 wt.%)		-	-	2.91	426	11.82	0.40
P25-Cu(0.5 wt.%)		-	-	2.89	429	9.60	0.37

Deposition method:
[a] Cu deposited by wetness impregnation (wi) before calcinations at 350°C
[b] Pd photodeposited (PD) by 2m10 conditions: 2000 ppm of catalyst in a mixture of water-methanol (10 vol.% methanol)
[c] Cu deposited by wetness impregnation (wi) and **NO** calcination was done
[d] Pd deposited by wetness impregnation before a reduction in H_2 at 300°C

Comparing the Pd content of those catalysts where Pd was introduced by PD (the six first rows in Table 7), it is observed that the content of Pd only reached up to 70 %, and at higher Pd content, 0.25 wt.%, this deposition scarcely reached 60 %. It seems that Cu, which was firstly deposited on P25, may affect the PD of Pd by interfering in the Pd reduction on the catalytic support.

5.1.2. Total Surface Area (BET)

5.1.2.1. w-Pd/TiO_2 (-WO_3) - CATHETER Lab catalysts

Figure 5.1 shows N_2 adsorption - desorption isotherms for NT-WO_3, P25-WO_3 and P25 supports. Porous materials with type IV isotherms were observed, containing an H2 type of hysteresis loop for the NT-WO_3 and H3 type of hysteresis loop for P25-WO_3 and P25, according to IUPAC [165]. The narrow hysteresis loops of P25-WO_3 and P25 may indicate pores with a slot shape. However, the hysteresis loop for NT-WO_3 is wider, whose pores have probably a shape with a narrower necks and wider bodies (ink bottle shape).

Figure 5.2 shows N_2 adsorption-desorption isotherms for three catalytic supports after the deposition of Pd and Table 3 above shows the S_{BET} and V_{PORE} determined with a physisorption analysis. Figure 5.2 shows that there are not important changes in the pore structure of these materials with respect to the supports.

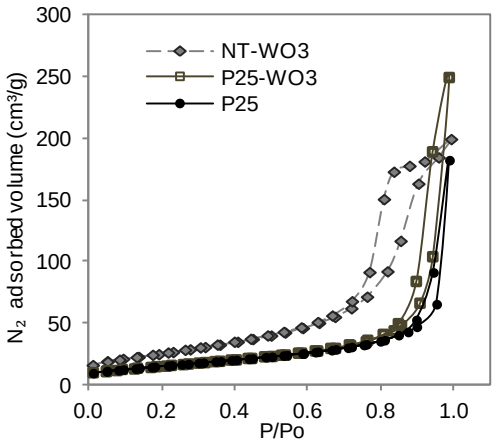

Figure 5.1. N_2 adsorption - desorption isotherms for the catalytic supports

For NT-WO_3 (104.6 m^2/g and 0.4541 cm^3/g), when Pd is photodeposited, the values of S_{BET} (94.13 m^2/g) and V_{PORE} (0.3691 m^3/g) were slightly reduced. The Pd nanoparticles could close some pores and fill others; therefore, the specific area is reduced as well as their pore volume. Looking at the hysteresis loop (Figure 5.2 (a)), Pd/NT-WO_3 has the same pore structure as NT-WO_3. Therefore, it can be concluded that the Pd nanoparticles could partially occlude the entrance of the pores without producing the plugging of the pores. Consequently, the pore structure is conserved but the pore volume and surface area decrease. Similar behaviour was observed for all the catalysts.

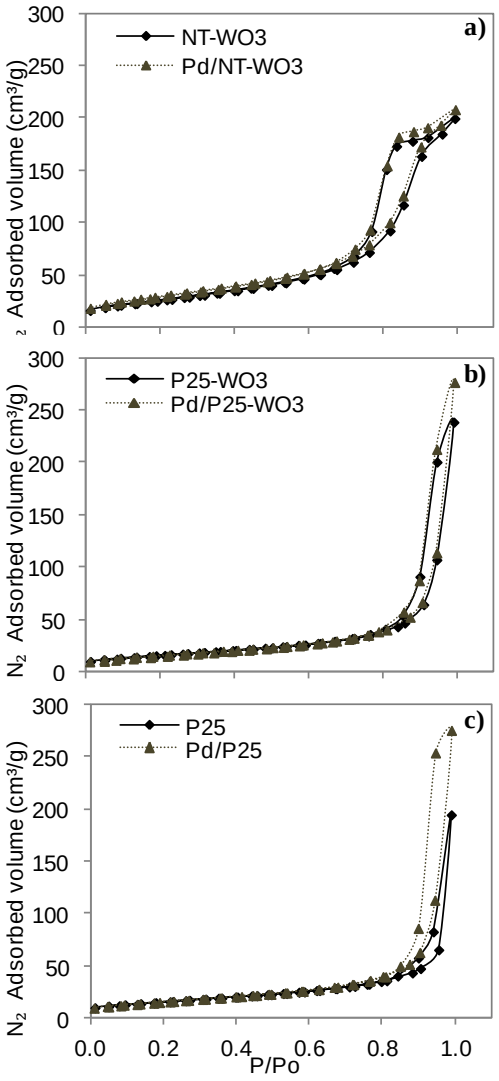

Figure 5.2. N_2 adsorption - desorption isotherms for: **a)** Pd(0.013 wt.%)/NT-WO_3; **b)** Pd(0.011 wt.%)/P25-WO_3 and **c)** Pd(0.009 wt.%)/P25

5.1.2.2. m-Pd/TiO_2 (-WO_3) - CATHETER Lab catalysts

Figure 5.3 (a), (c) and (e) show N_2 adsorption - desorption isotherms for NT-WO_3, P25-WO_3 and P25 with the Pd deposited in different amount by PD 2m10 method and Figure 5.3 (b), (d) and (f) when Pd is deposited under different conditions. With the incorporation of Pd, the hysteresis loop of the pores of NT-WO_3 (Figure 5.3 (a) and (b)) follows a H3 type, which could indicate that Pd nanoparticles are filling or clogging the pores of the support. When Pd load is increased from 0.1 toward 0.5 wt.% (Figure 5.3 (a), (c) and (e)), it is possible to see that there are not important changes in the shape of the isotherms, which means that no important change on the pore structure is produced.

From physisorption analysis, specific area (S_{BET}) and pore volume (V_{PORE}) were estimated (Table 4). For NT-WO_3, these values are 104.6 m^2/g and 0.45 m^3/g, respectively. The PD of Pd (0.1 wt.%) by 2m10 method produces a slight reduction of the S_{BET} and pore volumen (101.57 m^2/g and 0.37 m^3/g), which could explain the hysteresis loop change observed in Figure 5.3 (a) and (b). In this case, the Pd nanoparticles are dispersed on the surface of the support, therefore the pore structure is conserved. On the other hand, increasing the Pd content from 0.1 wt.% up to 0.5 wt.%, S_{BET} and pore volumen increase

lightly, but not significantly. In the case of P25-WO_3 and P25 supports, they show similar S_{BET} as well as after Pd deposition. This is probably because the Pd nanoparticles (5 - 7 nm) are located outside of the pores.

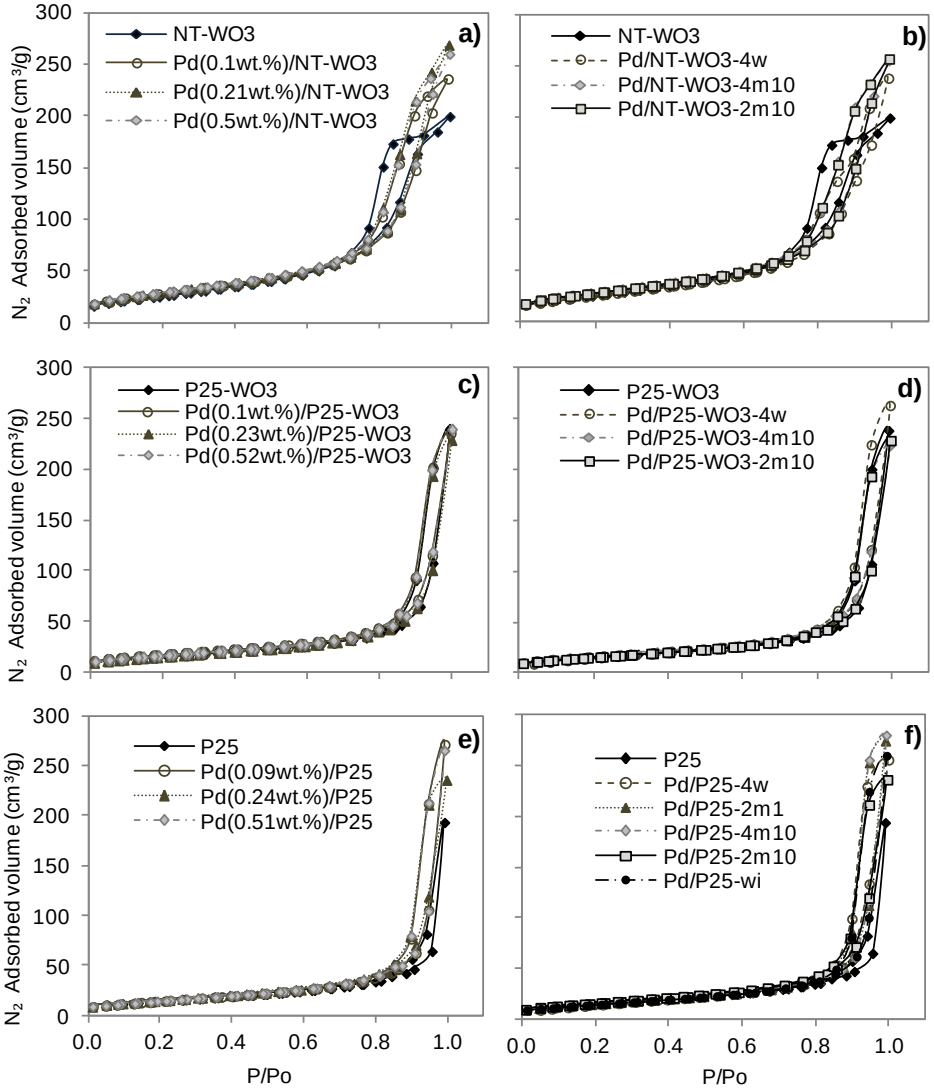

Figure 5.3. N_2 adsorption - desorption isotherms for Pd/NT-WO_3, Pd/P25-WO_3 and Pd/P25 catalysts, **a)**, **c)** and **e)** varying the Pd load by 2m10 method, and **b)**, **d)** and **f)** varying the Pd PD method using a nominal Pd load of 0.25 wt.%.

5.1.2.3. m-Pd/TiO_2 (-WO_3) - PCS Lab catalysts

Figure 5.4 shows N_2 adsorption - desorption isotherms for the Pd/NT-WO_3, Pd/P25-WO_3 and Pd/P25 catalysts prepared in PCS Lab. In this figure are shown two different amounts of Pd (0.25 and 2 wt.%) photodeposited under the two PD methods studied: PD 2m10 and 3.2m20 methods. The results presented in Figure 5.4 are quite similar to results in Figure 5.3, where after the Pd photodeposition, the catalysts show a porous materials with type IV isotherms and H3 hysteresis loop type according to IUPAC [165].

Comparing the Figure 5.4 (a) to Figure 5.1 for NT-WO_3 support, the results can be interpreted as Pd nanoparticles are filling the pores of the NT-WO_3 support. Regarding the amount of metal, it is observed that by increasing the Pd load from 0.25 toward 2 wt.% by 2m10 method, the N_2 adsorbed volume decreases, indicating some clogging of the pore structure. Additionally, moving from 2m10 toward

3.2m20 method for three group of catalysts (Figure 5.4 (a-c)), no important changes on the pore structure are observed.

Table 5 above shows the physisorption analysis with the S_{BET} and V_{PORE} values. The first difference between the catalysts prepared in PCS Lab and CATHETER Lab (see section 5.1.2.1 "*m-Pd/TiO₂ (-WO₃) - CATHETER Lab catalysts* ") is the much lower values in S_{BET}, especially for Pd/NT-WO_3 catalysts, prepared by the PD 2m10 method. The S_{BET} for Pd/NT-WO_3 catalyst prepared in PCS Lab is 9.48 m^2/g while the same catalysts but prepared in CATHETER Lab was 99.60 m^2/g. 10 times lower S_{BET} for - PCS catalyst.

Similar results were obtained for Pd/P25-WO_3 and Pd/P25 catalysts. The catalysts prepared in PCS Lab present a lower S_{BET}, 9.25 vs. 55.39 m^2/g for Pd/P25-WO_3 catalysts, and 9.25 vs 56.48 m^2/g for Pd/P25 catalysts, respectively. It means a S_{BET} around 6 times lower for Pd/P25-WO_3 and 3.4 times lower for Pd/P25 prepared in PCS Lab. The V_{PORE} does not present important changes but for the catalysts prepared in PCS Labs, these values were slightly higher but not significantly.

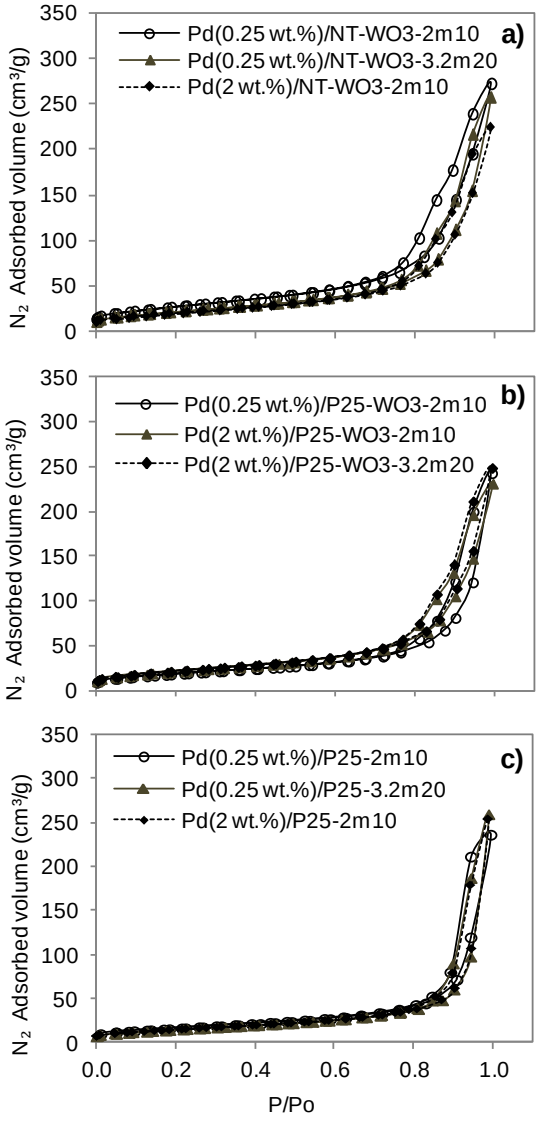

Figure 5.4. N_2 adsorption - desorption isotherms for catalysts prepared under different conditions and varying the Pd load: **a)** Pd/NT-WO_3; **b)** Pd/P25-WO_3 and **c)** Pd/P25 catalysts

5.1.2.4. m-Pt/TiO_2 (-WO_3) - PCS Lab catalysts

Figure 5.5 shows N_2 adsorption - desorption isotherms for Pt/NT-WO_3, Pt/P25-WO_3 and Pt/P25 catalysts, whose Pt deposition was performed by PD 2m10 and 3.2m20 methods, using two different amounts of Pt (0.25 and 2 wt.%). From Figure 5.5 is possible to classified these materials as porous materials with type IV isotherms, containing H3 hysteresis loop type according to IUPAC [165].

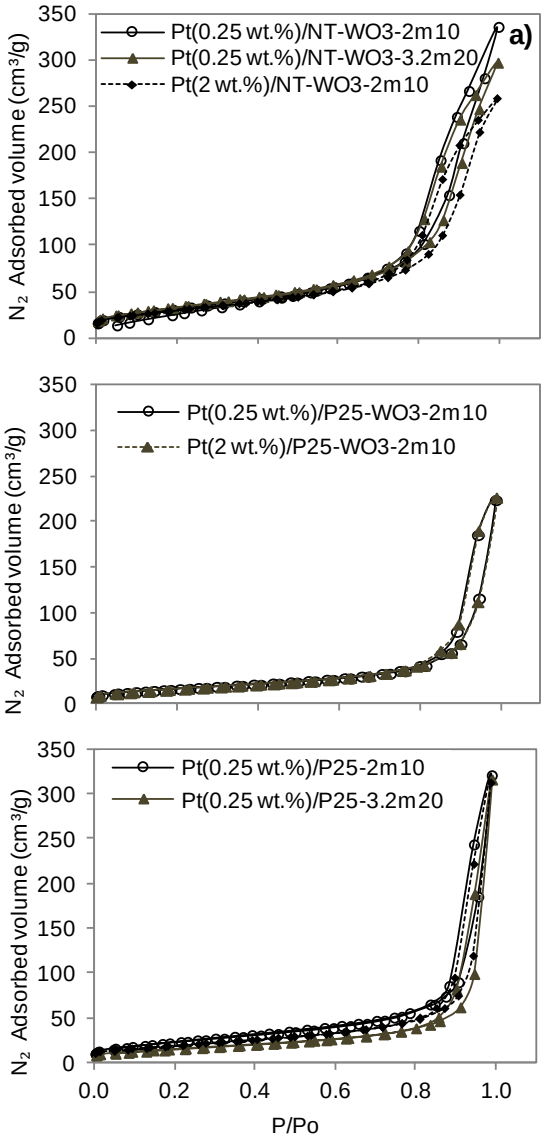

Figure 5.5. N_2 adsorption - desorption isotherms for catalysts prepared under different conditions and varying the Pt load: **a)** Pt/NT-WO_3; **b)** Pt/P25-WO_3 and **c)** Pt/P25 catalysts

The physisorption analysis (S_{BET} and V_{PORE}) are shown in Table 7. Similar to the catalysts presented in Table 6, the S_{BET} of these catalytic materials after metal deposition was much lower than their respective bare supports. For example, for those catalysts prepared in PCS Lab with Pt(0.25 wt%) by PD 2m10 method, S_{BET} for Pt/NT-WO_3 was 9.70 m^2/g and for Pt/P25-WO_3 and Pd/P25 catalysts, 11.22 and 26.7 m^2/g, respectively. These values correspond to around 11, 5 and 2 times lower the S_{BET} values of their respective bare - supports.

Although we do not have direct evidence to explain this phenomena, from results obtained in section "*5.1.1.1 m-Pd/TiO_2 (-WO_3) - CATHETER Lab catalysts* " we might think that the large differences

between the lamp irradiation system during the metal (Pt or Pd) PD in PCS lab (7 UV lamps of λ_{max}: 368 nm, 18 W/lamp for 4 h) and CATHETER Lab (one UV lamp of λ: 365 nm, 6 W for around 14 h) might lead to a production of larger nanoparticles in size that in the case of the catalysts Pd/NT-WO_3 or Pt/NT-WO_3.

These larger metal nanoparticles can be deposited and covering the entrance of the pores. For the other catalysts (Pd/ P25-WO_3, Pt/P25-WO_3, Pd/ P25 and Pt/ P25) the metal nanoparticles are deposited on the pores, reducing importantly the surface area of the support. The formation of larger metal nanoparticles could be related to the faster rate of nanoparticles deposition due to a higher number of incident photons during the photodeposition process.

5.1.2.5. Pd/TiO_2-Cu - CATHETER Lab catalysts

Figure 5.6 shows N_2 adsorption - desorption isotherms for P25-Cu catalysts. Porous materials with type IV isotherms were observed, containing an H3 hysteresis loop type according to IUPAC [165]. The same results were observed for catalysts containing Pd/P25-Cu (see Figure 5.7). Only Pd(0.1 wt.%)/P25-Cu(0.1 wt.%) catalyst presents type V isotherms, that it is characteristic of solids that contain open and partially blocked mesopores [147].

From physisorption analysis, S_{BET} and V_{PORE} were estimated in Table 7. For P25-Cu catalysts, the higher the amount of Cu, the higher the S_{BET} 9.60, 11.82 and 12.41 m^2/g for P25-Cu(0.5 wt.%), P25-Cu(1 wt.%) and P25-Cu(2 wt.%), respectively. In the case of the two catalysts containing Cu (1 wt.%) and Pd(0.25 wt.%) (row 1 and 8 of Table 7), S_{BET} did not change a lot comparing to P25-Cu(1 wt.%).

On the other hand, the S_{BET} of catalysts containing Cu (0.5 wt.) and Pd(0.1 wt.) (row 3, 5 and 9 of Table 7) was lower after Pd deposition, either by PD 2m10 or wi methods. When Pd was photodeposited on P25-Cu catalysts, the S_{BET} was less reduced, probably because this method, compared to wi method produces smaller Pd nanoparticles and they can deposit inside some pores. Larger nanoparticles might obstruct the pores, reducing more importantly the S_{BET} of the catalyst.

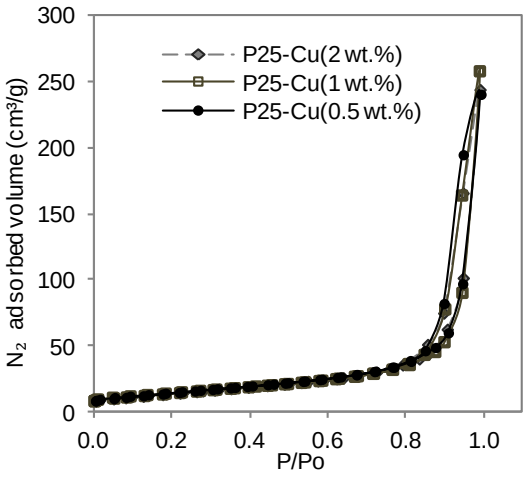

Figure 5.6. N_2 adsorption - desorption isotherms for P25-Cu catalysts

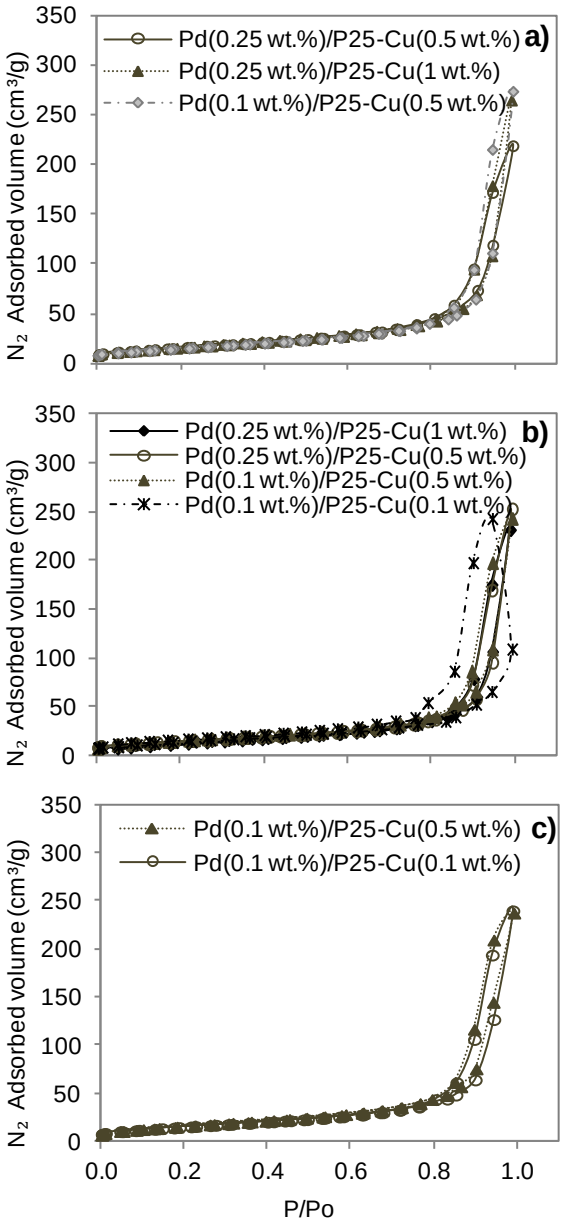

Figure 5.7. N_2 adsorption - desorption isotherms for Pd/P25-Cu catalysts prepared by: **a)** Cu: wi + C350 and Pd: wi + R300; **b)** Cu: wi + C350 and Pd: PD 2m10 and **c)** Cu: wi sC and Pd: PD 2m10

5.1.3. X-ray powder Diffraction (XRD)

5.1.3.1. w-Pd/TiO_2 (-WO_3) - CATHETER Lab catalysts

Figure 5.8 shows the X-ray diffraction patterns for the NT-WO_3, P25-WO_3 and P25 supports and after the deposition of Pd. All three supports exhibited similar diffraction lines referable to the anatase phases (A). Only P25 and P25-WO_3 exhibited the rutile phase (R). The absence of the rutile phase in NT-WO_3 is due to the synthesis protocol performed to obtain NT [75]. Rey and collaborators [75] also explain that the absence of peaks referable to WO_3 could be due to the low amount of WO_3 (around 5 wt.%). Therefore, the incorporation of WO_3 species has no significant effect on the TiO_2 structure. No effect of the Pd PD method on the crystalline phases of the supports (see Figure 5.9) was observed. Furthermore, due to the low amount of Pd in the sample, no diffraction lines corresponding to Pd were detected. This is also in concordance with the TEM results, which indicate the presence of smaller Pd nanoparticles, which can even be at atomic size level.

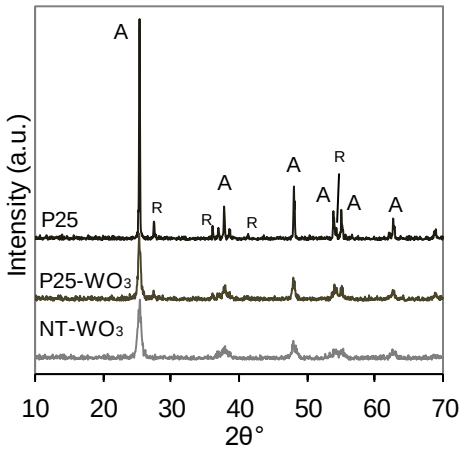

Figure 5.8. XRD patterns for P25, P25-WO_3 and NT-WO_3 supports

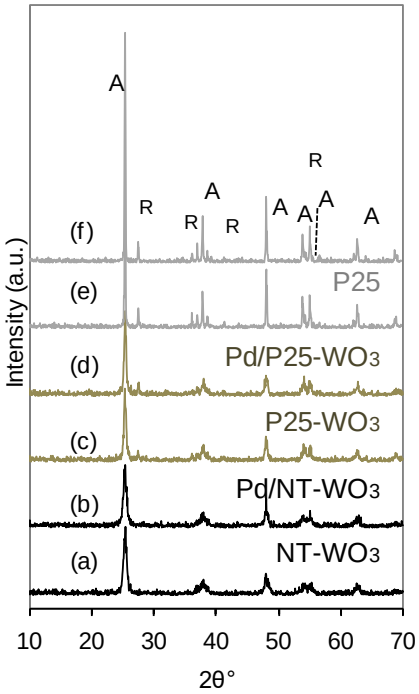

Figure 5.9. XRD patterns. a) NT-WO_3; b) Pd/NT-WO_3; c) P25-WO_3; d) Pd/P25-WO_3; e) P25; f) Pd/P25

5.1.3.1. m-Pd/TiO_2 (-WO_3) - CATHETER Lab catalysts

Figure 5.10 shows the X-ray diffraction patterns for Pd/NT-WO_3, Pd/P25-WO_3 and Pd/P25 catalysts. As it was discussed previously, all three supports exhibited similar diffraction lines referable to anatase phases (A). Only P25 and P25-WO_3 exhibited the rutile phase (R) and it was absent on NT-WO_3.

Regarding the effect of Pd PD method on the crystalline phases, in Figure 5.10 can be seen the XRD patterns of catalysts such as Pd(0.21 wt.%)/NT-WO_3 and Pd(0.5 wt.%)/P25 prepared by the PD 2m10 and 4m10 methods, respectively. No important changes are seen with the incorporation of Pd under such conditions. Peaks corresponding to Pd were not detected for these catalysts. The absence of signal corresponding to Pd species could suggest that they are incorporated as homogeneous and very small nanoparticles, might be in atomic size, as can be seen in TEM images. In order to see a peak corresponding to Pd, XRD measurements were done for three catalysts with the highest Pd loaded

prepared by PD. In Figure 5.10 only the Pd(0.5 wt.%)/NT-WO_3 sample (Figure 5.10 (a)) presents two very small peaks that correspond to Pd. For the other samples, Figure 5.10 (b)-(d), this Pd peak is not shown. This is probably due to the lower Pd loading.

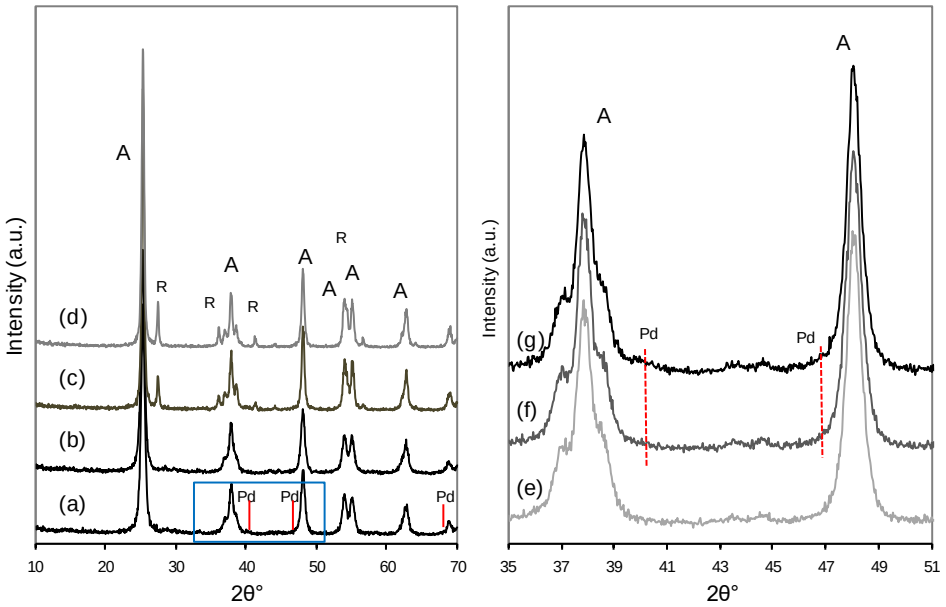

Figure 5.10. XRD patterns. **a)** Pd(0.5 wt.%)/NT-WO_3-2m10; **b)** Pd(0.21 wt.%)/NT-WO_3-2m10; **c)** Pd(0.5 wt.%)/P25-WO_3-2m10; **d)** Pd(0.5 wt.%)/P25-4m10; **e)** NT-WO_3; **f)** Pd(0.21 wt.%)/NT-WO_3-2m10; **g)** Pd(0.5 wt.%)/NT-WO_3-2m10

Consequently, NT-WO_3, Pd(0.21 wt.%)/NT-WO_3-2m10 and Pd(0.5 wt.%)/NT-WO_3 - 2m10 samples were analysed again in order to enhance the signal/noise ratio from 35 to 51° 2θ, angular step of 0.03° at 12s per step. The results for last XRD measurements are shown in Figure 5.10 (e)-(g). Comparing the XRD patterns from the Figure 5.10 ((a) and (b) vs. (c)), it can be observed that only for the highest Pd loading (0.5 wt.%) is possible to see a small prominence peak, corresponding to metallic Pd around 2θ=40.1°. These XRD patterns confirm the presence of smaller Pd nanoparticles that was also confirmed by TEM analysis.

5.1.3.2. m-Pd/TiO_2 (-WO_3) - PCS Lab catalysts

Figure 5.11, 5.12 and 5.13 shows the X-ray diffraction patterns for the Pd/P25, Pd/NT-WO_3 and Pd/P25-WO_3 catalysts prepared in PCS Lab after Pd deposition by PD 2m10 and PD 3.2m20 methods. The anatase phase (A) is observed in all the catalysts (Pd/P25, Pd/NT-WO_3 and Pd/P25-WO_3). Regarding the rutile phase (R), only Pd/P25 (Figure 5.12) and Pd/P25-WO_3 (Figure 5.13) show the presence of this rutile phase.

The addition of Pd did not produce any effect in the crystalline phase of the support using PD 3.2m20 or 2m10 methods (see Figures 5.11 - 5.13). Peaks corresponding to Pd (2θ around 40, 47 and 68°) [166] are not detected for catalysts containing 0.25 wt.% of Pd, but it is observed for catalysts containing 2 wt.% of Pd (Figure 5.11 (b), Figure 5.12 (b - c) and Figure 5.13 (b - c). Previously, it was commented that the absence of signal corresponding to Pd species would suggest very small Pd nanoparticles incorporation. From the results in Figures 5.11 - 5.13, it is supposed that for catalysts with the lower Pd

content, the metal nanoparticles are smaller in size than the catalysts containing 2 wt.% of Pd. Additionally, comparing both PD 2m10 and 3.2m20 methods, the peaks corresponding to Pd are slightly higher for PD 2m10 than for PD 3.2m20 method. This might suggest that the PD 3.2m20 method produces smaller Pd nanoparticles.

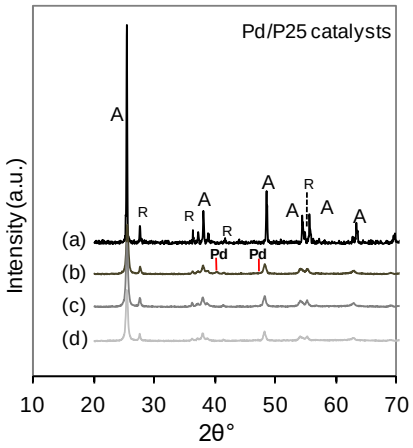

Figure 5.11. XRD patterns. **a)** P25; **b)** Pd(2 wt.%)/P25-3.2m20; **c)** Pd(0.25 wt.%)/P25-3.2m20; **d)** Pd(0.25 wt.%)/P25-2m10

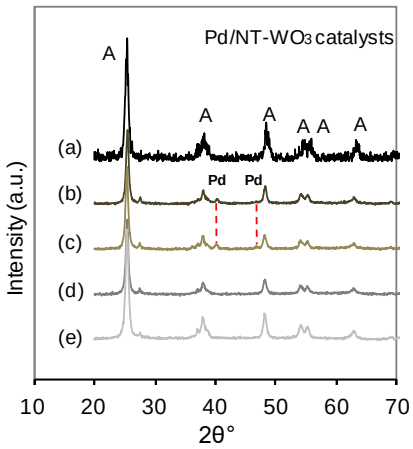

Figure 5.12. XRD patterns. **a)** NT-WO_3; **b)** Pd(2 wt.%)/NT-WO_3-3.2m20; **c)** Pd(2 wt.%)/NT-WO_3-2m10; **d)** Pd(0.27 wt.%)/NT-WO_3-3.2m20 and **d)** Pd(0.19 wt.%)/NT-WO_3-2m10

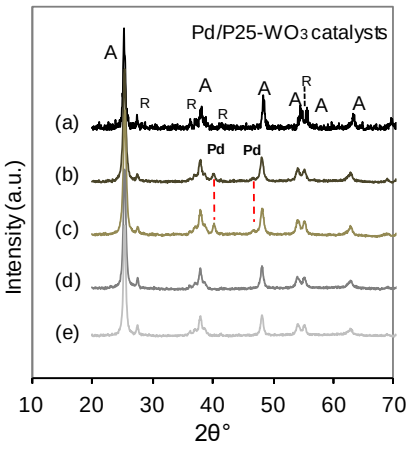

Figure 5.13. XRD patterns. **a)** P25-WO_3; **b)** Pd(2 wt.%)/P25-WO_3-3.2m20; **c)** Pd(2 wt.%)/P25-WO_3-2m10; **d)** Pd(0.28 wt.%)/ P25-WO_3-3.2m20 and **d)** Pd(0.23 wt.%)/ P25-WO_3-2m10

5.1.3.3. m-Pt/TiO_2 (-WO_3) - PCS Lab catalysts

Figures 5.14, 5.15 and 5.16 show the X-ray diffraction patterns for Pt/P25, Pt/NT-WO_3 and Pt/P25-WO_3 catalysts prepared in PCS Lab by PD 2m10 and PD 3.2m20 methods. Similar to previous analysis, all catalysts exhibited diffraction lines corresponding to the anatase phases (A), while only Pt/P25 and Pt/P25-WO_3 catalysts exhibited peaks referred to the rutile phase (R).

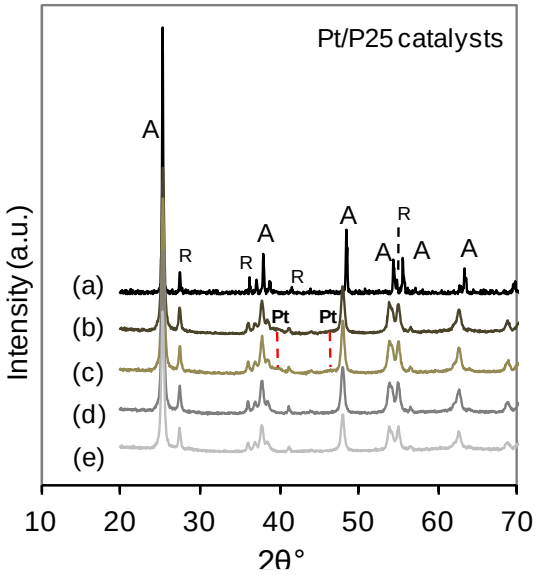

Figure 5.14. XRD patterns. **a)** P25; **b)** Pt(2 wt.%)/P25-3.2m20; **c)** Pt(2 wt.%)/P25-2m10; **d)** Pt(0.25 wt.%)/P25-3.2m20 and **e)** Pt(0.25 wt.%)/P25-2m10

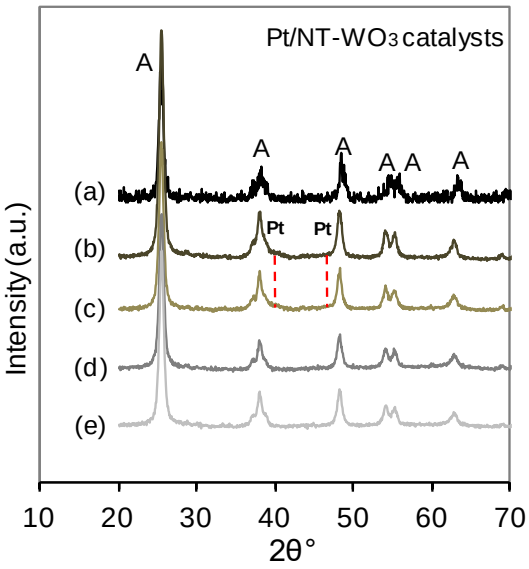

Figure 5.15. XRD patterns. **a)** NT-WO_3; **b)** Pt(2 wt.%)/NT-WO_3-3.2m20; **c)** Pt(2 wt.%)/NT-WO_3-2m10; **d)** Pt(0.25 wt.%)/NT-WO_3-3.2m20 and **d)** Pt(0.25 wt.%)/NT-WO_3-2m10

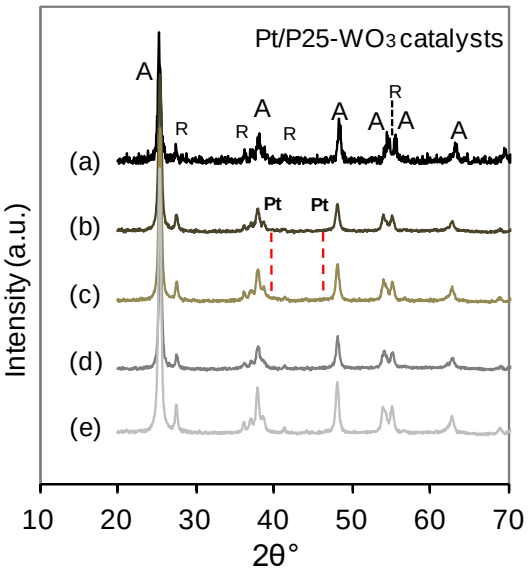

Figure 5.16. XRD patterns. **a)** P25-WO_3; **b)** Pt(2 wt.%)/P25-WO_3-3.2m20; **c)** Pt(2 wt.%)/P25-WO_3-2m10; **d)** Pt(0.25 wt.%)/ P25-WO_3-3.2m20 and **d)** Pt(0.25 wt.%)/ P25-WO_3-2m10

Neither for these catalysts were observed important changes on the crystalline phases after Pt PD by both 3.2m20 and 2m10 methods. Unlike the catalysts containing Pd prepared in PCS Lab, peaks corresponding to Pt are not seen clearly, neither for those catalysts containing 0.25 wt.% or 2 wt.% of Pt. For instance, for Pt/P25 (Figure 5.15 (b - c)) and Pt/NT-WO_3 (Figure 5.16 (b - c) catalysts, it is observed that around the 2θ values corresponding to Pt (40 and 46°)[167] scarcely arise some small prominences. Most probably, Pt nanoparticles are smaller in size on the three supports than Pd nanoparticles.

5.1.3.4. Pd/TiO_2-Cu - CATHETER Lab catalysts

Figure 5.17 shows the X-ray diffraction patterns for the P25-Cu(0.5 wt.%), P25-Cu(1 wt.%) and P25-Cu(2 wt.%) catalysts, where Cu was deposited by wi. All three catalysts exhibited similar diffraction lines referable to the anatase (A) and rutile (R) phases. In Figure 5.17 (a), no effect of the Cu deposition method is observed on the crystalline phases of the P25 support (see Figure 5.8 for P25 XRD patterns).Only in Figure 5.17 (b) at around 2θ=35.5° is observed a very small protuberance for P25-Cu(1 wt.%) that could correspond to CuO tenorite phase.

Figure 5.18 shows the X-ray diffraction patterns for several Pd/P25-Cu catalysts prepared by different methods. Cu and Pd content where varied and their deposition on P25 where changed from wi +C350 to wi sC for Cu, and from wi to PD 2m10. Similar to Figure 5.17, it not is observed important effects on the crystalline phases, after either Cu or Pd deposition. Furthermore, the presence of Pd or Cu was not detected, probably, due to the low amount of Pd and Cu (see Figure 5.18). By TEM results, it was observed the presence of very small metal nanoparticles in the samples.

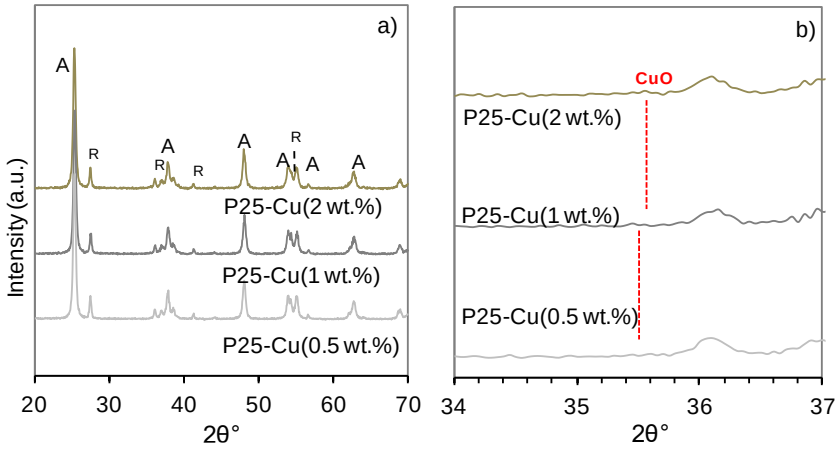

Figure 5.17. XRD patterns of P25-Cu (0.5 wt.%), P25-Cu(1 wt.%) and P25-Cu(2 wt.%) catalysts

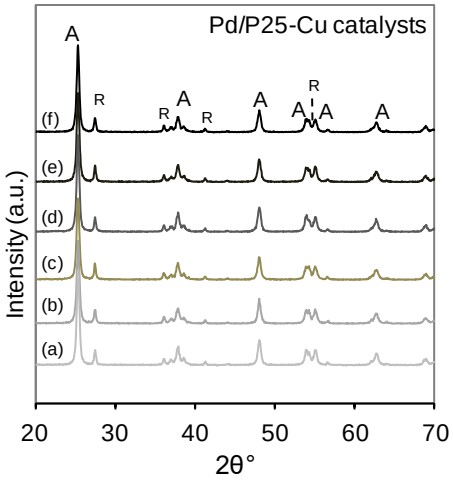

Figure 5.18. XRD patterns. **a)** Pd(0.1 wt.%)/P25-Cu(0.1 wt.%) (**Cu:** wi + C350 - **Pd:** PD2m10); **b)** Pd(0.1 wt.%)/P25-Cu(0.1 wt.%) (**Cu:** wi sC - **Pd:** PD2m10); **c)** Pd(0.25 wt.%)/P25-Cu(1 wt.%) (**Cu:** wi + C350 - **Pd:** PD2m10); **d)** Pd(0.1 wt.%)/P25-Cu(0.5 wt.%) (**Cu:** wi + C350 - **Pd:** wi+ R300); **e)** Pd(0.1 wt.%)/P25-Cu(0.1 wt.%) (**Cu:** wi sC - **Pd:** PD2m10).

5.1.4. High Resolution Transmission Electron Microscopy (HRTEM)

5.1.4.1. w-Pd/TiO_2(-WO_3) - CATHETER Lab catalysts

Figure 5.19 (a) shows that the sample containing Pd deposited on P25 is constituted by titania crystallites and some Pd nanoparticles of 5 - 7 nm in size. In the samples containing WO_3 on NT (sample Pd/NT-WO_3, Figure 5.19 (b)) or on P25 (sample Pd/P25-WO_3, Figure 5.19 (c)), Pd particles were not detected by STEM or HRTEM. This fact indicates the presence of very small nanoparticles (< 2 nm in size), that cannot be detected by the STEM experimental equipment used. This indicates that the addition of WO_3 produces a very high dispersion of the Pd. In the TEM images (Figure 5.19 (d)) we can see that the samples are constituted by well-dispersed TiO_2 particles of about 15 – 40 nm in size, which are mostly covered by other small (< 10 nm) WO_3 crystallites.

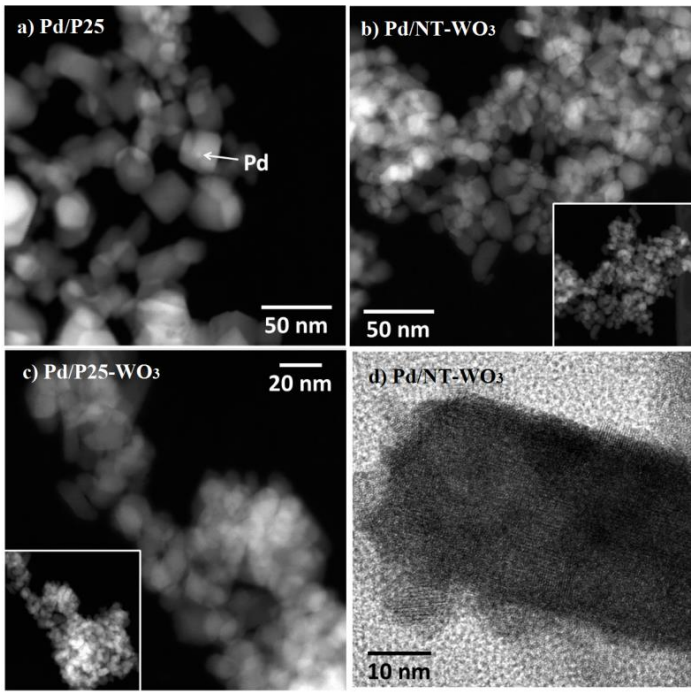

Figure 5.19. STEM-HAADF images for **a)** Pd/P25; **c)** Pd/NT-WO_3 and **e)** Pd/P25-WO_3 and HRTEM image for **b)** Pd/P25; **d)** Pd/NT-WO_3

5.1.4.2. m-Pd/TiO_2(-WO_3) - CATHETER Lab catalysts

Figure 5.20 (a - d, f) shows representative STEM-HAADF (scanning transmission electron microscope - high-angle annular dark-field) images for Pd/P25 catalysts, where Pd was deposited under different conditions. It is possible to see that these samples are constituted by titania crystallites very well dispersed and quite homogeneous in size mostly in the range 20 - 30 nm. In addition, on the titania crystallites, there are brighter nanoparticles, which correspond to Pd nanoparticles, some of them well dispersed with about 5 - 7 nm in size. In the EDX spectrum included in Figure 5.20 (a), it can be seen that there are signals of Ti and O arising from the titania support as well as Pd signals (the Cu signals are due to the copper grid used for TEM). Figure 5.20 (d) shows a general STEM view of the sample prepared by PD 2m1 method, where are displayed a large number of Pd nanoparticles in the range 3 - 15 nm with a wide size distribution. The area enclosed by the white square is shown in HRTEM mode in

Figure 5.20 (d). As expected, the bright nanoparticles in STEM mode show lattice fringes corresponding to Pd metal in HRTEM. Lattice fringes at 2.2 Å correspond to the (111) crystallographic planes of metallic Pd, and those at 3.6 Å correspond to the (101) crystallographic planes of anatase. There is no epitaxial relationship between titania and Pd nanoparticles.

Figure 5.20 (e - g) shows representative STEM-HAADF images for Pd/P25 catalysts with different amount of Pd, which were prepared by PD 2m10 method. Although all three samples exhibited titania nanoparticles of 20 - 30 nm in size, in contrast to the samples shown in Figure 5.20 (f) - (g) with 0.25 and 0.51 wt.% in Pd, respectively, the sample with the lowest Pd loading (Figure 5.20 (e) 0.09 wt.% in Pd, with "magnification image") does not show the presence of Pd nanoparticles. Therefore, taking into account that Pd nanoparticles can be identified in the samples with 0.25 and 0.52 wt.% of Pd, which are similar to Pd(0.09 wt.%)/P25, but with a higher Pd loading (0.25 and 0.51 vs. 0.09 wt.%), it is likely due to the low Pd loading resulting very small Pd nanoparticles that escape TEM detection. This fact can be seen in Figure 5.20 (f) and (g), where the lower the Pd load (0.5 toward 0.25 wt.%), the smaller the particle size (4 - 12 toward 5 - 7 nm, respectively).

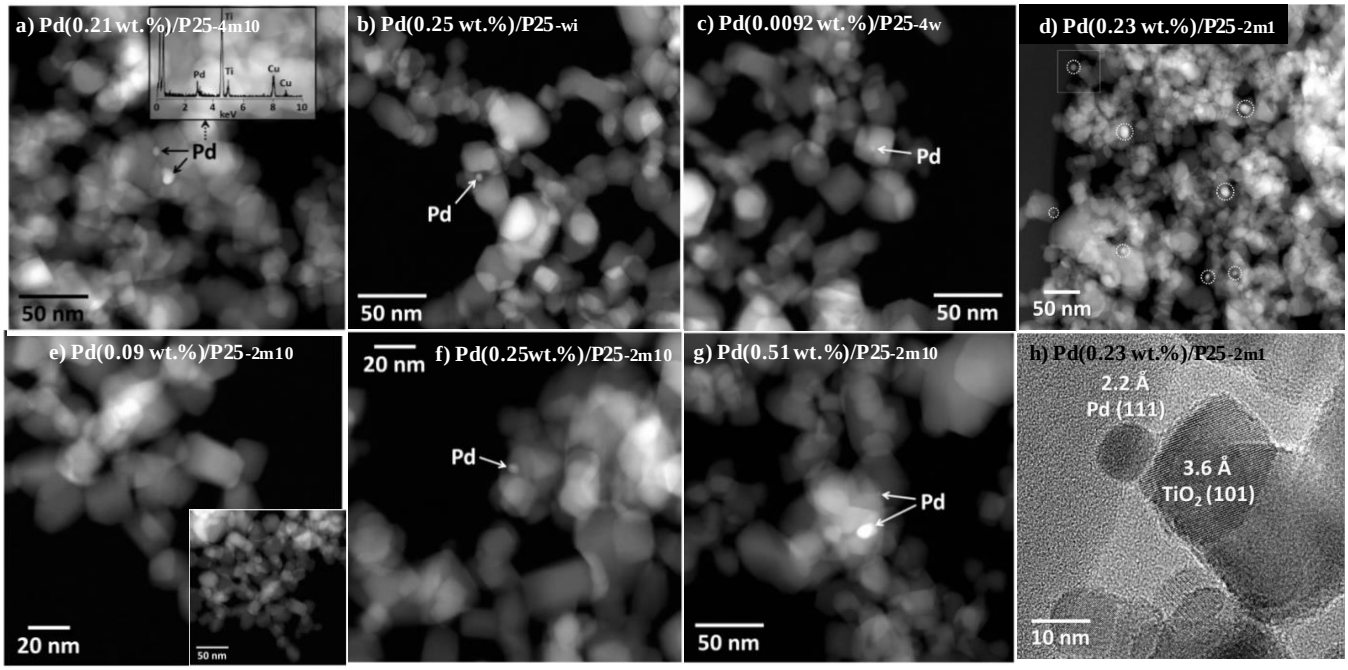

Figure 5.20. STEM-HAADF images for Pd/P25 catalysts, where Pd was deposited by **a)** PD 4m10; **b)** wetness impregnation; **c)** 4w; **d)** 2m1, **e)**, **f)** and **g)** PD 2m10, and **h)** 2m1

Figure 5.21 shows STEM images for catalysts based on Pd/TiO_2-WO_3, where Pd was obtained by PD. Sample Pd(0.21 wt.%)/NT-WO_3 (Figure 5.21 (a - b)) is constituted by two types of particles. Mainly it contains very small Pd nanoparticles of around 1 nm in diameter, but it also contain larger Pd particles from 4 up to 10 nm (see inside the white circles). An enlargement of Figure 5.21 (a) is shown in Figure 5.21 (b), where two particles of different size (1 and 4 nm) are marked inside black circles and a titania nanotube is clearly seen. EDX analysis show that titania and WO_3 are intimate mixed. In all cases, signals of both Ti and W occur together and this is also observed in all the samples based on Pd/TiO_2-WO_3. Sample Pd(0.1 wt.%)/NT-WO_3 (Figure 5.21 (c)) constituted by very small Pd nanoparticles, measuring 2 - 3 nm in size, are very well distributed onto the support. There are no large Pd particles. On the other hand, Pd(0.23 wt.%)/P25-WO_3 - 2m10 sample (Figure 5.21 (d - e)) is constituted mainly by

Pd nanoparticles of 6 - 8 nm in diameter, but Pd nanoparticles measuring about 2 nm can also be observed (Figure 5.21 (f), inside the white circle). Figure 5.21 (e) shows a representative STEM image with various Pd nanoparticles inside de white circles. The area enclosed in the white square is shown in small image in Figure 5.21 (d) in HRTEM mode. A careful analysis of the lattice fringes demonstrates that the bright particles in STEM mode correspond to Pd nanoparticles.

In HRTEM, Figure 5.21 (d), the lattice fringes measured at 2.2 Å correspond to the (111) crystallographic planes of metallic Pd, and the lattice fringes at 3.6 Å correspond to the (101) crystallographic planes of anatase. Pd(0.23 wt.%)/P25-WO_3-2m1 sample (Figure 5.21 (g)) contains Pd nanoparticles in the range 4 - 10 nm in diameter, although it also contains Pd nanoparticles of around 2 nm. This sample is virtually identical to the previous one (Figure 5.21 (e)). The Pd(0.1 wt.%)/P25-WO_3-2m10 sample (Figure 5.21 (h)) contains sub-nanometric Pd cluster. They are very hard to visualize and are at the detection limit of the microscope (see the weak bright dots inside the white circles). No larger particles are detected. All the particles are in the range of < 1 nm in size.

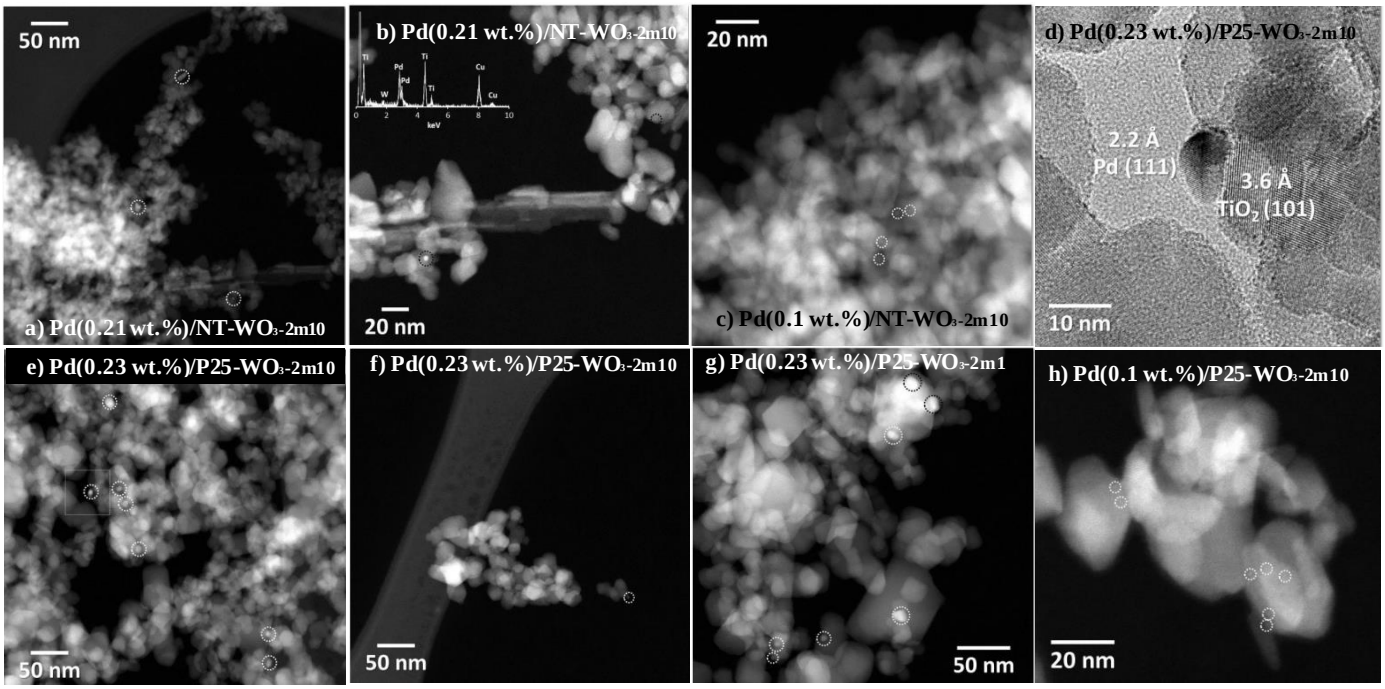

Figure 5.21. STEM images: Pd/TiO_2-WO_3 catalysts, where Pd was deposited by PD. **a-b)** Pd(0.21 wt.%)/NT-WO_3-2m10; **c)** HRTEM image: Pd(0.1 wt.%)/NT-WO_3-2m10; STEM images: **d-f)** Pd(0.23 wt.%)/P25-WO_3-2m10; **g)** Pd(0.23 wt.%)/P25-WO_3-2m1; **h)** Pd(0.1 wt.%)/P25-WO_3-2m10

The color of catalytic supports NT-WO_3, P25-WO_3 and P25 without the incorporation of Pd (Pd loading=0 wt.%) appeared whitish. When Pd is incorporated, either by PD-w, PD-m or wi methods, the catalysts seem to turn into a grayish colour, lighter or darker depending on the amount of Pd loaded and the deposition method. This metallic appearance might be characteristic of the presence of metallic palladium Pd^0. In addition, during the drying process at room temperature, most of the catalysts showed yellow traces, suggesting the oxidation of Pd while is drying and could explain the initial time activation needed in photocatalytic experiments for H_2 production.

5.1.4.3. m-Pd/TiO_2 (-WO_3) - PCS Lab catalysts

Figure 5.22 (a) shows a general image of the Pd(0.19 wt.%)/NT-WO_3 sample where Pd PD was performed in PCS Lab by the 2m10 method. This sample, which is composed by titania crystallites of 15 - 25 nm in size covered by a thin layer of WO_3 of less than about 2 nm in thickness. Figure 5.22 (b) corresponds to a HRTEM image. The lattice fringes at 3.5 Å correspond to the (101) crystallographic planes of anatase. The presence of blurry edges of titania is likely due to the presence of amorphous WO_3 layer.

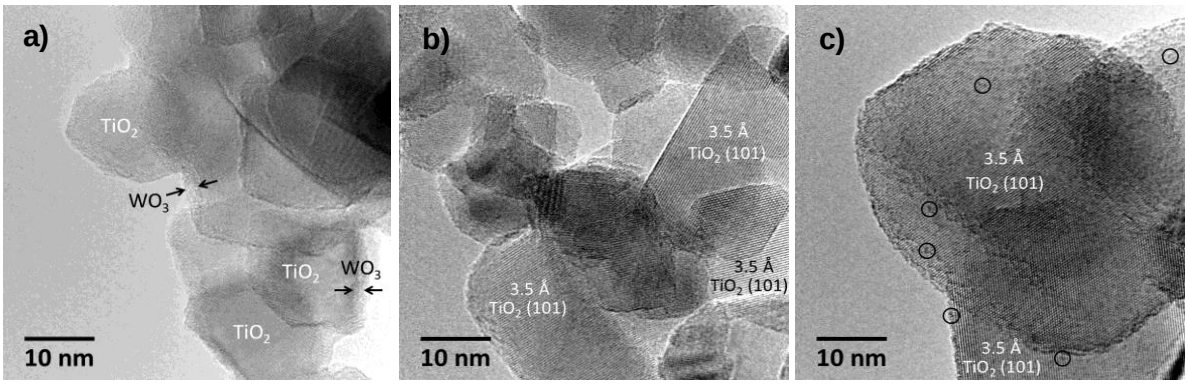

Figure 5.22. . HRTEM images for Pd(0.19 wt.%)/NT-WO_3 catalyst. Pd PD by 2m10 method.

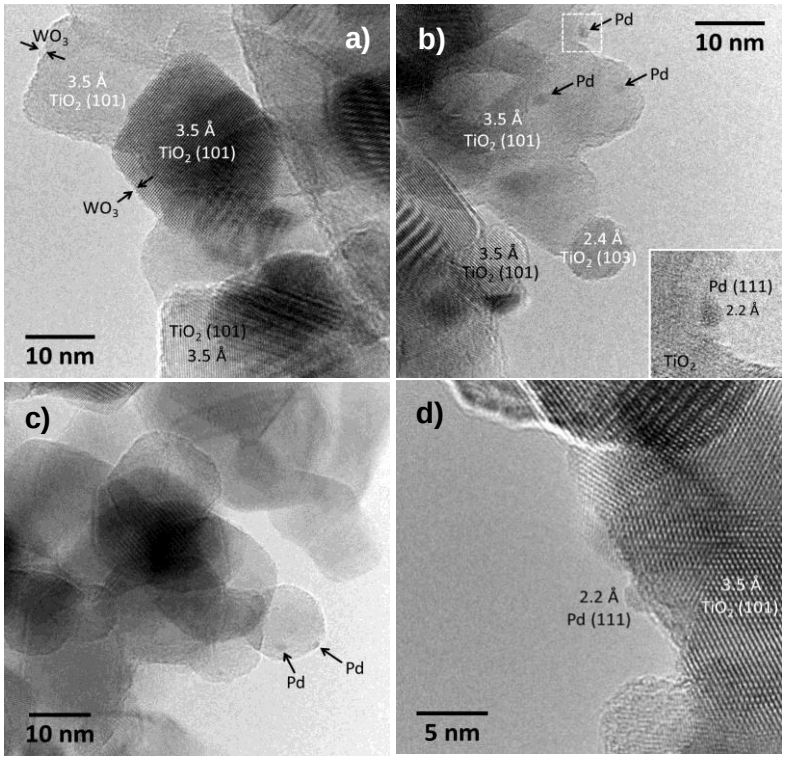

Figure 5.23. HRTEM images for Pd(2 wt.%)/NT-WO_3 catalyst. Pd PD by 2m10 method.

Pd is apparently visible as very small ensembles in Figure 5.22 (c) (some of them are marked inside black circles). Due to their small size it is not possible to unambiguously conclude that they correspond to Pd because no lattice fringes can be measured, but in any case, no well-defined Pd particles are present. These small Pd ensembles measure about 0.5 - 1 nm in size and are extraordinarily well dispersed over the anatase crystallites. Figure 5.23 (a) shows a general view of the Pd(2 wt.%)/NT-WO_3

sample. Again, well-defined planes at 3.5 Å are recognized and correspond to the (101) characteristic planes of anatase. Also, their surface is covered by a thin amorphous shell, which likely corresponds to WO_3. In this case, however, Pd nanoparticles are recognized, probably due to the higher Pd loading (2 wt.%).

Figure 5.23 (b) shows a HRTEM image, where several Pd nanoparticles are identified. One of them is enlarged in the inset of Figure 5.23 (b) and show lattice fringes at 2.2 Å, which correspond to the (111) planes of Pd. Other Pd particles are shown in Figure 5.23 (c). The size of the Pd nanoparticles is about 2.0 ± 0.4 nm. Figure 5.23 (d) shows another HRTEM image; a Pd nanoparticle showing the characteristic (111) crystallographic planes of palladium is identified.

5.1.4.4. m-Pt/TiO_2 (-WO_3) - PCS Lab catalysts

Figure 5.24 (a) shows a HRTEM image for the Pt(0.18 wt.%)/P25 sample where Pt was photodeposited by the 2m10 method. In the figure are observed small entities that are well dispersed over titania support (some of them marked inside black circles). They likely correspond to Pt ensembles, although an unambiguous identification is not possible. The size of the ensembles is about 0.5 nm.

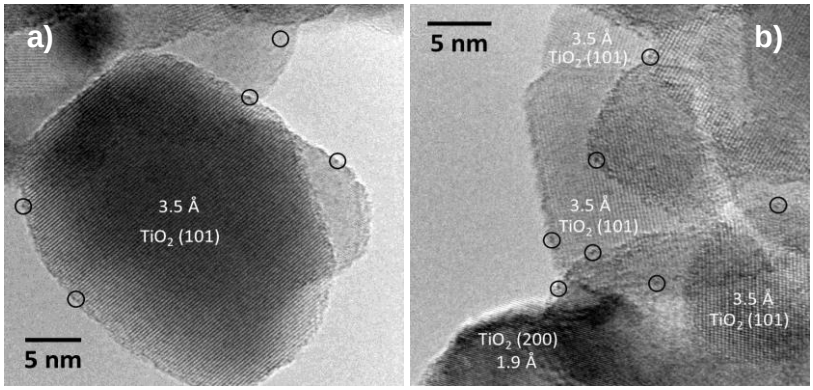

Figure 5.24. HRTEM images for Pt(0.18 wt.%)/P25 catalyst. Pt PD by 2m10 method.

Figure 5.24 (b) corresponds to another HRTEM image where, again, an extraordinary dispersion of entities (some of them indicated inside black circles) of about 0.5 nm is perfectly seen. In this sample, the titania crystallites show well-defined edges according to the almost absence of WO_3. The size of the titania crystallites is in the range of 10 - 40 nm in size.

The Pt(0.24 wt.%)/NT-WO_3 sample, in Figure 5.25, is constituted by anatase crystallites of about 10 - 40 nm in size, which are covered by a thin amorphous layer, possible WO_3. No Pt nanoparticles are identified, but a plethora of small entities of about 0.5 nm are spread over the anatase crystallites, as shown in the HRTEM images shown in Figures 5.25 (a, b and c). The Pt(0.21 wt.%)/P25-WO_3 sample in Figure 5.26 (a - b) is very similar to the previous one (Figure 5.25), except that the titania support particles are shorter, of about 15 - 25 nm in size. In addition, the blurred edges of the titania crystallites suggest the presence of WO_3. Figures 5.26 (a and b) show HRTEM images where entities of about 0.5 nm are extraordinarily well dispersed over titania, which likely correspond to platinum ensembles.

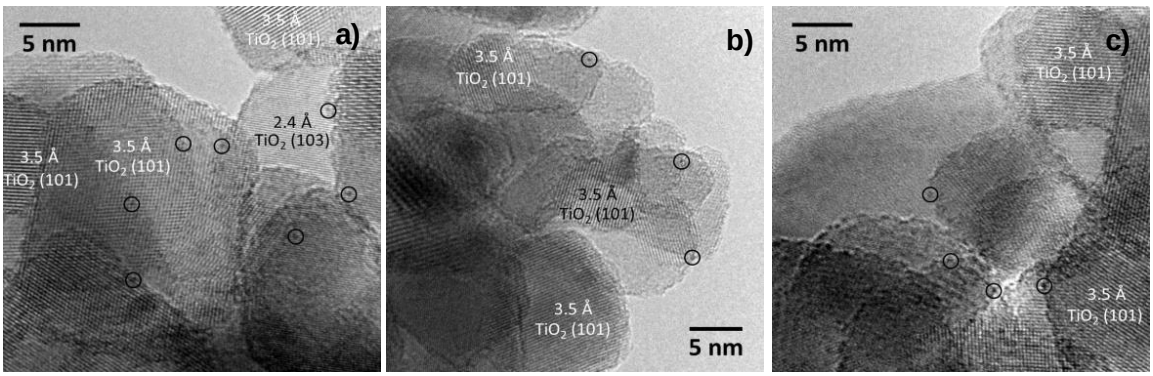

Figure 5.25. HRTEM images for Pt(0.24 wt.%)/NT-WO_3 catalyst. Pt PD by 2m10 method.

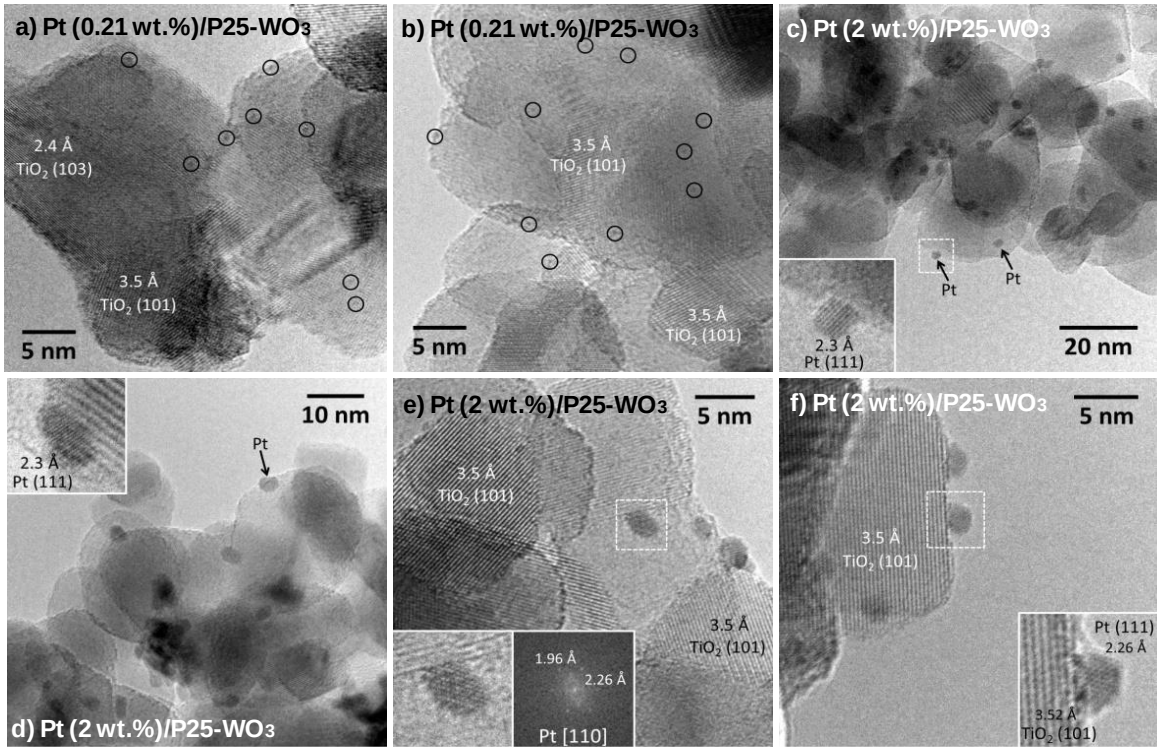

Figure 5.26. HRTEM images for Pt/P25-WO_3 catalysts. Pt PD by 2m10 method. **(a)** and **(b)** Pt(0.21 wt.%)/P25-WO_3 catalyst; **(c)**, **(d)**, **(e)**, **(f)** Pt(2 wt.%)/P25-WO_3 catalyst.

Figure 5.26 (c) shows a general view of the Pt(2 wt.%)/P25-WO_3 sample, where anatase crystallites of 15 - 25 nm in size are clearly decorated by Pt nanoparticles. The inset corresponds to an enlarged image of one of the Pt nanoparticles; lattice fringes at 2.3 Å correspond to the (111) crystallographic planes of Pt. Another HRTEM image is shown in Figure 5.26 (d). Pt nanoparticles measure about 2.9 ± 0.5 nm in size. Figure 5.26 (e) corresponds to another HRTEM image. The particle inside the white square is shown in the inset at higher magnification along with its Fourier Transform image, which shows spots at 2.26 and 1.96 Å corresponding to the (111) and (200) crystallographic planes of Pt, respectively.

The Fourier Transform pattern corresponds to an individual Pt nanoparticle oriented along the [110] crystallographic direction. Figure 5.26 (f) shows another HRTEM image, with another Pt nanoparticle oriented along the [110] crystallographic direction and supported over an anatase crystallite showing (101) planes at 3.52 Å.

5.1.4.5. Pd/TiO_2-Cu - CATHETER Lab catalysts

Figure 5.27 and 5.28 show representative STEM-HAADF images for Pd/P25-Cu catalysts. The sample Pd(0.25 wt.%)/P25-Cu(0.5 wt.%) (Figure 5.27), where Cu was firstly deposited on P25 by wi method and then was also deposited using again the wi method, contains two different morphologies. On one hand, individual metal nanoparticles of about 2 - 3 nm in size (see inside the white circles in Figures 5.27 (a)) and 5.27 (b)) are well distributed over the sample. On the other hand, metal aggregates with an undefined morphology are also observed (Figure 5.27 (a) and Figure 5.27 (b)). The EDX analysis of these aggregates show in all cases the coexistence of both Cu and Pd.

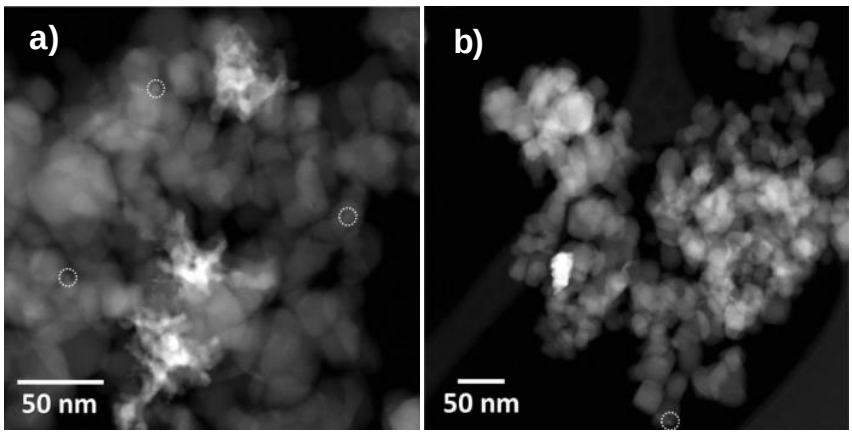

Figure 5.27. STEM images: Pd(0.25 wt.%)/P25-Cu(0.5 wt.%) catalyst. Cu and Pd deposited by wi C350 and wi, respectively.

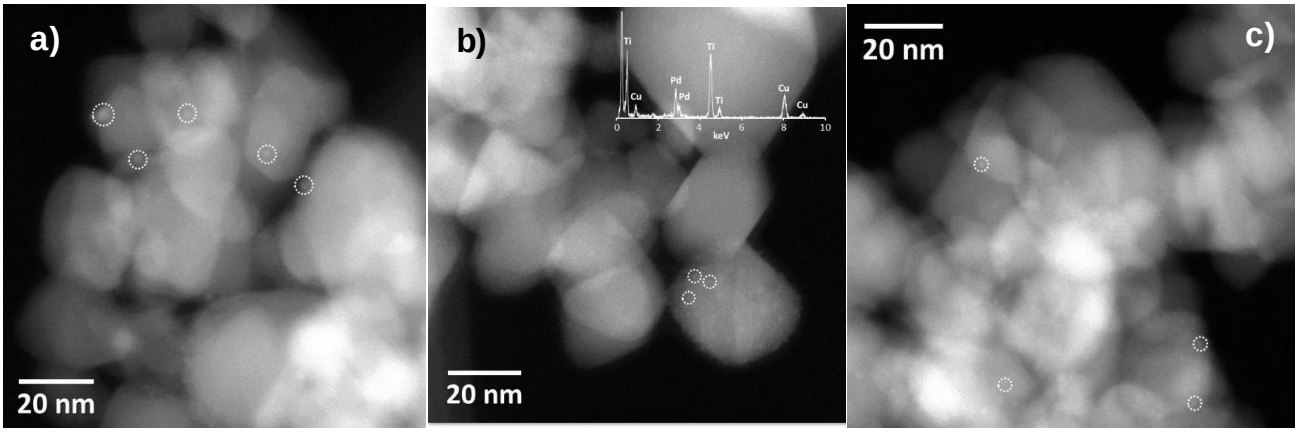

Figure 5.28. STEM images: Pd(0.25 wt.%)/P25-Cu(0.5 wt.%) catalysts. Cu and Pd deposited by wi C350 and PD 2m10, respectively.

On the other hand, for the sample Pd(0.25 wt.%)/P25-Cu(0.5 wt.%) (Figure 5.28), where Cu was also firstly deposited on P25 by wi method, and then Pd was photo-deposited using the PD 2m10 method, very small metal nanoparticles, which measure about 2 - 4 nm in diameter (Figure 5.28 (a)), are observed. Another STEM images are shown in Figures 5.28 (b) and 5.28 (c). The dispersion of the metal nanoparticles is excellent. EDX analysis cannot be performed over individual nanoparticles due to their small dimensions. However, in the EDX spectra recorded over selected areas the presence of Pd is evidenced.

5.1.5. Photoelectron Spectroscopy (XPS)

5.1.5.1. w-Pd/TiO_2(-WO_3) - CATHETER Lab catalysts

Figure 5.29 shows the surface chemical composition analysed by XPS for Pd/TiO_2(-WO_3) catalysts.

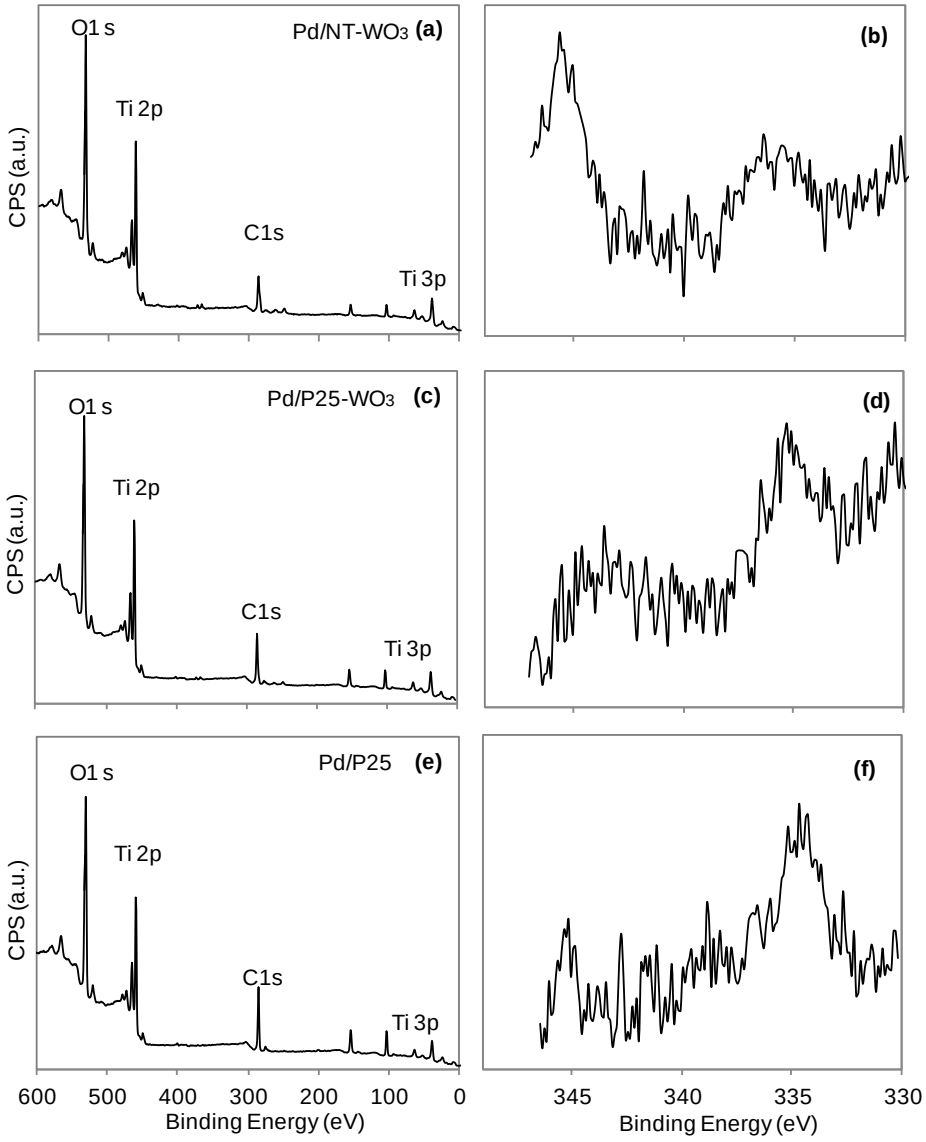

Figure 5.29. XPS full spectra of the catalysts (**a**, **c** and **e**). High-resolution XPS spectra of Pd 3d (**b**, **d** and **f**) spectral region for Pd/NT-WO_3, Pd/P25-WO_3 and Pd/P25 catalysts.

From the complete spectra for all the catalysts of Pd/P25 illustrated in Figure 5.29 (a) and (c) we can verify the presence of O, Ti and C with the O 1s, Ti 2p, C1 s and Ti 3p peaks at 531, 460, 285 and 38 eV, respectively. The Pd 3d XPS analyses for Pd/NT-WO_3 and Pd/P25 are shown in Figure 5.29 (b) and (d). For both samples, it is difficult to see very clear Pd peaks due to the low Pd content. However, it is possible to see two small prominences at around 336.7 eV and 341.9 eV, which are characteristic for Pd (Pd5/2 and Pd3/2 transitions, respectively) and correspond to Pd (II) species, which are probably PdO or $Pd(OH)_2$ [168].

5.1.5.2. m-Pd/TiO_2(-WO_3) - CATHETER Lab catalysts

Figure 5.30 shows the surface chemical composition analysed by XPS for Pd/P25 catalysts.

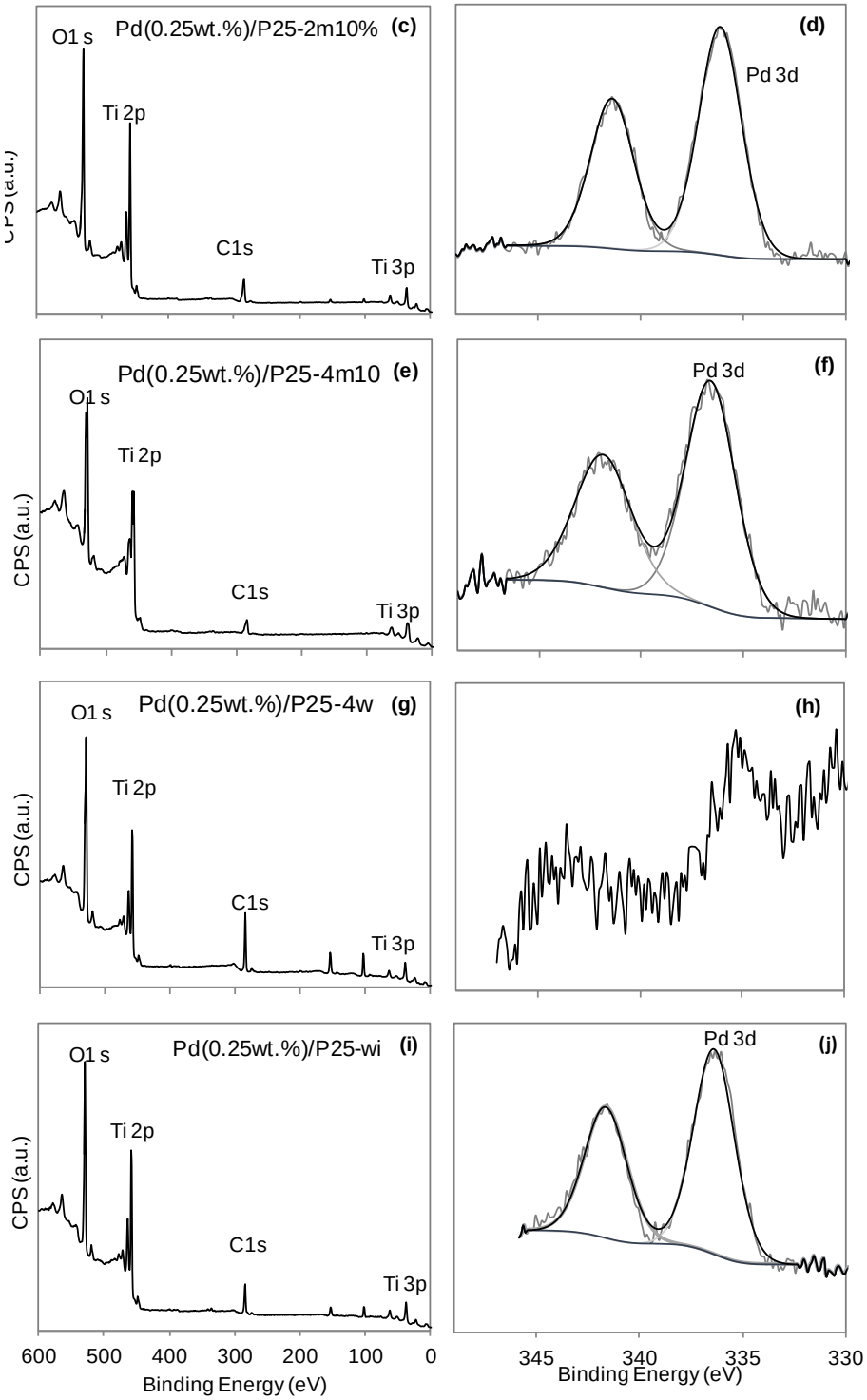

Figure 5.30. XPS full spectra of the catalysts (**c**, **e**, **g** and **i**). High-resolution XPS spectra of Pd 3d (**a**, **b**,**d f**, **h** and **j**) spectral region for Pd/P25 catalysts

From the complete spectra for all the catalysts of Pd/P25, in Figure 5.30 (c), (e), (g) and (i) is verified the presence of O, Ti and C with the O 1s, Ti 2p, C 1s and Ti 3p peaks at 531, 460, 285 and 38 eV, respectively. Regard to the Pd 3d XPS analysis (Figure 5.30 (a), (b), (d) , (f), (h) and (j)), for those Pd 3d signals that are well defined, in all cases Pd is oxidized at the surface. The binding energies recorded for 3d 5/2 at around 336.7 and 341.9 eV are characteristic for Pd(II) species, which likely could be PdO or

$Pd(OH)_2$ species [168]. When Pd amount was increased up to 0.25 wt.%, this molar ratio Pd/Ti increased also up to 0.009. In contrast, for the sample Pd(0.5 wt.%)/P25 the molar ratio Pd/Ti was 0.008. This fact, possibly means that some sintering of Pd ocurrs at higher Pd loadings. By changing the PD conditions from 2m10 toward 4m10 method, the Pd/Ti ratio decreases from 0.009 to 0.006. The sample prepared by wi method shows a Pd/Ti=0.010, which means a very good Pd dispersion and the sample prepared by PD-w does not show clear Pd peaks, which means that the dispersion is worse, provided that the Pd content is maintained constant.

5.1.5.3. m-Pd/TiO_2 (-WO_3) - PCS Lab catalysts

Figure 5.31 shows the surface chemical composition analysed by XPS for Pd(0.25 wt.%)/P25, Pd(0.25 wt.%)/NT-WO_3 and Pd(0.25 wt.%)/P25-WO_3 - PCS catalysts prepared by PD 2m10 and Figure 5.32 for Pd(0.25 wt.%/P25 - 3.2m20 and Pd(2 wt.%)/NT-WO_3 PCS catalysts. From the complete spectra of all the catalysts (Figure 5.31 and 5.32) is verified the presence of O, Ti and C with the O 1s, Ti 2p, C 1s and Ti 3p peaks at 531, 460, 285 and 38 eV, respectively.

In Figure 5.31, concerning the Pd 3d XPS analysis, the signals are well defined and for these catalysts, Pd is partially oxidized at the surface. For instance, on Pd(0.25 wt.%)/P25 surface, 54.01 % of Pd is oxidized, on Pd(0.25 wt.%)/NT-WO_3, 47.96 % of Pd is oxidized and for Pd(0.25 wt.%)/P25-WO_3 catalyst, 39.48 % of Pd is oxidized. In Figure 5.32, on the other hand, when Pd/P25 was prepared by the Pd PD 3.2m20 method, the amount of oxidized Pd (34.46 %) was lower and for Pd/NT-WO_3, when Pd content was higher (2 wt.%), the amount of oxidized Pd increased (62.28%). Probably, when the Pd PD is performed in a lower concentration of methanol, and when Pd content is too high, Pd nanoparticles on catalysts are more exposed to oxygen, which leads to a higher oxidation of Pd.

In comparison to those catalysts prepared in CATHETER Lab (Figure 5.30), where Pd was completely oxidized at the catalysts surface, the PCS catalysts showed an important portion of Pd reduced. Most likely, this difference is produced by differences in the photodeposition set up, more specifically the power of the lamp. Therefore, likely due to the most powerful lamp in PCS Lab, the photon exposition is higher and better, which lead to produce Pd nanoparticles more steady reduced on the catalytic supports.

The molar ratio Pd/Ti for catalysts in Figure 5.31 was 0.009, 0.012 and 0.021 for Pd/P25, Pd/NT-WO_3 and Pd/P25-WO_3, respectively. When Pd was increased, on Pd/NT-WO_3 (Figure 5.32), the Pd/Ti molar ratio increased up to 0.030. On the other hand, for the sample Pd(0.25 wt.%)/P25, when Pd was photodeposited by 2m10 method (Figure 5.31), the molar ratio of Pd/Ti was 0.009 and by the 3.2m20 method (Figure 5.32), the molar ratio Pd/Ti was 0.007. This fact might indicates that 2m10 method produced Pd nanoparticles better dispersed on the support than for the 3.2m20 method.

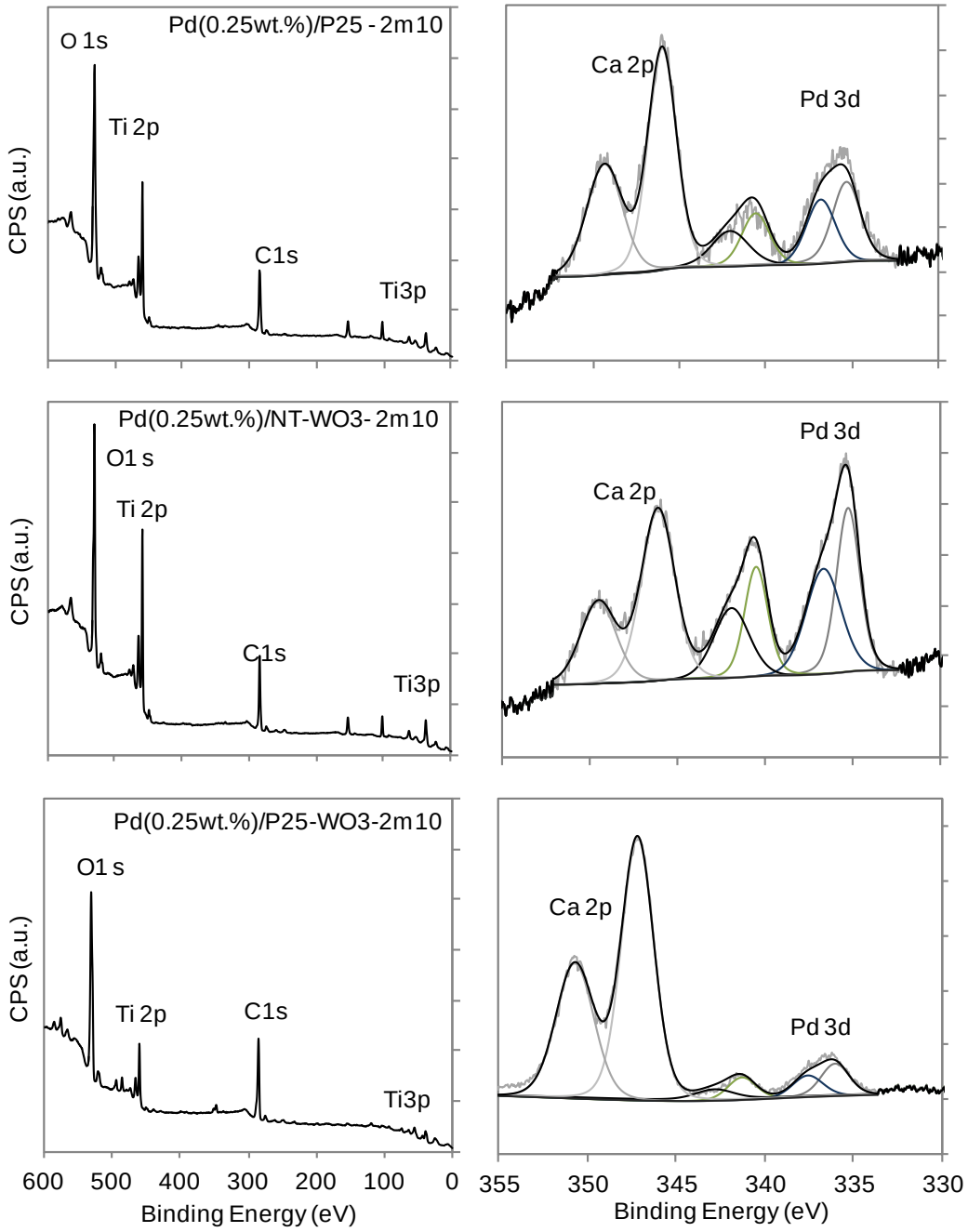

Figure 5.31. XPS full spectra and high-resolution XPS spectra of Pd 3d spectral region for Pd/P25, Pd/NT-WO_3 and Pd/P25-WO_3 - PCS catalysts. Pd deposited by PD 2m10 method

In Figure 5.31 is also possible to observe that for Pd/P25-WO_3, the Pd peak is smaller than on the other two catalysts, which could mean a worst Pd dispersion. When the metal content increases (Figure 5.32), on Pd/NT-WO_3, the Pd peaks are more relevant due to the increase of Pd content as well as probably due to a better dispersion of Pd nanoparticles.

It is particularly curious that for the PCS catalysts presented in Figure 5.31 and 5.32, peaks corresponding to Calcium (Ca) appears. This fact is probably due to the contamination of the catalysts (it is not clear where they come from). These Ca impurities may explain the very low S_{BET} values observed on these catalysts in Table 5.

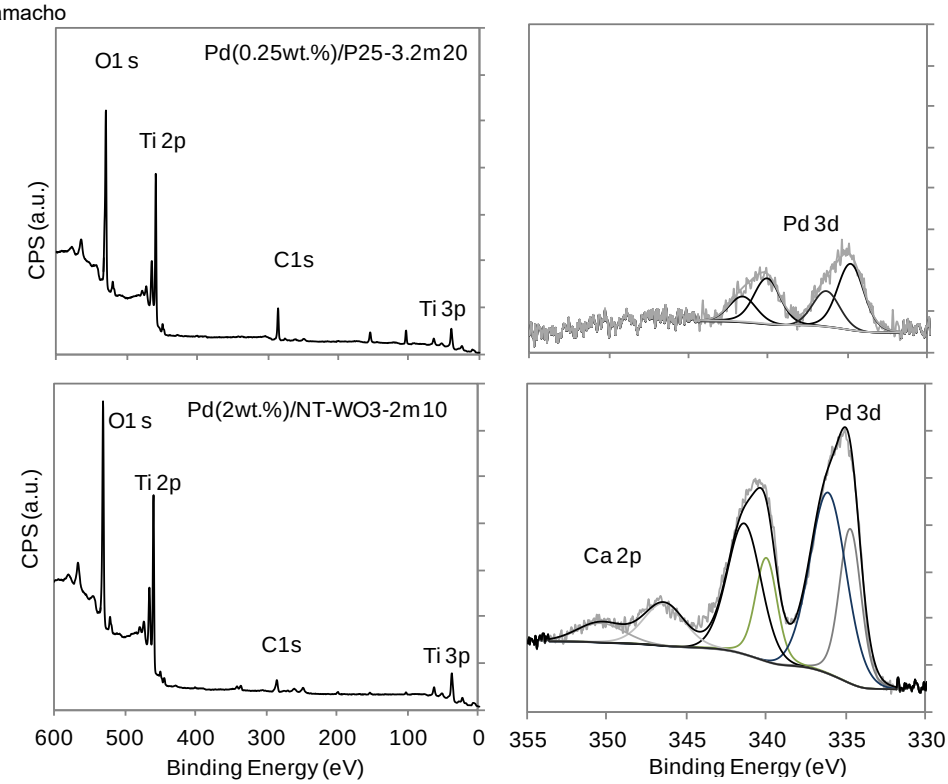

Figure 5.32. XPS full spectra and high-resolution XPS spectra of Pd 3d spectral region for Pd/P25 and Pd/NT-WO_3 - PCS catalysts. Pd deposited by PD 3.2m20 and 2m10 method, respectively.

5.1.5.4. m-Pt/TiO_2 (-WO_3) - PCS Lab catalysts

Figure 5.33 shows the surface chemical composition for Pt(0.18 wt.%)/P25, Pt(0.25 wt.%)/NT-WO_3 and Pt(0.25 wt.%)/P25-WO_3 catalysts, where Pt was introduced by PD using the 2m10 method.

From the complete spectra, all three catalysts show the presence of O, Ti and C with the O 1s, Ti 2p, C 1s and Ti 3p peaks at 531, 460, 285 and 38 eV, respectively. Concerning the Pt 4f XPS analysis for Pt/P25 sample, any signal is defined. For this sample, it was also scanned the region Pt 4d , which is equally valid than 4f but less intense and it was neither detected any signal though the fact there are some noisies in the background. From this result, besides the results shown in Table 6 and the HRTEM images (Figure 5.24), is possible to conclude that the Pt load (0. 18 wt.%) is very small to be detected due to the XPS detection limit. From HRTEM results, very small Pt particles (≈ 0.5 nm in size) have been observed. They are very well dispersed on the P25 support.

In the region corresponding to Pt 4f in Figure 5.33, for Pd(0.24 wt.%)/NT-WO_3 and Pd(0.21 wt.%)/P25-WO_3 samples, it is observed the presence of small peaks, which compared to the same region for Pd/P25 sample might suppose that Pt nanoparticles are better dispersed on the supports containing WO_3. From these XPS results is confirmed once again some contamination with Na and Ca of these materials. In order to determine the Pt/Ti molar ratio, the Pt 4d regions was used. But unfortunately, although this region was free of contributions of other elements, the sensibility for this region is lower, therefore, due to the already low Pt load, it was not possible to detecte Pt clearly, as it was possible for Pd.

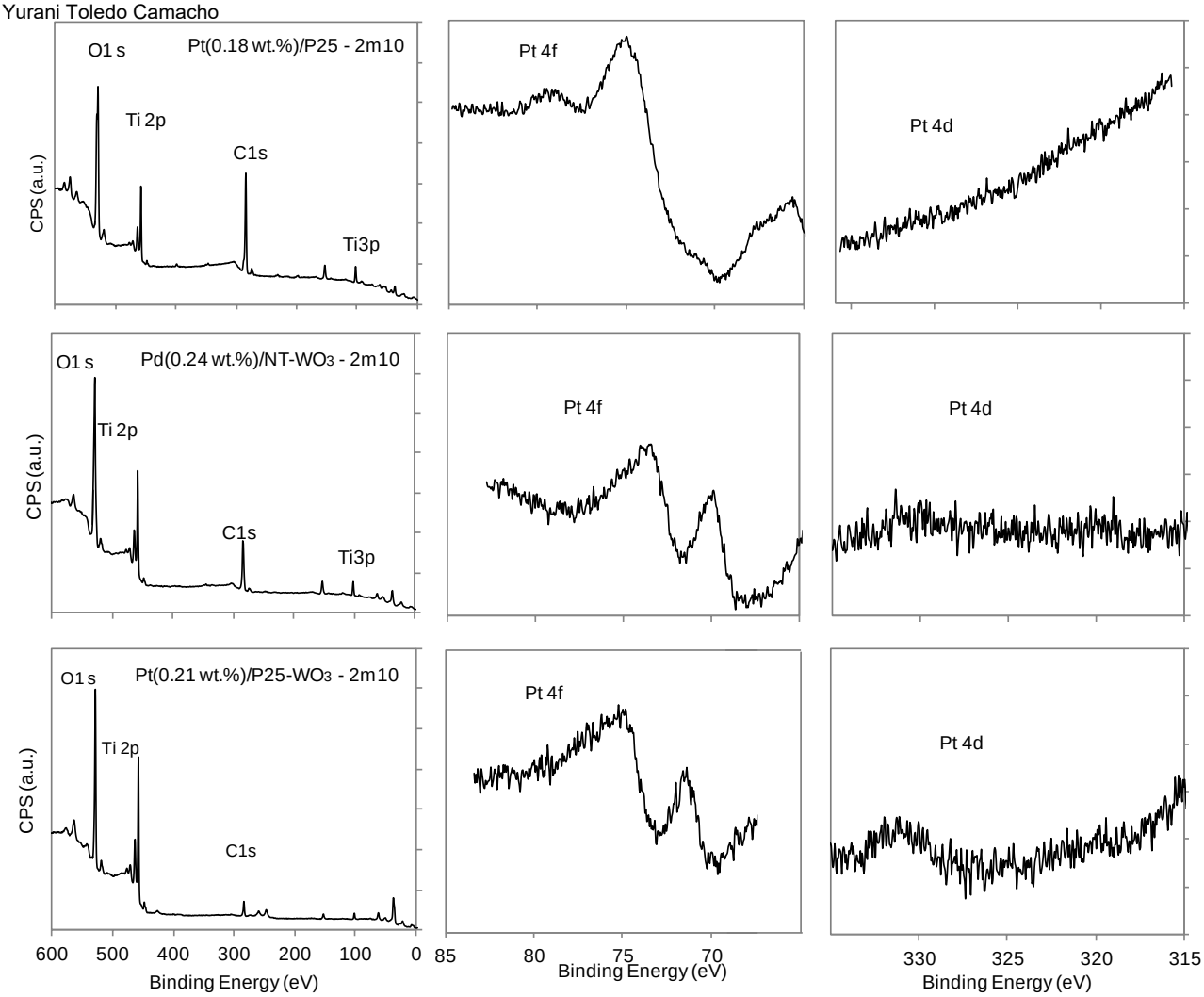

Figure 5.33. XPS full spectra and high-resolution XPS spectra of Pt 4f and Pt 4d spectral region for Pd(0.18 wt.%)/P25, Pd(0.24 wt.%)/NT-WO_3 and Pd(0.21 wt.%)/P25-WO3 - PCS catalysts. Pt deposited by PD 2m10 method.

5.1.6. Diffuse Reflectance UV-Vis

The optical band-gap was determined by means of Tauc's plot for indirect semiconductors ([Photon energy*Absorbance]$^{1/2}$ versus the Photon energy) obtained from diffuse reflectance spectra. Barium sulphate ($BaSO_4$) was used as standard. The diffuse reflectance spectrum was converted into absorbance using the Kubelka-Munk function. The band-gap results are summarized in Tables 3 - 7, together with the wavelength and absorption edge.

5.1.6.1. w-Pd/TiO_2(-WO_3) - CATHETER Lab catalysts

From Table 3, the band-gap values (Eg) for P25, NT-WO_3 and P25-WO_3 are 3.10, 2.97 and 3.08 eV, respectively. The DR-UV-Vis spectra (Figure 5.34) showed a higher optical absorbance near 400 nm for all the catalysts when Pd is incorporated. Table 3 shows that the incorporation of Pd produces a slight decrease in the band-gap and higher maximum absorption wavelength (nm) for all the catalysts. Pd/NT-WO_3 showed the lowest band-gap energy and highest maximum absorption wavelength (2.94 Eg; 422 nm). Nevertheless, the band-gap values are comparable to the literature for similar materials [75]. Some authors indicate that incorporating noble metals in semiconductor materials enhances light absorption towards the visible region, which can be attributed to a characteristic absorption of surface excitation due to plasmons of the metal nanoparticles [169][170].

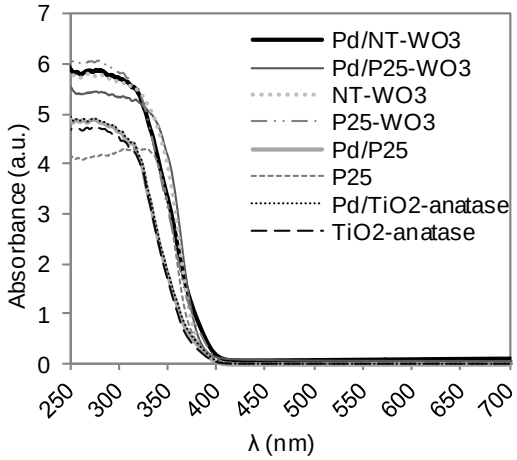

Figure 5.34. DR UV-Vis spectra for Pd/TiO_2(-WO_3) catalysts. Pd incorporation by PD-w

5.1.6.2. m-Pd/TiO_2(-WO_3) - CATHETER Lab catalysts

The band-gap and wavelength and absorption edge results for these group of catalysts are summarized in Table 4. The DR-UV-Vis spectra (Figure 5.35) for catalysts prepared by PD-m methods, showed a higher optical absorbance near 400 nm for all the catalysts when Pd is incorporated.

Similar to the catalysts with Pd incorporated by PD-w method, the metal deposition produces a slight decrease in the band-gap (Eg) and higher wavelength light absorption (nm) for all the catalysts. For instance, catalysts with 0.25 wt.% of Pd and deposited by the PD 2m10 method, the band-gap after metal deposition on three supports is 2.92, 2.89 and 2.99 eV for Pd/P25, Pd/NT-WO_3 and Pd/P25-WO_3 catalysts, respectively (vs. 3.10, 2.97 and 3.08 eV, of their respective supports: P25, NT-WO_3 and P25-WO_3). The catalyst with lowest band-gap energy and highest wavelength absorption light was Pd(0.25 wt.%)/NT-WO_3 - 2m10 (2.89 eV and 398 nm).

For Pd/P25 catalysts, the decreasing order of the light absorption values for the different metal PD methods is: 2m10 > 4m10 >2m5 > 2m1 > wi > 4w. For Pd/NT-WO_3 this order is 2m10 > 1m10 = 4w > 4m10 and for Pd/P25-WO_3 catalysts: 2m1 > 2m10 > 4m10 > 4w. As a result, the PD-m methods are shown to produce catalysts with higher wavelength absorption light than the PD-w and wi methods. Finally, in this group of catalysts, it is observed a slight trend where the catalysts with higher S_{BET}, such as Pd/NT-WO_3 catalysts (PD-m method), presented smaller band-gap. On the contrary, Pd/P25-WO_3 catalysts showed the lowest S_{BET} and the highest band-gap (Table 4).

5.1.6.3. m-Pd/TiO_2 (-WO_3) - PCS Lab catalysts

Table 5 shows the band-gap values (Eg) and the highest absorption light for the Pd/P25, Pd/NT-WO_3 and Pd/P25-WO_3 catalysts synthesized in PCS Lab. The DR-UV-Vis spectra (Figure 5.36) showed a higher optical absorbance near 400 nm for all the catalysts when Pd is incorporated. In Table 5 is also observed a slight decrease in band-gap (Eg) values after Pd deposition, either by PD 3.2m20 or 2m10 method.

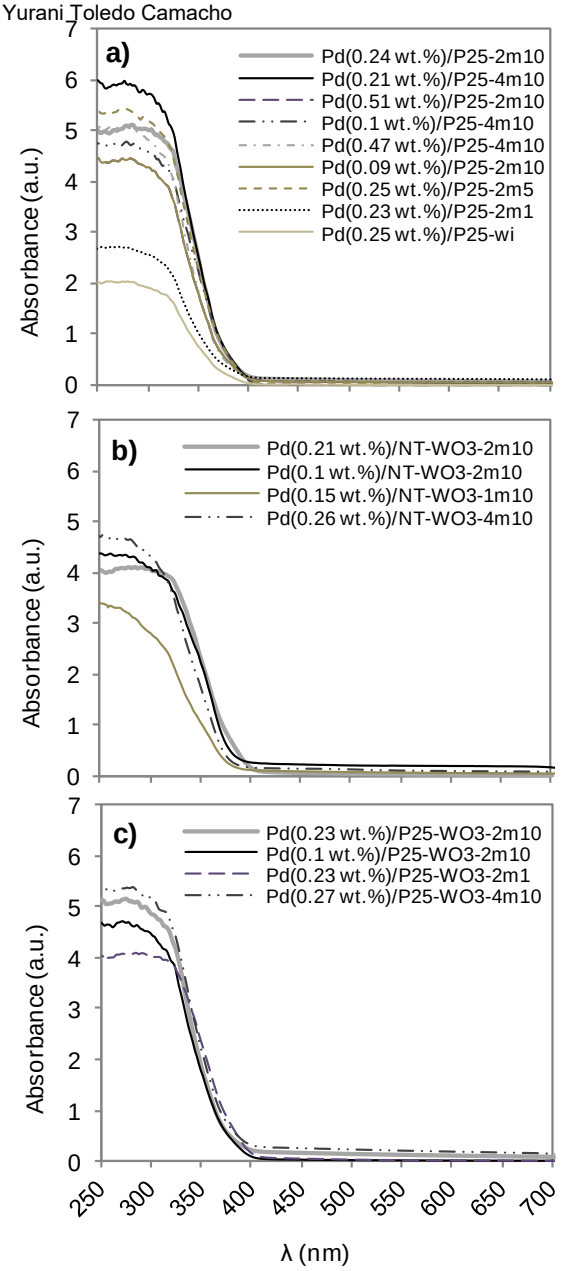

Figure 5.35. DR UV-Vis spectra for **a)**Pd/P25; **b)** Pd/NT-WO_3 and **c)** Pd/P25-WO_3 catalysts. Pd incorporation by different PD-m methods

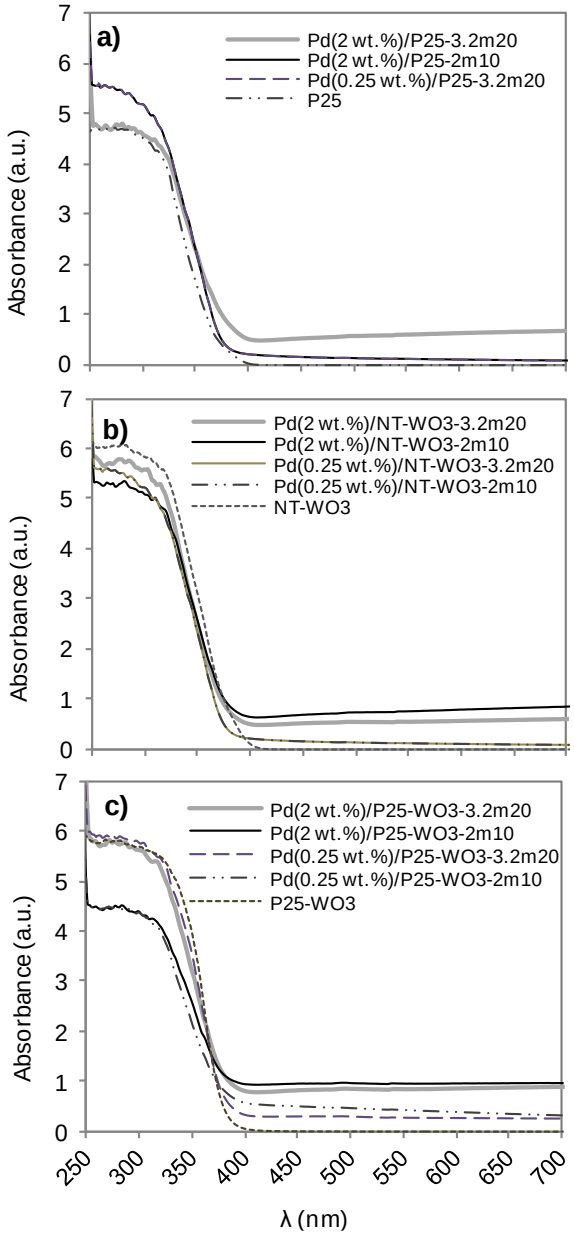

Figure 5.36. DR UV-Vis spectra for a)Pd/P25; b) Pd/NT-WO_3 and c) Pd/P25-WO_3 catalysts.Pd incorporation by two different PD-m methods: 3.2m20 and 2m1

For every group of catalyst, the catalysts that showed the lowest band-gap value are: Pd(2 wt.%)/P25 - 3.2m20 (2.87 eV and 432 nm), Pd(2 wt.%)/NT-WO_3 - 2m10 (2.88 eV and 430 nm) and Pd(2 wt.%)/P25-WO_3 - 2m10 (2.79 eV and 444 nm). Not important patterns are seen between both 0.25 and 2 wt.% of Pd, and neither on both PD 3.2m20 and 2m10 methods on the band-gap values.

For example, for Pd/P25 catalysts, the band-gap and the highest absorption light was improved, compared to P25 (3.10 eV and 399 nm), for all the catalysts, though the smallest improvement was observed for Pd(0.25 wt.%)/P25 - 3.2m20 (3.05 eV and 407 nm) and Pd(2 wt.%)/P25 - 2m10 (3.05 eV and 407 nm). In the case of Pd/NT-WO_3 catalysts, only two catalysts showed lower values of band-gap compared to the support NT-WO_3 (2.97 eV and 418 nm). These catalysts contain 2 wt.% of Pd. In this case, the worst results were shown for the lower Pd content (0.25 wt.) prepared by both PD methods (3.2m20 and 2m10). And finally, for all the Pd/P25-WO_3 catalysts, the band-gap was importantly improved, except for Pd(0.25

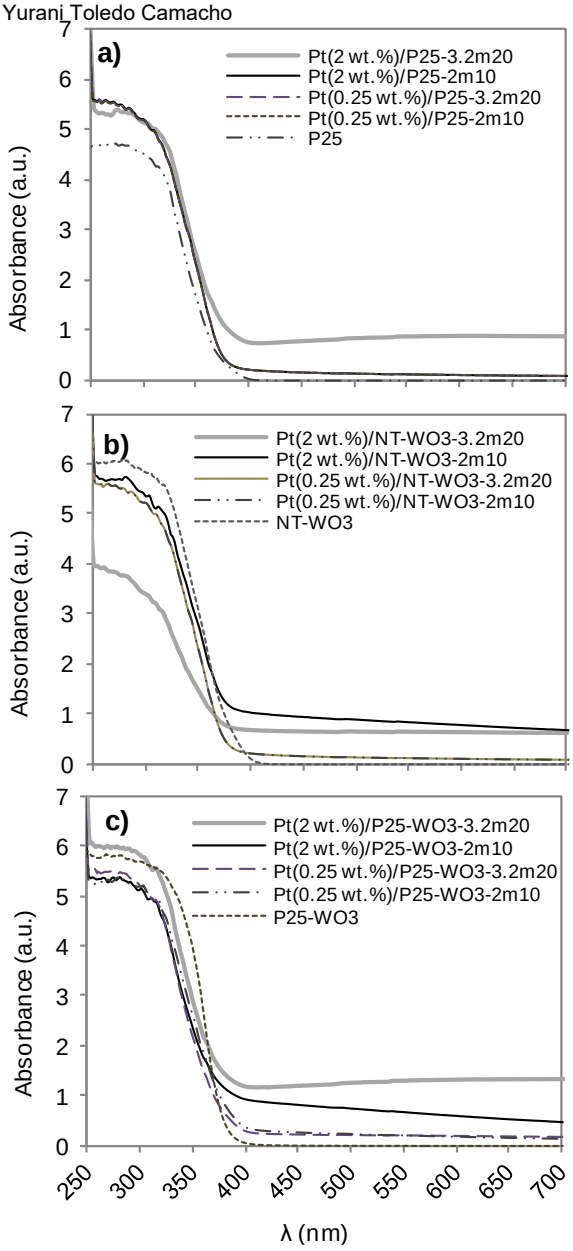

Figure 5.37. DR UV-Vis spectra for **a)** Pt/P25; **b)** Pt/NT-WO_3 and **c)** Pt/P25-WO_3 catalysts. Pt incorporation by two different PD-m methods: 3.2m20 and 2m10.

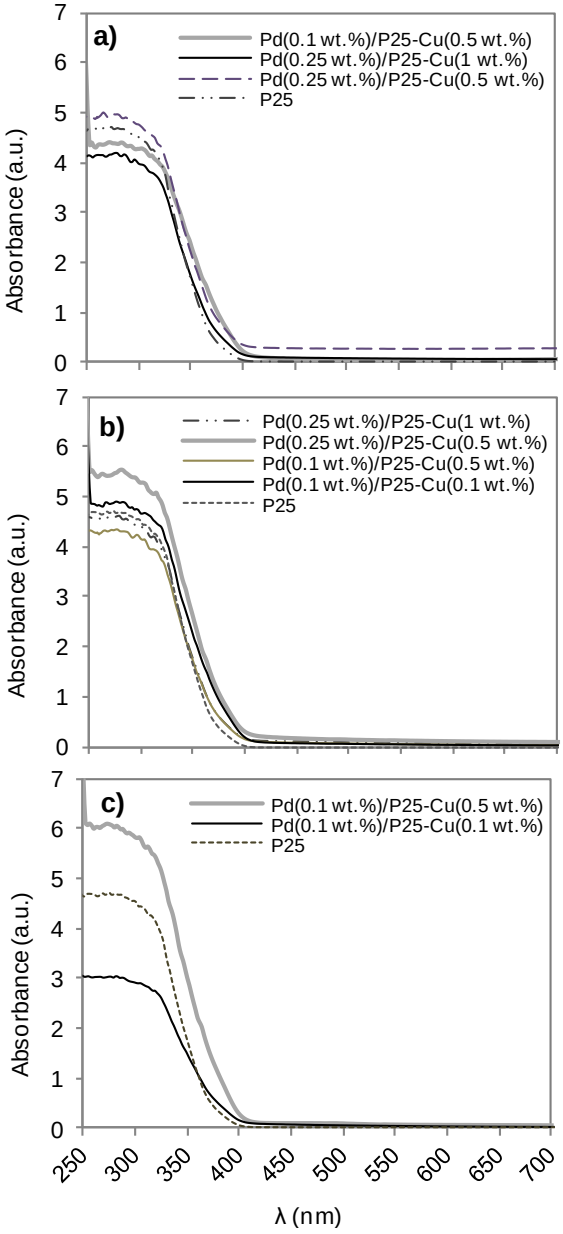

Figure 5.38. DR UV-Vis spectra for Pd/P25-Cu catalysts. Cu and Pd incorporated by **a)** Cu: wi+C350 and Pd: wi+R300; **b)** Cu:wi+C350 and Pd: PD 2m10 and, **c)** Cu: wi sC + Pd: PD 2m10

wt.%)/P25-WO_3 prepared by PD 3.2m20 method (3.03 eV and 410 nm). Any trend was neither observed regarding the relationship between the band-gap and S_{BET} values.

5.1.6.4. m-Pt/TiO_2 (-WO_3) - PCS Lab catalysts

Table 6 shows the band-gap values (Eg) and the highest absorption light for the Pt/P25, Pt/NT-WO_3 and Pt/P25-WO_3 catalysts synthesized in PCS Lab. The DR-UV-Vis spectra (Figure 5.37) showed a higher optical absorbance near 400 nm for all the catalysts when Pt is incorporated.

Unlike the catalysts presented in section 5.1.6.4, it seems that there is a kind of pattern regarding to the band-gap value and the metal deposition method. For those materials prepared by PD 3.2m20 method containing 2 wt.% of Pt, the band-gap is the lowest: Pt(2 wt.%)/P25 (2.86 eV and 434 nm), Pt(2 wt.%)/NT-WO_3 (2.80 eV and 444 nm) and Pt(2 wt.%)/P25-WO_3 (2.80 eV and 443 nm).

For Pt/P25 catalysts, the band-gap and the highest absorption light was improved for all the catalysts.

However, the smallest improvement was observed for Pt(0.25 wt.%)/P25 - 3.2m20 (3.06 eV and 405 nm). In the case of Pt/NT-WO_3 catalysts, similar to the catalysts containing Pd (Table 5), only the two catalysts containing 0.25 wt.% of Pt did not showed an improvement in their band-gap compared to the bared support (NT-WO_3). Pt/P25-WO_3 catalysts, showed the most important improvement in their band-gap. Any trend was observed regarding the relationship between the band-gap and S_{BET} values.

5.1.6.5. Pd/TiO_2-Cu - CATHETER Lab catalysts

Table 7 shows the band-gap values (Eg) and the highest absorption light for catalyst containing Pd and Cu. In Figure 5.38 is shown the DR-UV-Vis spectra for P25-Cu catalysts and in Figure 5.39 the DR-UV-Vis spectra for catalysts containing Pd. In Table 7 is possible to see that the band-gap values (Eg) for the catalysts containing only P25 and Cu is already lower that the precursor P25 (3.10 eV), where the lower the Cu content on P25, the lower is its band-gap value: P25-Cu(2 wt.%) (2.93 eV, 423 nm), P25-Cu(1 wt.%) (2.91 eV, 426 nm) and P25-Cu(0.5 wt.%) (2.89 eV, 429 nm). Regarding the Pd deposition method, the wi + R300 method produces catalysts with lower band-gap values.

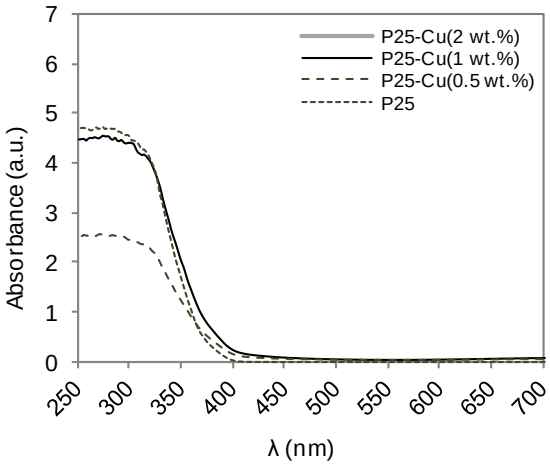

Figure 5.39. DR UV-Vis spectra for P25-Cu catalysts.

See for instance Pd(0.1 wt.%)/P25-Cu(0.5 wt.%) and Pd(0.25 wt.%)/P25-Cu(1 wt.%) catalysts, where Cu was deposited by wi C350 and Pd by both PD 2m10 and wi R300 method. For these catalysts, the Pd wi seems to improve band-gap and absorption light compared to the Pd PD, 2.85 eV and 435 nm vs. 2.95 eV and 421 nm, respectively, for Pd(0.1 wt.%)/P25-Cu(0.5 wt.%) catalysts and, 2.95 eV and 421 nm vs. 2.97 eV and 418 nm, respectively, for Pd(0.25 wt.%)/P25-Cu(1 wt.%) catalysts.

Regarding the Cu deposition method, the wi sC method produced catalysts with lower band-gap respect to the catalysts with calcinations protocol. See for example the Pd(0.1 wt.%)/P25-Cu(0.1 wt.%) (2.89 eV and 429 nm vs. 2.92 eV and 425 nm, respectively) and Pd(0.1 wt.%)/P25-Cu(0.5 wt.%) (2.89 eV vs. 429 nm vs. 2.95 eV and 421 nm) catalysts in Table 7. Concerning a relationship between band-gap values and S_{BET}, in every synthesis method group there is a slight tendency of lower band-gap values for catalysts with lower S_{BET}.

5.2. H_2 generation

Similarly to the previous section 5.1, the H_2 generation results are presented by groups of catalysts: w-Pd/TiO_2(-WO_3) - CATHETER Lab, m-Pd/TiO_2(-WO_3) - CATHETER Lab, m-Pd/TiO_2(-WO_3) - PSC Lab, m-Pt/TiO_2(-WO_3) - PSC Lab and Pd/TiO_2-Cu - CATHETER Lab catalysts. Photocatalytic H_2 tests were performed in four different systems: (i) Simulated solar light system (SSL-system), (ii) UVA light system (UVA-system), (iii) Pilot plant scale system (PPS-system) and (iv) small scale system (SS-system), that have been presented in section 4.8.

5.2.1. w-Pd/TiO_2(-WO_3) - CATHETER Lab catalysts

H_2 tests for w-Pd/TiO_2(-WO_3) catalysts were carried out in the SSL-system and UVA-system, using different catalyst concentrations and different amounts of methanol. The objective in this first experimental set was to determine a local optimal set of conditions under which H_2 generation is maximum. Additionally, some other parameters, such as the Pd amount, type of water and light source, were also studied to understand their effect on the H_2 evolution on these new catalytic materials.

5.2.1.1. Effect of the amount of catalyst and the catalyst nature

Figure 5.40 shows the H_2 evolution for Pd/NT-WO_3 and Pd/P25-WO_3 catalysts under solar light for different catalyst concentration: 86, 167, 333 and 500 ppm. A blank test without catalyst addition was also performed and no H_2 generation was observed. Under the experimental conditions (detailed under label of Figure 5.40), this result indicates an optimal catalyst concentration around 167 ppm. On one side, a lower amount of catalyst than the optimal probably implies not enough active sites to produce higher amounts of H_2, and on the other hand, a higher amount of catalyst involves higher light dispersion, which also leads to a lower H_2 generation. From Figure 5.40 is also possible to see that the Pd/NT-WO_3 catalyst produced higher H_2 evolution than the Pd/P25-WO_3 catalyst (around 30 % more).

Figure 5.41 shows the H_2 production for different catalysts based on Pd, TiO_2 and WO_3 under solar light. In this experimental set the highest H_2 production was achieved by Pd(0.013 wt.%)/NT-WO_3 (1.57 ml/min.gCat) followed by Pd(0.011 wt.%)/P25-WO_3 (1.06 ml/min.gCat) and Pd(0.009 wt.%)/P25 (0.73 ml/min.gCat). The NT-WO_3, P25-WO_3 and P25 supports scarcely reached to 0.499, 0.30 and 0.030 ml/min.gCat, respectively. These results indicate that the incorporation of very low amount of Pd improves the efficiency of the NT-WO_3, P25-WO_3 and P25 catalysts towards H_2 production by around three times for both NT-WO_3 and P25-WO_3, and up to 25 times for P25. Furthermore, the incorporation of WO_3 on the bare TiO_2 also increases the H_2 production.

In Figure 5.41 is observed that at the beginning of the irradiation there is an increase in H_2 evolution before a plateau is reached. Practically for all the catalysts, this induction period was around 60 - 80 min. Taking into account that the residence time (τ) in the SSL-system is near to 25 min (the total volume of the reactor is 750 ml and the flow inlet is 30 ml/min), the remaining time to reach the plateau may correspond to the formation of active sites for H_2.

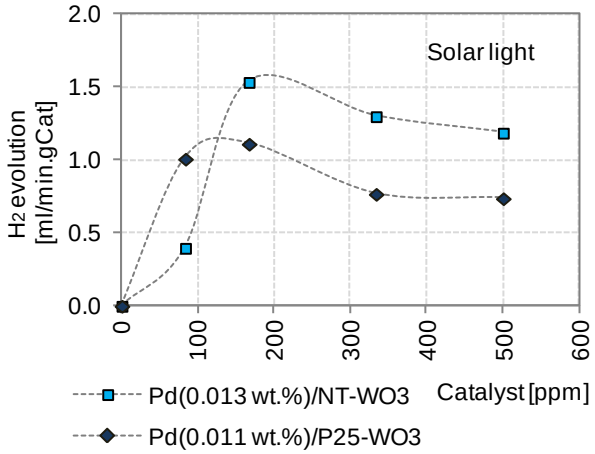

Figure 5.40. Effect of catalyst concentration on the H_2 generation for Pd/NT-WO_3 and Pd/P25-WO_3 catalysts. Experimental conditions: 600 ml of water - methanol (50 vol.%) solution under simulated solar light (Xe Lamp, 300 - 800 nm, 250 W/m^2, $I_{250-450nm}$: 6.5x10^{-4} Einstein/min).

Some authors have explained that this period could correspond to a photocatalytic reduction of an oxidized form of a metallic-co-catalyst [72][171][172] ($M^+ \rightarrow M^0$, M: metallic element). Konta et al [171] indicates that these induction periods suggest that some reduction processes occur on the catalyst at the beginning of the irradiation. Based on these ideas, it is possible to understand that before irradiation, Pd could be in an oxidized form (in agreement with the XPS results), then, after irradiation has started, Pd is reduced by the e^- that are photogenerated. Hence, when the irradiation time increases, more e^- are photogenerated; then, more metallic Pd is formed (Pd^0) and more hydrogen ions (H^+) are adsorbed on Pd surface.

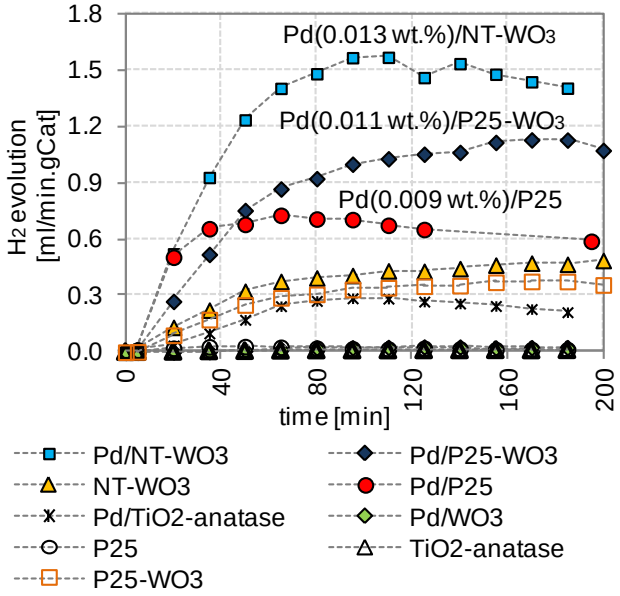

Figure 5.41. Effect of catalysts nature on the H_2 generation for different Pd/TiO_2(-WO_3) based catalysts. Experimental conditions: catalyst 167 ppm, 600 ml of a water - methanol (50 vol.%) solution under simulated solar light (Xe Lamp, 300 - 800 nm, 250 W/m^2, $I_{250-450\ nm}$: 6.5x10^{-4} Einstein/min).

The effect of the nature of the catalyst was also studied using tap water (conductivity < 907.6 µS/cm, Cl^- = 0.001 mg/L, total organic carbon (TOC): 3.93 mg/L, inorganic carbon (IC): 45.29 mg/L, pH 7.83) in the water - methanol solution (see Figure 5.42). In this case, because of the presence of tap water, the H_2 evolution decreased substantially (10 times lower). Similar to the results presented in Figure 5.41, in Figure 5.42 the Pd/NT-WO_3 and Pd/P25-WO_3 catalysts showed higher H_2 generation compared with the

rest of catalysts. Concerning the different H_2 evolution profiles, the catalysts containing Pd have a clear profile with an induction period at the beginning of the reaction followed by a plateau at the end of the experiment. Wan-Ting et al [72] suggested that this can be explained by some part of the metal being in an oxidized form that can be reduced during the irradiation. Furthermore, for the tap water, the content of salts or chlorine can also have some influence on the reduction of Pd nanoparticles by irradiation and this process is not completed, as it can be observed for most of the catalysts shown in Figure 5.42.

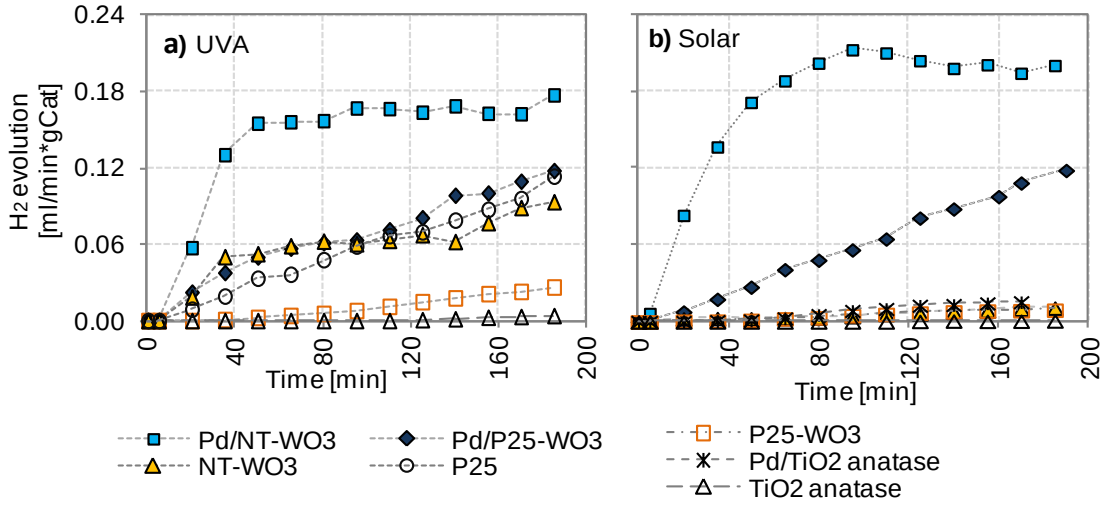

Figure 5.42. Effect of catalyst nature on the H_2 generation for different $Pd/TiO_2(-WO_3)$ based catalysts under **a)** UVA (λ 300 - 400 nm; 4 lamps of 15 W/lamp, $I_{250\text{-}450\ nm}$: $8.3x10^{-5}$ Einstein/min) and **b)** solar light (Xe Lamp, 300 - 800 nm, 250 W/m^2, $I_{250\text{-}450}$ nm: $6.5x10^{-4}$ Einstein/min). Experimental conditions: catalyst 500 ppm, 600 ml of a tap water - methanol (50 vol.%) solution.

5.2.1.2. Effect of methanol concentration

In order to understand the effect of sacrificial agent concentration on the H_2 production, different amounts of methanol (0, 5, 10 and 50 vol.%) were studied. Figure 5.43 shows the H_2 production on $Pd/NT\text{-}WO_3$ and $Pd/P25\text{-}WO_3$ catalysts at different methanol concentrations. It can be seen that under our experimental conditions, in the absence of methanol, water splitting did not take place (line corresponding to 0 vol.%), probably due to its high Gibbs free energy 238 kJ /mol [90][100].

When the sacrificial agent was added, H_2 was detected and its evolution increased with the increase of the amount of methanol. This outcome might be explained by the fact that methanol molecules act as holes (h^+) scavenger on the surface of the catalytic support; therefore, the more methanol added, the higher the probability of photogenerated h^+ being trapped by the organic compounds. As a result, photoexcited e^- are easily trapped by Pd, increasing the lifetime of the e^-/h^+ pair and increasing the H_2 generation. In the literature, it is not still clear what role the water and organic compound molecules play.

Some authors have suggested that photogenerated h^+ may be reduced when they are transferred directly towards the methanol or by intermediary species. These intermediary species such as hydroxyl radicals (•OH) or oxide ions (O^{2-}) are formed from the oxidation of water molecules or by the reduction of the remaining oxygen molecules (O_2) (even after deaeration) that are adsorbed on the photocatalytic surface, or both simultaneously [173]. Other authors have proposed that the dissociation of the organic

compounds can be complete and arrive to CO_2 and H_2O, or partially, where the reaction proceeds into the dissociation of next intermediary products [101][127]. Patsoura et al [67] also explained that adding organic compounds in photocatalytic reactions helps to clean up the catalyst surface from "poisons", which results in a higher H_2 evolution.

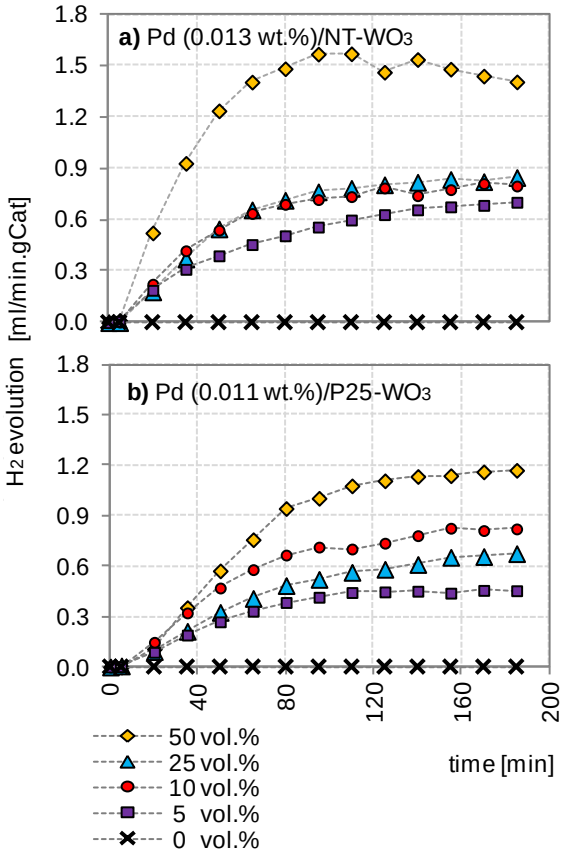

Figure 5.43. Effect of methanol concentration on the H_2 generation for **a)** Pd/NT-WO_3 and **b)** Pd/P25-WO_3 catalysts. Experimental conditions: catalyst 167 ppm, 600 ml of water - methanol mixtures under simulated solar light (Xe Lamp, 300 - 800 nm, 250 W/m^2, $I_{250-450\ nm}$: 6.5x10^{-4} Einstein/min).

5.2.1.3. Effect of type of water and the light source

Figure 5.44 compares the Pd/NT-WO_3 and Pd/P25-WO_3 catalysts toward the H_2 generation for the systems under UVA and solar light. Under UVA light, the H_2 evolution for Pd/NT-WO_3 and Pd/P25-WO_3 was 1.171 and 1.033 ml/min.gCat, respectively. Under solar light, the H_2 evolution was lower, 1.122 and 0.723 ml/min.gCat, respectively. The significant difference between Pd/NT-WO_3 and Pd/P25-WO_3, under solar light, could be due to the different structure of the NT, whose band - gap is narrower, which makes it easier to capture more photons from the near visible range, increasing the H_2 production.

The effect of the water matrix can be observed in Figure 5.44 (a) and (b)). This figure clearly shows the negative effect on H_2 evolution of the presence of salts in tap water. Under UVA light, the H_2 evolution using Pd/NT-WO_3 and Pd/P25-WO_3, using a milliQ-water - methanol solution, is around 7 and 9 times higher than those experiments carried out with a tap water - methanol solution, respectively. These results give us a first overview of the challenges to overcome for generating H_2 from wastewater of any nature. For instance, the wastewater from a real wastewater treatment plant is still loaded with impurities and other compounds, which can compete with the generation of H_2 or deactivate the catalyst.

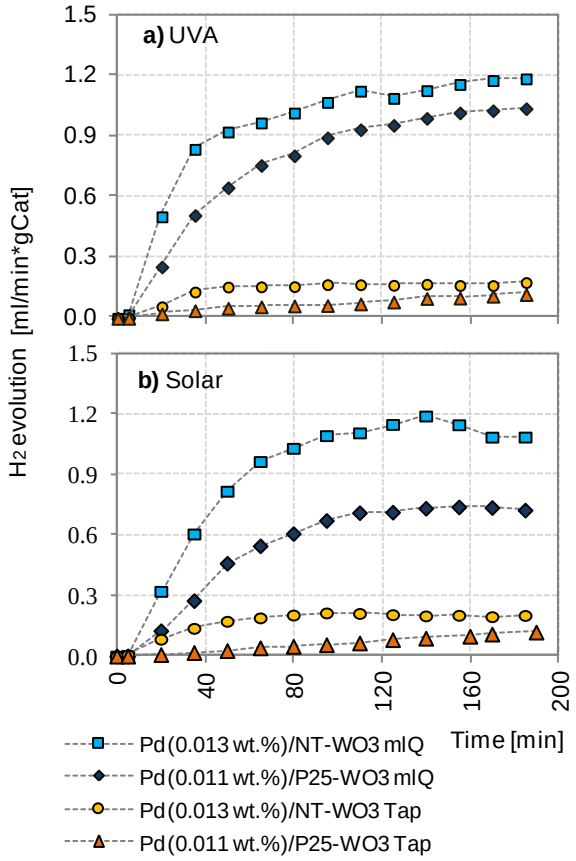

Figure 5.44. Effect of type of water on the H_2 generation under **a)** UVA and **b)** solar light. Experimental conditions: catalyst 500 ppm, 250 ml and 600 ml of a water - methanol (50 vol.%) solution for UVA and solar experiments, respectively.

5.2.1.4. Effect of the amount of photodeposited Pd

In order to understand the effect of the amount of photodeposited Pd on the H_2 evolution, Pd PD was performed varying the amount of Pd on the catalyst, from a concentration of 0 to 0.03 wt %. Figure 5.45 shows the effect of the amount of Pd photodeposited on the H_2 evolution for three Pd/P25-WO_3 catalysts.

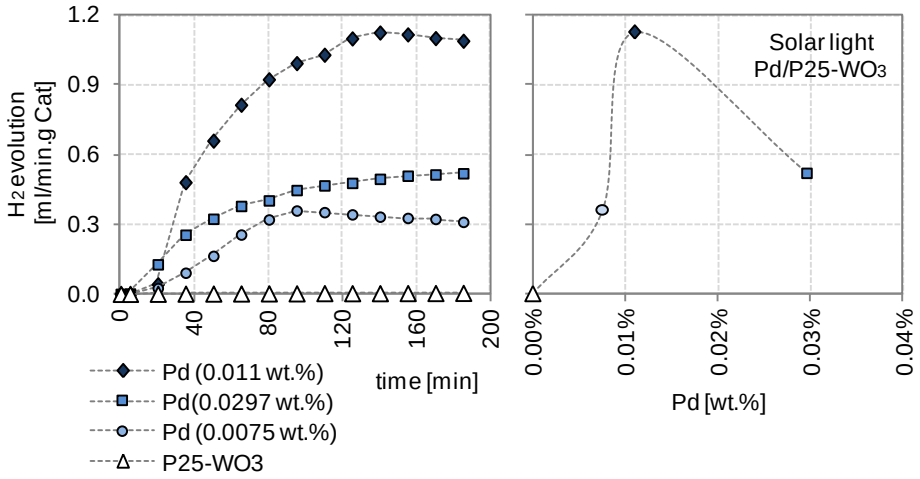

Figure 5.45. Effect of the amount of Pd deposited on the H_2 generation for Pd/P25-WO_3. Experimental conditions: 166.7 ppm of catalyst, 600 ml of water - methanol (50 vol.%) solution under simulated solar light (Xe Lamp, 300 - 800 nm, 250 W/m^2, $I_{250-450\ nm}$: 6.5x10^{-4} Einstein/min)

Concerning the effect of the amount of Pd on the H_2 generation, in Figure 5.45 is suggested that the optimal amount of Pd is 0.011 wt %. For Pd/P25-WO_3, the supports without Pd had very low H_2

production (0.004 ml/min.gCat). When 0.0075 wt.% of Pd is added to the catalyst, the H_2 evolution increases up to a plateau of 0.359 ml/min.gCat. Once the Pd is increased until 0.011 wt %, a large increase in the H_2 evolution was observed (1.125 ml/min.gCat). However, when the Pd added was 0.0297 wt %, a decrease was observed in the H_2 production (0.519 ml/min.gCat). Some authors explain that the high metal content in catalytic supports could create a shadow effect, and therefore the light absorption decreases [125][127]. This shadow effect is not easy to explain due to the amount of metal in this section is quite low. As it is seen in next sections, the metal content is increased (0.1 - 0.5 wt.%) and a similar behaviours is observed respect to an optimal amount of Pd but in a different range of Pd load.

5.2.1.5. Summary and specifics conclusions: w-Pd/TiO_2(-WO_3)-CATHETER Lab catalysts

In Table 8 is given some generals conclusions about the effect of the experimental conditions studied on the H_2 evolution in CATHETER Lab. Additionally, in order to see if there is any tendency relationship between some catalysts features, as S_{BET}, E_g and total volume of pores (TVP), with the H_2 evolution, in Figure 5.46 and is shown the H_2 evolution for w-Pd/TiO_2(-WO_3) catalysts vs. S_{BET}, where implicitly is also shown information about Eg (eV) (colour) and the TVP (smaller figure in Figure 5.46).

Table 8. Specific conclusions for w-Pd/TiO_2(-WO_3) - CATHETER Lab catalysts on the H_2 evolution

Effect of experimental conditions	
Amount of catalyst	A local optimal catalyst concentration around 167 ppm for both Pd/NT-WO_3 and Pd/P25-WO_3 catalysts, followed by 333 ppm and 500 ppm.
Catalyst nature	Pd/NT-WO_3 showed the highest H_2 evolution followed by Pd/P25-WO_3 and Pd/P25 catalysts.
Methanol concentration	A local optimal methanol concentration around 50 vol.% for both Pd/NT-WO_3 and Pd/P25-WO_3 catalysts, followed by 10 and/or 25 vol.%, and finally 5 vol.%. No H_2 evolution was observed in only water.
Type of water	Tap water decreases the H_2 evolution compared to milliQ water.
Amount of Pd photodeposited	A local optimal Pd load was observed, where 0.011 wt.% of Pd showed a higher H_2 evolution compared to a higher Pd load (0.0297 wt.%) and a lower (0.0075 wt.%).

Respect to the S_{BET}, in Figure 5.46 is not observed any strong tendency that allows us to conclude, for this group of catalysts, a direct improvement on H_2 evolution when the catalyst shows a high S_{BET} or TVP, or lower band-gap. It is important to clarify that when we say a "strong tendency", we are referring to the fact of seeing, for example in Figure 5.46, the points corresponding to the Pd/NT-WO_3 catalyst (●) or in fact the points corresponding to the Pd/P25-WO_3 catalyst (▼), more concentrated around a specific value of H_2 evolution, even when the experimental conditions (catalysts or methanol concentration, and Pd amount) are different. Moreover, it is possible to see some higher values in the H_2 evolution for Pd/NT-WO_3 catalysts, which shows the highest S_{BET} and TVP values. Regarding the variation in the experimental conditions, in Figure 5.46, the Pd/NT-WO_3 catalyst seems slightly more sensitive to the changes in the experimental conditions than Pd/P25-WO_3. This fact can be observed from the higher dispersion of data for Pd/NT-WO_3 catalyst along the H_2 evolution.

On the other hand, Figure 5.47 shows that mostly of the red marks are at higher H_2 evolution, and the highest red marks are around 167 ppm of catalysts concentration. Here is a relative stronger tendency observed on H_2 evolution at different experimental conditions.

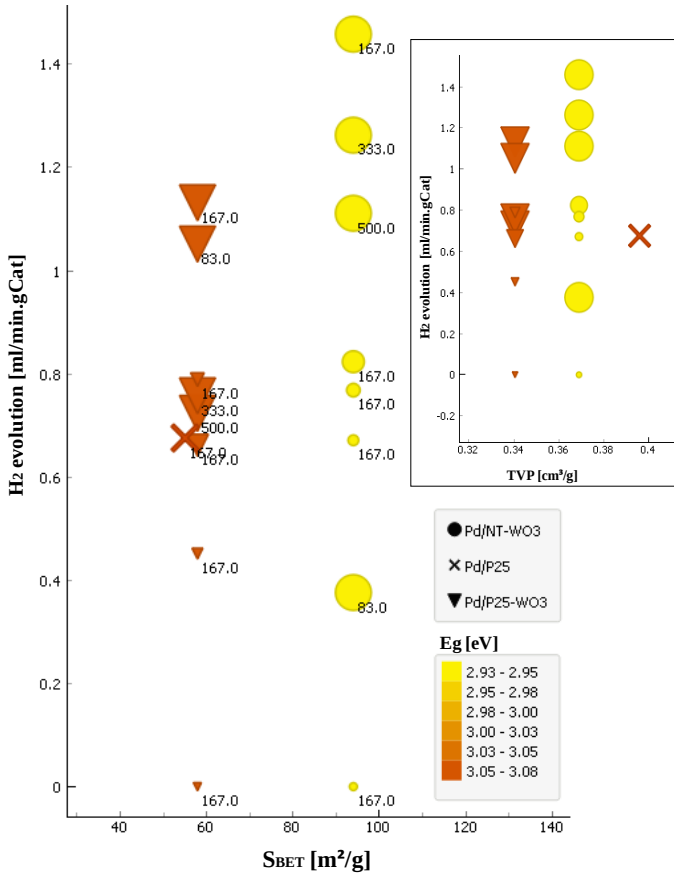

Figure 5.46. Data exploration for H_2 evolution for w-Pd/TiO_2(-WO_3) - CATHETER Lab catalysts related to SBET [m^2/g] and TVP [cm^3/g], band-gap (Eg) [eV] (**colour**), catalysts nature (**shape**), catalysts concentration [ppm] (**label**) and methanol concentration [vol.%] (size).

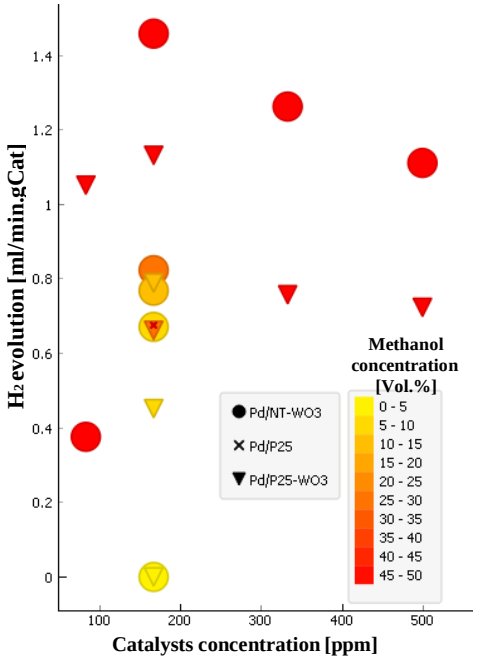

Figure 5.47. Data exploration for H_2 evolution for w-Pd/TiO_2(-WO_3) - CATHETER Lab catalysts related to the experimental conditions of catalysts concentration [ppm] (**axis x**), methanol concentration [Vol.%] (**colour**), catalysts nature (**shape**) and Pd load [wt.%] (**size**).

5.2.2. m-Pd/TiO_2(-WO_3) - CATHETER Lab catalysts

H_2 tests for m-Pd/TiO_2(-WO_3) - CATHETER Lab catalysts were also carried out in the SSL-system and UVA-system, but in PPS-system and the SS-system, as well. Regarding the H_2 experiment in the SS-system, they are presented in section 5.2.3. In this section, two types of sacrificial agents were used. Methanol, which is the simplest alcohol that can give us an initial overview about the behavior of these new catalysts (Pd/TiO_2-WO_3), and also glycerol, to compare with a more complex molecule. In addition, a real wastewater containing a mixture of organic compounds has been tested.

In order to understand the effect of Pd PD method on the H_2 evolution, the amount of Pd, catalyst concentration, sacrificial agent concentration and Pd addition time (in-situ and ex-situ) was varied in the catalyst preparation step. Additionally, the wi method was studied for Pd/P25 catalysts.

5.2.2.1. Effect of Pd photodeposition method

In Figure 5.48 is shown the H_2 evolution for Pd/P25 catalysts prepared by different PD methods. In order to compare the catalytic activity of the Pd nanoparticles, H_2 evolution is presented in this case per gram of Pd. Regarding the variation of the sacrificial agent concentration, it can be seen from Figure 5.48 (b, d, h and j curves), that there is an optimal methanol concentration around 10 vol.% in the PD which leads to produce a catalyst with the highest H_2 evolution.

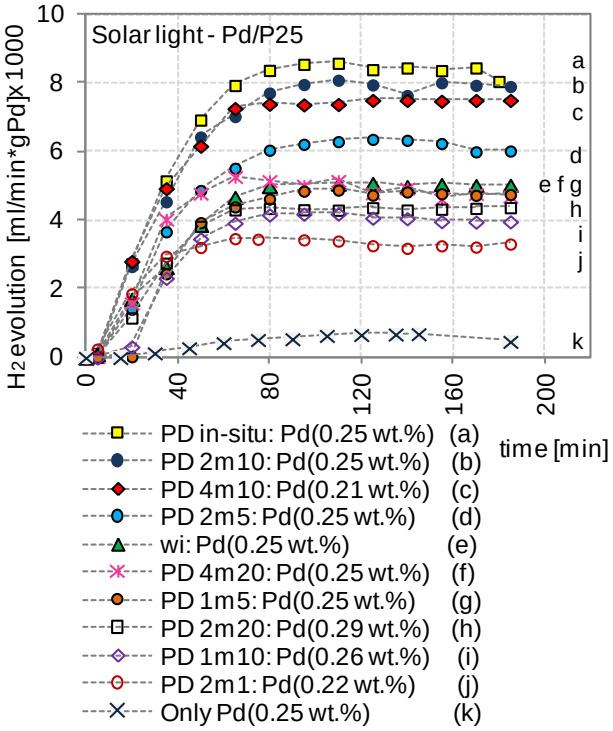

Figure 5.48. Effect of the Pd photodeposition method on the H_2 generation for Pd/P25 varying the Pd deposition method. Experimental conditions: catalysts 167 ppm, 600 ml of a water - methanol (50 vol.%) solution under simulated solar light (Xe Lamp, 300 - 800 nm, 250 W/m^2, $I_{250-450nm}$: 6.5x10^{-4} Einstein/min).

This highest H_2 production is also observed in Figure 5.49 (b) with Pd/P25-WO_3 prepared by PD 2m10 method, where there is a significant decrease of the H_2 evolution when methanol decreased. This fact revels the essential role of a sacrificial agent in the Pd PD, which may be related to the Pd nanoparticles size in agreement with TEM images of Pd/P25 (Figure 5.20 (f) and (d)) and Pd/P25-WO_3 (Figure 5.21 (e) and (g)) catalysts, where PD 2m1 method produces larger Pd nanoparticles than PD 2m10 method.

Comparing the catalysts prepared at the same methanol concentration but different catalyst concentration, Figure 5.48 (b, c and i curves), the slightly higher H_2 evolution for PD 2m10 (8120 ml/min.gPd) than 4m10 (7520 ml/min.gPd) method could correspond, probably, to the smaller band - gap of the catalyst prepared by PD 2m10 (2.92 vs. 2.95 eV). TEM image (Figure 5.20 (a and d curves)) corroborates that both samples are constituted by titania crystallites with 20 - 30 nm in size and Pd nanoparticles with 5 - 7 nm in size.

On the other hand, comparing PD 2m10 to PD 2m1 method, although they have similar amount of Pd deposited, the catalyst 2m10 is more active. This result could be related to the nanoparticles size. Figure 5.20 (d) shows a general STEM view of the catalyst prepared by the PD 2m1 method, showing a Pd nanoparticles size in the range of 3 - 15 nm. Although the fact that high methanol concentration in PD method could cause larger metal particles [117], in the case of the catalysts prepared by PD 2m1 method, the initial Pd nanoparticles deposited could act themselves as active sites. Therefore, even if the sacrificial agent concentration is low, this fact stimulate further Pd growth resulting in larger Pd nanoparticles.

A further analysis about the results of Figure 5.48 is shown in Figure 5.49, where is presented a relationship between the Pd / methanol ratio (mol Pd/mol MetOH) used in the PD solution (500 ml) (left

figure) and the photodeposition methods (right figure), and the H_2 evolution per gram of Pd (for both figures). Every point corresponds to different PD methods, which are: **(a)** 0.8m10, **(b**) 1m10, **(c)** 2m20, **(d)** 1m5, **(e)** 4m20, **(f**) 2m10, **(g)** 4m10, **(h)** 2m5 and **(i)** 2m1. Therefore, it seems there is an optimal Pd / MetOH ratio around $1.9x10^{-5}$- $3.8x10^{-5}$. The highest H_2 evolution, 7800 ml/min.gPd, was obtained for the catalyst prepared by PD 2m10 method.

A similar analysis is performed, taking into consideration the weight of catalyst and the amount of methanol ratio (gCat/L MetOH) (see right figure of Figure 5.49). The orange and yellowish colors bars correspond to PD "2mx" methods, where the catalyst concentration in the PD method was kept constant (2000 ppm) and the methanol concentration varied (1, 5, 10 and 20 vol.%). The dark and bluish colors bars correspond to PD "xm10" methods, where methanol concentration was constant (10 vol.%) and the amount of catalyst varied (1000, 2000 and 4000 ppm). In both groups is seen an optimal gCat/L MetOH ratio of around 20 for the 2m10 method. From this bar chart, there are two different method, 2m5 and 4m10, whose gCat/L MetOH ratio are 40. Both methods showed the highest H_2 evolution (see also point g and h in left figure of Figure 5.49). In order to corroborate this effect about the gCat/L MetOH ratio to the H_2 generation, two new methods were tested, which correspond to a 20 gCat/L MetOH ratio (1m5 and 4m20) (green bars). The H_2 evolution of the catalysts prepared by 1m5 and 4m20 method scarcely reached 49.06 and 49.52 ml/min.gCat, respectively. These values are lower than the obtained by the PD 2m10 method.

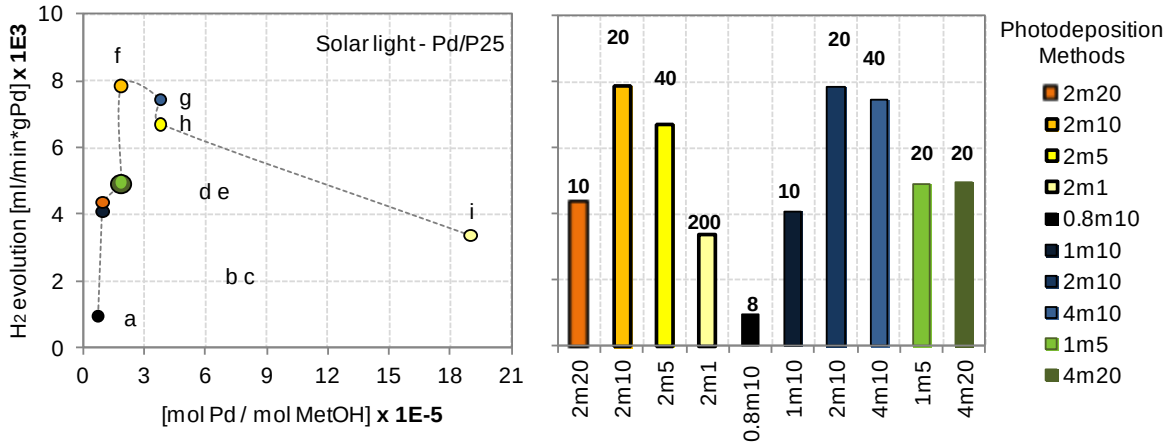

Figure 5.49. H_2 generation [ml/min.gPd] vs. mol Pd / mol MetOH ratio in the PD solution and bar chart of the gCat/L MetOH ratio. **(a)** 0.8m10, **(b)** 1m10, **(c)** 2m20, **(d)** 1m5, **(e)** 4m20, **(f)** 2m10, **(g)** 4m10, **(h)** 2m5 and **(i)** 2m1 methods

Regarding the results of these two last methods, 1m5 and 4m20 and taking into account that for all these PD methods, the volume and irradiation have not been changed, it could be considered then an optimal value of the photon flux to gram of catalyst ratio (einstein.min^{-1}/ gCat) or proportionally to mol of Pd (einstein.min^{-1}/ mol Pd). Hence, under this hypothesis, it is possible to understand that, in the case of 1m5 method, at lower amount of catalyst in the 500 ml of PD solution, under the same photon flux (compared to 2m10 method), there could be an overproduction of e^-/h^+ pairs, generated as a product of the higher number of photons reaching the photocatalytic support.

Consequently, when all the Pd nanoparticles in solution are deposited on the support but the photon flux supplied continues, more and more active sites are created (e^-/h^+ pairs). On these active sites, not only

methanol is oxidized in the VB, but also methanol degradation byproducts are reduced in the CB, therefore it could produce an additional adsorption of some organic molecules, which might poison the catalyst, retracting the photocatalytic activity toward the H_2. In the case of 4m20 method, the low efficiency toward H_2 could be due to the size of Pd, which is related to the concentration of methanol, where the higher the concentration of methanol, the higher the metal nanoparticles size [117], as was explained above. Regard to the catalyst prepared by wi (Figure 5.48 (e curve)), though it has the same amount of Pd than the catalysts prepared by PD 2m10 or PD 2m5 methods (or even higher then PD 4m10 method), it showed a lower H_2 evolution.

This result can be explained by the presence of larger Pd nanoparticles size (Figure 5.20 (b)). Bowker et al. [114] explained that the active sites of metal nanoparticles for the formation of the e^-/h^+ pair are placed around the edges of the metallic surface, where there is contact with the surface of the semiconductor support. Therefore, to increase the formation of e^-/h^+ pair and further the H_2 generation, it is necessary to maximize that contact zone, which increases when the nanoparticles size is lower. From these results, the order of H_2 generation for this kind of catalyst using different deposition methods was: PD in-situ > PD 2m10 > PD 4m10 > PD 2m5 > wi > PD 4m20 > PD 1m5 > PD 2m20 > PD 1m10 > PD 2m1.

Figure 5.50 presents the H_2 evolution per gram of catalysts for Pd/NT-WO_3 and Pd/P25-WO_3 catalysts prepared by PD in-situ, PD 2m10, PD 4m10, PD 1m10 (only for Pd/NT-WO_3) and PD 2m1 (only for Pd/P25-WO_3) methods. For these both families of catalysts, Pd/NT-WO_3 and Pd/P25-WO_3, the PD 2m10 method seems to be the best. Looking at the H_2 evolution per gram of catalysts, in the case of Pd/NT-WO_3, there is a slight difference between the three methods, even the catalysts prepared by PD 1m10, which only have 0.15 wt.% of Pd deposited, showed a significant H_2 evolution.

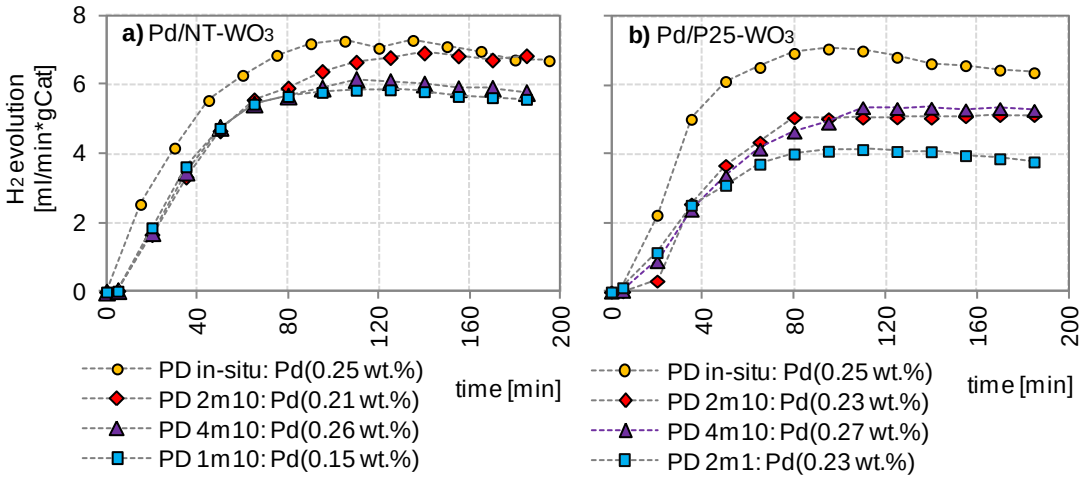

Figure 5.50. Effect of the Pd deposition method on the H_2 generation for **a)** Pd/NT-WO_3 and **b)** Pd/P25-WO_3 catalysts. Experimental conditions: catalysts 167 ppm, 600 ml of a water - methanol (50 vol.%) solution under simulated solar light (Xe Lamp, 300 - 800 nm, 250 W/m^2, $I_{250-450nm}$: 6.5x10^{-4} Einstein/min).

For Pd/NT-WO_3 and Pd/P25-WO_3 catalysts, the highest H_2 generation was obtained for PD in-situ (7.3 and 7.1 ml/min.gCat, respectively) followed by PD 2m10 (6.3 and 6.1 ml/min.gCat), PD 4m10 (6 and 5.9 ml/min.gCat, respectively). PD 1m10 and PD 2m1 methods did not improve the H_2 evolution (5.8 and 4.1 ml/min.gCat, respectively) with respect to the 2m10 method. Comparing both catalysts based on

Pd/TiO_2-WO_3 to Pd/P25 catalysts, they are not significantly affected by the concentration of the catalyst in the Pd PD, contrarily that was observed for Pd/P25 catalysts. These results demonstrate that the changes performed on some kind of materials to improve one or several properties are not easily extrapolated to other sort of materials, especially when it comes from new photocatalytic materials, where the extrapolation of catalytic behaviors without experimental work might lead to wrong conclusions. Concerning the induction period observed in Figures 5.48 and 5.50, and observed on w-Pd/TiO_2(-WO_3) catalysts as well, it could correspond to the reduction of an oxidized form of the metallic-co-catalyst toward its reduced form ($M^+ \rightarrow M^0$, M: metallic element)[72][171][172].

5.2.2.2. Effect of the amount of Pd

The effect of the amount of Pd in H_2 production was studied varying the amount of Pd from 0 to 0.5 wt.%. Figure 5.51 (a, c and d) shows the effect of the amount of Pd photodeposited on the H_2 evolution for Pd/P25, Pd/NT-WO_3 and Pd/P25-WO_3 catalysts, respectively. Figure 5.51 (b) suggests, for all the catalysts, an optimal amount of Pd photodeposited, around 0.25 wt.%.

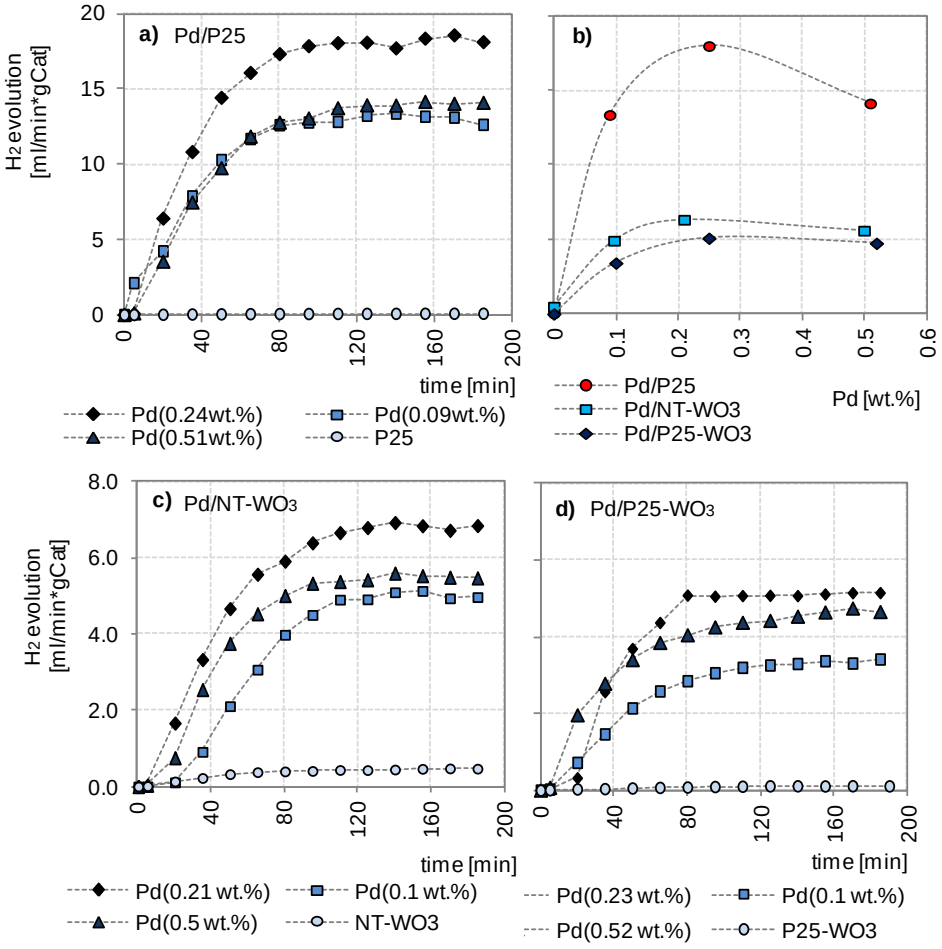

Figure 5.51. Effect of the amount of Pd deposited on the H_2 generation for Pd/P25(-WO_3) catalysts. Experimental conditions: catalysts 167 ppm, 600 ml of a water - methanol (50 vol.%) solution under simulated solar light (Xe Lamp, 300 - 800 nm, 250 W/m^2, $I_{250\text{-}450\ nm}$: 6.5x10^{-4} Einstein/min). Pd incorporation by PD-2m10 method

Furthermore, the supports without the presence of Pd showed very low H_2 evolutions (0.03, 0.5 and 0.003 ml/min.gCat, respectively). When 0.1 wt.% of Pd is incorporated, the H_2 evolution increased up to

a plateau of 13.37, 4.92 and 3.41 ml/min.gCat for Pd/P25, Pd/NT-WO_3 and Pd/P25-WO_3, respectively. Once the Pd was increased up to 0.25wt.%, the H_2 evolution increased as well (18, 6.33 and 5.08 ml/min.gCat). However, when the Pd amount increased up to 0.5 wt.%, a decrease in the H_2 evolution was observed (14.14, 5.69 and 4.74 ml/min.gCat). Some authors indicate that an increase of the amount of metal in the support, can produce a partial covering of the support by the metal, decreasing the amount of light absorption [125][127].

5.2.2.3. Effect of the light source

Figure 5.52 shows the H_2 evolution under UVA (UVA-system) and solar (SSL-system) light, in 250 ml and 600 ml of reaction volume, respectively. Under both kind of light, UVA and solar, the H_2 evolution for Pd/P25 was 19.18 and 16.45 ml/min.gCat, respectively. Under UVA light, the H_2 evolution of Pd/P25 was around a 15% higher than under solar light, and in the case of Pd/NT-WO_3 this difference was of about 18.3 % (8.35 and 6.82 ml/min.gCat, respectively). For Pd/P25-WO_3, the H_2 generation was higher under solar than UV light (4.22 vs. 5.13 ml/min.gCat, respectively).

In order to compare both systems under normalized conditions, it is necessary to determine the photon flux in both systems corresponding only to the UVA light (300 - 400 nm). This is calculated by the spectral distribution of the global radiation for the calculation (Table 9 and 10) given by the actinometric study of both lamps, the UVA and solar lamp, respectively. These photon fluxes were: $I_{300\text{-}40nm}$: $8.33x10^{-5}$ and $2.99x10^{-4}$ Einstein/min for the UVA reactor (250 ml) and solar reactor (600 ml), respectively.
Comparing the efficiencies toward H_2 for both systems, although the fact that the solar box system presents a higher photon flux, in the UVA system the three catalysts showed higher H_2 evolution. These results could be explained taking into account the geometry of the reactors as well as the volume of the liquid solution (250 and 600 ml), respectively.

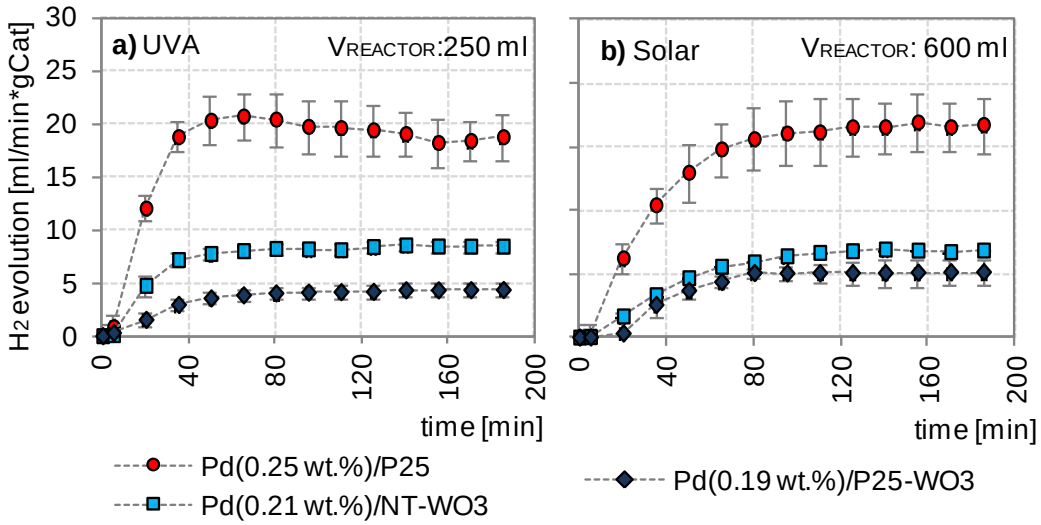

Figure 5.52. Effect of the light source on the H_2 generation, **a)** UVA (λ 300 - 400 nm; 4 lamps of 15 W/lamp, $I_{250\text{-}450\ nm}$: $8.3x10^{-5}$ Einstein/min) and **b)** solar light (λ: 300 - 800 nm; 250 W/m^2, $I_{250\text{-}450nm}$: $6.5x10^{-4}$ Einstein/min). Experimental conditions: catalyst 167 ppm, 250 ml and 600 ml of a water - methanol (50 vol.%) solution.

On the other hand, looking at the differences between Pd/P25 and both catalysts based on Pd/TiO_2-

WO_3, the lower efficiencies toward the H_2 of the latter catalysts are probably, due to the incorporation of WO_3, which might lead to produce more secondary products, such as aldehydes or carboxylic acids, that could be adsorbed on the catalysts surface, blocking the pathway toward higher H_2 evolution. Sakai et al. explained that in the interaction between Pd and WO_3 nanoparticles, the Pd might induce a multielectron reduction reaction, where the photoexcited e^- transferred toward Pd sites, could form also some superoxide anions on the surface [174].

Table 9. Spectral distribution of the global radiation for the calculation for solar lamp*****

% irradiation	Range [nm]	%	I [Einstein/min]**
0.4	280 - 300	1.585	$2.061x10^{-5}$
2.4	320 -360	19.01	$1.236x10^{-4}$
3.2	360 - 400	25.35	$1.648x10^{-4}$
5	400 - 440	39.6	$2.574x10^{-4}$
1.625	440 - 450	12.87	$8.366x10^{-5}$

*Xe lamp (300 - 800 nm; 250 W/m^2)
** Photon flux calculated from actinometry

Table 10. Spectral distribution of the global radiation for the calculation for UVA lamp*****

% irradiation	Range [nm]	%	I [Einstein/min]**
0.25	295 - 355	2.34	$1.959x10^{-6}$
3.71	355 - 364.7	34.74	$2.894x10^{-5}$
0.6	364.7 - 365.3	0.56	$4.665x10^{-7}$
0.49	365.3 - 370	4.59	$3.823x10^{-6}$
2.23	370 - 385	20.88	$1.739x10^{-5}$
0.97	385 - 390	9.08	$7.563x10^{-6}$
3.58	390 - 405	33.52	$2.792x10^{-5}$

* Philips TL-D 15W-BLB H8 (300 - 400 nm; 4 lamps of 15 W/lamp)
**Photon flux calculated from actinometry

Although deaerating was carried out before irradiation, probably oxygen from water or remaining from gas phase might contribute to the formation of that oxidizing agents, such as superoxide ($O_2^{\bullet-}$) or even hydroperoxy ($HO_2^{\bullet}$) radicals, in the Pd sites, occupying the active site for the H_2 generation. This idea could be corroborated in the bar chart of the Figure 5.53, where the TOC removal percentages was higher for Pd/TiO_2-WO_3 catalysts than for Pd/P25 catalyst, under both kind of lights.

Regarding the TOC removal, it can be observed that the catalysts that showed the highest H_2 generation, also showed the lowest TOC removal. This might indicate a higher concentration of by-product on some catalysts that could make the H_2 generation lower.

Previously was explained that although deaerating was carried out before irradiation, some remaining oxygen might contribute to the formation of oxidizing agents ($O_2^{\bullet-}$ or $HO_2^{\bullet}$) in the Pd sites, competing for the active site for H_2 production. Concerning Pd/TiO_2-WO_3 catalysts, Sánchez Martinez et al., in their study about the degradation of organic dyes using WO_3 nanoparticles [175], explained that the main contribution in the activity of WO_3 nanoparticles in the formation of hydroxide radicals (•OH) is when they are exposed to visible light irradiation. This could explain the higher TOC removal under solar light of the catalysts containing WO_3.

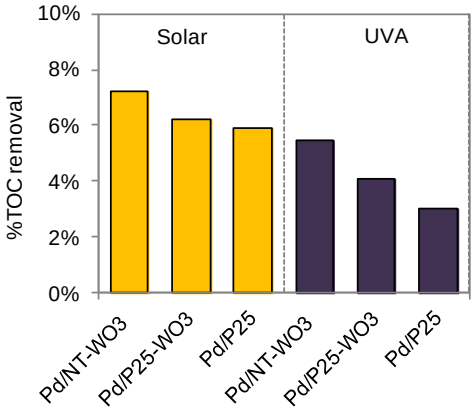

Figure 5.53. TOC removal %. Experimental conditions: catalysts 167 ppm, 600 ml of a water-methanol (50 vol.%) solution under simulated solar light (Xe Lamp, 300 - 800 nm, 250 W/m^2, $I_{250\text{-}450nm}$: 6.5x10^{-4} Einstein/min) and UVA (λ 300 - 400 nm; 4 lamps of 15 W/lamp, $I_{250\text{-}450\ nm}$: 8.3x10^{-5} Einstein/min) at free pH

5.2.2.4. Effect of the pH

The effect of the pH on the H_2 evolution was also studied in a experimental set where the pH of a water-glycerol (5 vol.%) were 2, 5 and 12, adding H_2SO_4,or KOH. The results are shown in Figure 5.54. For three catalysts the H_2 evolution is the highest at natural pH of the solution (pH 5). This experimental set was part of a study about photocatalytic H_2 generation using glycerol, instead of methanol. For Pd/P25 catalyst (Figure 5.54 (a)), the H_2 evolution in the plateau at pH 2, 5 and 12 is 2.1, 4.1 and 1.5 ml/min.gCat, respectively. The worst result is observed under basic conditions. In the case of catalysts containing WO_3, a similar behavior is observed (see Pd/P25-WO_3 in Figure 5.54 (c)). However, the values for H_2 generation under acidic and basic conditions were quite similar.

Concerning the effect of the solution pH on the photocatalytic H_2 generation, in the literature is talked about the identical electric point (IEP) or pH of zero point of charge (pHzpc) of TiO_2, which is the value of pH at which the net charges on the particle surface is zero. For TiO_2, it is 6.25 [120][134][135]. Accordingly to Y. Li, Y. Xie, S. Peng et al. [135], if the pH of solution is lower than 6.25, the TiO_2 surface is positively charged (see Eq. 5.2.2.1) and electrostatic actions can attract anions, which could improve the H_2 generation, but only if the sacrificial agent nature allows its own ionization at the pH value under study. If the pH is too low, what it could happen is that the ionization of the sacrificial agent is inhibited. In this way, the H_2 generation would be affected negatively.

$$TiOH + H^+ \leftrightarrow TiOH_2^+ \qquad pH < 6.25 \quad (5.2.2.1)$$

$$TiOH \leftrightarrow TiO^- + H^+ \qquad pH > 6.25 \quad (5.2.2.2)$$

If the pH solution is higher than 6.25, the TiO_2 surface is negatively charged (see Eq. 5.2.2.2) and electrostatic repulsion inhibit the adsorption of molecules from the sacrificial agent on the catalyst surface. It is important to highlight that the effect of the pH on the photocatalytic H_2 generation varied not only respect to the nature of the sacrificial agent in solution but also on the catalyst nature. For instance, for photocatalysts containing Cu (pHzpc: 6 - 6.5 [176]), the highest H_2 generation is observed under relatively acidic conditions in the solution (pH around 3 or 4) [74][177]. Under these conditions of weak acid pH, there is a higher concentration of protons, therefore a higher availability of solvated e^-. This higher concentration of solvated e^- in solution allows a better reduction of the Cu in solution on TiO_2,

hence, more stable catalyst and as a result is seen a higher H_2 generation on it. But, if this Cu photodeposition in-site is performed under strong acid conditions, a detrimental effect is seen on the catalyst stability. On another hand, on Pt/TiO_2 catalysts it has been observed a higher H_2 generation at pH 10 than at pH 2 or 6 [82]. In this survey, authors explain that at basic solution, the concentration of OH^- physisorbed increase; then, these groups participate in h^+ trapping processes, improving the H_2 generation. Modifying the sacrificial agent from azo-dyes to ethanol and using the same catalyst of Pt/TiO_2, the result of H_2 generation at low pH was different. In ethanol, the H_2 generation was more favored at neutral pH [67].

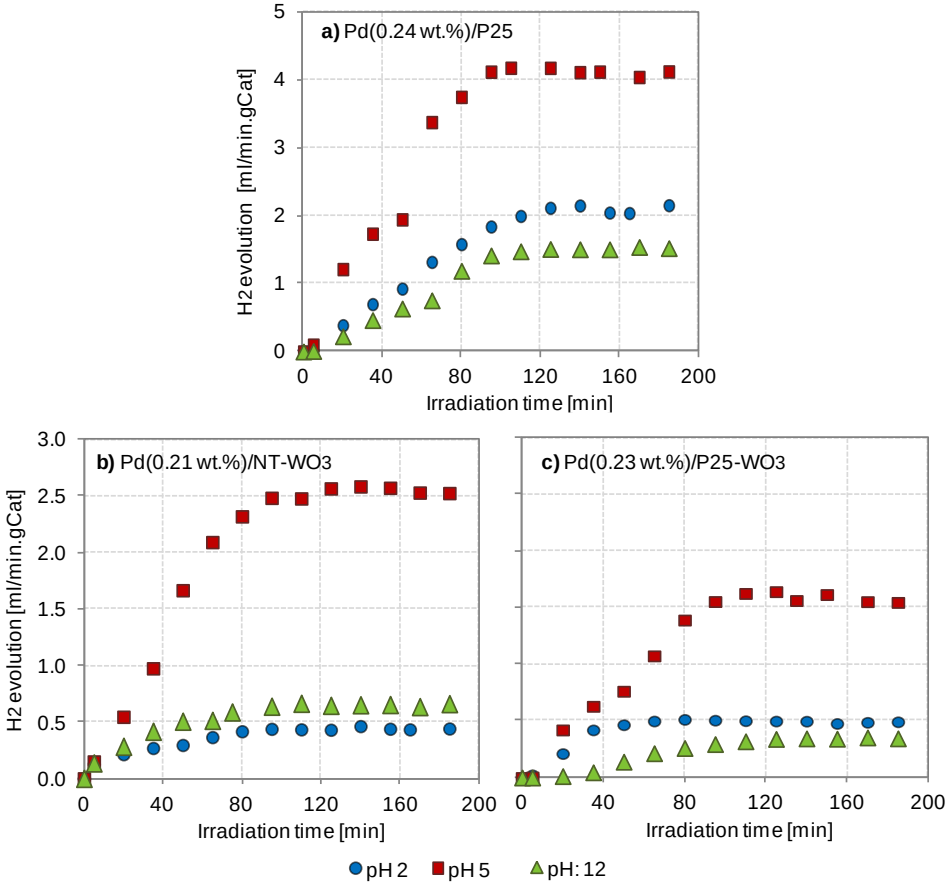

Figure 5.54. Effect of the pH on the H_2 generation for **a)** Pd(0.24 wt.%)/P25, **b)** Pd(0.21 wt.%)/NT-WO_3 and **c)** Pd(0.23 wt.%)/P25-WO_3 catalysts. Experimental conditions: catalyst 167 ppm, 600 ml of water - glycerol mixtures under simulated solar light (Xe Lamp, 300 - 800 nm, 250 W/m^2, $I_{250\text{-}450\ nm}$: 6.5x10^{-4} Einstein/min).

In Au/TiO_2 catalyst [178], the H_2 generation was the highest at pH 7.1 compared to pH 4.9, 2.6 and 13.5. In this study authors pointed that the pH after the photocatalytic reaction was generally lower than before the reaction. One example more is observed when oxalic acid is used to produce H_2 on Pt/TiO_2 [120]. In this latter study, the pH was varied from 2.4 to 6.8 and the highest H_2 production was observed at pH 2.9. Authors say that at different pH, there is a predominant species of the sacrificial agent. Then, some of these species are more reactive than others. If the predominant species is the most reactive one, then the H_2 evolution is higher. All in all, it is observed the adsorption of the sacrificial agent plays an important role on the H_2 generation, and this adsorption depends on many factors such as its own nature and the nature of the catalysts (or the co-catalyst nature). So, a general explanation of the effect of the pH on the H_2 evolution versus the pH is quite difficult because of several parameters can affect this process.

5.2.2.5. Catalysts reuse

This experimental set was also part of a study about photocatalytic H_2 generation using glycerol, instead of methanol. Figure 5.55 shows the H_2 generation in a water-glycerol (5 vol. %) solution on fresh and reused catalysts (two times) for Pd/25, Pd/NT-WO_3 and Pd/P25-WO_3 catalysts. It is seen than that the declining in the H_2 production is more important on the Pd(0.24 wt.%)/P25 catalyst (Figure 5.55 (a)) than on both catalysts containing WO_3. On the fresh Pd(0.24 wt.%)/P25 catalyst, the quantum yield (φ) decreases from 6.9 to 4.1 % after first reuse and decreases again up to 1.9 % after a second reuse. On fresh Pd(0.21 wt.%)/NT-WO_3 and Pd(0.23 wt.%)/P25-WO_3, the decrease of H_2 evolution was lower for reused catalysts.

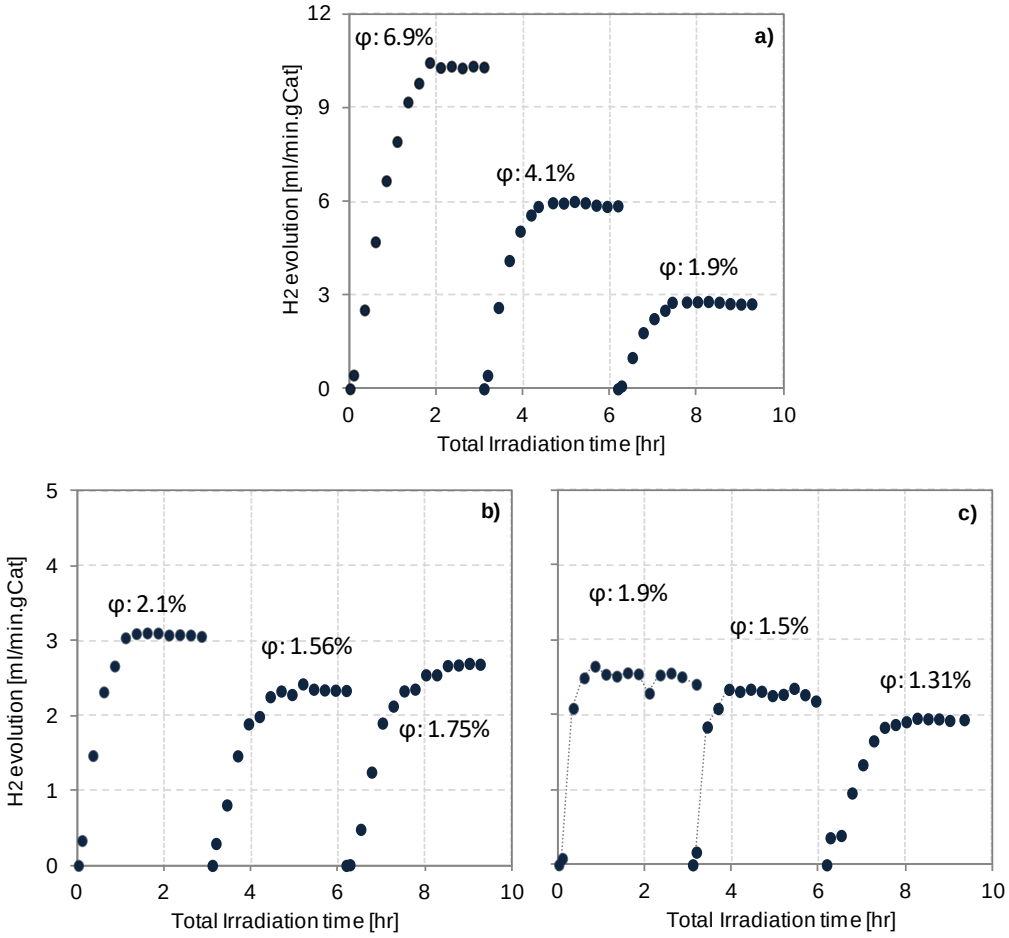

Figure 5.55. H_2 generation after reutilization for **a)** Pd(0.24 wt.%)/P25, **b)** Pd(0.21 wt.%)/NT-WO_3 and **c)** Pd(0.23 wt.%)/P25-WO_3 catalysts. Experimental conditions: catalyst 167 ppm, 600 ml of a water - **glycerol (5 vol.%)** solution under simulated solar light (λ: 300 - 800 nm; 250 W/m^2, $I_{250\text{-}450nm}$: 6.5x10^{-4} Einstein/min).

To explain the decrease in the H_2 evolution over Pd/P25 catalyst, some hypothesis could be considered. From Figure 5.53, it was seen that the %TOC removal was higher on the catalysts containing WO_3 than for Pd/P25. This result can be associated to the presence of WO_3 species, whose contribution might be related to the formation of oxidizing agents such as hydroxide radicals (•OH) [174][175]. The presence of those oxidizing agent on the catalyst surface might lead to produce secondary products that can be deposited on the Pd/TiO_2-WO_3 surface. Although these adsorbed by-products might block the pathway toward the H_2 generation on the Pd surface, on the other hand, they could work as H^+ ion source for the further H_2 generation as it was shown in the Eq. 2.1.6 and 2.1.7, and 2.2.14, 2.2.15. This fact allows to

the catalysts containing WO_3 to have a lower deactivation compared with Pd/P25 catalyst. The absence of an auxiliary oxidizing agent such as WO_3, increase the probability of a faster catalysts surface poisoning (seen for instance in Figure 5.61, 5.62 and 5.63 for catalysts containing Pd or Figure 5.68 for the catalysts containing Pt) and therefore, a faster depletion of the H_2 generation. Consequently, the simultaneous presence of Pd (or in fact Pt) and WO_3 make the catalyst more stable to poisoning, but decreasing the photocatalytic activity toward the H_2 evolution.

5.2.2.6. Catalyst reutilization – Old catalyst

Figure 5.56 shows the H_2 generation in a water-methanol (50 vol. %) solution on fresh (red marks) Pd/P25 catalysts and old Pd/25 catalysts after a photoactivation process. Old means that the catalyst was used one year after having been prepared. The "photoreduction 0 h" sample is the same catalyst called fresh Pd/P25, but one year later of its preparation without any reactivation process. Comparing these two catalysts, it is observed an important decrease in its photoactivity toward the H_2 production. While the H_2 evolution on the fresh catalysts reached the 17.99 ml/min.gCat in its plateau, on the photoreduction 0 h sample scarcely reached 7.23 ml/min.gCat. Around 2.5 times lower than the fresh catalyst.

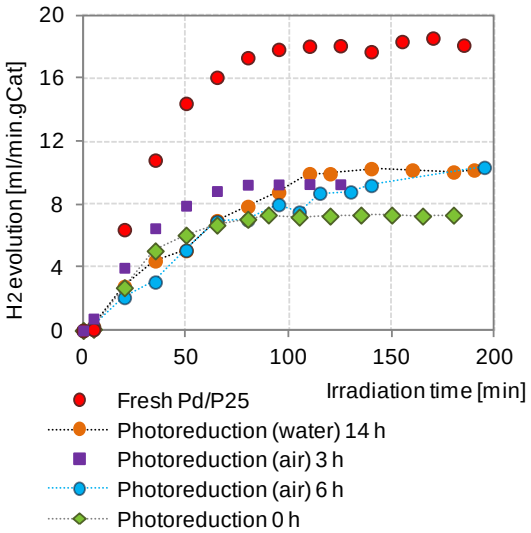

Figure 5.56. H_2 generation after reactivation for "old" Pd(0.24 wt.%)/P25 catalyst. Experimental conditions: catalyst 167 ppm, 600 ml of a water - methanol (50 vol.%) solution under simulated solar light (λ: 300 - 800 nm; 250 W/m^2, $I_{250\text{-}450nm}$: 6.5x10^{-4} Einstein/min).

In order to reactivate this catalyst, it was subjected to different photoreduction processes, all of them under an UV lamp (λ: 365 nm, 6 W). For both photoreduction (air) 3 h and photoreduction (air) 6 h samples, the reactivation consisted in the irradiation for 3 and 6 h, respectively, over the dry catalyst at room conditions, with only the catalyst scattered on a foil dish. For the photoreduction (water) 14 h sample followed the same procedure than for the Pd PD in water. Briefly, 2000 ppm of this catalyst was added to water under continuous stirring and deaerated with Ar for around 1 h before irradiation overnight (around 14 h) and dried at room temperature. As it can be seen in Figure 5.56, any of these reactivation attempts was able to recover the photocatalytic activity of the fresh catalyst. It is observed a slight activity improvement but not important.

In Figure 5.57 is seen the H_2 generation of old catalysts, Pd(0.24 wt.%)/P25, Pd(0.21 wt.%)/NT-WO_3 and

Pd(0.23 wt.%)/P25-WO_3, after 4 reutilizations cycles (blue marks). The red marks is the H_2 generation for the fresh catalysts. For Pd/P25 catalyst, the H_2 evolution in the plateau in every cycle was 7.3, 10.5, 16.9, 11.9 and 10.5 ml/min.gCat. From the first until the third cycle, the H_2 evolution increased. In the third cycle, the H_2 evolution is quite similar to the fresh catalyst (18 ml/min.gCat). This behaviour could be understood as a photoreactivation process. Therefore, after long time of its PD, the Pd, which may have been in contact with oxygen for instance while it was not used, is oxidized. When the catalyst is under irradiation again in the presence of a sacrificial agent, the Pd is reduced and the catalyst recovers its photocatalytic activity. The H_2 evolution in the fourth and fifth cycles indicates a poisoning effect.

In the case of the Pd/NT-WO_3, the profile after every cycle is not easy to understand. Alike Pd/P25 catalyst, the old Pd/NT-WO_3 catalyst in the first cycle is lower than the fresh catalyst as well (4.5 vs. 6.3 ml/min.gCat). However, unlike Pd/P25, the H_2 evolution in second and third cycle is progressively lower (4.0 and 2.7 ml/min.gCat, respectively) and then, in the fourth cycle it increases up to 5.4 ml/min.gCat, decreasing again in the last two cycles to 3.9 and 4.4 ml/min.gCat, respectively. On Pd/P25-WO_3 catalyst, the profile after every cycle is once again very different to the both previous catalysts.

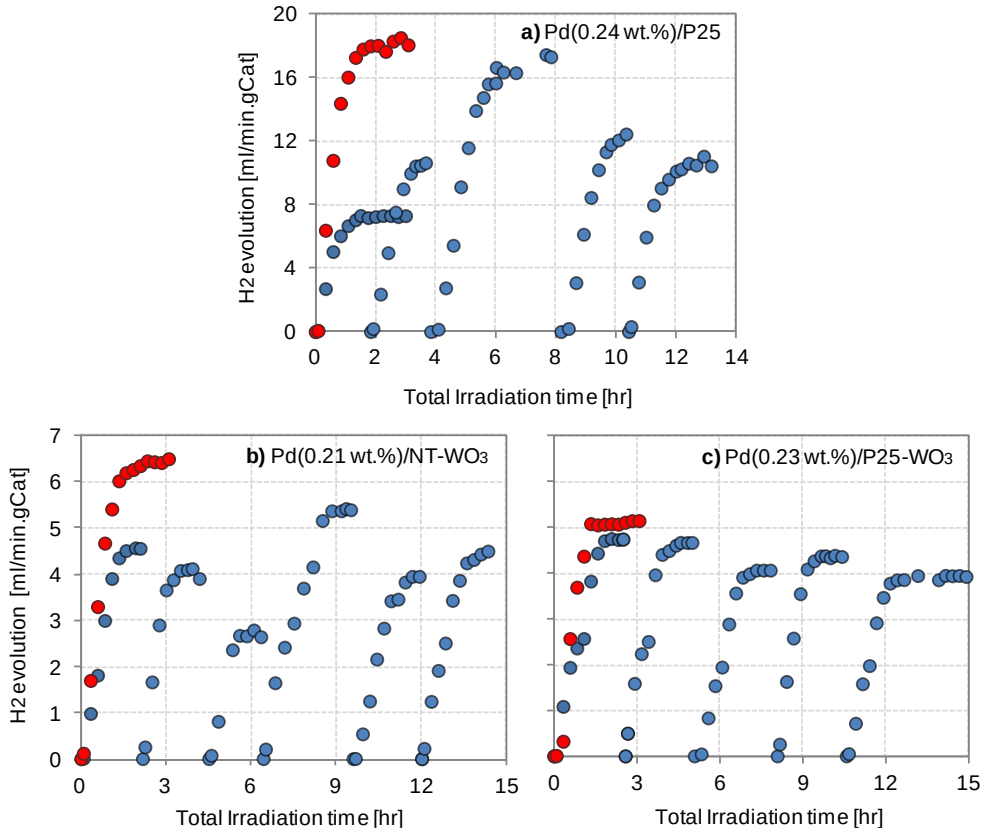

Figure 5.57. H_2 generation after reutilization for "old" catalyst (●). **a)** Pd(0.24 wt.%)/P25, **b)** Pd(0.21 wt.%)/NT-WO_3 and **c)** Pd(0.23 wt.%)/P25-WO_3 catalyst. Experimental conditions: catalyst 167 ppm, 600 ml of a water - methanol (50 vol.%) solution under simulated solar light (λ: 300 - 800 nm; 250 W/m^2, $I_{250\text{-}450nm}$: 6.5x10^{-4} Einstein/min). (●) Fresh catalyst.

On the opposite hand, although in generals terms Pd/P25-WO_3 presents the lowest H_2 evolution, it seems more stable than the other two catalysts in terms of deactivation as it has seen in Figure 5.55 and also in Figure 5.57 (c). Hence, in Figure 5.57 (c) is observed that the H_2 evolution on the old Pd/P25-WO_3 catalyst in the first cycle is quite similar to the fresh one (4.7 vs. 5.1 ml/min.gCat). In the next cycles, the H_2 evolution decreases slightly after each cycle: 4.7, 4.1, 4.4 and 3.9 ml/min.gCat.

5.2.2.7. Pilot plant testing

For H_2 test in the pilot plant (PPS-system), the optimal experimental conditions, accordingly to previous work performed in the same system were: catalysts 200 ppm in 25 L [33][103]. In this experimental set were used aqueous solutions of methanol (0.2, 0.37 and 5 vol.%) and glycerol (0.37 and 5 vol.%), and municipal wastewater under solar light for around 6 hours.

For all the catalysts tested in this system, the Pd was deposited by PD 2m10 method. H_2 evolution vs. accumulated solar UV energy per reactor volume unit, (Q (kJ/L)), in water-methanol or glycerol solutions is presented in Figure 5.58 (a). The accumulated solar UV energy was described in Eq. (4.8.3.1). Each point corresponds to every hour of irradiation. In this figure, it is possible to see three different concentrations of methanol or glycerol (5, 0.37 and 0.2 vol.%) for Pd/P25 and 0.37 vol.% for both Pd/TiO_2-WO_3 based catalysts.

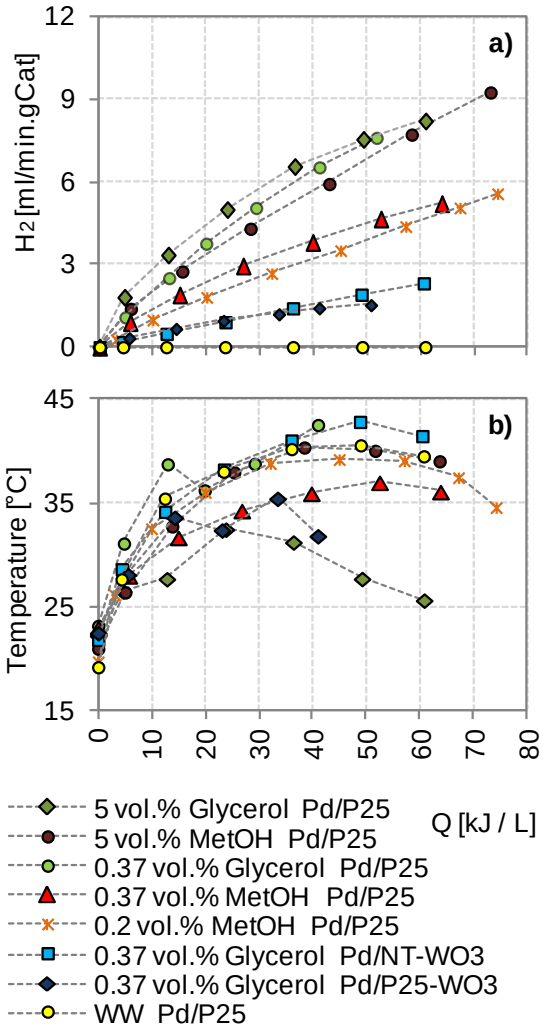

Figure 5.58. H_2 evolution vs. accumulated solar UV energy for Pd/TiO_2(-WO_3) catalysts. Experimental conditions: catalysts 200 ppm in 25 L in water-methanol (or glycerol) solution under solar light. WW: municipal wastewater from Almería, Spain

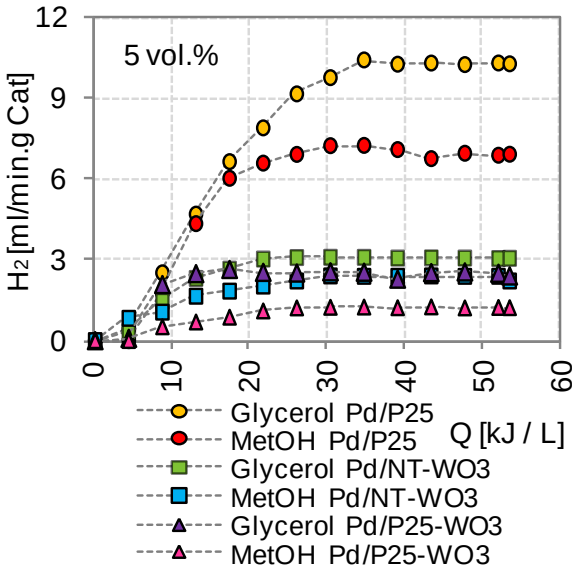

Figure 5.59. H_2 evolution vs. accumulated solar UV energy in the SSL-system. Experimental conditions: catalysts 167 ppm in 0.6 L under solar simulated light (λ: 300 - 800 nm; 250 W/m^2, $I_{250\text{-}450nm}$: 6.5x10^{-4} Einstein/min)

Comparing the effect of methanol concentration, the higher it is, the higher the H_2 generation. This outcome might be explained by the fact that methanol molecules act as h^+ scavenger in the surface of the catalytic support, therefore, the more methanol is added, the higher the probability of photogenerated

h^+ to be trapped by the organic compounds. As a result, photo excited e^- are more easily trapped by Pd, increasing the lifetime of the e^-/h^+ pair and increasing the H_2 generation. This fact could be explained looking at Figure 5.58 (b), which shows the temperature profile of the gas phase of the reactor vs. Q (kJ/L). It is possible to see that for the test at 5 vol.% glycerol, the temperature starts to decrease after 15 kJ/L, and comparing to the H_2 evolution (Figure 5.58 (a)), ca. at the same moment, it also decreases. This result could be explained by the fact that either the PPS-system or the catalyst under these experimental conditions is very sensitive to the temperature. A further study was performed to clarify this point in Figure 5.59.

In Figure 5.59, some additional tests performed at lab scale in the SSL-system are presented, where H_2 evolution was found to be higher with 5 vol.% glycerol than methanol. Although more complex molecules involve more difficult and longer oxidation mechanism, which would lead to lower capture of h^+ by glycerol and higher probabilities in e^-/h^+ recombination. Probably the higher oxidation state of its two methyl carbons (-1), compared to the only one in the methanol structure (-2), make glycerol possible to be oxidized easily by the photogenerated h^+, increasing the number of e^- available for further reaction on the Pd surface. Similar results can be found in the literature [33][125].

Concerning the H_2 evolution when municipal wastewater (WW) was used, it scarcely reached 0.003 ml/min.gCat. Table 11 shows the main physicochemical characteristics of the municipal wastewater, before and after the reaction. The low H_2 evolution using wastewater as source of electron donors is understandable due to the fact of the high impurities loads and metals that poison the catalyst by adsorption of all these compounds. In our previous study [179], H_2 tests were performed using water-methanol solutions prepared by milli-Q or tap water. It was clearly observed the decrease in the H_2 evolution when tap water was used in the photoreaction.

Table 11. Physicochemical characteristic of the wastewater during the photocatalytic H_2 generation.

time [h]	TOC mg/L	pH	σ mS/cm	Na [ppm]	NH_4+ [ppm]	K [ppm]	Mg [ppm]	Ca [ppm]	Cl^- [ppm]	Br^- [ppm]	PO_4^{3-} [ppm]	SO_4^{2-} [ppm]
0	109.2	7.5	2.37	262.1	100.4	29.3	50.3	95.8	421.3	2.5	11.1	99.1
1	105.8	7.5	2.20	-	-	-	-	-	-	-	-	-
2	104.2	7.7	2.09	-	-	-	-	-	-	-	-	-
3	103.5	7.8	2.14	256.9	99.2	28.7	49.6	92.5	413.3	2.6	9.1	91.5
4	102.9	7.7	2.13	-	-	-	-	-	-	-	-	-
5	100.2	7.6	2.30	-	-	-	-	-	-	-	-	-
6	99.7	7.7	2.13	253.7	96.9	27.8	48.7	87.9	409.6	2.5	8.4	91.2
	8.7%		10.1%	3.2%	1.2%	2.1%	3.3%	8.3%	2.8%	0.4%	18.6%	7.9%

* Experimental conditions: 200 ppm of the Pd(0.24 wt.%)/P25 catalyst in 25 L under solar light. WW: municipal wastewater from Almería, Spain. Free pH
Na: sodium; NH_4+; K: potassium; Mg: magnesium; Ca: calcium; Cl^-: chlorides; Br^-: bromides, PO_4^{3-}: phosphates; SO_4^{2-}: sulphates

The last grey row from Table 11 shows the TOC and some other physicochemical characteristic TOC removal (%) of the wastewater. Since TOC removal from Table 11 (8.7%) is similar in values to the TOC removal results presented in Figure 5.53, the H_2 evolution for WW on Pd/P25 catalyst (yellow points in

Figure 5.58) is not nearly comparable to those presented in Figure 5.48, due to H_2 evolution in Figure 5.58, scarcely reached to 0.003 ml/min.gCat. Although PPS-system did not reach to temperatures higher than 50 °C, in the WW were dissolved inorganic solids like sodium, calcium and sulphates that were adsorbed on the catalysts. Their removal between 3 and 8% (3.2, 8.3 7.9 % for sodium, calcium and sulphates, respectively) could be attribute to their adsorption on the catalysts surface.

These results demonstrate the challenges to overcome the photocatalytic H_2 generation by using wastewater treatment, which is mainly affected by the high concentration of impurities that could compete with the generation of H_2 or produce some deactivation of the catalyst by adsorption.

5.2.2.8. Summary and specific conclusions for m-Pd/TiO_2(-WO_3)-CATHETER Lab catalysts

In Table 12 are given some generals conclusions about the effect of the experimental conditions studied on the H_2 evolution in CATHETER Lab. Similar to the previous section, some additional analysis were performed in order to see if there is any relationship between S_{BET}, Pd PD method, E_g and Total V_{PORE}, with the H_2 evolution. In Figure 5.60 is shown the H_2 evolution for m-Pd/TiO_2(-WO_3) - CATHETER Lab catalysts vs. S_{BET}, where is also shown some information about Eg (eV) (colour) and the Total V_{PORE} (smaller figure in Figure 5.60).

Table 12. Specific conclusions for m-Pd/TiO_2(-WO_3) - CATHETER Lab catalysts on the H_2 evolution

Effect of experimental conditions	
Photodeposition method	For Pd/P25 catalysts, after in situ Pd photodeposition, the photodeposition 2m10 method showed the highest H_2 evolution (ml/min.gPd), that is near the results obtained by the photodeposition 4m10 and 2m5 methods. The wetness impregnation was in fourth place. For Pd/NT-WO_3 and Pd/P25-WO_3 catalysts, the in situ Pd photodeposition also showed the highest H_2 evolution, followed by the photodeposition 2m10 and 4m10 methods.
	The very low H_2 evolution on only Pd reveals the importance of a catalytic support for metal nanoparticles for the photocatalytic H_2 generation.
	In the photodeposition process, it seems to exist an optimal gCat/L MetOH ratio around 20, where the catalysts prepared under this ratio presented a higher H_2 evolution. However, we consider that this is not the unique parameter involved in the process of synthesizing a more efficient catalyst toward the H_2. The additional ratio might be the photon flux to gram of catalyst ratio (einstein.min^{-1}/ gCat), but this ratio was not demonstrated in this study.
Amount of Pd photodeposited	For three Pd/P25, Pd/NT-WO_3 and Pd/P25-WO_3 -2m10 catalysts, a local optimal Pd load was observed around 0.25 wt.%, in which H_2 evolution was the highest, followed by 0.5 and then 0.1 wt.% of Pd photodeposited.
Light source	Photocatalytic H_2 generation was higher under UVA than solar light.
pH	Natural pH showed the highest H_2 evolution on the three catalysts studied (Pd/P25, Pd/NT-WO_3 and Pd/P25-WO_3 -2m10). The worst H_2 evolution was observed at pH 2 for both catalysts containing P25 but on the catalysts containing the TiO_2 nanotubes (NT), the hydrogen evolution was the worst at pH 12.
TOC removal	Total organic carbon removal was higher under solar than UVA light.
Sacrificial agent nature	In both, PP-system (25 L) and SSL-system (600 ml), the H_2 evolution was higher in the water - glycerol solution than in water - methanol solution at the same concentration (vol.%) of sacrificial agent.

Respect to the S_{BET}, in Figure 5.60 is seen that data agglomerates in three zones, corresponding each zone to every group of catalysts, Pd/P25 (✖), Pd/NT-WO_3 (●) and Pd/P25-WO_3 (▼). Therefore, Pd/P25 and Pd/P25-WO_3 catalysts are located at around 60 m^2/g of S_{BET}, but Pd/P25 catalysts showed higher H_2 evolution (13 - 19 ml/min.gCat) whereas the Pd/P25-WO_3 showed the lower (4 - 6 ml/min.gCat). On the other hand, Pd/NT-WO_3 catalysts are located at higher values of S_{BET} compared to Pd/P25 and Pd/P25-WO_3 catalysts, but showing a lower H_2 evolution (5 - 7 ml/min.gCat) than Pd/P25. Not any strong

tendency is observed in Figure 5.60, but Pd/P25 catalysts seems to be more sensitive to the variation in the Pd amount. This fact can see from the wider range of H_2 evolution for Pd/P25 catalysts.

Furthermore, Pd/NT-WO_3 and Pd/P25-WO_3 showed similar H_2 evolution, even for catalysts with different Pd amount. Regards to the band-gap (represented by the colour bar in Figure 5.60, where the yellowish marks represent narrower and the reddish the wider band-gap), the Pd/NT-WO_3 catalysts that showed the narrowest band-gap, they did not present the highest H_2 evolution. It is considered that high S_{BET} and narrow band-gap are advantage characteristics of (photo)catalytic materials, but this not the case for Pd/P25 catalysts, which, controversially, showed, by far, a higher H_2 evolution than Pd/NT-WO_3, even having a much lower S_{BET} and lower band-gap value.

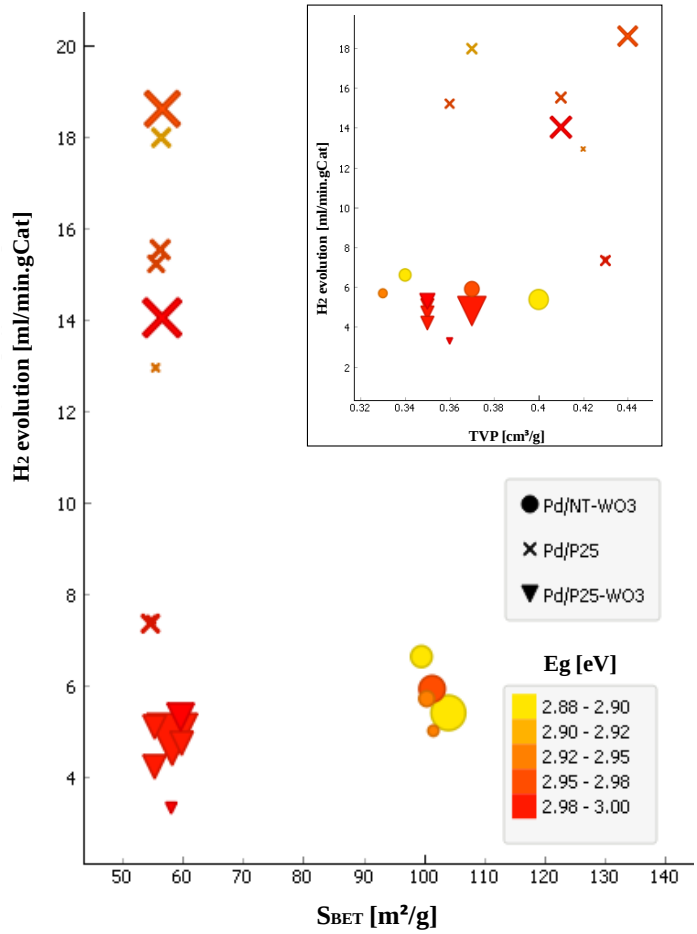

Figure 5.60. Data exploration for H_2 evolution for m-Pd/TiO_2(-WO_3) - CATHETER Lab catalysts related to S_{BET} [m^2/g] and VPT [cm^3/g]. band-gap (E_g, eV, **colour**), catalysts nature (**shape**) and amount of Pd [wt.%] (size). Experimental conditions: catalysts 167 ppm, 600 ml of water - methanol (50 vol.%) solutions under simulated solar light (Xe Lamp, 300 - 800 nm, 250 W/m^2, $I_{250\text{-}450\ nm}$: 6.5x10^{-4} Einstein/min).

In terms of TVP (smaller picture in Figure 5.60), for Pd/P25 catalysts, it seems the higher the TVP, the higher the H_2 evolution. On catalysts containing WO_3, this tendency is not clear. For instance, Pd/NT-WO_3 catalysts have TVP values from 0.33 to 0.4 cm^3/g, but the H_2 evolution hardly changed from around 6 ml/min.gCat. On the other side, TVP values for Pd/P25-WO_3 catalysts were between 0.35 - 0.37 cm^3/g, and the H_2 evolution scarcely varied.

5.2.2.9. Effect of the amount of catalyst and methanol concentration in the SS-system

H_2 tests in the SS-system with m-Pd/TiO_2(-WO_3) - CATHETER Lab catalysts are shown in this section. Therefore, the initial tests during the stay in PCS Lab correspond to the H_2 evolution in SS-system varying the catalyst and methanol concentrations with Pd/P25, Pd/NT-WO_3 and Pd/P25-WO_3 catalysts prepared in CATHETER Lab. From these results, it is possible to compare as well the H_2 evolution set up taking into account the quantum efficiency (ϕ) as it is explained afterwards in section 5.3.

Figure 5.61 (a - c) shows the H_2 evolution for Pd/NT-WO_3, Pd/P25-WO_3 and Pd/P25 catalysts for different catalysts concentration (200, 500, and 1000 ppm) and Figure 5.61 (d) shows a comparison of the three catalysts at their maximum H_2 evolution.

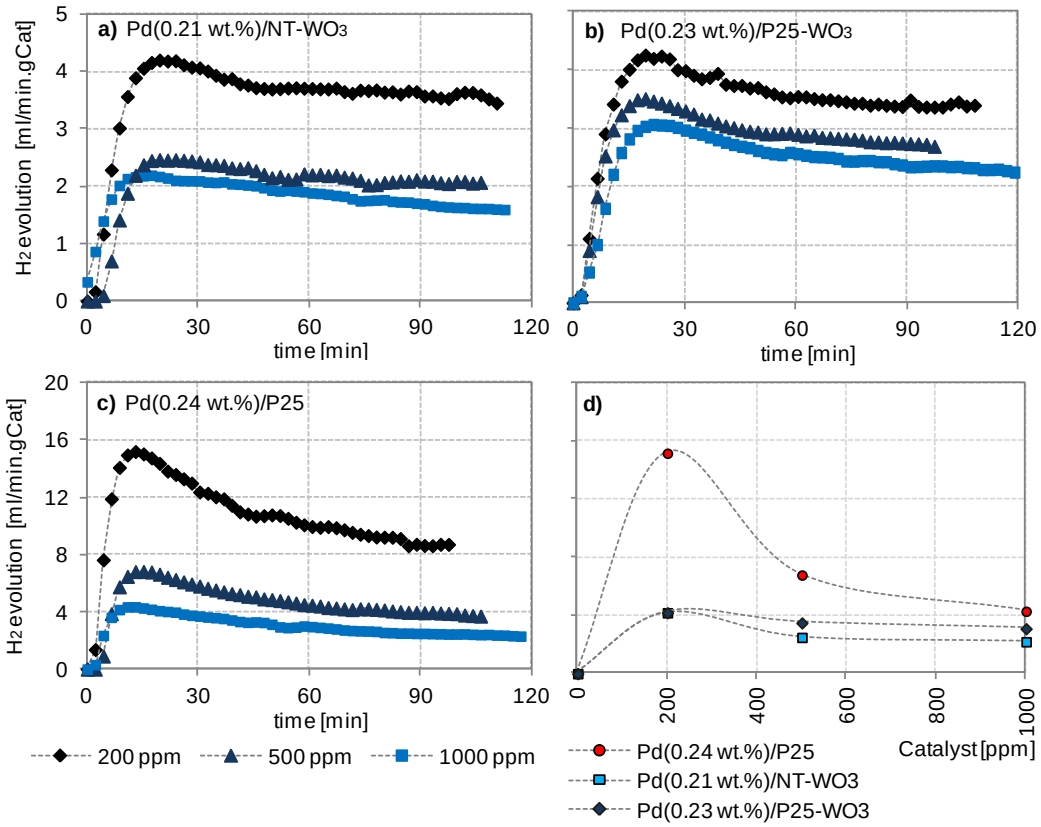

Figure 5.61. Effect of catalyst concentration on the H_2 generation for **a)** Pd/NT-WO_3, **b)** Pd/P25-WO_3 and **c)** Pd/P25 - CATHETER Lab catalysts in the SS system. Experimental conditions: water - methanol (50 Vol.%) solutions. Irradiation: Optical fiber UV/Vis-Emission: ca. 8W/cm^2 (280 - 700 nm), $I_{250-450nm}$: 3.88x10^{-5} Einstein/min.

For these catalysts, it is observed an optimal catalyst concentration around 200 ppm .This result corroborates the previous results where it was found 167 ppm and 200 ppm, as well, as the optimal catalyst concentration in the SSL-system and UVA-system, and the PPS-system. Regarding the H_2 evolution profiles versus time in SS-system, Pd/NT-WO_3, Pd/P25-WO_3 and Pd/P25 catalysts showed and initial period of induction for around 20 min for both catalysts containing WO_3 and around 13 min for Pd/P25. After this induction period, the H_2 evolution reaches a maximum value and then decreases slightly. In the case of 200 ppm of Pd/P25, the decrease seems slightly more pronounced as it can be observed in Figure 5.61 (c). This pronounced induction period for H_2 evolution than the observed in sections 5.2.1 and 5.2.2 (Figures 5.34 - 5.44) might be attributed to two different facts: (i) the smaller scale of the SS-system ($\tau_1 \approx 10\ \mathrm{min}$) compared to the SSL-system ($\tau_2 \approx 25\ \mathrm{min}$) and the UVA-system

($\tau_2 \approx 10$ min), where the smaller reaction volume, decreases the residence time, reaching faster the H_2 evolution plateau and (ii) the more powerful lamp in PCS Lab (Optical fiber UV/Vis-Emission: ca. 8W/cm^2 (280 - 700 nm), $I_{250\text{-}450nm}$: 3.88x10^{-5} Einstein/min.) might promote a faster reduction of the oxidized Pd.

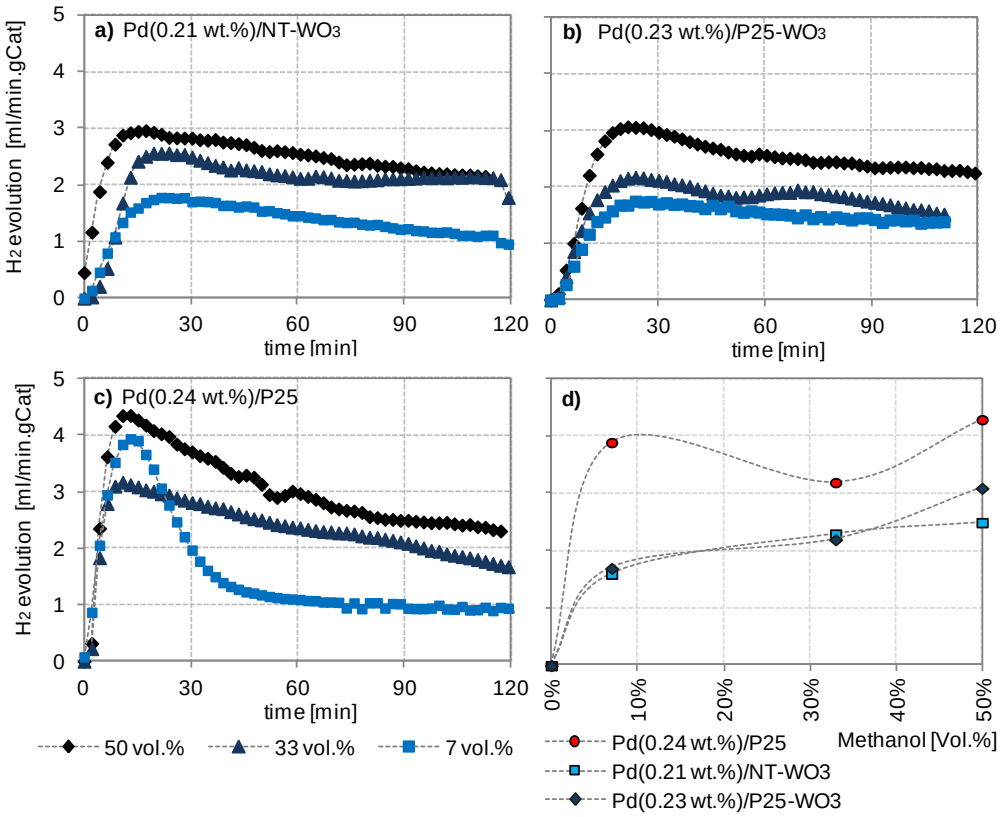

Figure 5.62. Effect of methanol concentration on the H_2 generation for **a)** Pd/NT-WO_3, **b)** Pd/P25-WO_3 and **c)** Pd/P25 - CATHETER Lab catalysts in the SS system. Experimental conditions: catalysts 1000 ppm, 15 ml of water - methanol solutions. Irradiation: Optical fiber UV/Vis-Emission: ca. 8W/cm^2 (280 - 700 nm), $I_{250\text{-}450nm}$: 3.88x10^{-5} Einstein/min.

Figure 5.62 presents the effect of methanol concentration on the H_2 evolution. It is observed, similar in previous results, that the concentration of methanol corresponding to 50 vol.% showed the highest H_2 evolution (among the concentration studied). In Figure 5.62 is easily observable the decrease in H_2 evolution after the induction period for Pd/P25 catalyst at the lowest methanol concentration (7 vol.%).

5.2.3. m-Pd/TiO_2(-WO_3) - PCS Lab catalysts

In this section, H_2 tests in the SS-system were performed using m-Pd/TiO_2(-WO_3) - PCS Lab catalysts. The influence of the Pd deposition method on the photocatalytic H_2 evolution, but comparing in this case, the Pd PD method follows by the PCS group (-3.2m20) with ours (-2m10) was studied. Additionally, in this section is shown some other results corresponding to possible by-products that are also obtained in the photocatalytic H_2 generation in the SS-system.

5.2.3.1. Effect of Pd photodeposition method

In Figure 5.63 is shown the H_2 evolution for Pd/NT-WO_3, Pd/P25-WO_3 and Pd/P25 catalysts prepared by two different PD method: 3.2m20 and 2m10 in PCS Lab. Similar to the CATHETER-Lab catalysts in Figures 5.61 and 5.62, the catalysts prepared in PCS Lab also showed H_2 evolution profiles with a maximum H_2 evolution at around 15 - 20 min for both catalysts containing WO_3, and 10 - 15 min for

Pd/P25, before observing a short induction period. After the maximum H_2 evolution, it decreased more slightly for some catalysts (catalysts containing 2 wt.% of Pd), and more pronounced for some others catalysts containing the lowest Pd load (0.25 wt.%). For Pd/NT-WO_3 catalysts, the catalyst Pd(0.19 wt.%)/NT-WO_3-2m10 showed the highest H_2 evolution, around 3.1 ml/min.gCat as its maximum value of H_2 evolution and 1.9 ml/min.gCat at the end of the irradiation time. The worst result was observed for the catalyst Pd(2 wt.%)/NT-WO_3-3.2m20* catalyst, though this latter presents a more steady plateau (1.4 and 1.1 ml/min.gCat as its maximum H_2 evolution and at the end of irradiation, respectively). In case of Pd/P25-WO_3 catalysts, there are no significant difference between all catalysts, even in their maximum H_2 evolution and at the end of the reaction (at around 2.0 and 1.5 ml/min.gCat, respectively).

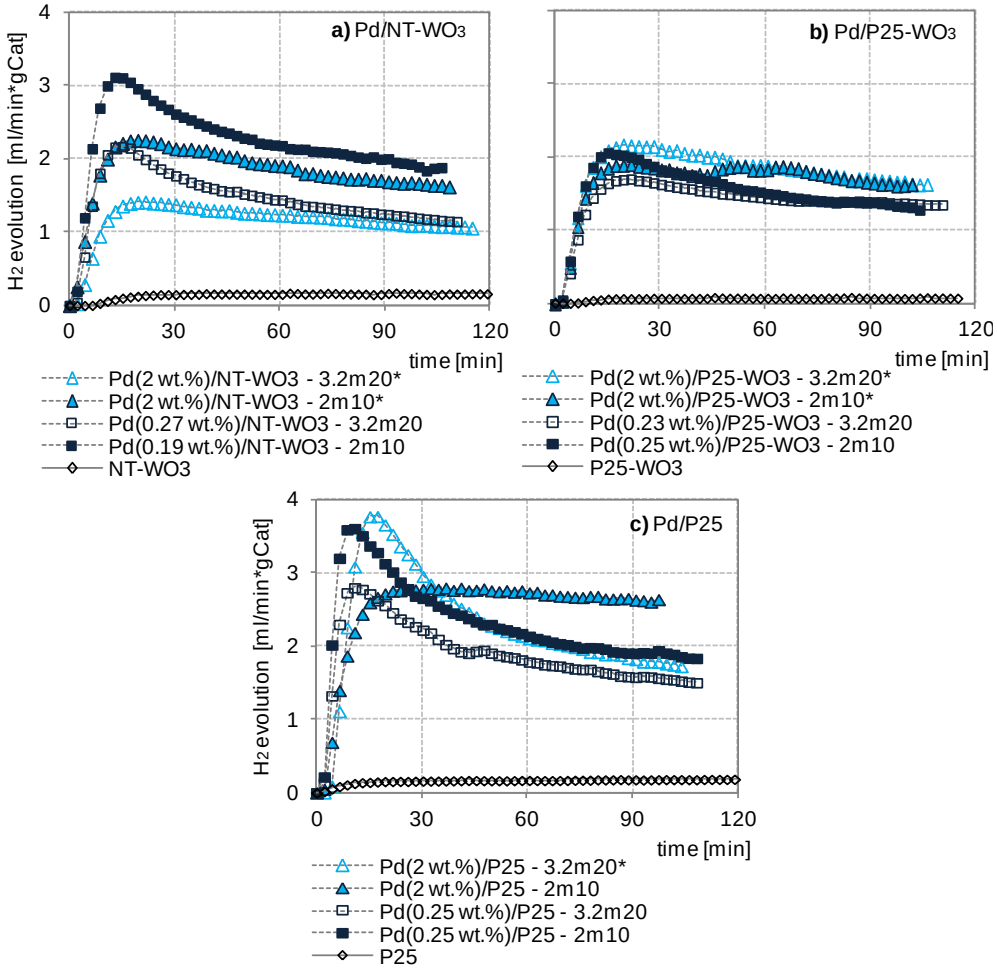

Figure 5.63. Effect of Pd photodeposition method on the H_2 generation for **a)** Pd/NT-WO_3; **b)** Pd/P25-WO_3 and **c)** Pd/P25 -PCS Lab catalysts in the SS-system. Experimental conditions: catalysts 167 ppm, 600 ml of a water - methanol (50 vol.%) solution. Irradiation: Optical fiber UV/Vis-Emission: ca. 8W/cm^2 (280 - 700 nm), $I_{250-450nm}$: 3.88x10^{-5} Einstein/min.* indicates the nominal Pd value

For Pd/P25 catalysts is possible to observe more differences in their H_2 evolution profiles, where three Pd(0.25 wt.%)/P25 - 2m10, Pd(2 wt.%)/P25 - 3.2m20* and Pd(0.25 wt.%)/P25 - 3.2m20 catalysts showed similar profile, short induction period, a maximum point in the H_2 evolution and then a constant decrease along the irradiation time. The two first showed the highest H_2 evolution while Pd(0.25 wt.%)/P25 - 3.2m20 catalyst showed the worst result for the H_2 evolution. On the other hand, Pd(2 wt.%)/P25 - 2m10 showed a totally different H_2 evolution profile, where after the induction period is seen a steady plateau (2.7 ml/min.gCat).

All in all, from the results observed in Figure 5.63 is possible to say that 2m10 method seems to have produced catalysts with higher H_2 evolution for three group of catalysts Pd/NT-WO_3, Pd/P25-WO_3 and Pd/P25. Additionally, comparing the amount of metal, increasing the Pd content up to 2 wt.% did not generate catalysts with any important higher activity towards H_2, as it was already concluded in section 5.2.2.

5.2.3.2. CO_2 and CO generation

Figure 5.64 - 5.65 show the H_2 evolution, in the blue and right axis as mol/min.gCat, together with the CO_2 and CO generation, in the red and left axis as mol/min.gCat, for Pd/P25, Pd/NT-WO_3 and Pd/P25-WO_3 prepared by 3.2m20 and 2m10 methods, using 2 and 0.25 wt.% of Pd.
For the three groups of catalyst, the H_2 evolution was two order of magnitude higher than the CO_2 and CO evolution was much lower that the CO_2. For both CO_2 and H_2 the evolution profile is quite similar where it is observed an induction period at the beginning of the reaction, a maximum value of CO_2 or H_2 evolution and finally, a decreasing plateau for Pd/P25 and Pd/NT-WO_3 catalysts. For Pd/P25-WO_3 catalysts (Figure 5.66), the plateau did not decrease as much as the other two catalysts.

Quite surprisingly, on this experimental set, the CO_2 and CO evolution were higher on Pd/P25 catalyst than on the catalyst containing WO_3. These results are opposite to those shown in section 5.2.2.3, Figure 5.53, where was seen that Pd/P25 catalysts presented the lowest %TOC removal. In Figure 5.64, the CO_2 evolution on Pd/P25 catalysts was around $4x10^{-6}$ - $6x10^{-6}$ mol/min.gCat in the plateau, whereas for Pd/NT-WO_3 (Figure 5.65) and Pd/P25-WO_3 (Figure 5.66), it was around $1x10^{-6}$ - $3x10^{-6}$ and $5x10^{-7}$ - $8x10^{-7}$ mol/min.gCat, respectively. To compare to the most known H_2/CO_2 molar ratio for the photoreforming process that is around 3 (check Eq. 2.2.3, described by Patsoura et al. [67]), in Table 13 is shown the H_2/CO_2 molar ratio for these catalysts. These numbers were determined by using the average of CO_2 and H_2 evolution in the plateau. From Table 13 we can see that the H_2/CO_2 molar ratios are far away from the value shown in literature (3). On Pd/P25 catalyst this molar ratio is the lowest, whereas Pd/P25-WO_3 catalysts showed the highest H_2/CO_2 molar ratios. Accordingly to these results, we consider that very few of the produced H_2 comes from a real photoreforming process of the alcohol.

This fact can be explained considering the chemical reaction exposed in section 2.2.2 to try to glimpse a reaction mechanism related to the photocatalytic H_2 generation. For instance, the mechanism explained by Bahruji et al. [96] in Eqs. (2.2.4) - (2.2.6), involves the oxidation of water molecules in the VB to produce •OH radicals, which attack organic molecules by abstracting an alpha hydrogen and forming at the end aldehydes (Eq. 2.2.6). Some competitive reactions for methyl groups (Eq. 2.2.7 and Eq. 2.2.8), where in Eq. 2.2.8 is shown the photoreforming of methyl groups toward CO_2 and H_2, can also be produced. On the other hand, Strataki et al. [110] and Husin et al. [111] explained that H^+ ions can be generated from both, water (Eqs. 2.2.4 or Eq. 2.2.9) and alcohol (Eq. 2.2.10), that can be later reduced on metal sites by photogenerated e^- in the CB to produce H_2 (Eq. 2.2.11). Romão et al. [81] explained the final formation of CO_2 as a longer pathway from the alcohol with intermediary products such as formaldehyde (Eq. 2.2.13) and formic acid (Eq. 2.2.14) to produce also H_2.

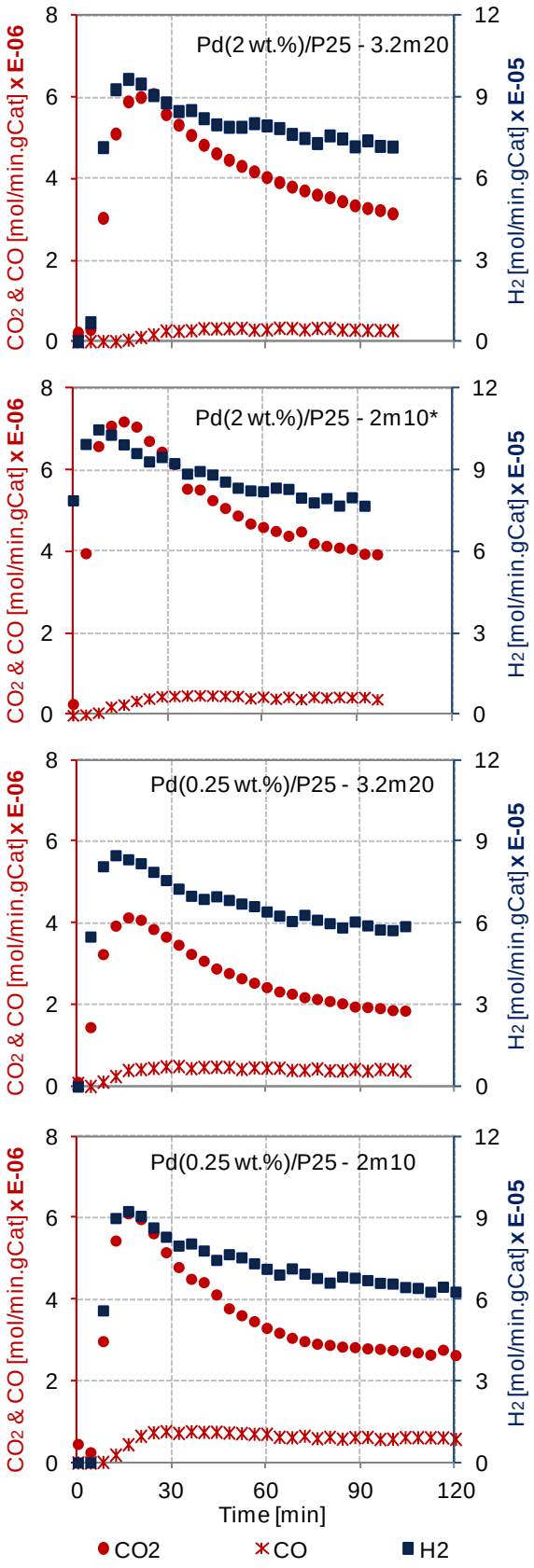

Figure 5.64. H_2, CO_2 and CO generation for Pd/P25 - PCS Lab catalysts. Experimental conditions: catalysts 1000 ppm, 15 ml of a water - methanol (50 vol.%) solution. Irradiation: Optical fiber UV/Vis-Emission: ca. 8W/cm^2 (280 - 700 nm), $I_{250\text{-}450nm}$: 3.88x10^{-5} Einstein/min.

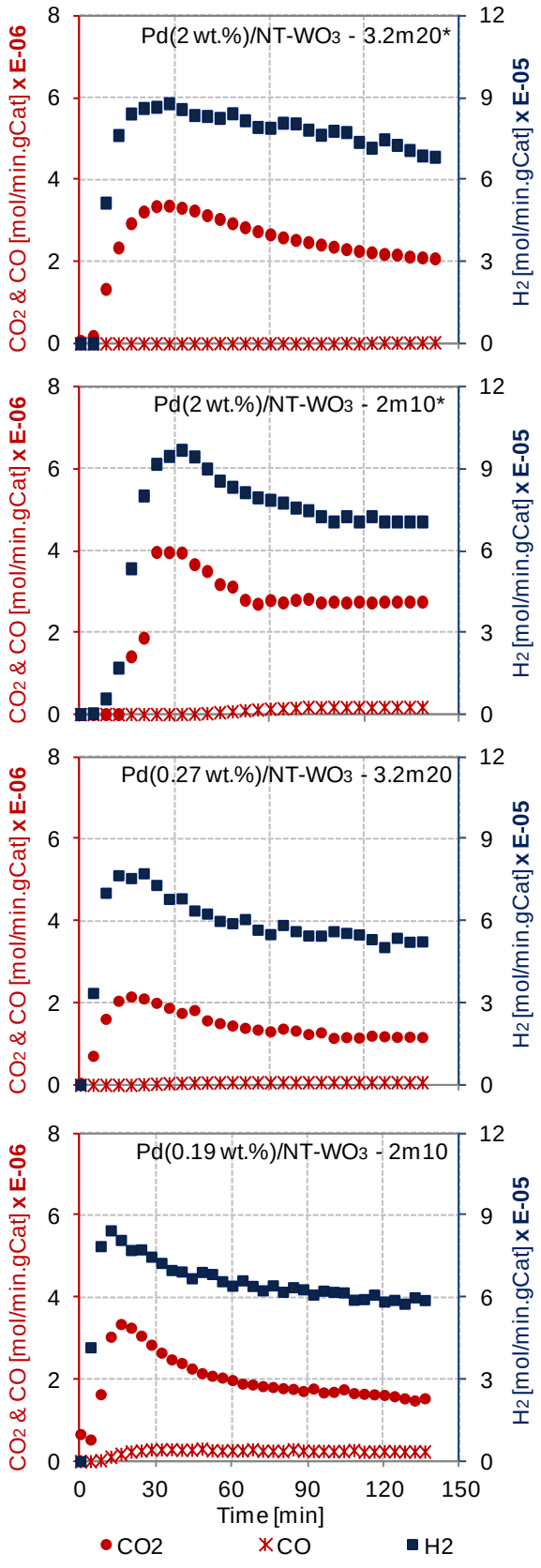

Figure 5.65. H_2, CO_2 and CO generation for Pd/NT-WO_3 - PCS Lab catalysts. Experimental conditions: catalysts 1000 ppm, 15 ml of a water - methanol (50 vol.%) solution. Irradiation: Optical fiber UV/Vis-Emission: ca. 8W/cm^2 (280 - 700 nm), $I_{250\text{-}450nm}$: 3.88x10^{-5} Einstein/min

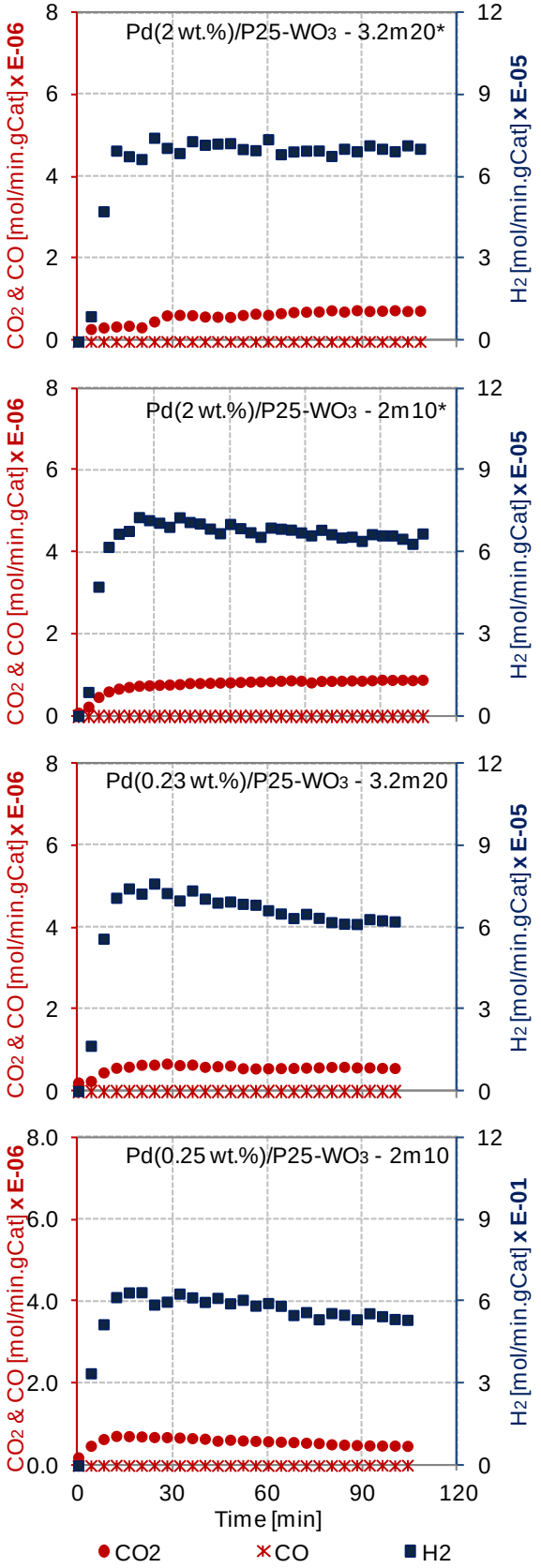

Figure 5.66. H_2, CO_2 and CO generation for Pd/P25-WO_3 - PCS Lab catalysts. Experimental conditions: catalysts 1000 ppm, 15 ml of a water - methanol (50 vol.%) solution. Irradiation: Optical fiber UV/Vis-Emission: ca. 8W/cm^2 (280 - 700 nm), $I_{250\text{-}450nm}$: 3.88x10^{-5} Einstein/min.

Table 13. H_2/CO_2 molar ratio for $Pd/TiO_2(-WO_3)$ - PCS Lab catalysts

Catalyst (Pd nominal)	H_2 (mol/min.gCat)	CO (mol/min.gCat)	CO_2 (mol/min.gCat)	H_2/CO_2 molar ratio
Pd(2 wt.%)/P25 - 3.2m20	8 x10-5	3 x10-7	4 x10-6	20
Pd(2 wt.%)/P25 - 2m10	9 x10-5	4 x 10-7	5 x10-6	18
Pd(0.25 wt.%)/P25 -3.2m20	7 x10-5	4 x10-7	3 x 10-6	23
Pd(0.25 wt.%)/P25 -2m10	7 x10-5	7 x10-7	4 x10-6	18
Pd(2 wt.%)/NT-WO_3 - 3.2m20	8 x10-5	0	3 x10-6	27
Pd(2 wt.%)/NT-WO_3 - 2m10	8 x10-5	1 x10-7	3 x10-6	27
Pd(0.25 wt.%)/NT-WO_3 - 3.2m20	6 x10-5	6 x10-8	1 x10-6	60
Pd(0.25 wt.%)/NT-WO_3 - 2m10	6 x 10-5	1 x10-6	2 x10-6	30
Pd(2 wt.%)/P25-WO_3 - 3.2m20	7 x10-5	0	7 x10-7	100
Pd(2 wt.%)/P25-WO_3 - 2m10	7 x10-5	0	8 x10-7	88
Pd(0.25 wt.%)/P25-WO_3 - 3.2m20	7 x10-5	0	6 x10-7	117
Pd(0.25 wt.%)/P25-WO_3 - 2m10	6 x10-5	0	6 x10-7	100

Although this previous explanation seems to be the most probable, we do not really know if more, or much more of the produced CO_2 moles are being strongly adsorbed on the catalysts. This latter fact could explain the progressive poisoning of the catalysts observed by the decreasing plateau (more pronounced in the SS-system, probably due to the more powerful lamp used in this system compared to the other light sources).

On the other hand, the lowest H_2/CO_2 molar ratios observed on Pd/P25, might suggest that on Pd/P25 catalysts, more H_2 is produced by photoreforming than on Pd/NT-WO_3 and Pd/P25-WO_3 catalysts. Therefore, connected to this second hypothesis, the higher mol H_2/mol CO_2 ratios for catalysts containing WO_3 than on Pd/P25 catalysts may be understood as much more CO_2 molecules strongly adsorbed on these catalysts (proportional to their respective H_2 evolution). This hypothetical CO_2 adsorbed (and not seen in the detector) might explain the fact of the already discussed higher %TOC removal on the catalyst containing WO_3. WO_3 species could promote, not only a higher mineralization of organic compounds, but also could lead to a higher CO_2 adsorption (or other by-products) on the catalyst. Consequently, the lower H_2 generation on these catalysts could be caused by a higher adsorption of poisoning substances on the catalytic surface.

5.2.3.3. Summary and specific conclusions for m-Pd/TiO_2(-WO_3)-PCS Lab catalysts

In Table 14 are given some generals conclusions about the effect of the catalyst and methanol concentration on the H_2 evolution for - CATHETER Lab catalysts in the SS-system in the PCS Lab. In addition, some conclusion are given about the Pd PD method, amount of Pd photodeposited and the CO_2 and CO generation for the - PCS Lab catalysts. Then, some additional analysis are performed to see if there is any tendency between S_{BET}, Pd PD method, E_g and Total V_{PORE}, with the H_2 evolution.

In Figure 5.67 is shown the H_2 evolution for m-Pd/TiO_2(-WO_3) catalysts vs. S_{BET}, where is also shown some information about Eg (eV) (colour) and the Total V_{PORE} (smaller figure in Figure 5.67). Similar to previous data, in Figure 5.67 we cannot see any strong tendency related to S_{BET}, band-gap and H_2 evolution.

Table 14. Specific conclusions for m-Pd/TiO_2(-WO_3) - PCS Lab catalysts on the H_2 evolution

Effect of experimental conditions	
Amount of catalyst* and methanol concentration * CATHETER Lab catalysts	The local optimal catalyst concentration was 200 ppm for the three catalysts: Pd/P25, Pd/NT-WO_3 and Pd/P25-WO_3 catalysts - CATHETER Lab, followed by 500 and1000 ppm. The optimal methanol concentration was 50 vol.% for the three catalysts: Pd/P25, Pd/NT-WO_3 and Pd/P25-WO_3 catalysts - CATHETER Lab.
Photodeposition method	For Pd/NT-WO_3 catalysts - PCS Lab, at the lowest Pd content (0.25 wt.%), the Pd photodeposition by 2m10 method was better than 3.2m20 method. On the other hand, at the highest Pd content (2 wt.%), 3.2m20 was better than 2m10 method. For Pd/P25-WO_3 catalysts - PCS Lab, there are no significant difference between 2m10 or 3.2m20 methods at both Pd content. For Pd/P25 catalysts - PCS Lab, at both Pd content, the Pd photodeposition by 2m10 method seems to be better than 3.2m20 method
Amount of Pd photodeposited	The H_2 evolution did not varied importantly when Pd content was increased from 0.25 toward 2 wt.%. It shows that all catalysts with the lowest Pd content were more efficient toward the H_2 per gram of metal.
CO_2 and CO generation	CO_2 and CO generation seems to be higher on Pd/P25 catalysts. On the other hand, the lowest CO_2 and CO evolution was observed for Pd/P25-WO_3 catalysts.

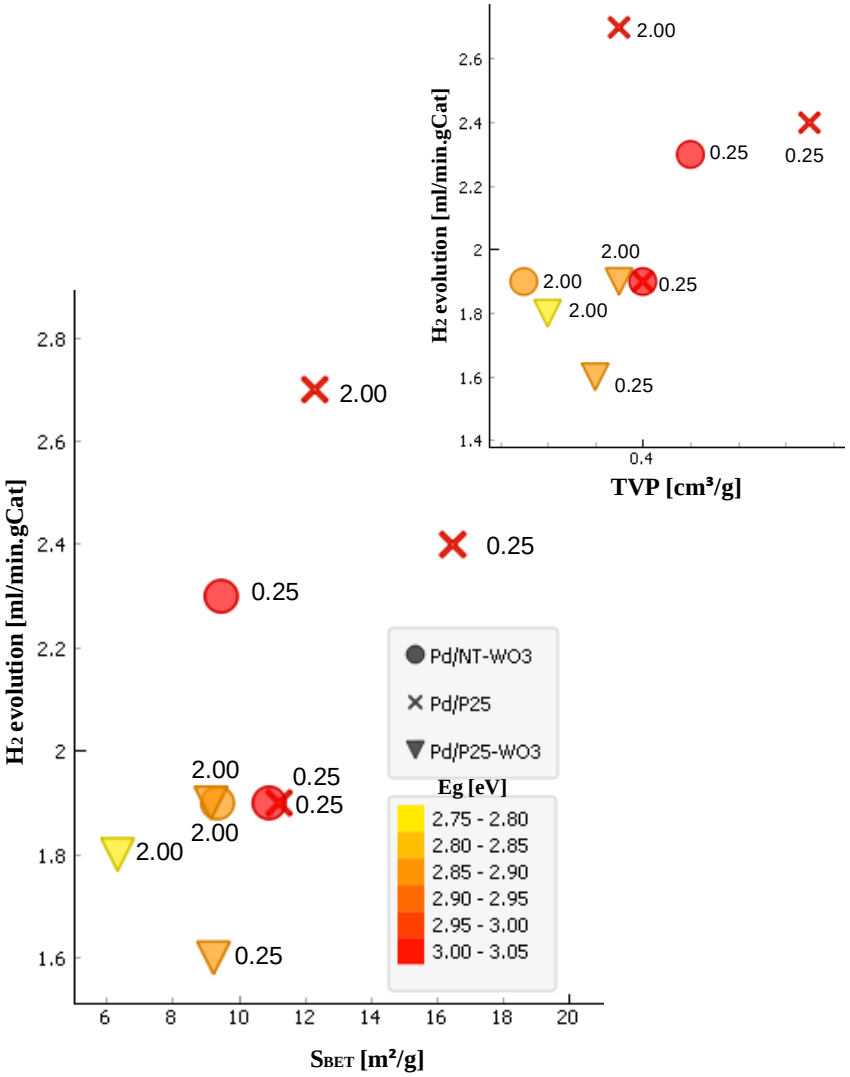

Figure 5.67. Data exploration for H_2 evolution for m-Pd/TiO_2(-WO_3) - PCS Lab catalysts related to S_{BET} [m^2/g] and VPT [cm^3/g]. band-gap (E_g, eV, **colour**), catalysts nature (**shape**) and amount of Pd [wt.%] (**label**). Experimental conditions: catalysts 1000 ppm, 15 ml of water - methanol (50 vol.%) solutions. Irradiation: Optical fiber UV/Vis-Emission: ca. 8W/cm^2 (280 - 700 nm), $I_{250-450nm}$3.88x10^{-5} Einstein/min.

5.2.4. m-Pt/TiO_2(-WO_3) - PCS Lab catalysts

H_2 tests results in the SS-system with m-Pt/TiO_2(-WO_3) - PCS Lab catalysts are presented in this section, in order to study the influence of the Pt deposition method on the photocatalytic H_2 evolution comparing the Pt PD method: 3.2m20 and 2m10. Besides, some results corresponding to the CO_2 and CO evolution are shown in the photocatalytic H_2 generation.

5.2.4.1. Effect of Pt photodeposition method

In Figure 5.68 is shown the H_2 evolution for Pt/NT-WO_3, Pt/P25-WO_3 and Pt/P25 catalysts prepared by two different PD methods: 3.2m20 and 2m10 in PCS Lab. The asterisk (*) designates the nominal amount of Pt.

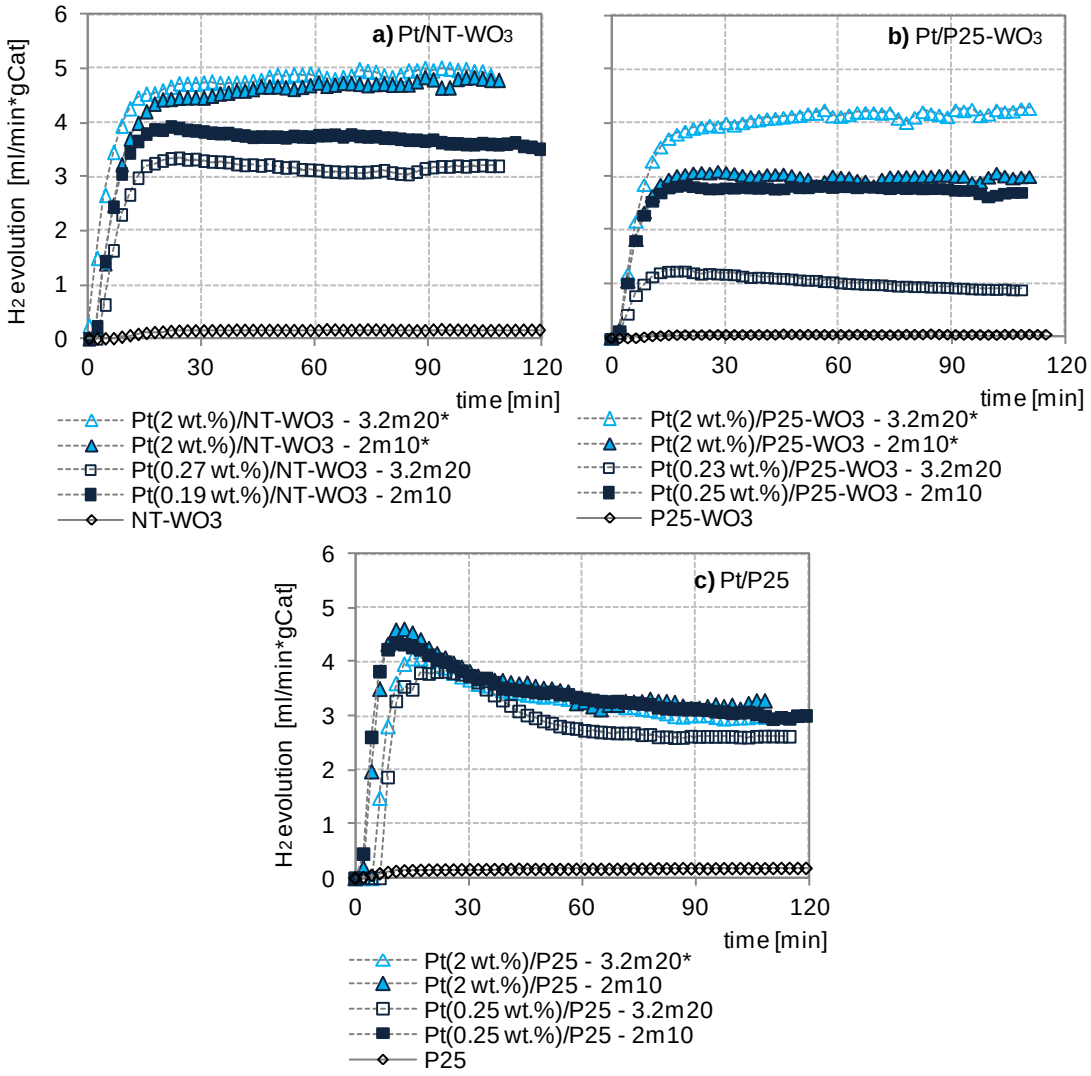

Figure 5.68. Effect of Pt photodeposition method on H_2 generation for **a)** Pt/NT-WO_3; **b)** Pt/P25-WO_3 and **c)** Pt/P25 catalysts. Experimental conditions: catalysts 1000 ppm, 15 ml of a water - methanol (50 vol.%) solution. Irradiation: Optical fiber UV/Vis-Emission: ca. 8W/cm^2 (280 - 700 nm), $I_{250-450nm}$: 3.88x10^{-5} Einstein/min.

Unlike the catalysts containing Pd and prepared in PCS Lab (Figure 5.62), in this case, the catalysts containing Pt showed a more steady plateau for all three group of catalysts. Therefore, in terms of their H_2 evolution profile, both groups of catalyst (Pt/NT-WO_3 and Pt/P25-WO_3) showed an induction period of about 15 min, whereas for Pt/P25 it was around 10 min. After the induction period, for the catalysts

containing WO_3, the H_2 evolution in the plateau was more constant. For Pt/P25 catalysts, the profile showed a maximum value in H_2 evolution, and then progressively decreased. These results show that the Pt/TiO_2(-WO_3) catalysts are more stable than the catalysts without WO_3. For Pt/NT-WO_3 catalysts, the catalyst containing 2 wt.% of Pt showed the highest H_2 evolution. Besides, for the catalysts containing 0.25 wt.% of Pt, the Pt PD 2m10 method seems to be better than the 3.2m20 method. Pt/P25-WO_3 catalysts, Pt(2 wt.%)/P25-WO_3 - 3.2m20 presented the highest H_2 evolution, whereas the catalyst prepared by the same method but 0.25 wt.% of Pt showed the lowest H_2 evolution of this group. Both Pt/P25-WO_3 catalysts whose Pt PD was performed by the 2m10 method, did not show differences. All Pt/P25 catalyst in Figure 5.68 did not show important differences between both 2m10 and 3.2m20 methods, and both Pt (0.25 and 2 wt.%) content.

From the results observed in Figure 5.68, it is possible to conclude that for both catalysts containing WO_3, the Pt PD by 3.2m20 method produces higher H_2 evolution. Besides, although the catalysts with highest Pt content showed more H_2 production, they have lower H_2 evolution when compared per gram of metal.

5.2.4.2. CO_2 and CO generation

Figures 5.69 - 5.71 show the H_2 evolution, in the blue and right axis as mol/min.gCat, together with the CO_2 and CO generation, in the red and left axis as mol/min.gCat, for Pt/P25, Pt/NT-WO_3 and Pt/P25-WO_3 prepared by 3.2m20 and 2m10 method, using 2 and 0.25 wt.% of Pt. For this group of catalysts, the H_2 evolution was two order of magnitude higher than the CO_2, and the CO evolution was much lower that CO_2. Alike CO_2 and CO generation for Pd/TiO_2(-WO_3) catalysts, the catalysts containing Pt also showed a similar profile for CO_2 and H_2 evolution, showing an induction period at the beginning of the reaction followed by a plateau that is quite similar in form between both CO_2 and H_2 evolution.

On this experimental set, the CO_2 and CO evolution were also higher on Pt/P25 catalysts than on the catalysts containing WO_3. For example, in Figure 5.69, the CO_2 evolution is around $5x10^{-6}$ mol/min.gCat in the plateau for both Pt/P25 catalysts containing the highest Pt content, while it was around $3.5x10^{-6}$ mol/min.gCat on the Pt/P25 catalysts containing the lowest Pt content.

For Pt/NT-WO_3 catalysts, the highest and the lowest CO_2 evolution was on the catalysts with Pt photodeposited by 3.2m20 method, 2 and 0.25 wt.% of Pt, respectively. The CO_2 evolution on Pt(2wt.%)/NT-WO_3 - 3.2m20 and Pt(0.13 wt.%)/NT-WO_3 - 3.2m20 catalysts was around $1x10^{-6}$ and $8x10^{-7}$ mol/min.gCat. For both catalysts prepared by Pt PD 2m10 method, the CO_2 was between $1x10^{-6}$ mol/min.gCat. Pt/P25-WO_3 catalysts showed the lowest values of the CO_2 evolution compared to Pt/P25 and Pt/NT-WO_3 catalysts, all of them similar or lower than $1x10^{-6}$ mol/min.gCat.

In Table 15 is presented the H_2/CO_2 molar ratio of these catalysts. Alike the catalysts containing Pd in Table 13, the H_2/CO_2 molar ratios on the catalysts containing Pt are also extremely high compared to the value of 3 depicted in literature. On Pt/P25 catalysts, the H_2/CO_2 molar ratio was also lower than both catalyst containing WO_3. Pt/P25-WO_3 catalysts showed the highest H_2/CO_2 molar ratios.

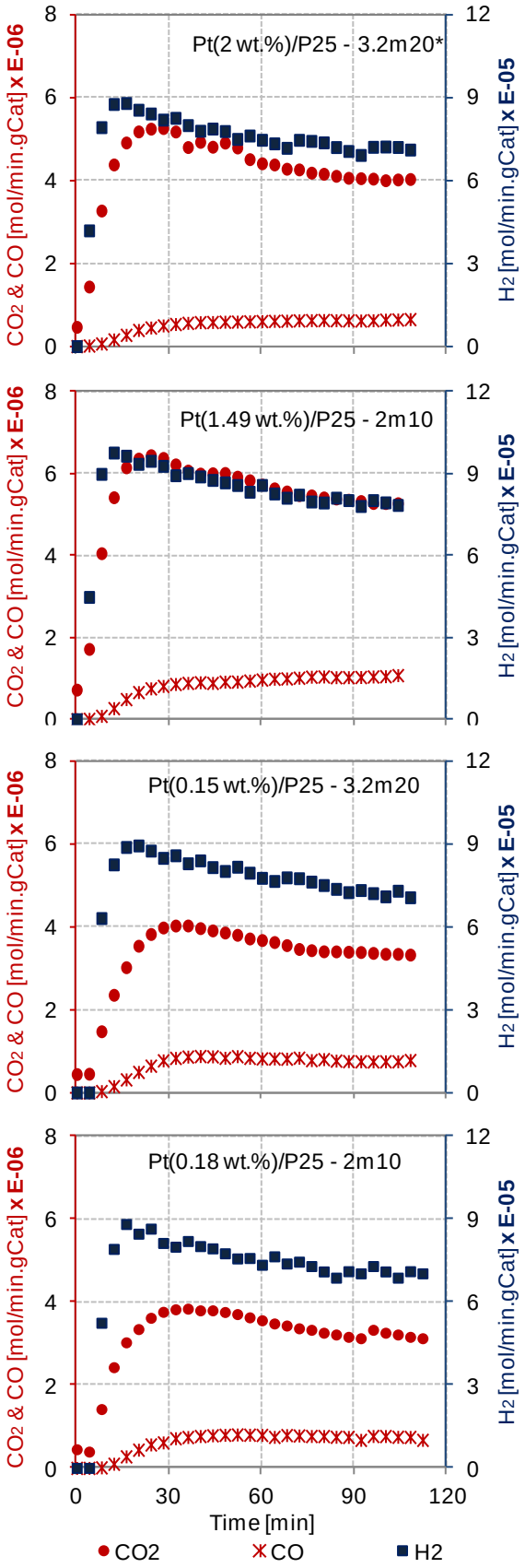

Figure 5.69. H_2, CO_2 and CO generation for Pt/P25 catalysts. Experimental conditions: catalysts 1000 ppm, 15 ml of a water - methanol (50 vol.%) solution. Irradiation: Optical fiber UV/Vis-Emission: ca. 8W/cm^2 (280 - 700 nm), $I_{250\text{-}450nm}$: 3.88x10^{-5} Einstein/min

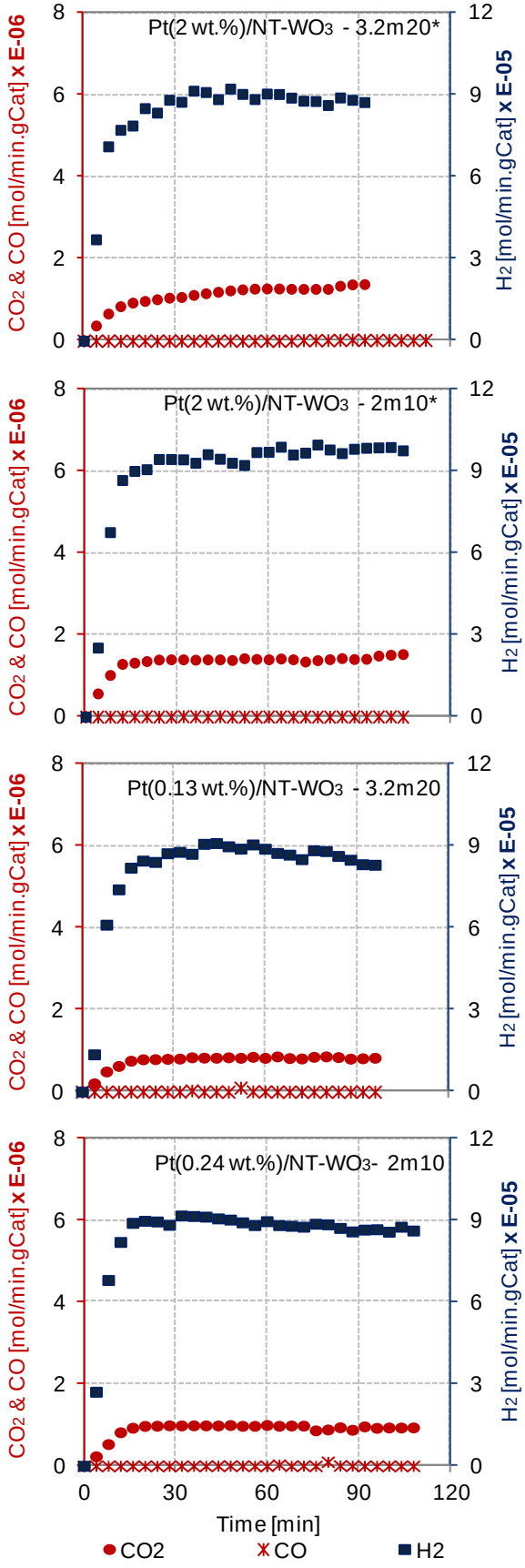

Figure 5.70. H_2, CO_2 and CO generation for Pt/NT-WO_3 catalysts. Experimental conditions: catalysts 1000 ppm, 15 ml of a water - methanol (50 vol.%) solution. Irradiation: Optical fiber UV/Vis-Emission: ca. 8W/cm^2 (280 - 700 nm), $I_{250-450nm}$: 3.88x10^{-5} Einstein/min.

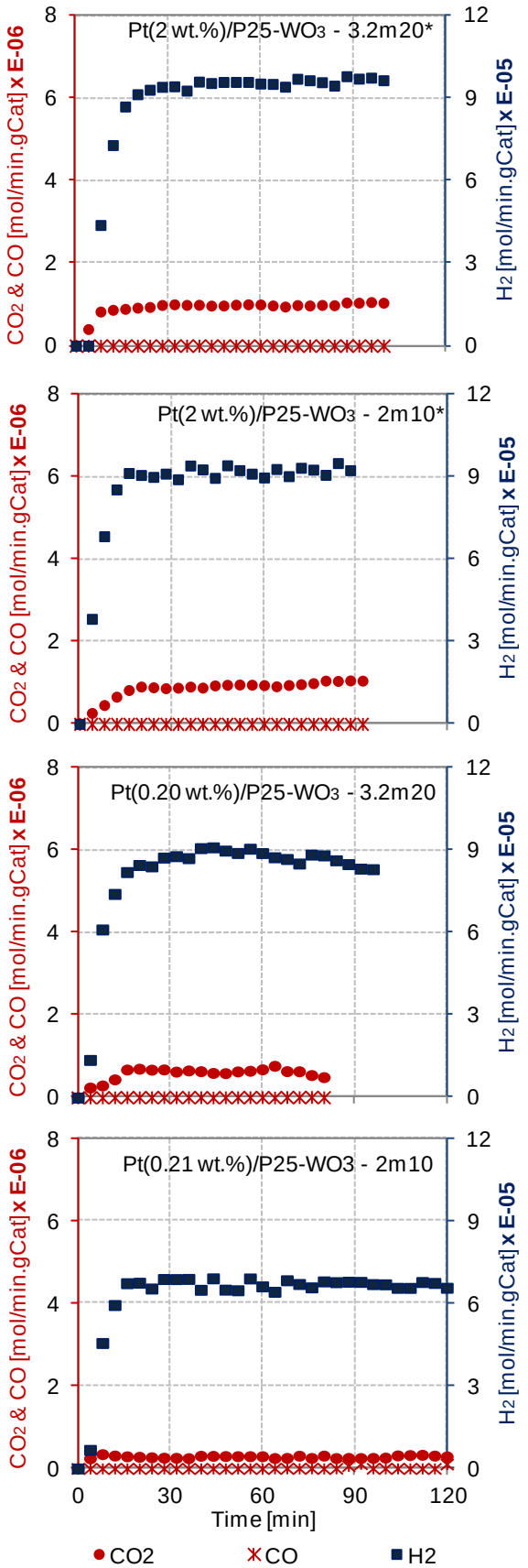

Figure 5.71. H_2, CO_2 and CO generation for Pt/P25-WO_3 catalysts. Experimental conditions: catalysts 1000 ppm, 15 ml of a water - methanol (50 vol.%) solution. Irradiation: Optical fiber UV/Vis-Emission: ca. 8W/cm^2 (280 - 700 nm), $I_{250-450nm}$: 3.88x10^{-5} Einstein/min

Table 15. H_2/CO_2 molar ratio for $Pt/TiO_2(-WO_3)$ catalysts

Catalyst (Pd nominal)	H_2 (mol/min.gCat)	CO (mol/min.gCat)	CO_2 (mol/min.gCat)	H_2/CO_2 molar ratio
Pt(2 wt.%)/P25 - 3.2m20	8 x10-5	6 x10-7	4 x10-6	20
Pt(2 wt.%)/P25 - 2m10	9 x10-5	9 x10-7	6 x10-6	15
Pt(0.25 wt.%)/P25 -3.2m20	8 x10-5	7 x10-7	4 x10-6	20
Pt(0.25 wt.%)/P25 -2m10	8 x10-5	7 x10-7	3 x10-6	27
Pt(2 wt.%)/NT-WO_3 - 3.2m20	9 x10-5	9 x10-9	1 x10-6	90
Pt(2 wt.%)/NT-WO_3 - 2m10	1 x10-4	0	1 x10-6	100
Pt(0.25 wt.%)/NT-WO_3 - 3.2m20	9 x10-5	0	8 x10-7	113
Pt(0.25 wt.%)/NT-WO_3 - 2m10	9 x10-5	0	1 x10-6	90
Pt(2 wt.%)/P25-WO_3 - 3.2m20	1 x10-4	0	1 x10-6	100
Pt(2 wt.%)/P25-WO_3 - 2m10	9 x10-5	0	1 x10-6	90
Pt(0.25 wt.%)/P25-WO3 - 3.2m20	6 x10-5	0	6 x10-7	100
Pt(0.25 wt.%)/P25-WO_3 - 2m10	6 x10-5	0	3 x10-7	200

5.2.4.3. Summary and specific conclusions for m-$Pt/TiO_2(-WO_3)$-PCS Lab catalysts

In Table 16 are given some generals conclusions about the effect of the PD method, the amount of Pt on the H_2 generation and the CO_2 and CO generation. Then, some additional analysis are performed to see if there is any tendency between S_{BET}, Pt PD method, E_g and Total V_{PORE}, with the H_2 evolution. In Figure 5.72 is shown the H_2 evolution for $Pt/TiO_2(-WO_3)$ catalysts vs. S_{BET}, and information about Eg (eV) (colour) and the Total V_{PORE} (smaller figure in Figure 5.72). There is not any tendency related to S_{BET}, TVP, band-gap and H_2 evolution.

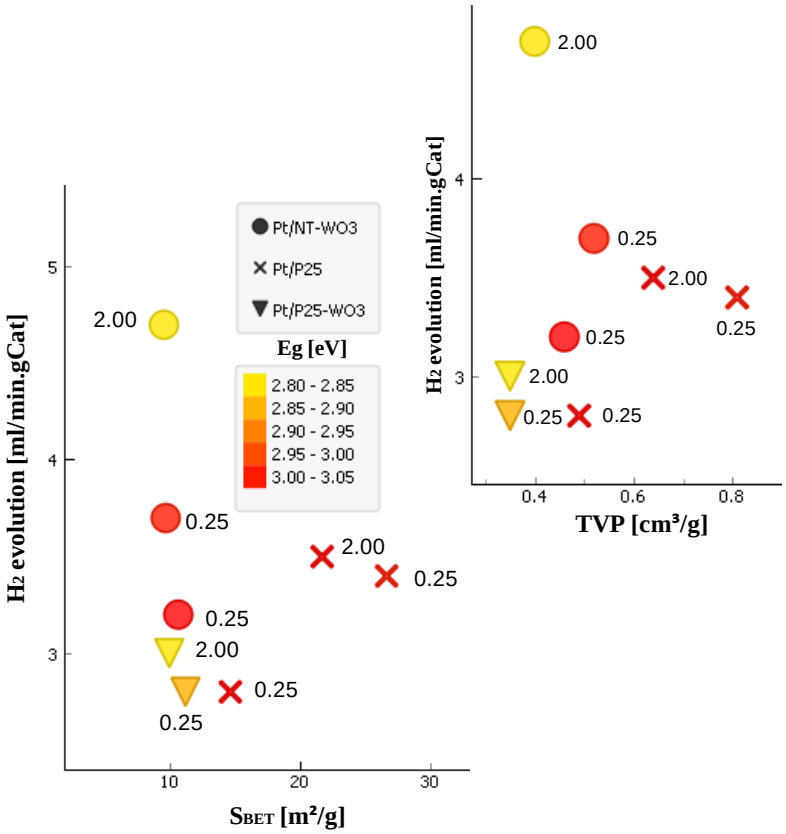

Figure 5.72. Data exploration for H_2 evolution for m-$Pt/TiO_2(-WO_3)$ - PCS Lab catalysts related to S_{BET} [m^2/g] and VPT [cm^3/g]. band-gap (E_g, eV, **colour**), catalysts nature (**shape**) and amount of Pt [wt.%] (**label**). Experimental conditions: catalysts 1000 ppm, 15 ml of water - methanol (50 vol.%) solutions. Irradiation: Optical fiber UV/Vis-Emission: ca. 8W/cm^2 (280 - 700 nm), $I_{250-450nm}$: 3.88x10^{-5} Einstein/min.

Table 16. Specific conclusions for m-Pt/TiO_2(-WO_3) catalysts on the H_2 evolution

Effect of experimental conditions	
Photodeposition method	Pt/P25-WO_3 catalysts, the H_2 evolution seems to be more sensitive to the Pt photodeposition method, either containing 0.25 or 2 wt.% of Pt. For both Pt/P25-WO_3 and Pt/P25 catalysts, no significant differences on the H_2 generation were observed. At the highest Pt content (2 wt.%) and for both catalysts containing WO_3, the 3.2m20 method showed higher H_2 evolution than the 2m10 method. In the case of Pt/P25, seems that the 2m10 method was very little higher than 3.2m20 method. At 0.25 wt.% of Pt and for three catalysts, 2m10 method showed higher H_2 evolution.
Amount of Pd photodeposited	For the three catalysts, the highest Pt content (2 wt.%), without matter the Pt photodeposition method, seems to have higher H_2 evolution. Although it is important to highlight than on none of the catalysts containing 2 wt.% Pt, the H_2 evolution was remarkable, taking into account that on these materials the metal content is almost 10 times higher than the catalysts containing 0.25 wt.% of Pt.
CO_2 and CO generation	CO_2 and CO generation seems to be higher on Pt/P25 catalysts. On the other hand, the worst CO_2 and CO evolution was observed on Pt/P25-WO_3 catalysts.

5.2.5. Attenuated Total Reflectance-Fourier Transform Infrared Spectroscopy

To understand the reaction mechanism occurring on the solid-liquid interface of this kind of catalysts, some in-situ ATR-FTIR spectroscopy experiments have been performed.

5.2.5.1. NT-WO_3 vs. Pd(0.21 wt.%)/NT-WO_3 - CATHETER Lab catalysts

Figure 5.73 shows the FTIR spectra between 2800 - 3900 cm^{-1} for NT-WO_3 and Pd(0.21 wt.%)/NT-WO_3 - CATHETER Lab catalysts in a water - methanol (~50 vol.%) solution at every 3 min up to 15 min of irradiation, and then at the final irradiation at 90 min. From these spectra, the most observable difference is located in the wavenumbers at around 3000 - 3600 cm^{-1}, where a wide band increases for NT-WO_3 but no peaks are observed for the catalyst containing Pd.

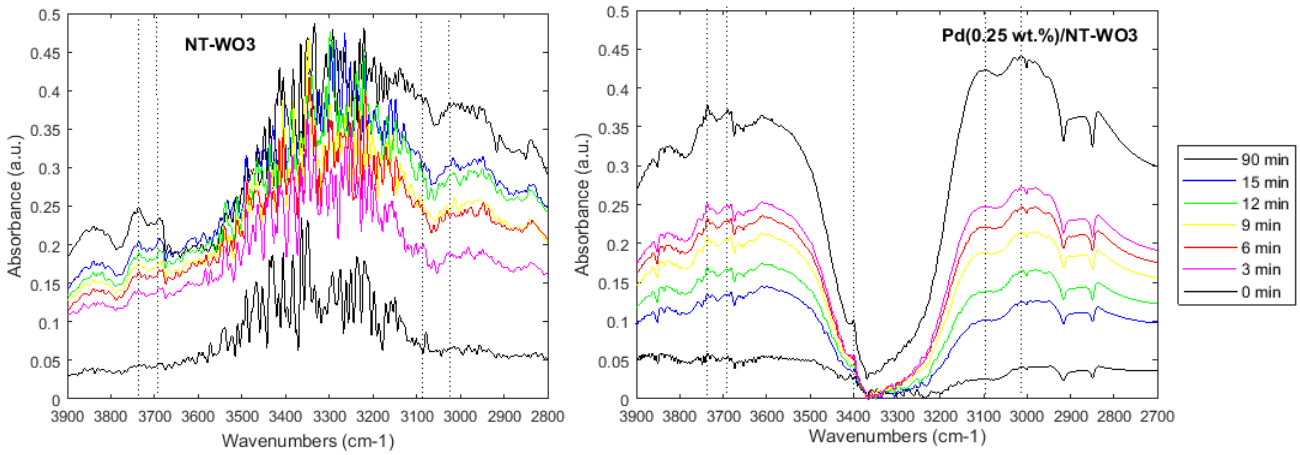

Figure 5.73. FTIR study: NT-WO_3 and Pd/NT-WO_3 - CATHETER Lab catalyst, 2800 - 3900 cm^{-1} range. Experimental conditions: catalysts 1000 ppm, 2ml of a water - methanol (50 vol.%) solution under 7 LED's lamp (365 nm). Pd PD by 2m10 method

The region 3000 - 3600 cm^{-1} is assigned to stretching H-bounds, and accordingly to Choi et al. [180] and Fernandez [163], correspond to the stretching band of O-H in CH_3OH. Furthermore, Buky [65] suggests a sharp peak at around 3400 cm^{-1} due to the stretching O-H bond in alcohols. On the other hand, Chen, T. et al. [181] and Gomes, J.F. et al [182] indicates that a broad band between 3100 - 3500 or between 3000 - 4000 cm^{-1}, respectively, can be assigned to the stretching H-bounds of O-H in H_2O. Taking into

account these previous studies, both bands could be overlapped. Maira A. et al. [183] suggested that the broad IR absorption in the 2800 - 3600 cm^{-1} range with a maximum at 3450 cm^{-1} corresponded to the superposition of stretching mode of hydroxyl groups, for instance, by hydrogen-bonds, symmetric and asymmetric stretching modes related to molecular water. Therefore, the increasing band with the irradiation time on NT-WO_3 might be interpreted as a growing concentration of OH species adsorbed on its surface, but it is not clear the proportion of OH species corresponding to H_2O and CH_3OH. For catalysts containing Pd, this adsorption of water molecules by H-bounds on the catalysts is not observed, or very few H-bounds are formed but not enough to see it in the spectra. The sharp peak at around 3400 cm^{-1} might correspond to methanol linked by H-bounds to the catalyst.

In more details, what it could be happening is, previously to the irradiation, H-bonds are formed between CH_3OH and/or H_2O molecules with the catalyst surface (likely on oxygen atoms, either from the TiO_2 or the WO_3). When the catalyst is under irradiation, it is activated, and therefore e^-/h^+ pairs are generated. On the h^+ from TiO_2 and probably from WO_3 as well, which are oxygen vacancies, CH_3OH and, most probably, H_2O molecules are dissociated [184]. From these dissociations, some $OH^\bullet$ groups ($OH^- + h^+ \rightarrow OH^\bullet$) are formed and they keep adsorbed on the catalyst. This $OH^\bullet_{(a)}$ can either form H-bounds or react with CH_3OH [184]. Accordingly to Sánchez de Armas et al [185], the breaking of the C-O bond in CH_3OH molecules is less favourable than its progressive dehydrogenation, therefore, the previous dissociation is most probable for H_2O.

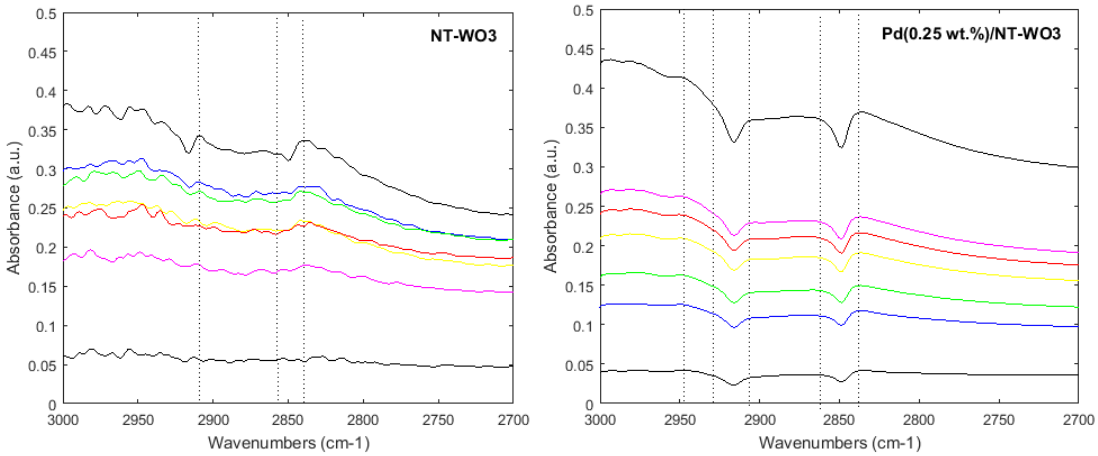

Figure 5.74. FTIR study: NT-WO_3 and Pd/NT-WO_3 - CATHETER Lab catalyst, 2700 - 3000 cm^{-1} range.

On the Pd(0.21 wt.%)/NT-WO_3 catalyst, we see from the Figure 5.69, no H-bounds from water but very little from methanol are formed between hydroxyl groups with the catalyst surface. This is probably due to the presence of Pd. After starting irradiation, $OH^\bullet_{(a)}$ groups, more probably from water than from methanol, are produced on the h^+. Due to the presence of Pd a lower e^-/h^+ recombination is produced. Consequently, more $OH^\bullet_{(a)}$ groups are produced and they kept adsorbed on the catalyst surface. As the $OH^\bullet_{(a)}$ groups are strong oxidizing agents, they can react with the CH_3OH molecules in the vicinity of the catalyst surface. On the h^+, methanol molecules are also adsorbed, but as the C-O dissociation might be less likely, less $OH^\bullet_{(a)}$ groups from methanol are produced. On the other hand, it is more likely that methanol molecules are dehydrogenated and H^+ ions are easily reduced on Pd by the photogenerated e^-. Additionally, from the reaction of the $OH^\bullet_{(a)}$ groups (adsorbed on the surface) with other methanol or water molecules in the vicinity of the catalytic surface, H_2 is also produced.

In the case of the catalytic support NT-WO_3, in Figure 5.73 is seen that H-bounds are formed between hydroxyl groups, either from methanol or water molecules, with the catalyst surface. Then, after irradiation, due to the higher e^-/h^+ recombination probabilities on these materials without an e^- trap, there is a lower generation of $OH^{\bullet}_{(a)}$ groups from the h^+. Then, on the NT-WO_3 actives sites of the surface the adsorption of $OH^{\bullet}_{(a)}$ groups, as well as methanol and water molecules by the H-bounds, can be performed. From the results, it seems that the NT-WO_3 surface is more saturated of these species. The high e^-/h^+ recombination probability leads to produce less $OH^{\bullet}_{(a)}$ groups, which might clean the catalysts surface by reacting with methanol or water molecules. But this lower concentration of $OH_{(a)}$ groups could lead to a poor cleaning of the catalysts surface, increasing their concentration as can be seen in Figure 5.73. The lower concentration of $OH^{\bullet}_{(a)}$ groups on NT-WO_3 also leads to a lower probability of methanol dissociation reaction, therefore, less H^+ are available for further H_2 production.

From the H_2 experiments it has been observed that the H_2 evolution is lower on NT-WO_3 than on the catalysts with the incorporation of Pd (Figure 5.41, 5.42, 5.51, 5.63, 5.68), which would support this analysis. The high generation of $OH^{\bullet}_{(a)}$ groups might lead, not only, to a cleaning effect of catalyst surface from these CH_3OH molecules, but also to a progressive production and accumulation of by-products on the surface of the catalyst. The first fact would explain the higher H_2 evolution on catalysts containing a metal and the second, the catalysts poisoning after certain irradiation time, which depends on the experimental condition as well.

At around 3700 cm^{-1} (Figure 5.73) it is seen two narrow bands that correspond to O-H stretching regions for surface hydroxyl groups from alcohols [180][181][183]. Furthermore, some bands located between 2000 - 2950 cm^{-1} (Figure 5.74) might correspond to symmetric (closer to 2950 cm^{-1}) and asymmetric (2925 cm^{-1}) C-H stretching in methanol, accordingly to Choi and Kang [180] and also Halasi et al. [186]. The two peaks in the region of 2880 and 2860 cm^{-1} corresponds to adsorbates such as CH_3O species [181][186]. These bands, corresponding to CH_3O species formation are scarcely observed on the catalyst without Pd. The band at around 3100 cm^{-1}(Figure 5.73), that increases with the irradiation time, corresponds to -CH stretching in R-CHO species and might suggest the formation of aldehydes [180]. According to Buky [65], two bands between 2700 - 2900 cm^{-1} correspond to C-H stretching for aldehydes at around 2840 and 2950 cm^{-1}.

In Figure 5.74 is possible to see a weak peak near to 2950 cm^{-1}, but not the second one at around 2850 cm^{-1}, or probably it is overlapping in the band corresponding to CH_3O species. This possible formation of aldehydes is more evident on Pd/NT-WO_3, but not on the catalyst without Pd. Figure 5.75 shows two very weak bands at around 2350 cm^{-1} (2355 and 2345 cm^{-1}), which are more clearly defined with the irradiation time and could be assigned to CO_2 [78][180]. The lines at 0 min may correspond to a minimal amount of CO_2 that could be referred to CO_2 present in the chamber before irradiation.

In Figure 5.76, the most observable band is between 1600 - 1800 cm^{-1} that could be assigned to a mode of stretching C=O of a carbonyl compound [65]. Although it seems there are some overlapping bands, for example the peaks at around 1750, 1700 and 1650 cm^{-1}. The band at around 1750 cm^{-1} is assigned

to stretching C=O of formic acid [78][163], 1700 cm^{-1} to carbonyl C-H of aldehydes and at around 1650 cm^{-1} to symmetrical scissoring of OH from H_2O [65][129][182]. The band corresponding to H_2O seems more clear on NT-WO_3, what could reflect the assumption of a higher adsorption of H_2O explained in the region 3000 - 3600 cm^{-1}.

Accordingly to Buky et al [65], the region 1550 - 1600 cm^{-1} is assigned to the formation of carboxylates. In this case, most probably methyl formate. Additionally, the two bands at around 1450 cm^{-1} can be assigned to the vibrational mode of asymmetric and symmetrical scissoring of CH_3 that correspond to the adsorption of CH_3OH [186]. The bands between 1350 - 1400 cm^{-1} correspond to -COO- symmetric mode (near to 1400 cm^{-1}) and C-H deformation of -COO- rocking (near to 1370 cm^{-1}) of adsorbed formate species [181]. The negative band near to 1250 cm^{-1} correspond to C-O stretching in carboxylic acids, associated to their desorption [163][182]. Accordingly to Fernández, G. [163], the band between 1200-1320 cm^{-1} might be assigned to stretching C-O corresponding to carboxylic acids, in this case, it might be formic acid. Although in this region appear bands that could correspond to carboxylic acid compounds, the fact that the wide band between 2400 - 3400 cm^{-1}, corresponding to H bounded to -COOH species [65][163] does not appear, indicates a very weak formic acid production.

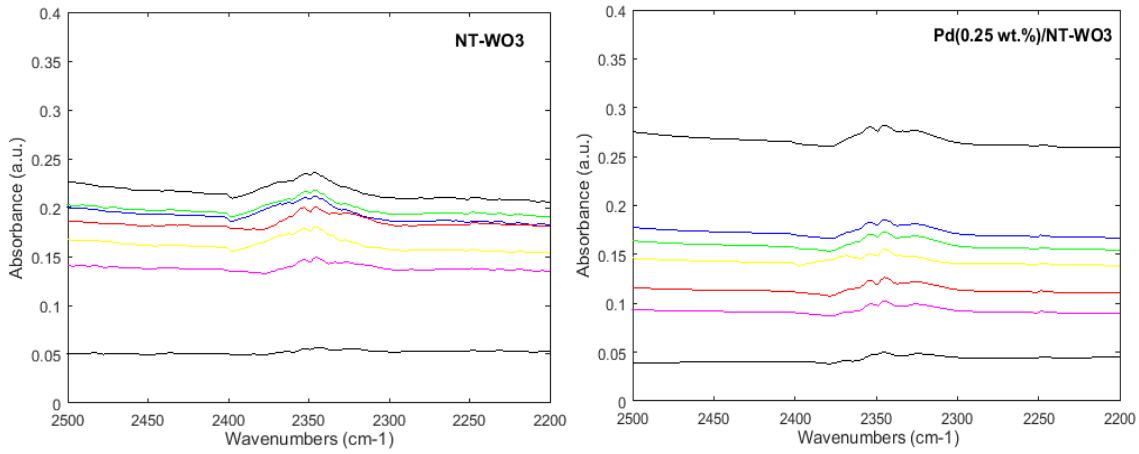

Figure 5.75. FTIR study: NT-WO_3 and Pd/NT-WO_3 - CATHETER Lab catalyst, 2200 - 2500 cm^{-1} range.

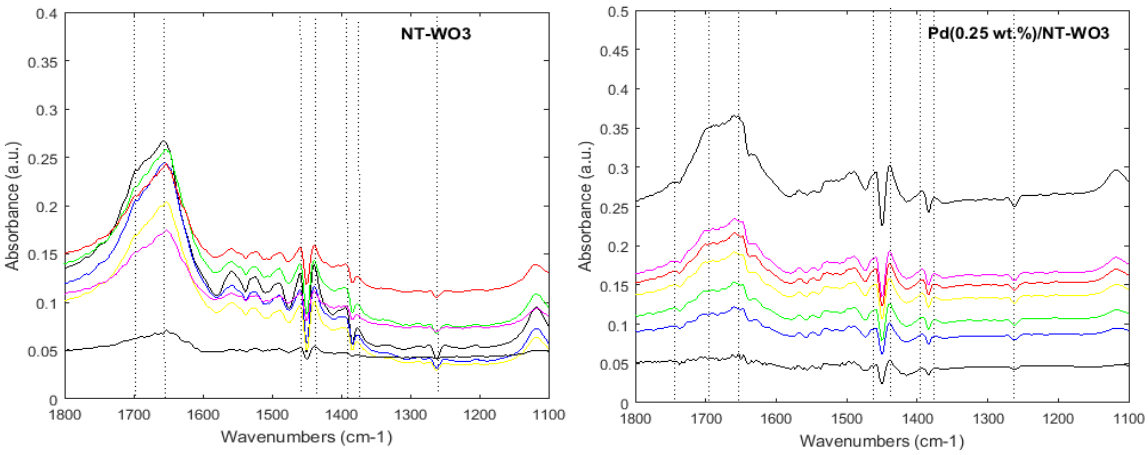

Figure 5.76. FTIR study: NT-WO_3 and Pd/NT-WO_3 - CATHETER Lab catalyst, 1100 - 1800 cm^{-1} range.

5.2.5.2. $P25\text{-}WO_3$ vs. Pd(0.25 wt.%)/$P25\text{-}WO_3$ - CATHETER Lab catalysts

Figure 5.77 shows the FTIR spectra between 2800 - 3900 cm^{-1} for $P25\text{-}WO_3$ and Pd(0.23 wt.%)/$P25\text{-}WO_3$-CATHETER Lab catalysts in a water - methanol (~50 vol.%) solution at every 3 min up to 15 min of irradiation, and then the final irradiation at 90 min. These results are comparable with the previous ones, where there is a band at around 3000 - 3600 cm^{-1} for the catalytic support $P25\text{-}WO_3$, but no band is seen for the catalyst containing Pd between 3200 - 3400 cm^{-1}. Pd/$P25\text{-}WO_3$ and $P25\text{-}WO_3$ show similar behaviour than for Pd/$NT\text{-}WO_3$ and $NT\text{-}WO_3$ catalysts, respectively.

At around 3700 cm^{-1} (Figure 5.77) are also observed two weak and narrow bands corresponding to O-H stretching regions for CH_3OH [180][181][183]. In Figure 5.78, the bands corresponding to symmetric and asymmetric C-H stretching in methanol at around to 2950 and 2925 cm^{-1} are scarcely observed on these two catalysts. The other two peaks in the region of 2880 and 2860 cm^{-1}, corresponding to dissociated CH_3O species [181][186] are also barely observed on $P25\text{-}WO_3$ and Pd/$P25\text{-}WO_3$ catalysts. The band around 3100 cm^{-1} (Figure 5.77), which corresponds to -CH stretching in R-CHO species [180] is not seen in the $P25\text{-}WO_3$ catalysts, but in the catalyst containing Pd, can be observed a soft shoulder. The two bands between 2700-2900 cm^{-1}, corresponding to C-H stretching for aldehydes at around 2840 and 2950 cm^{-1} [65], are also weak in Figure 5.78. Figure 5.79 shows two very weak bands at around 2350 cm^{-1} (2355 and 2345 cm^{-1}), corresponding to CO_2 [78][180].

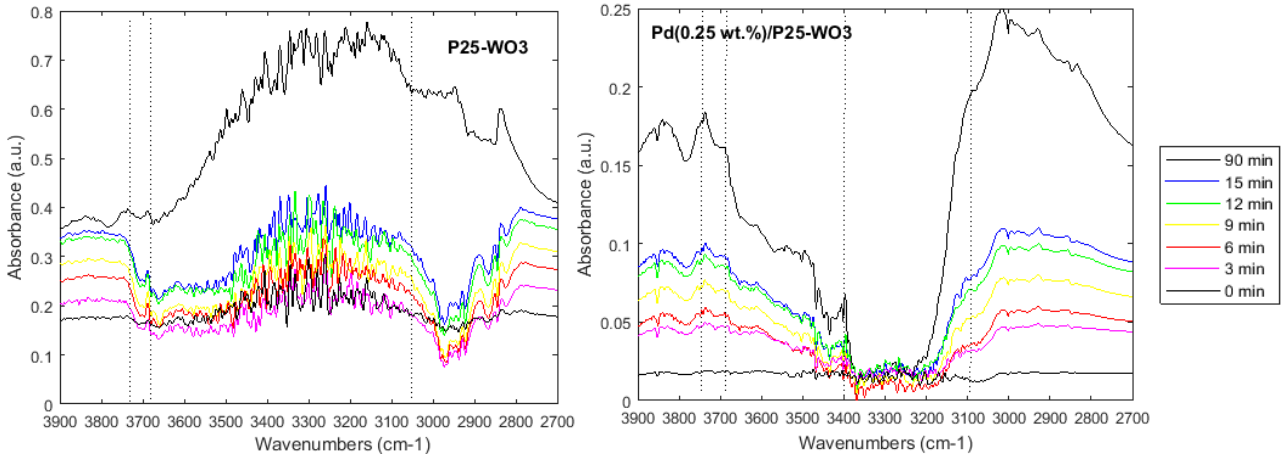

Figure 5.77. FTIR study: $P25\text{-}WO_3$ and Pd/$P25\text{-}WO_3$-CATHETER Lab catalyst, 2800 - 3900 cm^{-1} range. Experimental conditions: catalysts 1000 ppm, 2ml of a water - methanol (50 vol.%) solution under 7 LED's lamp (365 nm). Pd PD by 2m10 method.

In Figure 5.80, between 1600 - 1800 cm^{-1}, it seems that there is a band overlapping, where one peak is at around 1700 cm^{-1}, that correspond to stretching carbonyl C-H in aldehydes [163] and the peak at around 1650 cm^{-1} is assigned to H_2O scissoring mode [65][129]. Very similar to Pd/$NT\text{-}WO_3$ and $NT\text{-}WO_3$ catalysts, for $P25\text{-}WO_3$ and Pd/$P25\text{-}WO_3$ catalysts, in the region 1550 -1600 cm^{-1} are found some weak peaks that may be assigned to the formation of carboxylates like methyl formate, accordingly to Buky et al. [65]. Besides, in these two catalysts are seen two sharp bands at around 1450 cm^{-1} assigned to the vibrational mode of asymmetric and symmetrical scissoring of CH_3, which would correspond to the adsorption of CH_3OH [186] and two other bands between 1350 - 1400 cm^{-1} corresponding to -COO- symmetric mode (1400 cm^{-1}) and C-H deformation of -COO- rocking (at around 1370 cm^{-1}) of adsorbed

formate species [181]. The negative band near to 1250 cm-1 might correspond to C-O stretching in carboxylic acids, associated to its desorption [163][182].

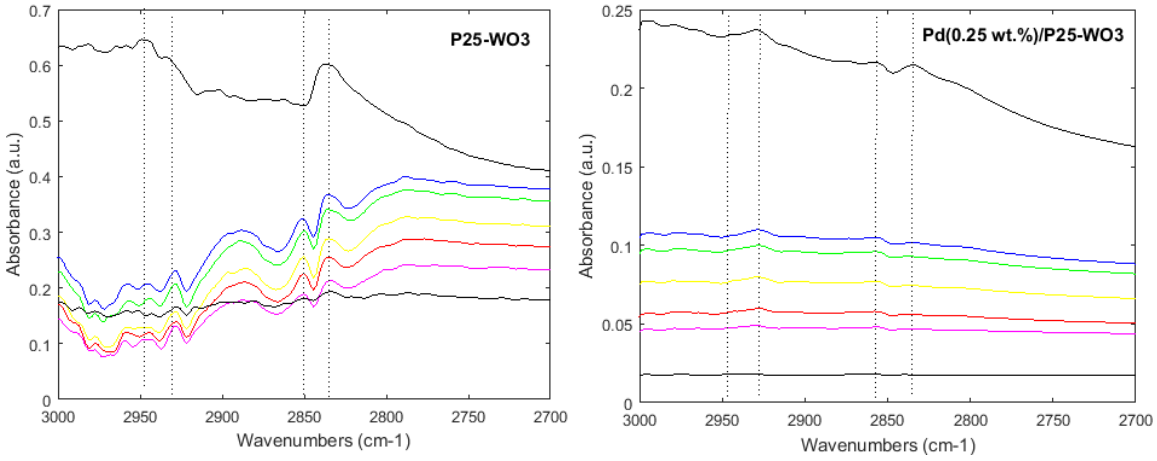

Figure 5.78. FTIR study: P25-WO_3 and Pd/P25-WO_3 - CATHETER Lab catalyst, 2700 - 3000 cm^{-1} range.

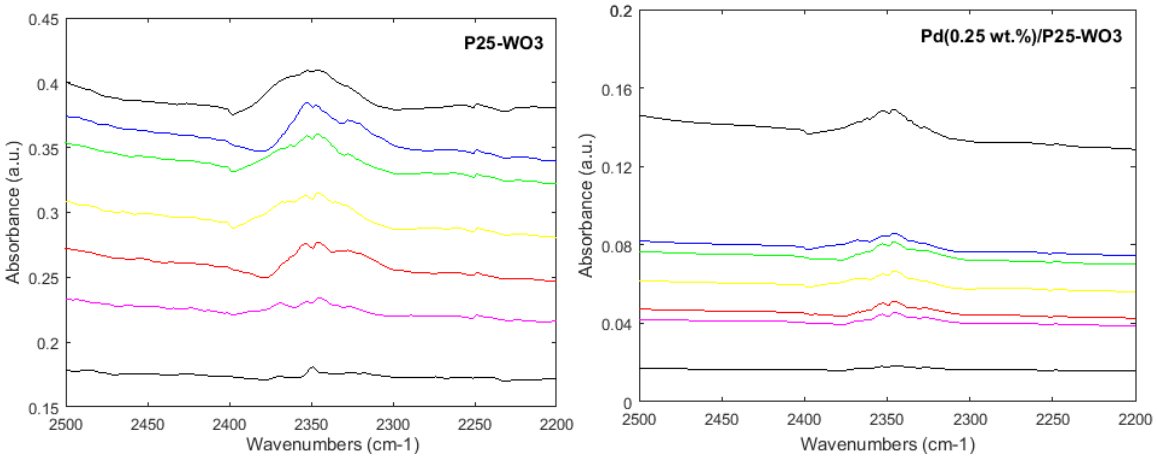

Figure 5.79. FTIR study: P25-WO_3 and Pd/P25-WO_3 - CATHETER Lab catalyst, 2200 - 2500 cm^{-1} range.

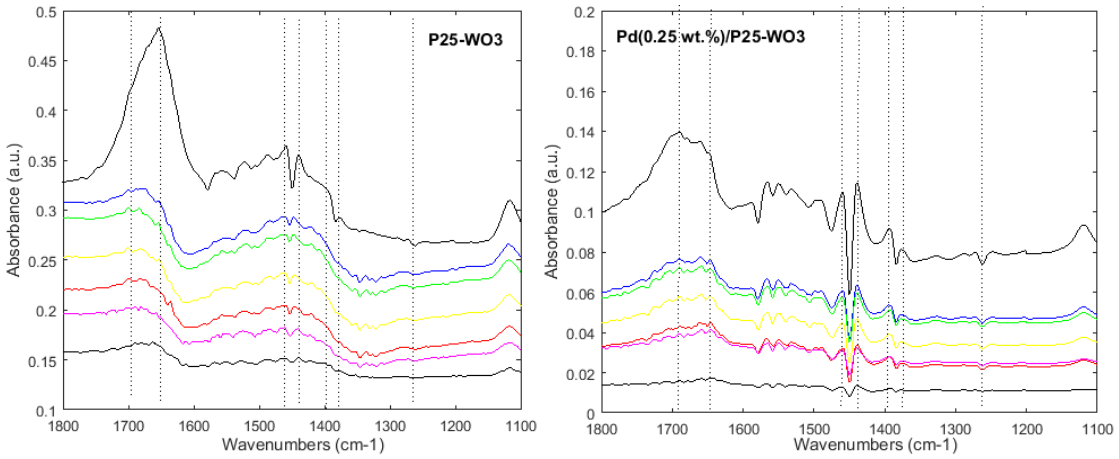

Figure 5.80. FTIR study: P25-WO_3 and Pd/P25-WO_3 - CATHETER catalyst, 1100 - 1800 cm^{-1} range.

5.2.5.3. Comparison: Pd(0.24wt.%)/P25, Pd(0.21wt.%)/NT-WO_3 and Pd(0.23 wt.%)/P25-WO_3

Figure 5.81 shows the FTIR spectra of Pd(0.24 wt.%)P25, Pd(0.21 wt.%)/NT-WO_3 and Pd(0.23 wt.%)/P25-WO_3 - CATHETER Lab catalysts at 90 minutes of irradiation, between 2800 - 3900 cm^{-1}. Comparing the three catalysts, the main observable difference is the 3100 - 3500 range, assigned to stretching H-bounds, corresponding to stretching OH groups in alcohols and/or water [65][163][180][181][182]. Only for Pd/P25 catalyst, there is a broad band in this region; meanwhile for Pd/NT-WO_3 and Pd/P25-WO_3 catalysts, this band does not appear. It seems that the presence of both WO_3 and Pd results in the suppression of H-bounds on the catalysts and not only the presence of Pd, as it was commented above. Mostly of these suppressed H-bound can come from the water because in Figure 5.81, for the three catalysts it can be seen a sharp peak at around 3400 cm^{-1} that correspond to stretching H-bounds related to alcohols [65].

For catalysts containing Pd and WO_3 (Pd/NT-WO_3 and Pd/P25-WO_3), the TiO_2 might be more hidden from the surface due to the presence of Pd and WO_3 nanoparticles. For catalysts containing only Pd (Pd/P25) or only WO_3 (NT-WO_3 and P25-WO_3), TiO_2 might be more exposed to the surface. This indicates the possibility of more water molecules forming H-bound on TiO_2 than on WO_3. This hypothesis would explain the broad band between 3100 - 3500 cm^{-1} on Pd/P25 that is not detected for Pd/NT-WO_3 and Pd/P25-WO_3 catalysts.

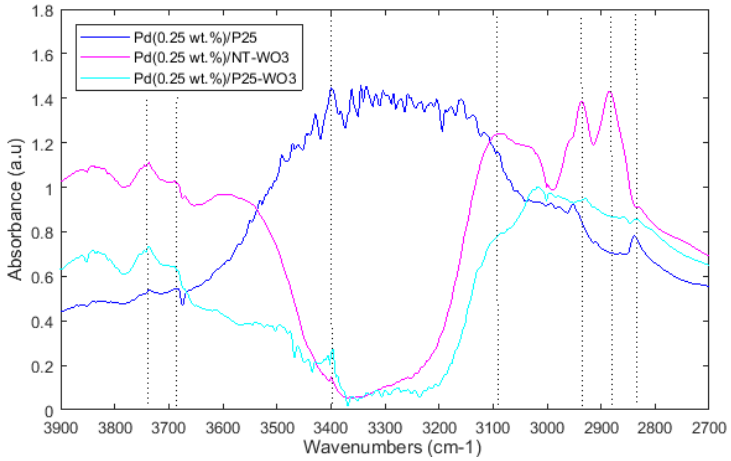

Figure 5.81. FTIR study: Pd/P25, Pd/NT-WO_3 and Pd/P25-WO_3 - CATHETER catalysts, 2700 - 3900 cm^{-1} range. Experimental conditions: catalysts 1000 ppm, 2ml of a water - methanol (50 vol.%) solution under 7 LED's lamp (365 nm). Pd PD 2m10 method.

In Figure 5.81 can be also seen, in the region 2800 - 3100 cm^{-1} some bands for the three catalysts. The band at around 3100 cm^{-1} corresponds to -CH stretching in R-CHO species [180]. For both Pd/NT-WO_3 and Pd/P25-WO_3 catalysts it is weakly observed but not for Pd/P25 catalyst. The bands corresponding to -CH stretching in alcohols (near to 2950 and 2900 cm^{-1}) [180][186] and the one assigned to CH_3O species [181][186](2850 cm^{-1}) are higher for Pd/NT-WO_3 than for Pd/P25-WO_3 catalyst, what it could suggest more adsorption of CH_3O species on the catalyst containing the nanotubes of TiO_2. It might make a difference to Pd/P25-WO_3, related to the H_2 evolution, which is higher on Pd/NT-WO_3.

In Figure 5.82 the two slight weak bands at around 2350 cm^{-1} are assigned to CO_2 [180][78]. It seems that on both catalysts containing WO_3, its adsorption is little higher than on Pd/P25 catalyst. These

results could corroborate the results in Table 13, where it was observed a higher CO_2 evolution on Pd/P25 than on Pd/NT-WO_3 and Pd/P25-WO_3, but it was attributed to a lower adsorption of CO_2 on its surface. This higher surface adsorption of CO_2 on both catalysts containing WO_3 might suggest a possible cause of their lower H_2 generation compared to Pd/P25, poisoning

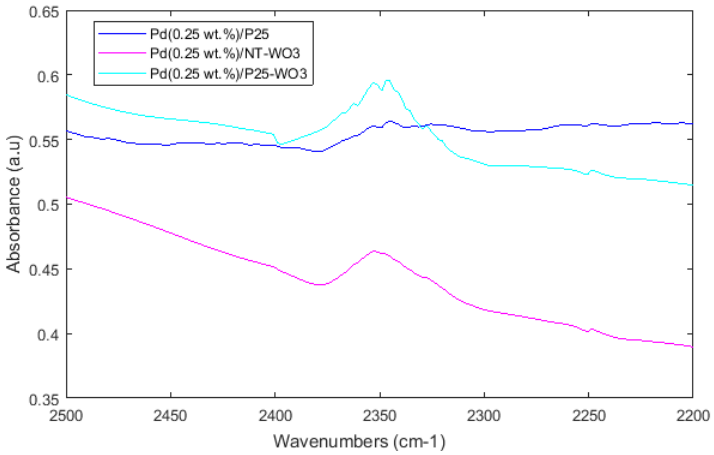

Figure 5.82. FTIR study: PdP25, Pd/NT-WO_3 and Pd/P25-WO_3 - CATHETER Lab catalysts, 2200 - 2500 cm^{-1} range.

In Figure 5.83, in the 1100 - 1800 cm-1 range is seen for the three catalysts a band between 1800 - 1600 cm^{-1}. This band is assigned to stretching C=O of a carbonyl compound [65]. In this region seems to be two overlapping bands, where the nearest peak to 1700 cm^{-1} corresponds to stretching carbonyl C-H aldehydes. This band is not observed for Pd/P25 catalyst. The peak at 1650 cm^{-1} [163] can be attributed to the scissoring mode of H_2O [65][129]. Here is observed a weak shoulder for both Pd/TiO_2-WO_3 catalysts, but a clear maximum for Pd/P25. The weak band at around 1750 cm^{-1} is assigned to stretching C=O of formic acid [78][163]. The bands in the region 1600 - 1550 cm^{-1}, accordingly to Buky et al. [65], indicates the formation of carboxylates, most probably methyl formate.

Two bands at around 1450 cm^{-1} are assigned to the vibrational mode of asymmetric and symmetrical scissoring of CH_3 correspond to the adsorption of CH_3OH [186]. The bands between 1400 - 1350 cm^{-1} correspond to -COO- symmetric mode (near to 1400 cm^{-1}) and C-H deformation of -COO- rocking (near to 1370 cm^{-1}) of adsorbed formate species [181]. The negative band near to 1250 cm^{-1} correspond to C-O stretching in carboxylic acids, associated to their desorption [163][182].

In the 1000 - 1200 cm^{-1} region in Figure 5.83 is observed three bands for both catalysts containing WO_3. The bands at around 1120 and 1025 cm^{-1} correspond to stretching C-O in alcohols and the peak near to 1000 cm^{-1} is assigned to stretching C=O in CH_3O species [65][163][180]. The bands at around 980 and 920 cm^{-1} might be assigned to scissoring C-H of aldehydes [163] and bending C-O-H in carboxylic acids [180], respectively, and the pick at around 825 cm^{-1} might correspond to bending of C-O-H of carboxylic acids [163].These band are only observable on Pd/NT-WO_3 and Pd/P25-WO_3 catalysts. The broad band below 1000 cm^{-1}, in Figure 5.83, for Pd/P25 correspond to H_2O. For catalysts containing WO_3 it is not observed that could be related to the explanation given in the region 3500 - 3100 cm^{-1}.
All in all, for both catalysts based on Pd/TiO_2-WO_3, the low desorption of CO_2, seems progressively to poison their catalytic surface, decreasing their activity toward the H_2 generation compared to Pd/P25.

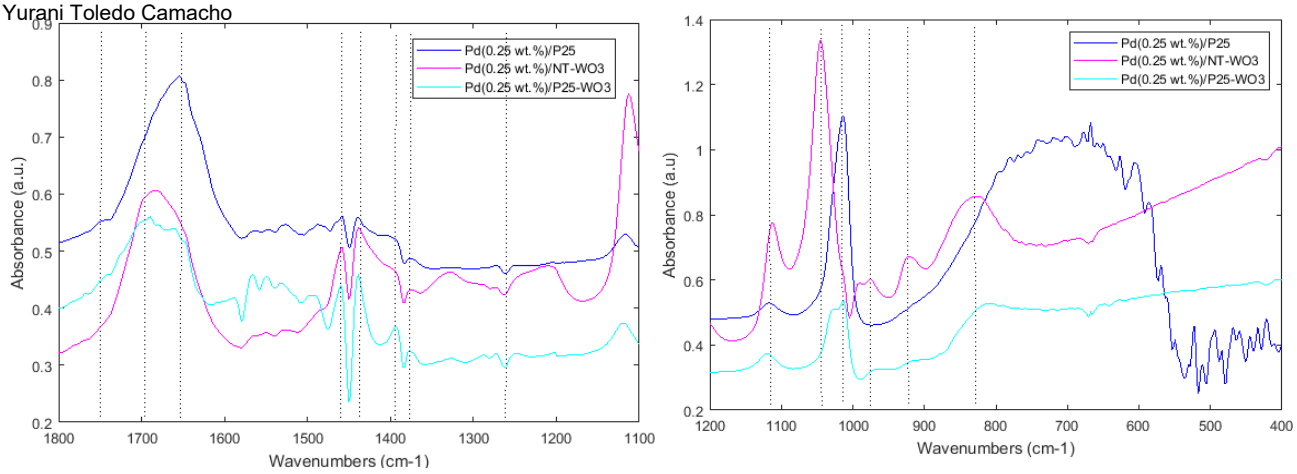

Figure 5.83. FTIR study: Pd/TiO_2(-WO_3) - CATHETER Lab catalysts, 1100 - 1800 cm^{-1} and 400 -1200 cm^{-1} range.

5.2.5.4. Comparison: Pd(0.25 wt.%)/P25- PCS Lab and Pd(2 wt.%)/P25 - PCS Lab catalysts

Figure 5.84 shows FTIR spectra for Pd(0.25 wt.%)/P25 and Pd(2 wt.%)/P25* - PCS catalysts between 2800 - 3900 cm^{-1} and 2700 - 3000 cm^{-1} range at 90 min of irradiation. The most visible difference is located at around 3100 - 3600 cm^{-1}, where no band is seen for the catalyst containing 2 wt.% of Pd.

Surprisingly, contrarily to the Pd(0.24 wt.%)/P25 - CATHETER Lab catalyst, the Pd(0.25 wt.%)/P25 - PCS Lab catalyst does not show the characteristic band corresponding to water between 3000 - 3600 cm^{-1}. Moreover, on the catalyst containing 2 wt.% of Pd, this band referred to water is observed. Probably, the oxidation state of Pd on the clean catalyst has something to do on this fact: the higher the portion of metal oxidized, the higher the adsorption of OH in water from H-bounds. Therefore, for the Pd(0.25 wt.%)/P25 - PCS Lab catalyst, it was observed from XPS analysis that Pd was 54% oxidized at the surface, then the adsorption of water by H-bound is lower on -PCS Lab catalysts than the -CATHETER Lab catalysts. In the case of Pd(2 wt.%)/P25 - PCS Lab catalysts observed in Figure 5.84, most probably the Pd is partially oxidized in a higher proportion than the Pd(0.25 wt.%)P25 seen in Figure 5.84. That is why on the catalyst containig 2 wt.% of Pd is seen the band corresponding to the adsorption of OH in water from H-bounds, but this band seems weaker than the band observed in Figure 5.81 for the Pd/P25 catalyst.

For the catalyst containing 0.25 wt.% in Figure 5.84 is observed more clearly the two bands at around 3700 cm^{-1} corresponding to O-H stretching for OH groups in alcohols [180][181][183], also the sharp peak in 3400 cm^{-1} referred to stretching OH groups in methanol by H-bounds [65], and the bands corresponding to -CH stretching in alcohols (near to 2950 and 2900 cm^{-1}) [180][186]. These peak are not so clear on the catalysts containing 2 wt.% of Pd. The other two peaks in the region of 2880 and 2860 cm^{-1}, corresponding to dissociated CH_3O species [181][186] are also barely observed on the catalyst containing 2 wt.% of Pd.

In Figure 5.85, in the 2200 - 2500 cm^{-1} range is observed for both catalysts very weak peaks related to CO_2. For both catalysts is seen a band at around 1650 cm^{-1} corresponding to symmetrical scissoring of OH of H_2O [65][129][182]. The two bands at around 1450 cm^{-1} can be assigned to the vibrational mode of asymmetric and symmetrical scissoring of CH_3 that correspond to the adsorption of CH_3OH [186]. The

bands at around 1100 and 1020 cm^{-1} correspond to stretching C-O in alcohols [65][163][180] and peak near to 1000 cm^{-1} is assigned to stretching C=O in CH_3O species. The bands at around 980 and the one nearer to 900 cm^{-1} might be assigned to scissoring C-H of aldehydes [163] and bending C-O-H in carboxylic acids [180], respectively.

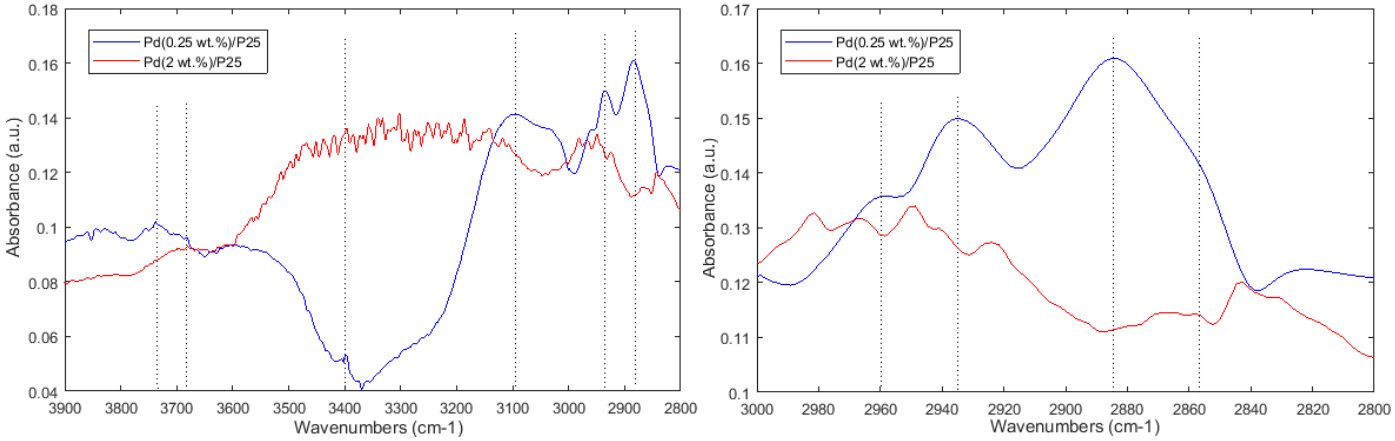

Figure 5.84. FTIR study: Pd/P25 - PCS Lab catalysts (2700 - 3900 cm^{-1}) and 2700 - 3000 cm^{-1} range. Experimental conditions: catalysts 1000 ppm, 2ml of a water - methanol (50 vol.%) solution under 7 LED's lamp (365 nm). Pd PD 3.2m20 method.

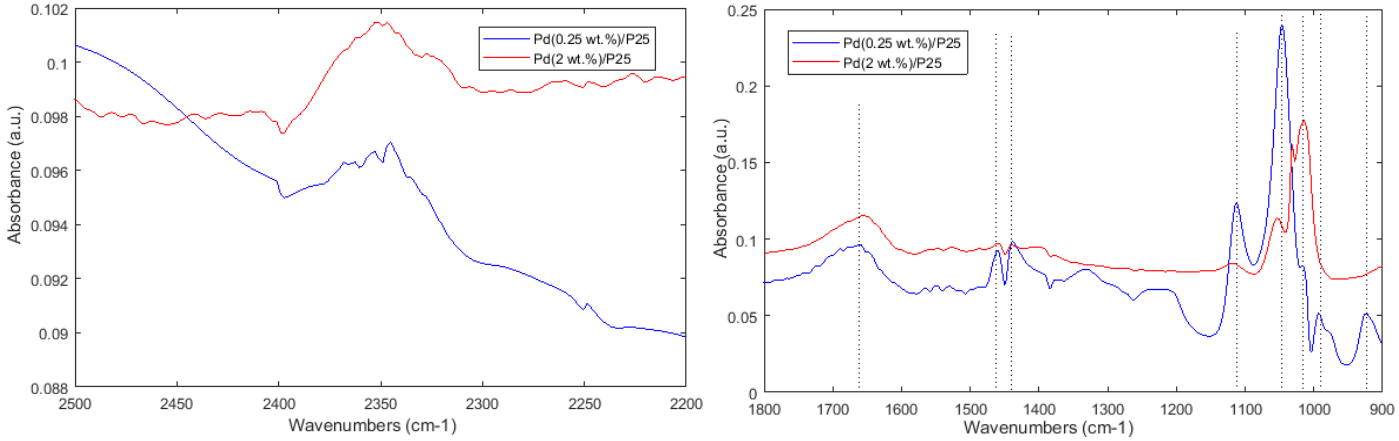

Figure 5.85. . FTIR study: PdP25 - PCS Lab catalysts, 2200 - 2500 cm^{-1} and 1100 -1800 cm^{-1} range.

5.2.5.5. Comparison: Pt(0.13 wt.%)/NT-WO_3, Pt(2 wt.%)/NT-WO_3 and Pd(0.27 wt.%)/NT-WO_3

Figure 5.86 shows the FTIR spectra comparison for Pt(0.13 wt.%)/NT-WO_3, Pt(2 wt.%)/NT-WO_3 and Pd(0.27 wt.%)/NT-WO_3 - PCS Lab catalysts between 2700 - 3900 cm^{-1} range at 90 min of irradiation. Only for the catalyst containing 2 wt.% of Pt is observed a signal between 3100 - 3500 cm^{-1} corresponding to water. For both Pd(0.27 wt.%)/NT-WO_3 and Pt(0.13 wt.%)/NT-WO_3, the band attributed to stretching OH by H-bounds in water is not seen.

Similar to Pd(0.21 wt.%)/NT-WO_3 - CATHETER Lab catalyst, the same catalysts but prepared in PCS Lab does not show the characteristic band attributed to water between 3000 - 3600 cm^{-1}, and the same absence is seen for the catalysts containing 0.25 wt.% of Pt. It confirms once again the possible suppression of OH adsorption of water from H-bounds due to the simultaneous presence of a metal, in this case, Pt, and WO_3. In the case of the highest metal content, some noise are observed in this region, which might mean very little adsorption of water by H-bounds on Pt(2 wt.%)/NT-WO_3, but this band is not specially appreciated as it was on Pd(2 wt.%)/P25 catalyst in Figure 5.84. From these results we could

conclude that only the simultaneous presence of few amount of metal, either Pd or Pt, and WO_3, suppress the H-bound from water.

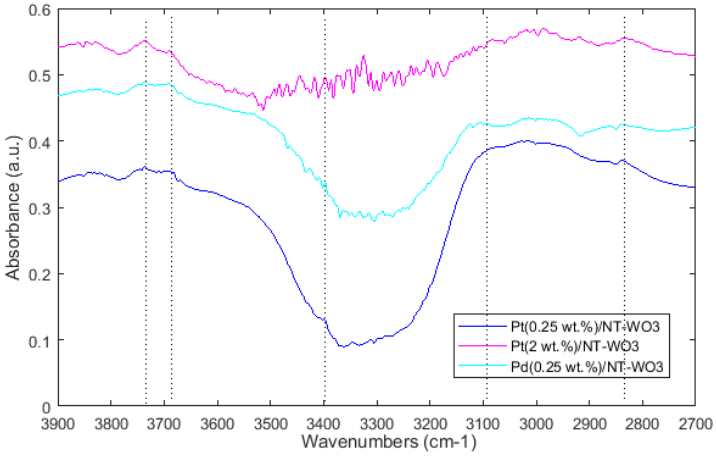

Figure 5.86. FTIR study: Pt/NT-WO_3 and Pd/NT-WO_3 - PCS Lab catalysts, 2700 - 3900 cm^{-1} range. Experimental conditions: catalysts 1000 ppm, 2ml of a water - methanol (50 vol.%) solution under 7 LED's lamp (365 nm). Pd PD 3.2m20 method.

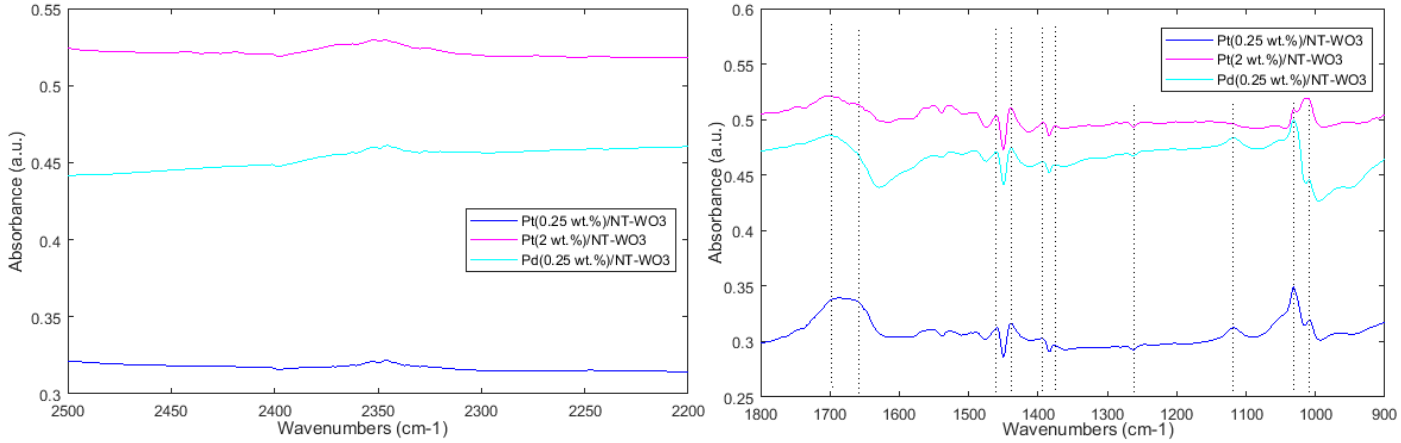

Figure 5.87. FTIR study: Pt/NT-WO_3 and Pd/NT-WO_3 - PCS Lab catalysts, 2200 - 2500 cm^{-1} range.

In Figure 5.87, in the 2200 - 2500 cm^{-1} range is observed for three catalysts very weak peaks related to CO_2. In Figure 5.87, the band at around 1700 cm^{-1} assigned to carbonyl C-H of aldehydes is seen for the three catalysts and the peak at around 1650 cm^{-1} attributed to symmetrical scissoring of OH of H_2O [65][129][182] seems more clear on Pt(0.27 wt.%)/NT-WO_3 PCS Lab catalyst. The two bands at around 1450 cm-1 is assigned to the vibrational mode of asymmetric and symmetrical scissoring of CH_3 that correspond to the adsorption of CH_3OH [186]. The bands at around 1100 and 1020 cm^{-1} correspond to stretching C-O in alcohols [65][163][180] and they are more clear for both catalysts containing 0.25 wt.% of metal. The peak close to 1000 cm^{-1} is assigned to stretching C=O in CH_3O species.

5.2.5.6. Comparison: Pd(0.23 wt.%)/P25-WO_3 and Pd(2 wt.%)/P25-WO_3 - PCS Lab catalysts

Figure 5.88 shows the FTIR spectra between 2800 - 3900 cm^{-1} for Pd(0.23 wt.%)/P25-WO_3 and Pd(2 wt.%)/P25-WO_3 - PCS Lab catalysts in a water - methanol (~50 vol.%) solution at every 3 min up to 15 min of irradiation, and then the final irradiation at 90 min. Quite comparable with previous ones, where there is a band at around 3000 - 3600 cm^{-1} for the catalyst containing 2 wt.% of metal, but no band is seen for the catalyst containing 0.25 wt.% of Pd. Once again is confirmed the fact that the simultaneous

presence of few amount of Pd and WO_3, suppress the adsorption of OH of water. The highest presence of Pd lead to a higher adsorption of water on the catalyst, even containing WO_3. For Pd(0.23 wt.%)/P25-WO_3 is seen, at around 3700 cm^{-1}, two bands corresponding to O-H stretching regions for CH_3OH [180][181][183] and a sharp peak in 3400 cm^{-1} corresponding to stretching O-H in alcohols [65]. This is not clearly observed for Pd(2 wt.%)/P25-WO_3*. The band at around 3100 cm^{-1} (Figure 5.88), which corresponds to -CH stretching in R-CHO species [180] is not seen in the Pd(2 wt.%)/P25-WO_3 catalyst, but it is, weakly, for the Pd(0.23 wt.%)/P25-WO_3. Figure 5.89 shows two weak bands corresponding to CO_2 [78][180] for both catalysts, and in Figure 5.90 is observed for Pd(0.23 wt.%)/P25-WO_3 a weak band at around 1700 cm^{-1} corresponding to stretching carbonyl C-H in aldehydes [163], but not for Pd(2 wt.%)/P25-WO_3. Instead, only for this latter, a clear peak is seen at around 1650 cm^{-1}, which is assigned to H_2O scissoring mode [65][129].

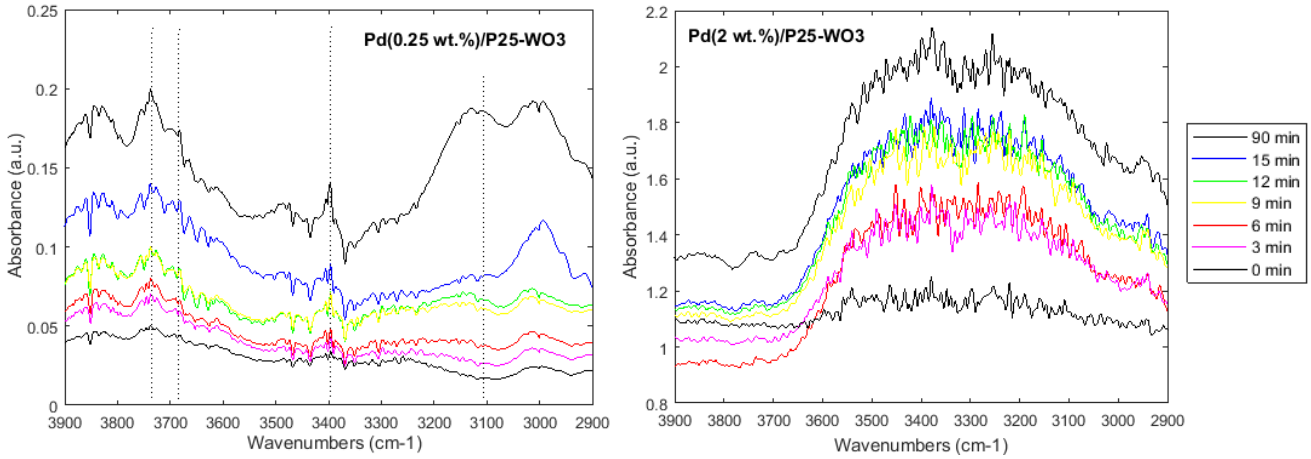

Figure 5.88. FTIR study: Pd/P25-WO_3 - PCS Lab catalysts, 2700 - 3900 cm^{-1} range. Experimental conditions: catalysts 1000 ppm, 2ml of a water - methanol (50 vol.%) solution under 7 LED's lamp (365 nm). Pd PD 3.2m20 method.

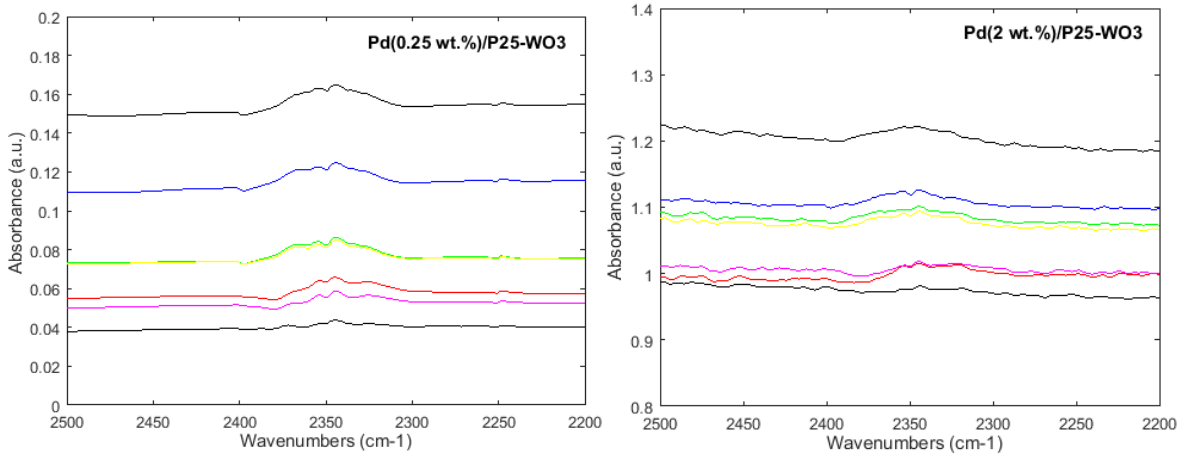

Figure 5.89. FTIR study: Pd/P25-WO_3 - PCS Lab catalysts, 2200 - 2500 cm^{-1} range.

For both catalysts, the sharp bands seen at around 1450 cm^{-1} can be attributed to the vibrational mode of asymmetric and symmetrical scissoring of CH_3, which would correspond to the adsorption of CH_3OH [186] and two other bands between 1350 - 1400 cm^{-1} that correspond to -COO- symmetric mode (1400 cm^{-1}) and C-H deformation of -COO- rocking (at around 1370 cm^{-1}) of adsorbed formate species [181]. The bands at around 1100 and 1020 cm^{-1} correspond to stretching C-O in alcohols [65][163][180], and the peak close to 1000 cm^{-1} is assigned to stretching C=O in CH_3O species.

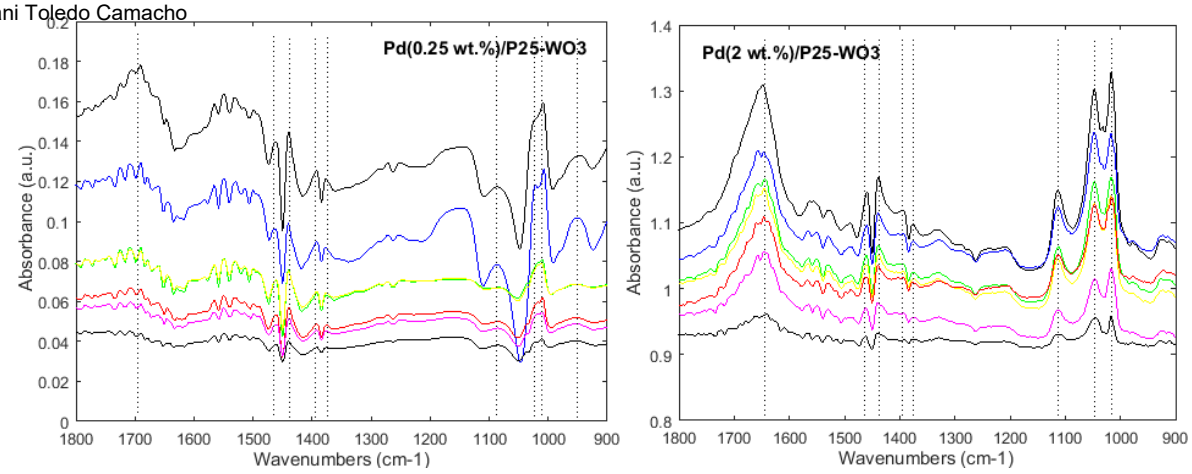

Figure 5.90. FTIR study: Pd/P25-WO_3 - PCS Lab catalysts, 900 - 1800 cm^{-1} range.

5.2.6. Pd/TiO_2-Cu - CATHETER Lab catalysts

In order to test a different metal, in this work we also wanted to explore some Cu supported P25 catalysts and see its effect on the H_2 evolution. Additionally, in this short section the effect of both Cu and Pd noble metal on the photocatalytic H_2 generation have been studied.

5.2.6.1. Effect of the Cu amount

Figure 5.91 represents the H_2 evolution vs. the irradiation time for three P25-Cu catalysts, where Cu content was varied: 0.5, 1 and 2 wt.%. It is observed. Firstly, it is observed that H_2 generation on bared-P25 is quite low compared to the catalysts containing Cu. Previously was explained that it is attributed to the high probability of the e^-/h^+ pairs recombination due to the absence of an e^- trap.

When Cu was incorporated, the H_2 evolution increased significantly. On P25 it was 0.017 ml/min.gCat and when was 0.5 wt.% of Cu was incorporated on P25, the H_2 evolution reaches up to 6.55 ml/min.gCat. When Cu was increased up to 1 wt.%, the H_2 evolution was improved but not so importantly as the previous improvement. And then, increasing once again the Cu content until 2 wt%, the H_2 evolution was declined, even it was lower than the H_2 evolution for P25-Cu(0.5 wt.%). The improvement on the H_2 evolution might be partially ascribed to the lower band-gap observed in three catalysts: 2.89, 2.91 and 2.93 eV for P25-Cu(0.5 wt.%), P25-Cu(1 wt.%) and P25-Cu(2 wt.%), respectively. Hence, Cu might work as an active trap centre for e^- due to heterojunction phenomena, preventing the e^-/h^+ pair recombination [102].

The existence of an optimal Cu load has been referred as an indicative of interfacial active sites in the peripheries of Cu particles[187]. Therefore, with the incorporation of 0.5 or 1 wt.% of Cu, the total peripheral length of Cu increased and also did the reactive zone for e^- trapping. From STEM images in Figures 5.27 and 5.28 is determined that the Cu nanoparticles were around 2 - 4 nm in size. Then, when the amount of Cu was increased up to 2 wt.%, similar that it was observed for Pd nanoparticles, the Cu nanoparticles size could increase (no STEM images showed for this catalyst). As a consequence, the Cu nanoparticles may be overlapped, forming clusters, reducing the reactive zone for e^- trapping. From XRD results, in Figure 5.17 (b), it was observed that Cu is on the surface of catalysts as CuO tenorite. From

literature, it is found that the incorporation of Cu can be in different chemical forms on the semiconductor, but it depends on the preparation condition [74][188][189][190][191].

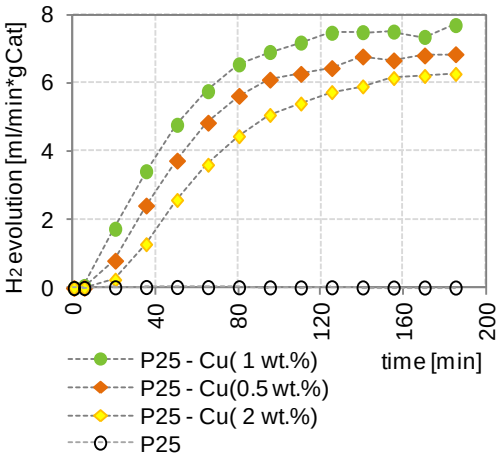

Figure 5.91. Effect of Cu content on H_2 generation for P25-Cu catalysts. Experimental conditions: 600 ml of water - methanol (50 vol.%) solution under simulated solar light (Xe Lamp, 300 - 800 nm, 250 W/m^2, $I_{250\text{-}450nm}$: 6.5x10^{-4} Einstein/min). Cu deposition by wi

Concerning the H_2 evolution profile, for the three catalysts, P25-Cu(0.5 wt.%), P25-Cu(1 wt.%) and P25-Cu(2 wt.%) it follows an initial induction period where H_2 evolution increased faster up to a plateau. Then, in the plateau it keeps close constant until the end of the irradiation. As it was explained before, the residence time (τ) in the SSL-system is near to 25 min (total volume of reactor is 750 ml and the flow inlet is 30 ml/min). Looking at induction period of three catalysts in Figure 5.91, which is around 120 min, it could be deduced that the remaining time up to reach the plateau might correspond to the formation of active sites for H_2.

The theories of H_2 generation on CuO theories are diverse [74]. Though we have seen that on Pd, the nanoparticle size has an important role on the H_2 generation, but for CuO nanoparticles, there are different opinions [186][191][192]. In the short review of Clarizia et al [74] is commented that the e^- transferring from TiO_2 toward CuO arises the Fermi level of TiO_2, which results in a more negative potential of the CB of CuO, promoting in that way the water reduction or H^+ ions reduction.

5.2.6.2. Effect of Pd photodeposition on P25-Cu catalysts

Pd photodeposition in-situ and ex-situ was performed on P25-Cu catalysts in order to observe the effect of a second co-catalyst on the H_2 evolution.

Figure 5.92 shows H_2 evolution for P25-Cu catalysts with some additional lines corresponding to their respective H_2 evolution when Pd was photodeposited in-situ to the reaction system. Therefore, in this figure is possible to see that only for the catalyst with the lowest content of Cu, P25-Cu(0.5 wt.%), when 0.25 wt.% of Pd was added directly to the reaction solution, the H_2 evolution increased from 6.70 up to 8.68 ml/min.gCat. On the opposite side, when Pd was added to the reaction containing the catalysts with 1 or 2 wt.% of Cu on P25, the H_2 evolution decreased from 7.50 to 7.18 ml/min.gCat and from 6.36 to 4.83 ml/min.gCat, respectively. Although it is not clear, the effect when Pd is photodeposited in-situ might be that Pd nanoparticles are deposited as Pd^0 as they are already under photo-reductive

conditions (reductive photodeposition) [117]. Then, in spite H_2 might be forming, in presence of CuO, this H_2 could be participating in the CuO reduction on the TiO_2 towards Cu^0 [194].

Figure 5.93 presents the H_2 evolution of two P25-Cu catalysts and their respective catalysts when 0.25 wt.% was photodeposited ex-situ. Additionally, Pd was also deposited by wi on P25-Cu(0.5 wt.%) catalyst. For the catalysts with 0.5 wt.% of Cu is seen that H_2 evolution was improved when Pd was photodeposited ex-situ, but it was not better than the catalysts with Pd photodeposited in-situ (8 ml/min.gCat). When Pd was incorporated by wi, the H_2 evolution was 9.61 ml/min.gCat. For P25-Cu(1 wt.%), when Pd was photodeposited ex-situ, the H_2 evolution was 8.41 ml/min.gCat.

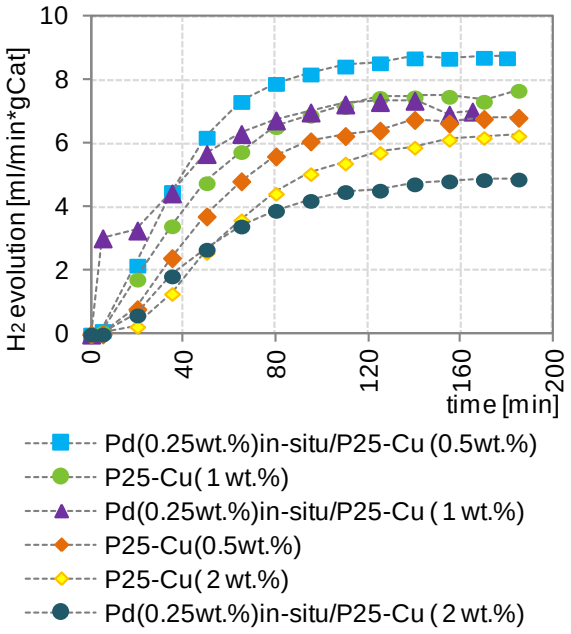

Figure 5.92. Effect of in-situ Pd PD on H_2 generation for P25-Cu catalysts. Cu deposition by wi and Pd PD in-situ.

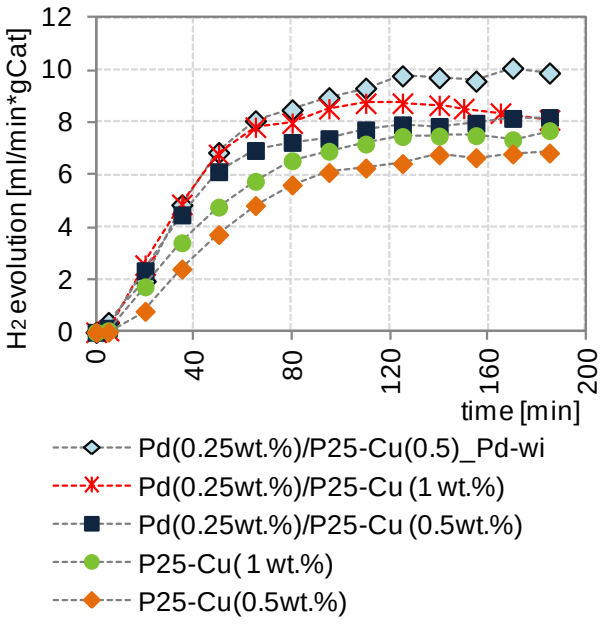

Figure 5.93. Effect of in-situ Pd PD on H_2 generation for P25-Cu catalysts. Cu deposition by wi and Pd PD in-situ.

It seems there is not a synergy effect between CuO and Pd when CuO content is 1 or 2 wt.%. Only at low CuO content was observed an improvement. Probably the presence of two co-catalysts would produce a shadow effect on P25. On this regards, it can be observed in Table 7 a slight detrimental in the maximum light absorption for the catalyst containing 1 wt.% of Cu and 0.25 wt.% of Pd, 426 nm for P25-Cu(1 wt.%) and 418 for Pd(0.25 wt.%)/P25-Cu(1 wt.%) deposited Cu by wi+C350 and Pd by PD 2m10. On the other hand, the similar maximum light absorption was observed for the catalysts containing 0.5 wt.% of Cu when 0.25 wt.% of Pd was added, 429 nm for both P25-Cu(0.5 wt.%) and Pd(0.25 wt.%)/P25-Cu(0.5 wt.%).

Another explanation of the H_2 evolution detriment when Pd is incorporated might be that a Cu content higher than 0.5 wt.% might be leading to the formation of Pd cluster, which work as e^-/h^+ recombination centres because the average distance between trapping sites decreases when the number of the cluster increase [194].

5.3. Results comparison

In results comparison we present firstly the section "*5.3.1 Quantum yield*", where it is shown the quantum yield calculation and in section "*5.3.2 Quantum yield and H2 generation set-up comparison*" the most representative quantum yield for each one of the group of catalysts mentioned above in the respective reaction system where they were tested (SSL-system, UVA-system, PPS-system or SS-system). Additionally, some data exploration for H_2 generation and φ (%) in the SSL-system are presented in order to see if there is a tendency pattern between the catalysts nature, amount of Pd and Pd PD method on the H_2 generation or the quantum yield.

5.3.1. Quantum yield calculation

In the present work, two types of hole scavenger sacrificial agents have been used. Methanol is the simplest alcohol, which can give an overview about the behavior of the new catalysts developed (Pd/TiO_2-WO_3) in this investigation, and also glycerol, to compare with a more complex molecule. In addition, a real wastewater containing a mixture of organic compounds has been tested. Therefore, in order to have a better knowledge about the photocatalytic activity of these materials, they are also compared in terms of quantum yields. The quantum yield (QE or φ) (%) was calculated according to the literature as follows [121]:

$$\varphi = \frac{\frac{n(H_2\ molecules\ formed)}{unit\ time}}{\frac{n\ (photons\ exposed)}{unit\ time}} . 100 \quad (\%) \qquad (5.2.1.1)$$

For Eq. (5.2.1.1), H_2 molecules formed are calculated from H_2 rate (mol/min.gCat), taking into account the amount of catalyst used in a typical photocatalytic experiment; and the photons exposed are determined taking into account actinometrical data.

5.3.2. Quantum yield and H_2 generation set-up comparison

Tables 17 - 25 show the quantum yields for the most representative catalysts in every group of catalysts in the different photocatalytic configuration set-up studied in this investigation. Then, each table shows information about the total volume of H_2 produced during the irradiation time, rate of H_2 (mol/min.gCat), H_2 evolution (ml/min.gCat) and the quantum yield φ(%).

Table 17. Quantum yields for w-Pd/TiO_2(-WO_3) - CATHETER Lab catalysts in the SSL-system

Catalyst	Weight% (ICP-OES)	Total volume of H_2 [ml]	Rate H_2 [mol/min.gCat]	H_2 evolution [ml/min.gCat]*	Quantum Yield φ (%)
$Pd/NT-WO_3$-4w	0.013	31.8	6.5 x10-5	1.5 ± 0.3**	1.0
$Pd/P25-WO_3$-4w	0.011	16.8	5.1 x10-5	1.1 ± 0.3	0.8
Pd/P25-4w	0.009	14.6	3.0 x10-5	0.7 ± 0.4	0.5
$NT-WO_3$	-	5.0	2.1 x10-5	0.5	0.3
Pd/TiO_2-A-4w***	0.007	1.3	1.1 x10-5	0.2	0.2
$P25-WO_3$	-	0.1	1.7 x10-7	0.004	0.0
P25	-	0.0	8.0 x10-7	0.02	0.0
TiO_2-A	-	0.0	4.1 x10-7	0.01	0.0

*** Experimental conditions:** catalyst 167 ppm, 600 ml of a water - methanol (50 vol.%) solution under simulated solar light (Xe Lamp, 300 - 800 nm, 250 W/m^2, $I_{250\text{-}450\ nm}$: 6.5x10^{-4} Einstein/min). Irradiation time: 185 min

** The uncertainty was estimated taking into account the repeatability, resolution and accuracy equipment and calibration curve.
*** A: Anatase

For w-Pd/TiO_2-WO_3 - CATHETER Lab catalysts in the SSL-system (Table 17), the highest φ is 1% for the catalyst containing the NT, followed by the 0.8 % for the catalyst containing P25 and WO_3 and the 0.5 % of Pd/P25. The total volume of H_2 produced on Pd(0.013 wt.%)/NT-WO_3-4w, Pd(0.011 wt.%)/P25-WO_3-4w and Pd(0.009 wt.%)/P25-4w in 185 min was scarcely 31.8, 16.8 and 14.6 ml. Now, contrary to these catalysts, for m-Pd/TiO_2-WO3 - CATHETER Lab catalysts in the SSL-system, different Pd/P25 catalysts with nominal Pd(0.25 wt.%) showed higher H_2 and φ values than those catalysts containing WO_3. Here is possible to observe the influence of the Pd PD method on the catalyst activity toward the photocatalytic H_2 generation. On one hand, the presence/absence of a sacrificial agent in the PD method, where for Pd(21 wt.%)/P25-4m10, Pd(0.26 wt.%)/NT-WO_3-4m10 and Pd(0.27 wt.%)/P25-WO_3-4m10, the φ was 10.4, 5.1 and 7.2 points higher than their respective catalysts prepared by -4w method. Here is very important to take under consideration the fact of the real Pd deposited on the catalysts.

Table 18. Quantum yields for m-Pd/TiO_2(-WO_3) -CATHETER Lab catalysts in the SSL-system

Catalyst	Weight% (ICP-OES)	Total volume of H_2 [ml]	Rate H_2 [mol/min.gCat]	H_2 evolution [ml/min.gCat]*	Quantum Yield φ (%)
Pd in-situ/P25	0.25	345	8.4 x10-4	20.1	14.5
Pd/P25-2m10	0.24	295	8.0 x10-4	17.9 ± 1.9	11.8
Pd/P25-2m5	0.25	243	7.1x10-4	16 ± 1.4	11
Pd/P25-4m10	0.21	227	6.8 x10-4	15.2 ± 1.5	10.4
Pd/P25-2m10	0.09	195	5.2x10-4	11.6 ± 1.6	8.0
Pd/P25-wi	0.25	183	4. 9x10-4	11 ± 1.8	7.6
Pd/P25-2m10	0.51	197	5.3x10-4	11.8 ± 2.3	8.3
Pd/P25-2m1	0.23	117	4. 4x10-4	9.8 ± 1.9	6.7
Pd in-situ/NT-WO_3	0.25	108	3.1x10-4	7.0	4.9
Pd in-situ/P25-WO_3	0.25	103	3.0x10-4	6.8	4.7
Pd/NT-WO_3-2m10	0.21	106	2.8x10-4	6.6 ± 0.5	4.1
Pd/NT-WO_3-4m10	0.26	83	2.8x10-4	6.2 ± 0.6	4.1
Pd/NT-WO_3 -1m10	0.15	76	2.9x10-4	6.5 ± 0.9	3.9
Pd/P25-WO_3-4m10	0.27	70	2.4x10-4	5.3 ± 0.4	3.6
Pd/P25-WO_3-2m10	0.23	66	2.4x10-4	5.1 ± 0.7	3.4
Pd/P25-WO_3-2m1	0.23	54	2.1x10-4	4.7 ± 0.6	3.4

*** Experimental conditions:** catalyst 167 ppm, 600 ml of a water - methanol (50 vol.%) solution under simulated solar light (Xe Lamp, 300 - 800 nm, 250 W/m^2, $I_{250\text{-}450\ nm}$: 6.5x10^{-4} Einstein/min). Irradiation time: 185 min.

On the other hand, looking at Table 18, we see other parameters, such as the sacrificial agent concentration and the catalyst concentration in the PD solution, that exert an influence on the φ values. For instance, for the Pd/P25 catalysts such as Pd in-situ/P25, Pd/P25-2m10, Pd/P25-2m5, Pd/P25-4m10, Pd/P25-wi, Pd/P25-2m1 containing nominal Pd(0.25 wt.%), the φ was different: 14.5, 11.8 11, 10.4, 7.6 and 6.7 % respectively. Another example is seen for the Pd(0.25 wt.%) in-situ samples containing WO_3, where for Pd in-situ/NT-WO_3 and Pd in-situ/P25-WO_3 catalysts, the φ was 4.9 and 4.7 %, respectively, and on Pd(0.21 wt.%)/NT-WO_3 and Pd(0.23 wt.%)/P25-WO_3-2m10 catalysts, the φ was 4.1 and 3.4 %, respectively. In this later example, we see that only by changing the moment where Pd is added to the PD solution, the φ also changes.

Now, testing the same three Pd(0.24wt.%)/P25-2m10, Pd(0.21 wt.%)/NT-WO_3-2m10 and Pd(0.23 wt.%)/P25-WO_3-2m10 catalysts in the SSL-system and UVA-system, we also see different φ values for the same catalysts. For example, in the SSL-system (Table 18), the total volume of H_2 produced on Pd(0.24wt.%)/P25-2m10, Pd(0.21 wt.%)/NT-WO_3-2m10 and Pd(0.23 wt.%)/P25-WO_3-2m10 catalysts in

185 min was 295, 106 and 66 ml, and in the UVA-system (Table 19) they produced 186, 56 and 28 ml, respectively. In terms of φ, in the SSL-system, φ was 11.8, 4.1 and 3.4 %, and in the UVA-system, it was 41.2, 18.8 and 9.9 %, respectively. It means than only by changing the set-up configuration, the φ was totally different. Of course, it is probably due to the type of irradiation (solar vs. UVA light), though it could also be due to the way as the irradiation is distributed (according to the location of the lamp), but this fact reflects once more the sensitivity of this parameter, the φ, to conclude if a catalyst is good or not. Hence, up to this point is possible to observe the importance of a good definition of the reaction system when we are comparing our photocatalysts with other results from literature.

In Table 20 is possible to observe that in the PPS-system, the highest φ was 2.2 % for the Pd(0.24 wt.%)/P25 - 2m10 in a water-glycerol (5 vol.%) solution and 2.1 % in methanol (5 vol.%). Their respective total volume of H_2 in 6 hours of natural solar irradiation were 8608 and 8277 ml. In Table 21 is seen that for the same catalyst but in the SSL-system and in the same glycerol concentration (5 vol.%), the φ was 6.9 % and the total volume of H_2 produced in 185 min was only 150 ml. Here, once again is observed the differences in the quantum yields values for the same catalysts tested in a different set-up configuration for the photocatalytic H_2 generation.

Table 19. Quantum yields for m-Pd/TiO_2(-WO_3) - CATHETER Lab catalysts in the UVA-system

Catalyst	Weight % (ICP-OES)	Total volume of H_2 [ml]	Rate H_2 [mol/min.gCat]	H_2 [ml/min.gCat]*	Quantum Yield φ (%)
Pd/P25-2m10	0.25	186	8.6x10-4	19.2 ± 3.7	41.2
Pd/NT-WO_3-2m10	0.21	56	3.7x10-4	8.4 ± 0.6	18.8
Pd/P25-WO_3-2m10	0.23	28	1.9x10-4	4.2 ± 0.6	9.9

* **Experimental Conditions**: catalysts 166.67 ppm, 250 ml of a water-methanol (50 vol.%) solution under UVA light (300-400 nm; 4 lamps of 15 W/lamp, $I_{250\text{-}450\ nm}$: $8.3x10^{-5}$ Einstein/min). Irradiation time: 185 min.

Table 20. Quantum yields for m-Pd/TiO_2(-WO_3) - CATHETER Lab catalysts in the PPS-system

Catalyst	Weight% (ICP-OES)	Sacrificial Agent	Total volume of H_2 [ml]	Max. rate H_2 [mol/min.gCat]	Max. H_2 evolution [ml/min.gCat]*	Quantum Yield φ (%)
Pd/P25-2m10	0.24	5 vol.% Glycerol	8608	3.7 x10-4	8.2	2.2
		5 vol.% Methanol	8377	4.1 x10-4	9.3	2.1
		0.37 vol.% Glycerol	6921	3.4 x10-4	7.6	2.4
		0.37 vol.% Methanol	4832	2.3 x10-4	5.2	1.3
		0.2 vol.% Methanol	3762	2.5 x10-4	5.6	1.0
Pd/NT-WO_3-2m10	0.21	0.37 vol.% Methanol	1849	1.1 x10-4	2.3	0.6
Pd/P25-WO_3-2m10	0.23	0.37 vol.% Methanol	1642	6.8 x10-5	1.5	0.5

*** Experimental Conditions:** catalyst 200 ppm, 25 L of a water-sacrificial agent solution under solar light (Incident radiation that corresponds to wavelength below 400 nm; $Q_{UV,n}$on the experimental days of autumn in Almería (around 10 h to 16 h) is 30 - 35 kJ/L. Irradiation time around 6 h.

On one hand, the much higher total volume of H_2 observed in the PPS-system is associated to the largest scale of the photocatalytic H_2 configuration set-up and on the other hand, the lowest φ values are associated to the real number of photons being absorbed by the catalysts, which is strongly associated to the configuration set-up itself and the irradiation system. When three Pd(0.24wt.%)/P25, Pd(0.21 wt.%)/NT-WO_3 and Pd(0.23 wt.%)/P25-WO_3-2m10 catalysts were tested in the PPS-system in a water-methanol (0. 37 vol.%) solution, the φ fall down until 1.3, 0.6 and 0.5 %. Taking into account, that the work volume was 25 L, the total volume of H_2 produced for these three catalysts in a water-methanol (0. 37 vol.%) in 6 hour of natural solar irradiation was 4832, 1849 and 1642 ml. In this table is possible to

see the influence of the sacrificial agent nature on the activity of the catalysts toward the photocatalytic H_2 generation.

Moving on to the SS-system, Table 22 shows the φ values for m-Pd/TiO_2(-WO_3) - CATHETER Lab catalysts tested in the SS-system. Checking only those tests performed in **200 ppm of catalyst** and in a **water-methanol (50 vol.%) solution**, is possible to observe the differences in the total volume of H_2 of Pd(0.24 wt.%)/P25-2m10, Pd(0.21 wt.%)/NT-WO_3-2m10 and Pd(0.23 wt.%)/P25-WO_3-2m10 in the SSL-system (Table 18), UVA-system (Table 19) and SS-system (Table 22). With these results can see the influence of the H_2 set-up on the H_2 evolution or the quantum efficiency results. For instance, though the superpower lamp in the SS-system, the reaction system is not able to absorb all the photons emitted, then, the φ fall down, as it is observed in Figure 5.94.

Table 21. Quantum yields for m-Pd/TiO_2(-WO_3) - CATHETER Lab catalysts in the SSL-system

Catalyst	Weight% (ICP-OES)	Sacrificial Agent	Total volume of H_2 [ml]	Max. rate H_2 [mol/min.gCat]	Max. H_2 evolution [ml/min.gCat]*	Quantum Yield φ (%)**
Pd/P25-2m10	0.24	Glycerol	150	4.5 x10-4	10.1	6.9
Pd/P25-2m10	0.24	Methanol	113	3.1 x10-4	7.0	4.8
Pd/NT-WO_3-2m10	0.21	Glycerol	56	1.4 x10-4	3.1	2.1
Pd/P25-WO_3-2m10	0.23	Glycerol	43	1.1 x10-5	2.5	1.4

*** Experimental conditions:** catalyst 167 ppm, 600 ml of a water - sacrificial agent (5 vol.%) solution under simulated solar light (Xe Lamp, 300 - 800 nm, 250 W/m^2, $I_{250\text{-}450\ nm}$: 6.5x10^{-4} Einstein/min). Irradiation time: 185 min

Table 22. Quantum yields for m-Pd/TiO_2(-WO_3) - CATHETER Lab catalysts in the SS-system

Catalyst	Weight% (ICP-OES)	Catalyst and Sacrificial agent Concentration	Total volume of H_2 [ml]	Rate H_2 [mol/min.gCat]	H_2 evolution [ml/min.gCat]*	Quantum Yield φ (%)**
Pd/NT-WO_3-2m10	0.21	200 ppm; 50 vol.%	1.2	1.7 x10-4	3.8	1.3
		500 ppm; 50 vol.%	1.9	9.9 x 10-5	2.2	1.9
		1000 ppm; 50 vol.%	3.7	1.1 x10-4	2.5 ± 0.2	4.3
		1000 ppm; 7 vol.%	2.7	9.8 x10-5	2.2 ± 0.1	3.8
		1000 ppm; 33 vol.%	3.5	5.8 x10-5	1.3 ± 0.2	2.4
Pd/P25-WO_3-2m10	0.23	200 ppm; 50 vol.%	1.3	1.6 x10-4	3.6	1.3
		500 ppm; 50 vol.%	2.6	1.3 x10-4	3.0	2.6
		1000 ppm; 50 vol.%	6.5	1.1 x10-4	2.5 ± 0.4	4.4
		1000 ppm; 7 vol.%	1.5	8.3 x10-5	1.9 ± 0.1	3.2
		1000 ppm; 33 vol.%	2.6	6.8 x10-5	1.5 ± 0.2	2.6
Pd/P25-2m10	0.24	200 ppm; 50 vol.%	3.4	4.9 x10-4	11	3.7
		500 ppm; 50 vol.%	5.0	2.2 x10-4	4.8	4.1
		1000 ppm; 50 vol.%	5.4	1.4 x10-4	3.1	5.2
		1000 ppm; 7 vol.%	4.0	1.0 x10-4	2.3 ± 0.1	4.0
		1000 ppm; 33 vol.%	2.7	6.0 x10-5	1.3 ± 0.6	2.1

*** Experimental conditions:** 15 ml of a water - methanol solution under irradiation of an Optical fiber UV/Vis-Emission: ca. 8W/cm^2 (280-700 nm, $I_{250\text{-}450\ nm}$: 3.88x10^{-5} Einstein/min). Irradiation time: 120 min

In order to have a global view of this fact, Figure 5.94 shows the data exploration for φ values for these three catalysts of reference: Pd(0.24 wt.%)/P25, Pd(0.21 wt.%)/NT-WO_3 and Pd(0.23 wt.%)/P25-WO_3 - 2m10 - CATHETER Lab catalyst. The highest φ values on all three H_2 set-up are on Pd/P25 catalyst, followed by Pd/NT-WO_3 and Pd/P25-WO_3. The UVA-system shows the highest φ values for three catalysts and the SS-system the worst results. Pd/P25 catalyst shows to be more sensitive to changes in the H_2 set-up, while Pd/P25-WO_3 does not. From these results it seems the UVA-system is the most efficient set-up for the photocatalytic H_2 generation. For m-Pd/TiO_2(-WO_3) and m-Pt/TiO_2(-WO_3) - PCS Lab catalysts, in Table 23 and 24 are presented their φ values. For these two groups, the H_2 test in the SS-system were performed in 1000 ppm of catalyst and in a water-methanol (50 vol.%) solution. For the

catalysts containing Pd, among the both metal PD methods studied in PCS Lab, -2m10 and 3.2m20 method, those catalysts prepared by 2m10 method trended to show the highest φ values. And concerning the amount of Pd, only for Pd/NT-WO_3, the φ values were higher at the lower Pd content, meanwhile for Pd/P25 and Pd/P25-WO_3 catalysts, the catalyst containing the higher amount of Pd presented a higher φ value. For the catalysts containing Pt, the highest φ values seem to be more related to the higher amount of metal.

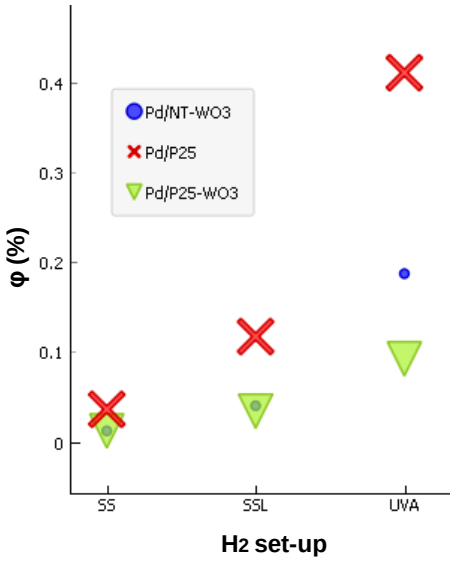

Figure 5.94. Data exploration for φ (%) in SSL, UVA and SS-system for Pd/TiO_2(-WO_3) - CATHETER Lab catalysts. Catalysts nature (**colour** and **shape**) and amount of Pd [wt.%] (**size**). **Experimental conditions: SSL and UVA systems**: catalyst 167 ppm, 600 (SSL), 250 (UVA) ml of water - methanol (50 vol.%) solution. **SS-system**: catalyst 200 ppm, 15 ml of water - methanol (50 vol.%) solution.

Table 23. Quantum yields for m-Pd/TiO_2(-WO_3) - PCS Lab catalysts in the SS-system

Catalyst	Weight% (ICP-OES)	Total volume of H_2 [ml]	Rate H_2 [mol/min.gCat]	H_2 evolution [ml/min.gCat]*	Quantum Yield φ (%)
Pd/NT-WO_3-2m10	0.19	3.8	1.0 x10-4	2.3	3.9
	2	3.2	8.5 x10-5	1.9	3.3
Pd/NT-WO_3-3.2m20	0.27	2.6	6.7 x10-5	1.5	2.6
	2	2.0	5.5 x10-5	1.2	2.1
Pd/P25-WO_3-2m10	0.25	2.7	7.1 x10-5	1.6	2.7
	2	2.9	8.0 x10-5	1.8	3.1
Pd/P25-WO_3-3.2m20	0.23	2.5	6.6 x10-5	1.5	2.5
	2	3.0	8.4 x10-5	1.9	3.2
Pd/P25-2m10	0.25	4.0	1.1 x 10-4	2.4	4.0
	2.01	4.6	1.2 x10-4	2.7	4.7
Pd/P25-3.2m20	0.25	3.5	8.6 x10-5	1.9	3.3
	2	4.1	1.1 x10-4	2.4	4.0

*** Experimental conditions:** 15 ml of a water - methanol solution under irradiation of an Optical fiber UV/Vis-Emission: ca. 8W/cm^2 (280-700 nm, $I_{250-450\ nm}$: 3.88x10^{-5} Einstein/min). Irradiation time: 120 min

For instance, comparing the φ values of these two group of - PCS Lab catalysts in the SS-system (Table 23 and 24) with the SSL-system (Table 25), it is seen that for the catalysts containing Pt, the φ values in the SS-system for Pd/P25, Pd/NT-WO_3 and Pd/P25-WO_3 are 5.8, 6.3 and 4.8%, respectively, while in the SSL-system, they are 9.7, 4.4 and 3.5%, respectively. From these results is once again seen that the φ values not only reflect the catalytic efficiency of a material toward the H_2, but also it is closely conditioned by the reaction system. The φ values for three supports P25, NT-WO_3 and P25-WO_3 in the SS-system are 0.3, 0.3 and 0.1 %.

In Figures 5.95 and 5.96, both group -CATHETER Lab and -PCS Lab of catalysts are compared in terms of the H_2 evolution in both SSL- and SS-system. Figures 5.95 and 5.96 shows the H_2 generation in the SSL-system and SS-system, respectively, for three Pd/P25, Pd/NT-WO_3 and Pd/P25-WO_3 catalysts, where Pd was photodeposited in the CATHETER Lab (red markers) and PCS Lab (blue markers). The Pd PD of both group of catalysts (- CATHETER Lab and - PCS Lab catalysts) was carried out using the same PD conditions of methanol concentration (10 vol. %), catalyst concentration (2000 ppm) and Pd amount (0.25 wt.%) but varying the number of photons emitted by the lamp.

In this way, for the catalysts labelled as CATHETER Lab, which were prepared in Tarragona, the PD was performed using an UV lamp (λ: 365 nm, 6 W for around 14 h, **$5.55x10^{23}$ photons emitted**) and the catalysts labeled as PCS Lab, which were prepared in Enschede, the PD was carried out using 7 UV lamps (λ_{max}: 368 nm, 18 W/lamp for 4 h, **$3.33x10^{24}$ photons emitted**). The number of photons emitted by the lamp (4 h of irradiation) in PCS Lab is 6 times higher than the lamp in CATHETER Lab (14 h or irradiation) for the PD procedure.

Table 24. Quantum yields for m-Pt/TiO_2(-WO_3) - PCS Lab catalysts in the SS-system

Catalyst	Weight% (ICP-OES)	Total volume of H_2 [ml]	Rate H_2 [mol/min.gCat]	H_2 evolution [ml/min.gCat]*	Quantum Yield φ (%)
Pt/NT-WO_3-2m10	0.24	6.2	1.6 x10-4	3.7	6.3
	2	7.5	2.1 x10-4	4.7	8.2
Pt/NT-WO_3-3.2m20	0.13	5.3	1.4 x10-4	3.2	5.5
	2	8.1	2.2 x10-4	4.9	8.4
Pt/P25-WO_3-2m10	0.21	4.9	1.2 x10-4	2.8	4.8
	2	5.1	1.3 x10-4	3.0	5.2
Pt/P25-WO_3-3.2m20	0.2	2.0	4.7 x10-5	1.1	1.8
	2	6.4	1.9 x10-4	4.2	7.2
Pt/P25-2m10	0.18	5.6	1.5 x10-4	3.4	5.8
	1.49	6.2	1.6 x10-4	3.5	6.1
Pt/P25-3.2m20	0.15	5.0	1.2 x10-4	2.8	4.7
	2	5.5	1.5 x10-4	3.3	5.7

*** Experimental conditions:** 15 ml of a water - methanol solution under irradiation of an Optical fiber UV/Vis-Emission: ca. 8W/cm^2 (280-700 nm, $I_{250\text{-}450\ nm}$: $3.88x10^{-5}$ Einstein/min). Irradiation time: 120 min.

Table 25. Quantum yields for Pd/TiO2(-WO3) and Pt/TiO_2(-WO_3) - PCS Lab catalysts in the SSL-system

Catalyst	Weight% (ICP-OES)	Total volume of H_2 [ml]	Rate H_2 [mol/min.gCat]	H_2 evolution [ml/min.gCat]*	Quantum Yield φ (%)
Pd/P25-2m10	0.25	220	3.8 x10-4	8.4	5.8
Pd/NT-WO_3-2m10	0.19	184	3.4 x10-4	7.6	5.2
Pd/P25-WO_3-2m10	0.25	65	2.4x10-4	5.4	3.7
Pt/P25-2m10	0.18	180	6.3 x10-4	14.2	9.7
Pt/NT-WO_3-2m10	0.24	89	2.9x10-4	6.5	4.4
Pt/P25-WO_3-2m10	0.21	78	2.3x10-4	5.1	3.5

*** Experimental conditions:** catalyst 167 ppm, 600 ml of a water - methanol (50 vol.%) solution under simulated solar light (Xe Lamp, 300 - 800 nm, 250 W/m^2, $I_{250\text{-}450\ nm}$: $6.5x10^{-4}$ Einstein/min). Irradiation time: 185 min

In Figure 5.95, in the SSL-system, the Pd/P25-CATHETER Lab catalyst showed a higher H_2 evolution than Pd/P25-PCS Lab catalyst. Then, the H_2 evolutions in the plateau for Pd/P25-CATHETER Lab and PCS Lab catalysts are 17.9 and 8.4 ml/min.gCat, respectively. On the other hand, though on both catalysts containing WO_3, the H_2 evolution on -PCS Lab catalyst was slightly higher than on the -CATHETER Lab catalysts, they are not importantly higher. For instance, on Pd/NT-WO_3 catalysts, the H_2 evolution in the plateau was 7.6 and 6.3 ml/min.gCat for -PCS Lab and -CATHETER Lab catalyst,

respectively (1.2 times). On Pd/P25-WO_3-PCS Lab and -CATHETER Lab catalysts, both are in practice similar (5.4 and 5.1 ml/min.gCAT, respectively).

A first fact to comment on regard the results presented in Figures 5.95 and 5.96 is the one related to the configuration system for the metal photodeposition. Despite the lamp for PD in PCS Lab emitted 6 times more photons during the PD time than the lamp for PD in CATHETER Lab ($3.33x10^{24}$ vs. $5.55x10^{23}$ photons), the catalysts prepared in the PCS Lab were not importantly better.

In Figure 5.96, this is corroborated once again more, where in the SS-system, the Pd/P25-CATHETER Lab and Pd/P25-WO_3 -CATHETER Lab catalysts presented higher H_2 evolution than their respective -PCS Lab catalysts. In the case of Pd/P25-WO_3, both are quite similar.

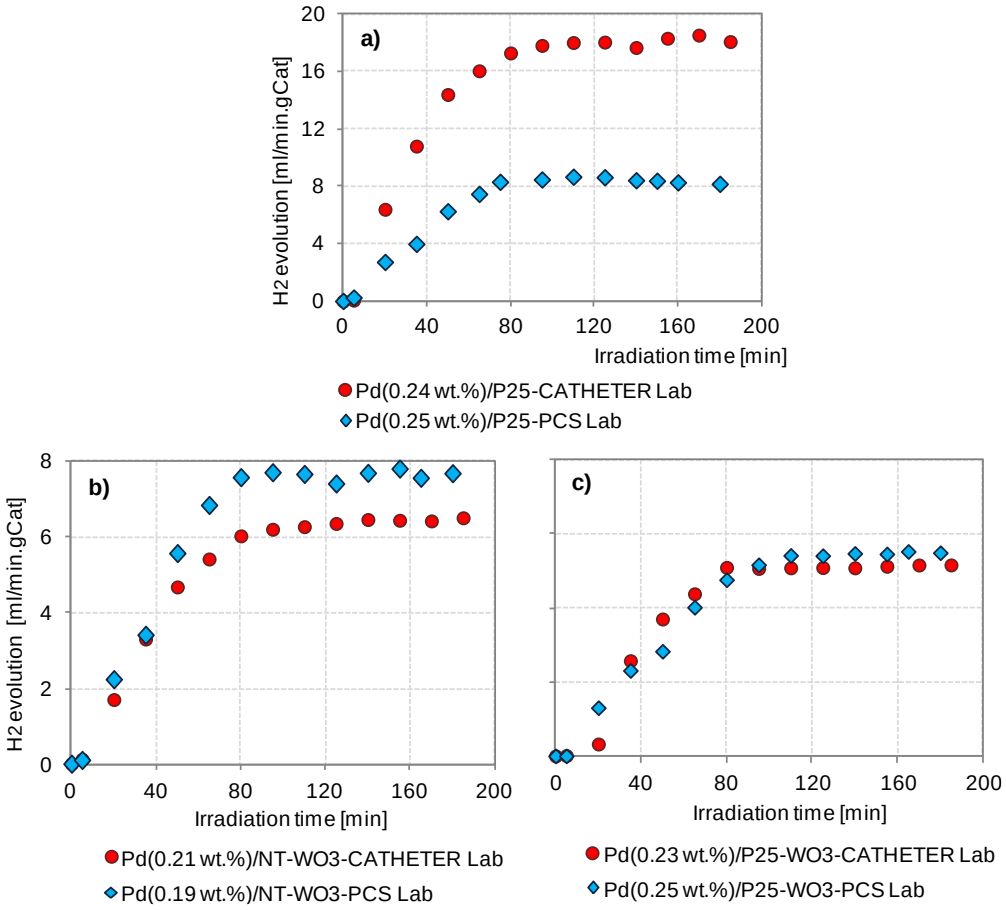

Figure 5.95. H_2 generation in the **SSL-system** (Tarragona) comparing place of catalyst preparation. **a)** Pd/P25; **b)** Pd/NT-WO_3 and **c)** Pd/P25-WO_3. Experimental conditions: catalyst 167 ppm, 600 ml of a water - methanol (50 vol.%) solution under simulated solar light (λ: 300 - 800 nm; 250 W/m^2, $I_{250\text{-}450nm}$: $6.5x10^{-4}$ Einstein/min).

Therefore, we see that the PD configuration itself plays an important role in the synthesis of more efficient photocatalysts toward the H_2. It means that not only in the photocatalytic reaction system for H_2 generation is important to ensure a maximum absorption of photons, but also in the photodeposition system (synthesis of the material). It must say that most probably the Ca impurities observed by XPS analysis on the -PCS Lab catalysts contribute negatively on the H_2 evolution, for instance a direct effect was observed in the important diminishing in the S_{BET} of all the -PCS Lab catalysts. The second fact is related to the H_2 evolution data and its reaction configuration system. From literature it can be found many research works, where the H_2 evolution is presented as an isolated number and not data about any actinometrical test is shown. Even, in some of them, incomplete information is shown concerning the

experimental conditions, in some cases we do not know even the reaction volume. Without giving detailed information, these facts make the photocatalytic materials comparison process much more difficult and the definition of a good photocatalytic material more complex. Besides, as it is seen in next example, the reaction configuration system also plays an important role on the H_2 evolution data of any photocatalyst.

For instance, if we did not know which catalysts are in Figure 5.95 and 5.96 and in case we had incomplete information about experimental conditions and actinometrical data, we could conclude the catalysts in Figure 5.96 are much better than the catalysts presented in Figure 5.95. This conclusion would be wrong because they are the same material. So, in this example (comparison of Figures 5.95 and 5.96) is observed clearly, how important is the reaction configuration system to obtain a higher H_2 generation.

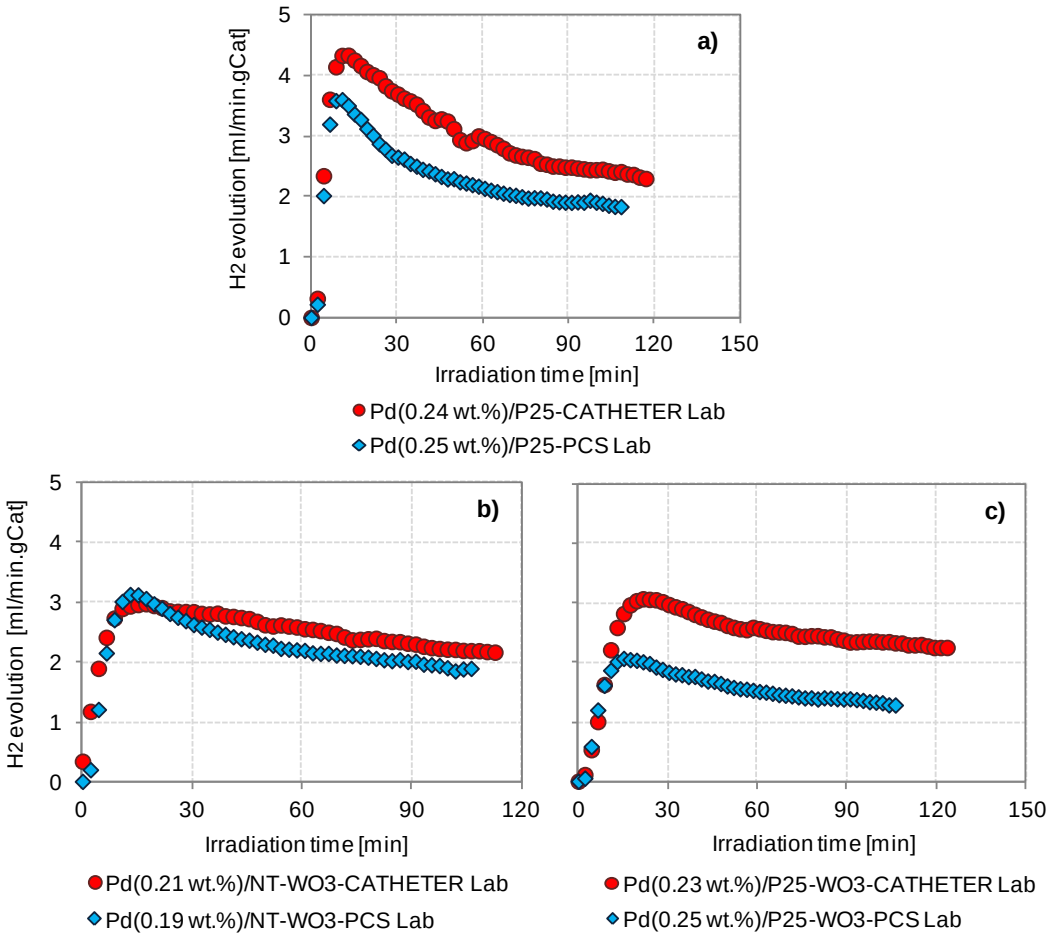

Figure 5.96. H_2 generation in the **SS-system** (Enschede) comparing place of catalyst preparation. **a)** Pd/P25; **b)** Pd/NT-WO_3 and **c)** Pd/P25-WO_3. Experimental conditions: catalyst 1000 ppm, 15 ml of a water - methanol (50 vol.%) solution under Irradiation: Optical fiber UV/Vis-Emission: ca. 8W/cm^2 (280 - 700 nm), $I_{250\text{-}450nm}$: 3.88x10^{-5} Einstein/min.

5.3.3. Literature Comparison

Concerning the literature comparison under solar light, from Table 26 it can be seen that Yang et. al [121] have obtained the highest φ values (10 %) with Pt(1 wt.%)/TiO_2 and Pd(1 wt.%)/TiO_2 catalysts in 100 ml of ethanol, and Patsoura et. al [67] reached 8.97 % with Pd(0.5 wt.%)/TiO_2 in 60 ml of a water-methanol solutions. Regarding the results of φ values under solar light, the catalysts studied in this thesis seem to be good, not only because some of their φ values are higher than the literature values, but also,

because the amount of metal deposited on most of the supports is between 0.1- 0.25 wt.%, meaning lower amount of noble metal, so this factor might become our competitive point, if we take into account the high price of palladium.

Table 26. Comparison of quantum yield for H_2 production[a] for different photocatalytic materials

Catalyst	Irradiation	Sacrificial Agent	Rate H_2 [mol/min.gCat]	Φ (%)[a]
Pt(0.5 wt.%)/TiO_2 [135]	Visible	0.01 vol.% $ClCH_2COOH$ in 0.1 L	5.6x10-6 1.5x10-6	2.3 0.6
Pt(0.5wt.%/CdS(50 %)-TiO_2/FTO [107]	Monochromatic light (470 nm)	20 vol.% EtOH in 0.1 L	-	20
Pt(0.5wt.%/CdS(50 mol%)-TiO_2 [107]	Solar simulated	Na_2SO_3; Na_2S 0.007 M; 0.0048 M in 0.06 L	1.1x10-5 (r_{max})	2.7
1 wt.%$Pd_{shell}Au_{core}$/TiO_2 [101]	UV LED (365 nm)	25 vol.% Glycerol in 0.025 L	3.3x10-4	37.6
Pt(0.5 wt.%)/TiO_2 DP Pt(1.5 wt.%)/TiO_2 DP Pt(0.5 wt.%)/TiO_2 IMP Pd(0.5 wt.%)/TiO_2 DP [125]	UV	10 vol.% Pronan-2-ol in 0.085 L	1.1x10-3 1.1x10-3 1.2x10-3 1.1x10-3	13.3 13.3 13.5 13.3
Pd(1 wt.%)/TiO_2 [121] Pt(1 wt.%)/TiO_2 [121] Rh(1 wt.%)/TiO_2 [121]	Solar	100 vol.% EtOH (0.1 L)	5.5x10-5 5x10-5 2x10-5	10 10 4
Pt(0.5 wt.%)/TiO_2 [67]	Solar	0.003 vol.% (0.85 mM) MetOH	4.6x10-6	0.5
	Solar	0.005 vol.% (0.86 mM) EtOH	9.5x10-6	1.0
	Solar	52 vol.% (8.91 M) EtOH	8.7x10-5	9.0
	UV	3.3 vol.% (0.57 M) EtOH in 0.06 L	4.5x10-4 (r_{max})	17.1
Film Pt/TiO_2 [110]	Black light 365 nm	80 vol.% EtOH 80 vol.% MetOH 40 vol.% EtOH 40 vol.% MetOH in 0.09 L	1.8x10-4 1.5x10-4 1.5x10-4 1.1x10.4	36.4 30.1 29.4 22.4
Pt(1 wt.%)-$BaTi_4O_9$ [195]	UV	20 vol.% EtOH in 0.1 L	2.4X10-4	5.9
Pt(0.1wt.%)/$SrTiO_3$:Rh(1%) [171]	420 nm	10 vol.% MetOH in 0.15 L	9.6x10-7	2.6
$NaTaO_3$ [86] Au-Pd (0.95wt.%)/$NaTaO_3$ [86]	UV 254 nm	Water splitting in 0.2 L	3.5x10-6 2.8x10-5	1 6.5
NiO(0.2 wt.%)/$NaTaO_3$:La(2mol%) [91]	270 nm	Water splitting in 0.3 L	3.3x10-4	28
Pd(0.5 wt.%)/TiO_2 [115]	UV 365 nm	10 vol.% Glycerol 10 vol.%1,2-ethanediol 10 vol. %1,2-propanediol	6.9x10-4 5.8x10-4 7.9x10-4	- - -
Pd(1 wt.%)/TiO_2 [115]		10 vol.% Glycerol in 0.2 L	7.4x10-4	-
Pd(0.5 wt.%)/TiO_2 [196]	Solar spectrum	0.5 vol.% MetOH 1.7 vol.% Triethanolamine	2.7x10-5 5.7x10-5	- -
Pd(0.3 wt.%)/TiO_2 [96]	400 W Xenon arc lamp	0.1 vol.% Ag. in 100 ml	-	-
Pd(0.1 mol%)/TiO_2 [197]	UV 365 nm	50 vol.% MetOH	4.1x10-7	-
Pt(0.5 wt.%)/P25 [81]	280-650 nm	10 vol.% (2.48 M) MetOH in 15 ml	5.5x10-6	5.5% (AQE)
Pt/TiO_2-N [33] Pt/CdS-ZnS [33]	Solar	0.37 vol.% (0.05 M) Glycerol in 25 L	5.5x10-5 3.5x10-5	3.2 2

[a] Quantum yield [121], [101], [110]

From Table 26 is seen that the photocatalytic oxidation of organic compounds on semiconductor materials has been widely studied and it is due to the fact that the VB of the most common semiconductors is more positive than the oxidation potential of most of the organic functional groups,

which in turn means soft operational conditions because the photocatalytic degradation allows room temperature and pressure, few additives, and relatively short reaction times[70].

Table 27 shows results achieved by different catalysts based on noble metal (Pd, Pt or Au) supported on TiO_2 performed in the same PPS-system using 0.05 M of sacrificial agents. The quantum yield φ(%) determination for this experimental set is similar to Eq. 5.2.1.1, where the photons exposed (which is similar to photons accumulated), were determined by the radiometer. The first three catalysts in Table 27 were prepared in CATHETER Lab by the 2m10 PD method. Regarding the results φ, Pd(0.25 wt.%)/P25 catalysts seem to be good enough compared to previous work in the same system for Au (0.5 wt.%)/TiO_2 catalyst, 2.37 vs. 2.34 % in glycerol and 1.33 vs. 0.21 % in methanol. On the other hand, though the fact that the efficiencies of both catalysts, Pd/NT-WO_3 and Pd/P25-WO_3, appear still low (0.57 and 0.47 %, respectively), it is important to highlight that in the literature, the amount of noble metal deposited is 0.5 and 2 wt % (vs. 0.25 wt.% in ours catalysts). These two catalysts have a competitive factor if we take into account the high price of some precious metal (1380.92 €/oz for Au, 1497.3 €/oz for Pt and 1408,81 €/oz for Pd, according to the informative prices from the London market (LBMA) consulted on 21/05/2019, at 10.52 h Spanish time).

Table 27. Comparison of H_2 productions and quantum yields[a]

Catalyst	Sacrificial Agent	H_2 μmol/L_{gas}	Φ (%)
Pd/P25	Glycerol	4239	2.37
	Methanol	2942	1.33
Pd/NT-WO_3	Glycerol	1308	0.57
Pd/P25-WO_3	Glycerol	902	0.47
Pt/(TiO_2-N)	Formic acid	3027	1.29
TiO_2-N [33]	Formic acid	1250	0.53
Au/TiO_2 [103]	Formic acid	6400	2.73
	Glycerol	5500	2.34
	Methanol	500	0.21

* Pilot plant experimental conditions: catalyst concentration: 200 ppm, 25 L of water - methanol (0.20 vol.%), glycerol (0.37 vol.%) or formic acid (0.19 vol.%) solution under solar light. Au (0.5 wt.%) and Pt (2 wt.%),

CHAPTER 6

Conclusions

Recommendations

Conclusions

Taking into account the main objectives of this doctoral thesis, the main conclusions are:

- New materials based on Pd/TiO_2(-WO_3) and Pt/TiO_2(-WO_3) have been developed for the photocatalytic hydrogen generation from aqueous organic solutions, where the TiO_2-WO_3 supports were supplied by the Department of Chemical Engineering and Physical Chemistry in the University of Extremadura, and the metal was photodeposited in CATHETER Lab. Although these materials presented good activity toward the hydrogen generation compared to the available literature, they were not exceptionally good for wastewater treatment due to their sensitiveness to be poisoned by suspended solids in real wastewaters.

- In general words, concerning the development of new catalytic materials, in this thesis was extensively studied the metal photodeposition. Then, it was observed that according to the metal photodeposition conditions on the three NT-WO_3, P25-WO_3 and P25 supports, hydrogen generation was importantly influenced. Therefore, after studying different catalyst (4000, 3200, **2000** and 1000 ppm) and methanol concentrations (20, **10**, 5 and 1 and 0 vol.%), metal amount (2, 0.5, **0.25** and 0.1 wt.%) and metal nature (Pd and Pt) in the photodeposition solution, it was found that the highest hydrogen evolution was obtained specially by the catalysts containing 0.25 wt.% of Pd or Pt, where the metal was deposited by the photodeposition called 2m10 method (2000 ppm of catalyst support in a water-methanol (10 vol.%) solution.
  Moreover, it seems that in the photodeposition solution exists not only an optimal amount of catalyst to volume of methanol (gCat/L MetOH) ratio, but also an optimum photon flux to gram of catalyst (einstein.min^{-1}/gCat) ratio. This latter was not studied but the gCat/L MetOH ratio was around 20.

- Regarding the reactions conditions, hydrogen generation was also affected by their changes. Hence, after modifying the catalyst (86, **167**, **200**, 333, 500 and 1000 ppm) and sacrificial agent concentration (**50**, 33, 25, 10, 5, 0.37, 0.2 and 0 Vol.%), the sacrificial agent nature (methanol, glycerol and real wastewater), pH (12, **natural** and 2) and the water matrix (tap or **milliQ**), it was found that in the solar simulated light system (SSL-system), the catalysts produced more efficiently hydrogen under the next experimental conditions set: 167 ppm of catalysts at 50 vol.% of methanol in milliQ water and natural pH.

- The total organic compound (TOC) removal percentage on Pd/TiO_2(-WO_3) - 2m10 catalysts was found to be higher under solar light than UVA light. On both catalysts containing WO_3, TOC removal was higher as well, showing the Pd(0.21 wt.%)/NT-WO_3 catalyst the highest TOC removal between all three catalysts. Pd/P25 catalysts showed the worst results in terms of TOC removal, although their hydrogen generation results were the opposite. The presence of WO_3 species might promote TOC removal.

In view of the wide number of catalysts studied in this doctoral thesis, next are the most significant conclusion, divided by group of catalysts, related to the catalysts features and experimental conditions on the hydrogen results :

- The hydrogen evolution seemed to be more importantly affected by the changes in the experimental conditions such as the catalyst and methanol concentration, type of water matrix, but not on the features itself of every catalyst. For this group of catalysts, hydrogen generation was higher for the catalysts containing WO_3, in decreasing order Pd/NT-WO_3 > Pd/P25-WO_3 > Pd/P25. Most probably, it is related to the smaller Pd nanoparticles size on the catalysts containing WO_3. With respect to the S_{BET}, V_{PORE} and band-gap of the **w-Pd/TiO_2(-WO_3) - CATHETER Lab catalysts**, it was not observed any strong tendency on the hydrogen evolution. The S_{BET} and TVP for both catalytic supports containing WO_3 decreased after Pd deposition, while for P25 increased. The band-gap was narrower after Pd photodeposition. The Pd nanoparticle size was smaller on Pd/NT-WO_3 and Pd/P25-WO_3 catalysts than on Pd.

- For **m- Pd/TiO_2(-WO_3) - CATHETER Lab catalysts**, it was neither observed any strong relation to the S_{BET}, V_{PORE} and band-gap values on the hydrogen generation. The S_{BET} and TVP for both catalytic supports containing WO_3 decreased or kept nearly constant after Pd deposition either by changing the method or the amount of metal deposited, while for P25, S_{BET} and TVP values increased after Pd photodeposition, and a narrower band-gap was observed for all the catalysts after the Pd photodeposition. The Pd nanoparticle size was smaller for all those catalysts containing the lowest content of Pd (0.1 wt.%) and larger for the highest content of Pd (0.5 wt.%). On this group of catalysts was also observed a stronger difference over the hydrogen evolution when experimental conditions were changed, but not better response over the hydrogen evolution was observed under specific values in the catalyst features, such as at higher S_{BET} or lower band-gap. For this group of catalysts, hydrogen generation was higher on Pd/P25-2m10 catalysts than on both catalysts containing WO_3.

- For the **m-Pd/TiO_2(-WO_3) - PCS Lab catalysts** and **m-Pt/TiO_2(-WO_3) - PCS Lab catalysts** no tendency was observed between the S_{BET}, V_{PORE} and band-gap values on the hydrogen generation. The S_{BET} values of these catalysts were surprisingly much lower than the - CATHETER Lab catalysts, specially Pd/NT-WO_3. This could be due to some impurities of Ca observed after the XPS characterization. The V_{PORE} values for the catalysts containing NT-WO_3 and P25-WO_3 supports was nearly the same before and after the Pd photodeposition. When Pt was photodeposited, the V_{PORE} values were higher on the catalysts containing NT-WO_3. For Pd/P25 and Pt/P25 catalysts, V_{PORE} values were higher after the metal photodeposition. For all these catalysts, the band-gap was narrower after the metal photodeposition. Regarding the metal nanoparticle size, these catalysts (- PCS Lab catalysts) presented smaller nanoparticles than the - CATHETER Lab catalysts. For this group of catalysts, hydrogen generation was also higher on Pd/P25-2m10 catalysts than on both catalysts containing WO_3.

- For **Pd/P25-Cu CATHETER Lab catalysts**, it was observed the S_{BET} values was importantly reduced when Cu was deposited, either on only P25 or Pd/P25 catalysts. The band-gap values were also narrower, for all the catalysts studied containing Cu, the maximum absorption was around 420 - 440 nm.

  The P25-Cu catalysts showed an optimal Cu load around 1 wt.%, where the hydrogen generation was higher; moreover, though the hydrogen generation on P25-Cu catalysts was much higher than on bared-P25, the Pd/Cu-P25 in general showed a poor hydrogen evolution compared to the catalysts without Cu.

From the ART-FTIR results, the main difference observed between the catalysts studied was the absence of H-bounds from water, especially in the region 3000 - 3600 cm^{-1}. Therefore:

- On the Pd/TiO_2-WO_3 and Pt/TiO_2-WO_3 catalysts containing the lowest nominal content of metal (0.25 wt.%) was not seen adsorption of stretching OH by H-bound from water. It seems that the simultaneous presence of WO_3 and low amount of metal (Pd or Pt) suppress the adsorption of H-bounds from water molecules on the catalysts. Moreover, for the Pd/TiO_2-WO_3 and Pt/TiO_2-WO_3 catalyst containing the highest metal content, this broad band was observed. Probably due to the synthesis conditions of these catalysts, when they contain a high amount metal, it is mostly oxidized. Therefore, this higher proportion of metal oxidized might lead to a higher adsorption of water by H-bonds. This fact is more clearly observed on Pd/P25 catalysts with the lowest Pd content, where for the Pd/P25-CATHETER Lab catalyst, the Pd was present as PdO or $Pd(OH)_2$ and the broad band corresponding to H-bound from water was seen. Meanwhile, for the Pd/P25-PCS Lab catalysts, the Pd was only partially oxidized, then, the formation of H-bound was not observed.

- Regarding the reaction mechanism on this kind of materials, from ART-FTIR results were seen some IR absorption bands related to OH stretching by H-bound from water and methanol molecules, C-H stretching and CH_3 scissoring from methanol, -CH stretching and C-H carbonyl from aldehydes species, C-O stretching and C=O from possible formic acid and also some CH_3O species from methanol. Although from IR spectra was seen very little but no clear adsorption of CO and CO_2 on the catalysts, the CO and CO_2 formation was detected from the gas chromatography.

Recommendations

The main contribution of this thesis is related to the development of new catalytic materials for the photocatalytic hydrogen generation, where we attempted to go to a deeper understanding of the reaction mechanism on these photocatalysts. Therefore, continuing in this research line and considering the results showed in this dissertation, we consider it would be interesting to explore these ideas for future work:

- To study some other alternatives for the Pd photodeposition method, such as a deeper analysis related to the gram of catalyst to liter of methanol rate (g Cat/L MetOH) and more importantly the photon flux to gram of catalyst ratio (einstein.min^{-1}/ gCat) for the family of m-Pd/TiO_2(-WO_3) catalysts. In this case, using the same light source and varying the time of irradiation.
- To compare the catalysts where Pd was photodeposited under different light sources to observe its effect on the catalyst features as Pd nanoparticles size, for instance, and see its effect on the hydrogen evolution.
- To perform more hydrogen generation experiments using different wastewater sources.
- To test the same photocatalytic materials (Pd/P25-, Pd/NT-WO_3- and Pd/P25-WO_3-CATHETER Lab catalysts (PD 2m10)) in different set-up for H_2 generation and study the quantum efficiency in each case.

CHAPTER 7

Publications and Communications

PUBLISHED and ongoing ARTICLES

S.Y. Toledo Camacho, A. Rey, M.D. Hernández-Alonso, J. Llorca, F. Medina, S. Contreras. Pd/TiO_2-WO_3 photocatalysts for hydrogen generation from water-methanol mixtures. Appl. Surf. Sci. 455 (2018). 570–580. doi:10.1016/j.apsusc.2018.05.122.

S.Y. Toledo-Camacho, A. Rey, M.I. Maldonado, J. Llorca, S. Contreras, F. Medina. Photocatalytic hydrogen production from water-methanol and -glycerol mixtures using Pd/TiO_2(-WO_3) catalysts and validation in a solar pilot plant. 2019. To submitte in September to the International-journal-of-hydrogen-energy

POSTER PRESENTATIONS

S.Y. Toledo-Camacho, A. Rey, S. Contreras, F. Medina. "Pd/TiO_2-WO_3 Catalysts for photocatalytic hydrogen generation from water-methanol mixtures". 3° International Symposium on Catalysis for Clean Energy and Sustainable Chemistry (CCESC2016). Madrid (Spain), 7 - 9 September 2016.

S.Y. Toledo-Camacho, A. Ibtihel, T. Hammedi, A. Rey, S. Contreras, F. Medina. "Photocatalytic materials for hydrogen generation from water-methanol mixtures. 10th Word Congress of Chemical Engineering (WCCE10)". Barcelona (Spain), 1 - 5 October 2017.

S.Y. Toledo-Camacho, A. Rey, M.I. Maldonado, S. Contreras, F. Medina. "Photocatalytic Hydrogen generation in a solar pilot plant using Pd/TiO_2(-WO_3) based catalysts". 10th European Meeting on Solar Chemistry and Photocatalysis: Environmental Applications (SPEA10), Almeria (Spain), 4 - 8 June, 2018.

ORAL PRESENTATIONS

S.Y. Toledo Camacho, S. Contreras, F. Medina. "Development of new materials for hydrogen production and wastewater treatment by photocatalysis". Canada-Spain Workshop on AOPs: AOPs and Ozone Fundamental Updates and Current Industrial Applications. Barcelona (Spain), 7 -8 July 2016

S.Y. Toledo Camacho, F. Medina, S. Contreras. "Development of new materials for hydrogen production and wastewater treatment by photocatalysis". IV National Meeting of Groups of Photocatalysis. Badajoz (Spain), 22 - 23 September 2016.

S.Y. Toledo Camacho, A. Rey, F. Medina, S. Contreras. 13th European Congress on Catalysis (EUROPACAT2017), Catalysis - A Bridge to the future. Florence (Italy), 27 - 31 August 2017.

S.Y. Toledo Camacho, A. Rey, G. Mul, S. Contreras, F. Medina. "Photocatalytic hydrogen generation from water-methanol mixtures over $Pd/TiO_2(-WO_3)$ catalysts (M: Pd and Pt)". V National Meeting of Groups of Photocatalysis. Las Palmas de Gran Canaria (Spain), 10 - 12 September 2018

S.Y. Toledo Camacho, A. Rey, G. Mul, S. Contreras, F. Medina. "Photocatalytic hydrogen generation from water-methanol mixtures over $Pd/TiO_2(-WO_3)$ catalysts (M: Pd and Pt)". Joint UK&Ireland/Spain Semiconductors Photochemistry Meeting. Las Palmas de Gran Canaria (Spain), 11 - 12 September 2018.

Bibliography

[1] J. Hanania, J. Jenden, J. Donev, Fuel vs flow - Energy Education, Energy Publ. . (2015). http://energyeducation.ca/encyclopedia/Fuel_vs_flow (accessed February 10, 2018).

[2] T. A. Boden, G. Marland, R.J. Andres, Global Fossil-Fuel CO_2 Emissions, Carbon Dioxide Inf. Anal. Center, Oak Ridge Natl. Lab. U.S. Dep. Energy, Oak Ridge, Tenn.,U.S.A. (2017). doi:10.3334/CDIAC/00001_V2010.

[3] Carbon Dioxide Information Analysis Center (CDIAC), Global Fossil Fuel Carbon Emissions - Graphics, (2018). https://cdiac.ess-dive.lbl.gov/trends/emis/glo_2010.html (accessed January 7, 2019).

[4] AAAS.org staff report, AAAS Reaffirms Statements on Climate Change and Integrity | American Association for the Advancement of Science, (2009). https://www.aaas.org/news/aaas-reaffirms-statements-climate-change-and-integrity (accessed July 22, 2019).

[5] Ipcc 2014, Climate Change 2014 Synthesis Report Summary Chapter for Policymakers, (2014) 32. https://www.ipcc.ch/site/assets/uploads/2018/02/AR5_SYR_FINAL_SPM.pdf (accessed February 12, 2018).

[6] B. Dudley, S. Dale, BP Statistical Review of World Energy June 2017, (2017) 49. https://www.bp.com/content/dam/bp-country/de_ch/PDF/bp-statistical-review-of-world-energy-2017-full-report.pdf (accessed February 22, 2018).

[7] US Department of Energy, Wind Energy Benefits, Wind Water Progr. (2010) 6–7. https://www1.eere.energy.gov/wind/pdfs/51783.pdf (accessed February 25, 2018).

[8] World Energy Council, Energy Resources - Wind, (2019). https://www.worldenergy.org/data/resources/resource/wind/ (accessed January 7, 2019).

[9] Asociación Empresarial Eólica, Wind energy in Spain | Asociación Empresarial Eólica, (2017). https://www.aeeolica.org/en/about-wind-energy/wind-energy-in-spain/ (accessed February 25, 2018).

[10] O. Gökhan Eğilmez, Gürsel A. Süer,Özgüner, World â€™ s largest Science , Technology & Medicine Open Access book publisher :, Des. Control Appl. Mechatron. Syst. Eng. (2012) 135–152. doi:10.5772/67458.

[11] Statkraft, Hydropower, (2009). https://www.statkraft.com/globalassets/old-contains-the-old-folder-structure/documents/hydropower-09-eng_tcm9-4572.pdf (accessed February 28, 2018).

[12] Conserve Energy Future, Various Pros and Cons of Hydroelectric Power - Conserve Energy Future, (n.d.). https://www.conserve-energy-future.com/pros-and-cons-of-hydroelectric-power.php (accessed February 26, 2018).

[13] A. Uihlein, D. Magagna, Wave and tidal current energy - A review of the current state of research beyond technology, Renew. Sustain. Energy Rev. 58 (2016) 1070–1081. doi:10.1016/j.rser.2015.12.284.

[14] Bureau of Ocean Energy Management, Ocean Wave Energy | BOEM, (n.d.). https://www.boem.gov/Ocean-Wave-Energy/ (accessed March 26, 2018).

[15] M. Lehmann, F. Karimpour, C. a. Goudey, P.T. Jacobson, M.R. Alam, Ocean wave energy in the United States: Current status and future perspectives, Renew. Sustain. Energy Rev. 74 (2017) 1300–1313. doi:10.1016/j.rser.2016.11.101.

[16] Alternative energy tutorials, Tidal Energy and how tidal energy creates electricity, (2010). http://www.alternative-energy-tutorials.com/tidal-energy/tidal-energy.html (accessed March 26, 2018).

[17] E. Block, Tidal power: an update, Renew. Energy Focus. 9 (2008) 58–61. doi:10.1016/S1755-0084(08)70069-3.

[18] A.G.L. Borthwick, Marine Renewable Energy Seascape, Engineering. 2 (2016) 69–78. doi:10.1016/J.ENG.2016.01.011.

[19] L.Y. Bronicki, Introduction to geothermal power generation, Elsevier Ltd, 2016. doi:10.1016/B978-0-08-100337-4.00001-2.

[20] U.S. Energy Information Administration, Geothermal - Energy Explained, Your Guide To Understanding Energy - Energy Information Administration, (2017). https://www.eia.gov/energyexplained/index.cfm?page=geothermal_home (accessed March 27, 2018).

[21] W. A. Elders, J.N. Moore, Geology of geothermal resources, Elsevier Ltd, 2016. doi:10.1016/B978-0-08-100337-4.00002-4.

[22] R. DiPippo, Overview of geothermal energy conversion systems: Reservoir-wells-piping-plant-reinjection, Elsevier Ltd, 2016. doi:10.1016/B978-0-08-100337-4.00008-5.

[23] J. Khan, M.H. Arsalan, Solar power technologies for sustainable electricity generation - A review, Renew. Sustain. Energy Rev. 55 (2016) 414–425. doi:10.1016/j.rser.2015.10.135.

[24] Z. Liu, L. Zhang, G. Gong, H. Li, G. Tang, Review of solar thermoelectric cooling technologies for use in zero energy buildings, Energy Build. 102 (2015) 207–216. doi:10.1016/j.enbuild.2015.05.029.

[25] X.-Z. Gao, Z.-X. Hou, Z. Guo, X.-Q. Chen, Reviews of methods to extract and store energy for solar-powered aircraft, Renew. Sustain. Energy Rev. 44 (2015) 96–108. doi:10.1016/J.RSER.2014.11.025.

[26] S.S. Chandel, M. Nagaraju Naik, R. Chandel, Review of solar photovoltaic water pumping system technology for irrigation and community drinking water supplies, Renew. Sustain. Energy Rev. 49 (2015) 1084–1099. doi:10.1016/J.RSER.2015.04.083.

[27] G. Pirasteh, R. Saidur, S.M.A. Rahman, N.A. Rahim, A review on development of solar drying applications, Renew. Sustain. Energy Rev. 31 (2014) 133–148. doi:10.1016/J.RSER.2013.11.052.

[28] Y. Tian, C.Y. Zhao, A review of solar collectors and thermal energy storage in solar thermal applications, Appl. Energy. 104 (2013) 538–553. doi:10.1016/J.APENERGY.2012.11.051.

[29] E. Cuce, P.M. Cuce, A comprehensive review on solar cookers, Appl. Energy. 102 (2013) 1399–1421. doi:10.1016/J.APENERGY.2012.09.002.

[30] S.A. Kalogirou, Solar thermal collectors and applications, 2004. doi:10.1016/j.pecs.2004.02.001.

[31] Solar Energy Technologies office, Linear Concentrator System Basics for Concentrating Solar Power | Department of Energy, (2013). https://www.energy.gov/eere/solar/articles/linear-concentrator-system-basics-concentrating-solar-power (accessed April 17, 2018).

[32] K. Mazloomi, C. Gomes, Hydrogen as an energy carrier: Prospects and challenges, Renew. Sustain. Energy Rev. 16 (2012) 3024–3033. doi:10.1016/j.rser.2012.02.028.

[33] K. Villa, X. Domènech, S. Malato, M.I. Maldonado, J. Peral, Heterogeneous photocatalytic hydrogen generation in a solar pilot plant, Int. J. Hydrogen Energy. 38 (2013) 12718–12724. doi:10.1016/j.ijhydene.2013.07.046.

[34] É. Karácsonyi, L. Baia, a. Dombi, V. Danciu, K. Mogyorósi, L.C. Pop, G. Kovács, V. Coşoveanu, a. Vulpoi, S. Simon, Z. Pap, The photocatalytic activity of TiO_2/WO_3/noble metal (Au or Pt) nanoarchitectures obtained by selective photodeposition, Catal. Today. 208 (2013) 19–27. doi:10.1016/j.cattod.2012.09.038.

[35] I. Dincer, C. Acar, Review and evaluation of hydrogen production methods for better sustainability, Int. J. Hydrogen Energy. (2015). doi:10.1016/j.ijhydene.2014.12.035.

[36] A. Kudo, Y. Miseki, Heterogeneous photocatalyst materials for water splitting., Chem. Soc. Rev. 38 (2009) 253–278. doi:10.1039/b800489g.

[37] I. Dincer, Hydrogen and Fuel Cell Technologies for Sustainable Future, Jmie. 2 (2008) 1–14. http://jjmie.hu.edu.jo/files/V2/001-v2-1.pdf.

[38] IEA - Hydrogen Co-ordination Group, Hydrogen Production and Storage, (2006). https://www.iea.org/publications/freepublications/publication/hydrogen.pdf (accessed April 24, 2018).

[39] C.A. Schwengber, H.J. Alves, R.A. Schaffner, F.A. Da Silva, R. Sequinel, V.R. Bach, R.J. Ferracin, Overview of glycerol reforming for hydrogen production, Renew. Sustain. Energy Rev. 58 (2016) 259–266. doi:10.1016/j.rser.2015.12.279.

[40] P. Parthasarathy, K.S. Narayanan, Hydrogen production from steam gasification of biomass: Influence of process parameters on hydrogen yield - A review, Renew. Energy. 66 (2014) 570–579. doi:10.1016/j.renene.2013.12.025 Review.

[41] J.C. García, Producción de hidrógeno mediante electrolizadores. Estado del arte de la tecnología. - Ingeniería Química, Prod. Hidrógeno Median. Electrolizadores. Estado Del Arte La Tecnol. (2012). http://www.ingenieriaquimica.net/articulos/302-produccion-de-hidrogeno-mediante-electrolizadores-estado-del-arte-de-la-tecnologia-electrolizadore (accessed March 8, 2018).

[42] S. Moreau, Global_Trends_and_missions, (2017). https://ieahydrogen.org/pdfs/Global-Outlook-and-Trends-for-Hydrogen_Dec2017_WEB.aspx (accessed March 9, 2018).

[43] A. Fujishima, K. Honda, TiO_2 photoelectrochemistry and photocatalysis, Nature. 213 (1972) 8656. https://electrochem.org/dl/ma/203/pdfs/2729.pdf%5Cnpapers2://publication/uuid/F6B805BA-46E0-443A-B666-4F5841D3D337.

[44] S.Z. Baykara, Experimental solar water thermolysis, Int. J. Hydrogen Energy. 29 (2004) 1459–1469. doi:10.1016/j.ijhydene.2004.02.011.

[45] A. Zuttel, a. Remhof, a. Borgschulte, O. Friedrichs, Hydrogen: the future energy carrier, Philos. Trans. R. Soc. A Math. Phys. Eng. Sci. 368 (2010) 3329–3342. doi:10.1098/rsta.2010.0113.

[46] E.J. García Jarana, M. B; Sánchez-Oneto, J.; Portela Miguélez, J. R.; Nebot Sanz, E.; Martinez de la Ossa, GENERACIÓN DE HIDRÓGEN A PARTIR DE BIOMASA MEDIANTE GASIFICACIÓN EN AGUA SUPERCRITICA (GASC), (2008) 30–36. https://www.researchgate.net/profile/Enrique_Martinez_de_la_Ossa/publication/273698921_Generacion_de_hidrogeno_a_partir_de_biomasa_mediante_gasificacion_en_agua_supercritica/links/553e6de20cf210c0bdaaa4c1/Generacion-de-hidrogeno-a-partir-de-biomasa-median.

[47] L. Gavilà Terrades, Different biomass conversion strategies for valuable chemical production, TDX (Tesis Dr. En Xarxa). (2017). http://www.tesisenred.net/handle/10803/457135 (accessed March 13, 2018).

[48] M. Balat, G. Ayar, Biomass energy in the world, use of biomass and potential trends, Energy Sources. 27 (2005) 931–940. doi:10.1080/00908310490449045.

[49] P.S. Daniel Ciolkosz, Extension Associate, Introduction to Biomass Combustion - eXtension, eXtension. (2014). http://articles.extension.org/pages/31758/introduction-to-biomass-combustion (accessed March 14, 2018).

[50] L. García Moreno, Producción catalítica de hidrógeno mediante reformado con vapor de compuestos oxigenados, Universidad Rey Juan Carlos, 2017. https://eciencia.urjc.es/bitstream/handle/10115/14646/Tesis_Lourdes_Garcia_Moreno.pdf?sequence=1&isAllowed=y.

[51] Biofuels - Biofuel Information - Guide to Biofuels, (n.d.). http://biofuel.org.uk/ (accessed March 21, 2018).

[52] Biofuels - European Commission, (n.d.). https://ec.europa.eu/energy/en/topics/renewable-energy/biofuels (accessed March 22, 2018).

[53] A.L. Woiciechowski, A. Bianchi, P. Medeiros, C. Rodrigues, L. Porto, D.S. Vandenberghe, Green Fuels Technology, (2016). doi:10.1007/978-3-319-30205-8.

[54] S.P. Long, A. Karp, M.S. Buckeridgec, D.J. Murphyf, S. Onwona-Agyemang, A. Vonshakh, Feedstocks for Biofuels and Bioenergy, (n.d.). http://www.bashanfoundation.org/contributions/Vonshak-A/vonshaksustainability.pdf (accessed March 26, 2018).

[55] P.R.D. La Piscina, N. Homs, Use of biofuels to produce hydrogen (reformation processes), Chem. Soc. Rev. 37 (2008) 2459. doi:10.1039/b712181b.

[56] K.S. Avasthi, R.N. Reddy, S. Patel, Challenges in the production of hydrogen from glycerol-a biodiesel byproduct via steam reforming process, Procedia Eng. 51 (2013) 423–429. doi:10.1016/j.proeng.2013.01.059.

[57] D. Nagarajan, D.J. Lee, A. Kondo, J.S. Chang, Recent insights into biohydrogen production by microalgae – From biophotolysis to dark fermentation, Bioresour. Technol. 227 (2017) 373–387. doi:10.1016/j.biortech.2016.12.104.

[58] A. Sharma, S.K. Arya, Hydrogen from algal biomass: A review of production process, Biotechnol. Reports. 15 (2017) 63–69. doi:10.1016/j.btre.2017.06.001.

[59] M.Y. Azwar, M. A. Hussain, A. K. Abdul-Wahab, Development of biohydrogen production by photobiological, fermentation and electrochemical processes: A review, Renew. Sustain. Energy Rev. 31 (2014) 158–173. doi:10.1016/j.rser.2013.11.022.

[60] K. Sasikala, P.R. Rao, ENVIRONMENTAL REGULATION FOR OPTIMAL BIOMASS, Int. J. Hydrogen Energy. 16 (1991) 597–601. doi:10.1016/0360-3199(91)90082-T.

[61] M.J. Barbosa, J.M.S. Rocha, J. Tramper, R.H. Wijffels, Acetate as a carbon source for hydrogen production by photosynthetic bacteria, J. Biotechnol. 85 (2001) 25–33. doi:10.1016/S0168-1656(00)00368-0.

[62] P. Hillmer, H. Gest, H_2 metabolism in the photosynthetic bacterium Rhodopseudomonas capsulata: H_2 production by growing cultures, J. Bacteriol. 129 (1977) 724–731. https://www.ncbi.nlm.nih.gov/pmc/articles/PMC235005/.

[63] J.M. Herrmann, Heterogeneous photocatalysis: State of the art and present applications, Top. Catal. 34 (2005) 49–65. doi:10.1007/s11244-005-3788-2.

[64] J.M. Herrmann, Heterogeneous photocatalysis: Fundamentals and applications to the removal of various types of aqueous pollutants, Catal. Today. 53 (1999) 115–129. doi:10.1016/S0920-5861(99)00107-8.

[65] R.A. Buky, TUNNING FUNCTIONALITY OF PHOTOCATALYTIC MATERIALS: AN INFRARED STUDY ON HYDROCARBON OXIDATION, University of Twente, 2016. doi:10.3990/1.9789036540650.

[66] M. Pelaez, N.T. Nolan, S.C. Pillai, M.K. Seery, P. Falaras, A.G. Kontos, P.S.M. Dunlop, J.W.J. Hamilton, J.A. Byrne, K. O'Shea, M.H. Entezari, D.D. Dionysiou, A review on the visible light active titanium dioxide photocatalysts for environmental applications, Appl. Catal. B Environ. 125 (2012) 331–349. doi:10.1016/j.apcatb.2012.05.036.

[67] A. Patsoura, D.I. Kondarides, X.E. Verykios, Photocatalytic degradation of organic pollutants with simultaneous production of hydrogen, Catal. Today. 124 (2007) 94–102. doi:10.1016/j.cattod.2007.03.028.

[68] K. Maeda, D. Lu, K. Domen, Direct water splitting into hydrogen and oxygen under visible light by using modified TaON photocatalysts with d0 electronic configuration, Chem. - A Eur. J. 19 (2013) 4986–4991. doi:10.1002/chem.201300158.

[69] A. García, M.C. Cotto, J. Ducongé, F. Márquez, Nuevos Fotocatalizadores para la Producción de Hidrógeno, (2014) 2–13. https://www.researchgate.net/publication/274194082_Nuevos_Fotocatalizadores_para_la_Produccion_de_Hidrogeno.

[70] R. Molinari, C. Lavorato, P. Argurio, Recent progress of photocatalytic membrane reactors in water treatment and in synthesis of organic compounds. A review, Catal. Today. 281 (2017) 144–164. doi:10.1016/j.cattod.2016.06.047.

[71] A. Fujii, Z. Meng, C. Yogi, T. Hashishin, T. Sanada, K. Kojima, Preparation of Pt-loaded WO_3 with different types of morphology and photocatalytic degradation of methylene blue, Surf. Coatings Technol. 271 (2015) 251–258. doi:10.1016/j.surfcoat.2014.11.070.

[72] W.-T. Chen, A. Chan, D. Sun-Waterhouse, T. Moriga, H. Idriss, G.I.N. Waterhouse, Ni/TiO_2: A promising low-cost photocatalytic system for solar H_2 production from ethanol–water mixtures, J. Catal. 326 (2015) 43–53. doi:10.1016/j.jcat.2015.03.008.

[73] H. Bahruji, M. Bowker, C. Brookes, P.R. Davies, I. Wawata, The adsorption and reaction of alcohols on TiO_2 and Pd/TiO_2 catalysts, Appl. Catal. A Gen. 454 (2013) 66–73. doi:10.1016/j.apcata.2013.01.005.

[74] L. Clarizia, D. Spasiano, I. Di Somma, R. Marotta, R. Andreozzi, D.D. Dionysiou, Copper modified-TiO_2 catalysts for hydrogen generation through photoreforming of organics. A short review, Int. J. Hydrogen Energy. 39 (2014) 16812–16831. doi:10.1016/j.ijhydene.2014.08.037.

[75] A. Rey, P. García-Muñoz, M.D. Hernández-Alonso, E. Mena, S. García-Rodríguez, F.J. Beltrán, WO_3-TiO_2 based catalysts for the simulated solar radiation assisted photocatalytic ozonation of emerging contaminants in a municipal wastewater treatment plant effluent, Appl. Catal. B Environ. 154–155 (2014) 274–284. doi:10.1016/j.apcatb.2014.02.035.

[76] D. Hufschmidt, D. Bahnemann, J.J. Testa, C. a. Emilio, M.I. Litter, Enhancement of the photocatalytic activity of various TiO_2 materials by platinisation, J. Photochem. Photobiol. A Chem. 148 (2002) 223–231. doi:10.1016/S1010-6030(02)00048-5.

[77] S.N. Frank, A.J. Bard, Heterogeneous Photocatalytic Oxidation of Cyanide Ion in Aqueous Solutions at TiO_2 Powder, J. Am. Chem. Soc. 99 (1977) 303–304. doi:10.1021/ja00443a081.

[78] T. Sano, S. Kutsuna, N. Negishi, K. Takeuchi, Effect of Pd-photodeposition over TiO_2 on product selectivity in photocatalytic degradation of vinyl chloride monomer, J. Mol. Catal. A Chem. 189 (2002) 263–270. doi:10.1016/S1381-1169(02)00353-9.

[79] D. Chatterjee, S. Dasgupta, Visible light induced photocatalytic degradation of organic pollutants, J. Photochem. Photobiol. C Photochem. Rev. 6 (2005) 186–205. doi:10.1016/j.jphotochemrev.2005.09.001.

[80] K.. Padrón, B. Gonzáles, F. Forcade, I. Zumeta, E. Vigil, Propiedades Ópticas del dióxido de titanio mesoporoso y nanocristalino obtenido con la técnica del Doctor Blade, Rev. Cuba. Física. 33 (2016) 27–31. http://www.revistacubanadefisica.org/index.php/rcf/article/view/10.

[81] J. Romão, R. Salata, S.Y. Park, G. Mul, Photocatalytic methanol assisted production of hydrogen with simultaneous degradation of methyl orange, Appl. Catal. A Gen. 518 (2016) 206–212. doi:10.1016/j.apcata.2015.10.020.

[82] A. Patsoura, D.I. Kondarides, X.E. Verykios, Enhancement of photoinduced hydrogen production from irradiated Pt/TiO_2 suspensions with simultaneous degradation of azo-dyes, Appl. Catal. B Environ. 64 (2006) 171–179. doi:10.1016/j.apcatb.2005.11.015.

[83] M.I. Badawy, M.Y. Ghaly, M.E.M. Ali, Photocatalytic hydrogen production over nanostructured mesoporous titania from olive mill wastewater, Desalination. 267 (2011) 250–255. doi:10.1016/j.desal.2010.09.035.

[84] J. Kim, D.W. Hwang, H.G. Kim, S.W. Bae, J.S. Lee, W. Li, S.H. Oh, Highly efficient overall water splitting through optimization of preparation and operation conditions of layered perovskite photocatalysts, Top. Catal. 35 (2005) 295–303. doi:10.1007/s11244-005-3837-x.

[85] A. Ishikawa, T. Takata, T. Matsumura, J.N. Kondo, M. Hara, H. Kobayashi, K. Domen, Oxysulfides $Ln_2Ti_2S_2O_5$ as Stable Photocatalysts for Water Oxidation and Reduction under Visible-Light Irradiation, J. Phys. Chem. B. 108 (2004) 2637–2642. doi:10.1021/jp036890x.

[86] J. Rodríguez-Torres, C. Gómez-Solís, L.M. Torres-Martínez, I. Juárez-Ramírez, Synthesis and

characterization of Au-Pd/$NaTaO_3$ multilayer films for photocatalytic hydrogen production, J. Photochem. Photobiol. A Chem. 332 (2017) 208–214. doi:10.1016/j.jphotochem.2016.08.026.

[87] X.-Y. Zhang, H.-P. Li, X.-L. Cui, Y. Lin, Graphene/TiO_2 nanocomposites: synthesis, characterization and application in hydrogen evolution from water photocatalytic splitting, J. Mater. Chem. 20 (2010) 2801. doi:10.1039/b917240h.

[88] M. Bowker, H. Bahruji, J. Kennedy, W. Jones, G. Hartley, C. Morton, The Photocatalytic Window: Photo-Reforming of Organics and Water Splitting for Sustainable Hydrogen Production, Catal. Letters. (2014) 214–219. doi:10.1007/s10562-014-1443-x.

[89] J. Kennedy, H. Bahruji, M. Bowker, P.R. Davies, E. Bouleghlimat, S. Issarapanacheewin, Hydrogen generation by photocatalytic reforming of potential biofuels: Polyols, cyclic alcohols, and saccharides, J. Photochem. Photobiol. A Chem. 356 (2018) 451–456. doi:10.1016/j.jphotochem.2018.01.031.

[90] A. A. Ismail, D.W. Bahnemann, Photochemical splitting of water for hydrogen production by photocatalysis: A review, Sol. Energy Mater. Sol. Cells. 128 (2014) 85–101. doi:10.1016/j.solmat.2014.04.037.

[91] H. Kato, K. Asakura, A. Kudo, Highly efficient water splitting into H_2 and O_2 over lanthanum-doped $NaTaO_3$ photocatalysts with high crystallinity and surface nanostructure, J. Am. Chem. Soc. 125 (2003) 3082–3089. doi:10.1021/ja027751g.

[92] A. Kudo, Development with of Photocatalyst the Aim at Photon Materials Energy for Water Conversion Splitting, J. Ceram. Soc. Japan. 109 (2001) S82–S88. doi:10.2109/jcersj.109.1270_S81.

[93] H.Y. Lin, H.C. Huang, W.L. Wang, Preparation of mesoporous In-Nb mixed oxides and its application in photocatalytic water splitting for hydrogen production, Microporous Mesoporous Mater. 115 (2008) 568–575. doi:10.1016/j.micromeso.2008.02.036.

[94] K. Maeda, K. Domen, New non-oxide photocatalysts designed for overall water splitting under visible light, J. Phys. Chem. C. 111 (2007) 7851–7861. doi:10.1021/jp070911w.

[95] P. Lianos, Production of electricity and hydrogen by photocatalytic degradation of organic wastes in a photoelectrochemical cell. The concept of the Photofuelcell: A review of a re-emerging research field, J. Hazard. Mater. 185 (2011) 575–590. doi:10.1016/j.jhazmat.2010.10.083.

[96] H. Bahruji, M. Bowker, P.R. Davies, F. Pedrono, New insights into the mechanism of photocatalytic reforming on Pd/TiO_2, Appl. Catal. B Environ. 107 (2011) 205–209. doi:10.1016/j.apcatb.2011.07.015.

[97] D. Jing, W. Tang, C. Xing, L. Guo, Study on photocatalytic hydrogen production in simulated organic pollutants over cadmium sulfide composite photocatalyst, J. Fuel Chem. Technol. 39 (2011) 135–139. doi:10.1016/S1872-5813(11)60014-5.

[98] Y. Li, K. Zhang, S. Peng, G. Lu, S. Li, Photocatalytic hydrogen generation in the presence of ethanolamines over Pt/$ZnIn_2S_4$ under visible light irradiation, J. Mol. Catal. A Chem. 363–364 (2012) 354–361. doi:10.1016/j.molcata.2012.07.011.

[99] X. Wang, X.Y. Li, Photocatalytic hydrogen generation with simultaneous organic degradation by a visible light-driven CdS/ZnS film catalyst, Mater. Sci. Eng. B Solid-State Mater. Adv. Technol. 181 (2014) 86–92. doi:10.1016/j.mseb.2013.11.015.

[100] X. Zhang, M. Yang, J. Zhao, L. Guo, Photocatalytic hydrogen evolution with simultaneous degradation of organics over $(CuIn)_{0.2}Zn_{1.6}S_2$ solid solution, Int. J. Hydrogen Energy. 38 (2013) 15985–15991. doi:10.1016/j.ijhydene.2013.10.014.

[101] R. Su, R. Tiruvalam, A.J. Logsdail, Q. He, C. a Downing, M.T. Jensen, N. Dimitratos, L. Kesavan, P.P. Wells, R. Bechstein, H.H. Jensen, S. Wendt, C.R. a Catlow, C.J. Kiely, G.J. Hutchings, F. Besenbacher, Designer titania-supported Au-Pd nanoparticles for efficient photocatalytic hydrogen production., ACS Nano. 8 (2014) 3490–7. doi:10.1021/nn500963m.

[102] L. Clarizia, G. Vitiello, G. Luciani, I. Di Somma, R. Andreozzi, R. Marotta, In situ photodeposited nanoCu on TiO_2 as a catalyst for hydrogen production under UV/visible radiation, Appl. Catal. A Gen. 518 (2016) 142–149. doi:10.1016/j.apcata.2015.07.044.

[103] S.Y. Arzate Salgado, R.M. Ramirez Zamora, R. Zanella, J. Peral, S. Malato, M.I. Maldonado, Photocatalytic hydrogen production in a solar pilot plant using a Au/TiO_2 photo catalyst, Int. J. Hydrogen Energy. 41 (2016) 11933–11940. doi:10.1016/j.ijhydene.2016.05.039.

[104] M.R. St. John, A.J. Furgala, A.F. Sammells, Hydrogen generation by photocatalytic oxidation of glucose by platinized n-titania powder, J. Phys. Chem. 87 (1983) 801–805. doi:10.1021/j100228a021.

[105] M. De Oliveira Melo, L.A. Silva, Photocatalytic production of hydrogen: An innovative use for biomass derivatives, J. Braz. Chem. Soc. 22 (2011) 1399–1406. doi:10.1590/S0103-50532011000800002.

[106] H. Zhou, J. Pan, L. Ding, Y. Tang, J. Ding, Q. Guo, T. Fan, D. Zhang, Biomass-derived hierarchical porous

CdS/M/TiO_2 (M = Au, Ag, pt, pd) ternary heterojunctions for photocatalytic hydrogen evolution, Int. J. Hydrogen Energy. 39 (2014) 16293–16301. doi:10.1016/j.ijhydene.2014.08.032.

[107] V.M. Daskalaki, M. Antoniadou, G. Li Puma, D.I. Kondarides, P. Lianos, Solar light-responsive Pt/CdS/TiO_2 photocatalysts for hydrogen production and simultaneous degradation of inorganic or organic sacrificial agents in wastewater, Environ. Sci. Technol. 44 (2010) 7200–7205. doi:10.1021/es9038962.

[108] Y. Li, G. Lu, S. Li, Photocatalytic transformation of rhodamine B and its effect on hydrogen evolution over Pt/TiO_2 in the presence of electron donors, J. Photochem. Photobiol. A Chem. 152 (2002) 219–228. doi:10.1016/S1010-6030(02)00210-1.

[109] K.C. Christoforidis, P. Fornasiero, Photocatalytic Hydrogen Production: A Rift into the Future Energy Supply, ChemCatChem. 9 (2017) 1523–1544. doi:10.1002/cctc.201601659.

[110] N. Strataki, V. Bekiari, D.I. Kondarides, P. Lianos, Hydrogen production by photocatalytic alcohol reforming employing highly efficient nanocrystalline titania films, Appl. Catal. B Environ. 77 (2007) 184–189. doi:10.1016/j.apcatb.2007.07.015.

[111] H. Husin, W.-N. Su, H.-M. Chen, C.-J. Pan, S.-H. Chang, J. Rick, W.-T. Chuang, H.-S. Sheu, B.-J. Hwang, Photocatalytic hydrogen production on nickel-loaded $La_xNa_{1-x}TaO_3$ prepared by hydrogen peroxide-water based process, Green Chem. 13 (2011) 1745. doi:10.1039/c1gc15070g.

[112] M. Bowker, P. Stone, R.A. Bennett, N. Perkins, Formic acid adsorption and decomposition on TiO_2(110) and on Pd/TiO_2(110) model catalysts, Surf. Sci. 511 (2002) 435–448. doi:10.1016/S0039-6028(02)01540-6.

[113] M. Bowker, D. James, P. Stone, R. Bennett, N. Perkins, L. Millard, J. Greaves, A. Dickinson, Catalysis at the metal-support interface: Exemplified by the photocatalytic reforming of methanol on Pd/TiO_2, J. Catal. 217 (2003) 427–433. doi:10.1016/S0021-9517(03)00074-5.

[114] M. Bowker, C. Morton, J. Kennedy, H. Bahruji, J. Greves, W. Jones, P.R. Davies, C. Brookes, P.P. Wells, N. Dimitratos, Hydrogen production by photoreforming of biofuels using Au, Pd and Au-Pd/TiO_2 photocatalysts, J. Catal. 310 (2014) 10–15. doi:10.1016/j.jcat.2013.04.005.

[115] Z.H.N. Al-Azri, W.T. Chen, A. Chan, V. Jovic, T. Ina, H. Idriss, G.I.N. Waterhouse, The roles of metal co-catalysts and reaction media in photocatalytic hydrogen production: Performance evaluation of M/TiO_2 photocatalysts (M = Pd, Pt, Au) in different alcohol-water mixtures, J. Catal. 329 (2015) 355–367. doi:10.1016/j.jcat.2015.06.005.

[116] H. Tong, S. Ouyang, Y. Bi, N. Umezawa, M. Oshikiri, J. Ye, Nano-photocatalytic materials: Possibilities and challenges, Adv. Mater. 24 (2012) 229–251. doi:10.1002/adma.201102752.

[117] K. Wenderich, Photodeposition of platinum nanoparticles on well-defined tungsten oxide, University of Twente, 2016.

[118] Cocatalizador-Cocatalyst | Centro Español de Plásticos, (n.d.). https://cep-plasticos.com/es/contenido/cocatalizador-cocatalyst (accessed July 9, 2018).

[119] Slamet, Anny, Setiadi, Photocatalytic Hydrogen Generation from Glycerol and Water using Pt loaded N-doped TiO_2 Nanotube, Int. J. Eng. Technol. 11 (2011) 91–95. https://www.researchgate.net/publication/282866260_Photocatalytic_Hydrogen_Generation_from_Glycerol_and_Water_using_Pt_loaded_N-doped_TiO_2_Nanotube.

[120] Y. Li, G. Lu, S. Li, Photocatalytic hydrogen generation and decomposition of oxalic acid over platinized TiO_2, Appl. Catal. A Gen. 214 (2001) 179–185. doi:10.1016/S0926-860X(01)00491-4.

[121] Y.Z. Yang, C.H. Chang, H. Idriss, Photo-catalytic production of hydrogen form ethanol over M/TiO_2 catalysts (M = Pd, Pt or Rh), Appl. Catal. B Environ. 67 (2006) 217–222. doi:10.1016/j.apcatb.2006.05.007.

[122] H. Yan, J. Yang, G. Ma, G. Wu, X. Zong, Z. Lei, J. Shi, C. Li, Visible-light-driven hydrogen production with extremely high quantum efficiency on Pt-PdS/CdS photocatalyst, J. Catal. 266 (2009) 165–168. doi:10.1016/j.jcat.2009.06.024.

[123] J. Haber, J.H. Block, B. Delmon, Manual of methods and procedures for catalyst characterization (Technical Report), Pure Appl. Chem. 67 (1995) 1257–1306. doi:10.1351/pac199567081257.

[124] D. V Bavykin, A. a Lapkin, P.K. Plucinski, L. Torrente Murciano, J.M. Friedrich, F.C. Walsh, Deposition of Pt, Pd, Ru and Au on the surfaces of titanate nanotubes, 39 (2006). doi:10.1007/s11244-006-0051-4.

[125] F.J. López-Tenllado, J. Hidalgo-Carrillo, V. Montes, a. Marinas, F.J. Urbano, J.M. Marinas, L. Ilieva, T. Tabakova, F. Reid, A comparative study of hydrogen photocatalytic production from glycerol and propan-2-ol on M/TiO_2 systems (M=Au, Pt, Pd), Catal. Today. 280 (2017) 58–64. doi:10.1016/j.cattod.2016.05.009.

[126] J.G. Kang, Y. Sohn, Interfacial nature of Ag nanoparticles supported on TiO_2 photocatalysts, J. Mater. Sci. 47 (2012) 824–832. doi:10.1007/s10853-011-5860-6.

[127] Slamet, Ratnawati, J. Gunlazuardi, E.L. Dewi, Enhanced photocatalytic activity of Pt deposited on titania

nanotube arrays for the hydrogen production with glycerol as a sacrificial agent, Int. J. Hydrogen Energy. 42 (2017) 24014–24025. doi:10.1016/j.ijhydene.2017.07.208.

[128] N. Bao, L. Shen, T. Takata, K. Domen, Self-Templated Synthesis of Nanoporous CdS Nanostructures for Highly Efficient Photocatalytic Hydrogen Production under Visible Light Self-Templated Synthesis of Nanoporous CdS Nanostructures for Highly Efficient Photocatalytic Hydrogen Production under, Synthesis (Stuttg). (2008) 110–117. doi:10.1021/cm7029344.

[129] J.L. Contreras, M. A. Ortiz, R. Luna, G. A. Fuentes, M. Gordon, J. Salmones, B. Zeifert, M. Gordon, T. Vázquez, Production of hydrogen from ethanol using Pt/hydrotalcite catalysts stabilized with tungsten oxides, J. New Mater. Electrochem. Syst. 15 (2012) 215–223.

[130] H. Wang, X. Yuan, Y. Wu, H. Huang, X. Peng, G. Zeng, H. Zhong, J. Liang, M.M. Ren, Graphene-based materials: Fabrication, characterization and application for the decontamination of wastewater and wastegas and hydrogen storage/generation, Adv. Colloid Interface Sci. 195–196 (2013) 19–40. doi:10.1016/j.cis.2013.03.009.

[131] S. Zhang, B. Peng, S. Yang, Y. Fang, F. Peng, The influence of the electrodeposition potential on the morphology of Cu_2O/TiO_2 nanotube arrays and their visible-light-driven photocatalytic activity for hydrogen evolution, Int. J. Hydrogen Energy. 38 (2013) 13866–13871. doi:10.1016/j.ijhydene.2013.08.081.

[132] Y. Lee, E. Kim, Y. Park, J. Kim, W.H. Ryu, J. Rho, K. Kim, Photodeposited metal-semiconductor nanocomposites and their applications, J. Mater. 4 (2018) 83–94. doi:10.1016/j.jmat.2018.01.004.

[133] M. Maicu, M.C. Hidalgo, G. Colón, J. A. Navío, Comparative study of the photodeposition of Pt, Au and Pd on pre-sulphated TiO_2 for the photocatalytic decomposition of phenol, J. Photochem. Photobiol. A Chem. 217 (2011) 275–283. doi:10.1016/j.jphotochem.2010.10.020.

[134] F. Zhang, J. Chen, X. Zhang, W. Gao, R. Jin, N. Guan, Simple and low-cost preparation method for highly dispersed Pd/TiO_2 catalysts, Catal. Today. 93–95 (2004) 645–650. doi:10.1016/j.cattod.2004.06.023.

[135] Y. Li, Y. Xie, S. Peng, G. Lu, S. Li, Photocatalytic hydrogen generation in the presence of chloroacetic acids over Pt/TiO_2, Chemosphere. 63 (2006) 1312–1318. doi:10.1016/j.chemosphere.2005.09.004.

[136] R. Camposeco, S. Castillo, I. Mejía-Centeno, J. Navarrete, J. Marín, Characterization of physicochemical properties of Pd/TiO_2 nanostructured catalysts prepared by the photodeposition method, Mater. Charact. 95 (2014) 201–210. doi:10.1016/j.matchar.2014.06.017.

[137] C. Shifu, C. Lei, G. Shen, C. Gengyu, The preparation of coupled WO_3/TiO_2 photocatalyst by ball milling, Powder Technol. 160 (2005) 198–202. doi:10.1016/j.powtec.2005.08.012.

[138] M. Xiao, L. Wang, X. Huang, Y. Wu, Z. Dang, Synthesis and characterization of WO_3/titanate nanotubes nanocomposite with enhanced photocatalytic properties, J. Alloys Compd. 470 (2009) 486–491. doi:10.1016/j.jallcom.2008.03.003.

[139] I. Paramasivam, Y.C. Nah, C. Das, N.K. Shrestha, P. Schmuki, WO3/TiO2 nanotubes with strongly enhanced photocatalytic activity, Chem. - A Eur. J. 16 (2010) 8993–8997. doi:10.1002/chem.201000397.

[140] C. Zhao, Photocatalytic Treatment of Microcystin-LR-Containing Wastewater Using Pt/WO_3 Nanoparticles under Simulated Solar Light, Open J. Appl. Sci. 2 (2012) 86–92. doi:10.4236/ojapps.2012.22011.

[141] J. Gong, W. Pu, C. Yang, J. Zhang, Novel one-step preparation of tungsten loaded TiO_2 nanotube arrays with enhanced photoelectrocatalytic activity for pollutant degradation and hydrogen production, Catal. Commun. 36 (2013) 89–93. doi:10.1016/j.catcom.2013.03.009.

[142] H. Gao, P. Zhang, J. Hu, J. Pan, J. Fan, G. Shao, One-dimensional Z-scheme TiO_2/WO_3/Pt heterostructures for enhanced hydrogen generation, Appl. Surf. Sci. 391 (2017) 211–217. doi:10.1016/j.apsusc.2016.06.170.

[143] M.D. Hernández-Alonso, S. García-Rodríguez, B. Sánchez, J.M. Coronado, Revisiting the hydrothermal synthesis of titanate nanotubes: new insights on the key factors affecting the morphology., Nanoscale. 3 (2011) 2233–2240. doi:10.1039/c1nr10081e.

[144] M.D. Hernández-Alonso, S. García-Rodríguez, S. Suárez, R. Portela, B. Sánchez, J.M. Coronado, Highly selective one-dimensional TiO_2-based nanostructures for air treatment applications, Appl. Catal. B Environ. 110 (2011) 251–259. doi:10.1016/j.apcatb.2011.09.009.

[145] J.S. Romão, M.S. Hamdy, G. Mul, J. Baltrusaitis, Photocatalytic decomposition of cortisone acetate in aqueous solution, J. Hazard. Mater. 282 (2015) 208–215. doi:10.1016/j.jhazmat.2014.05.087.

[146] D.A.S.U. Skoog, F.J.U. of K. Holler, S.R.M.S.U. Crouch, Principios de análisis instrumental, Sexta edic, México D.F., 2008. https://www.academia.edu/37326567/Principios_de_análisis_instrumental_6ta_Edición_Douglas_A._Skoog_LIBROSVIRTUAL.

[147] M. Thommes, K. Kaneko, A. V. Neimark, J.P. Olivier, F. Rodriguez-Reinoso, J. Rouquerol, K.S.W. Sing,

Physisorption of gases, with special reference to the evaluation of surface area and pore size distribution (IUPAC Technical Report), Pure Appl. Chem. 87 (2015) 1051–1069. doi:10.1515/pac-2014-1117.

[148] X-Ray Crystallography, (n.d.). https://www.tulane.edu/~sanelson/eens211/x-ray.htm (accessed October 29, 2018).

[149] T.E. Microscopy, Transmission Electron Microscopy, 2016. doi:10.1007/978-3-319-26651-0.

[150] Mundo microscópio, El microscopio electrónico - Mundo Microscopio, (2018). https://www.mundomicroscopio.com/microscopio-electronico/ (accessed October 24, 2018).

[151] Differencebetween.net, Difference Between TEM and SEM | Difference Between | TEM vs SEM, Differ. Between TEM SEM. (2012). http://www.differencebetween.net/science/difference-between-tem-and-sem/ (accessed January 11, 2019).

[152] E. Stach, MSE 582 Transmission Electron Microscopy Skills, (2008). https://nanohub.org/resources/4020/download/2008.02.04-MSE582-L11.pdf (accessed January 11, 2019).

[153] Shimadzu Corporation, ABC's of the Diffuse Reflection Method : SHIMADZU (Shimadzu Corporation), (2018). https://www.shimadzu.com/an/ftir/support/ftirtalk/talk1/intro.html (accessed November 1, 2018).

[154] J.P. Blitz, T. José, B. Vidal, Diffuse Reflectance Spectroscopy, 1998. http://dx.doi.org/10.2136/sssabookser5.5.c13.

[155] Shimadzu Corporation, Measurements of Band Gap in Compound Semiconductors - Band Gap Determination from Diffuse Reflectance Spectra -, Measurement. (1800) 2–3.

[156] Shimadzu Corporation, TOC Technique- SCT-UAQ 05_2.pdf, (n.d.). http://www.icra.cat/files/equipament/SCT-UAQ 05_2.pdf.

[157] P. Whitehead, Total Organic Carbon (TOC) and its Measurement, (2018). https://www.elgalabwater.com/blog/total-organic-carbon-toc (accessed November 5, 2018).

[158] I. Bisutti, I. Hilke, M. Raessler, Determination of total organic carbon – an overview of current methods, 23 (2004). doi:10.1016/j.trac.2004.09.003.

[159] R.F. Thompson, W.A. Spencer, This Week ' s Citation Classic, Science (80-.). (1979) 1985.

[160] S. Goldstein, J. Rabani, The ferrioxalate and iodide-iodate actinometers in the UV region, J. Photochem. Photobiol. A Chem. 193 (2008) 50–55. doi:10.1016/j.jphotochem.2007.06.006.

[161] Y. Zuo, Kinetics of photochemical/chemical cycling of iron coupled with organic substances in cloud and fog droplets, Geochim. Cosmochim. Acta. 59 (1995) 3123–3130. doi:10.1016/0016-7037(95)00201-A.

[162] A. Safarzadeh-Amiri, J.R. Bolton, S.R. Cater, Ferrioxalate-mediated photodegradation of organic pollutants in contaminated water, Water Res. 31 (1997) 787–798. doi:10.1016/S0043-1354(96)00373-9.

[163] G. Fernández, Determinación Estructural, in: Google, Academia Minas de Oviedo, Oviedo, 2014: pp. 26–66. https://books.googleusercontent.com/books/content?req=AKW5QafHCEvVavcRjcmunnIBjJEElVgiA7gHmt-VwK7FGr_Ro54jZ7DHyFDdTSrb9mEj9prX-1AR8R6LM3XbUrpmM0P0A9hd05NMQyF1QjOp-Pt96oGmGrguIc6X9Kd6h91Yjj7pfyKy3UGRVbKVqaeZrTVID7QyK0QG1yC2EURm1Q54aashDtyBSjRXRN_9puu8SWyEK (accessed May 9, 2018).

[164] A. Aristizábal Castrillón, Catalytic Denitration of Drinking Water : Carbon Based Catalysts, Universitat Rovira i Virgili, 2012.

[165] K.S.W. Sing, D.H. Everett, R. a. W. Haul, L. Moscou, R. a. Pierotti, J. Rouquérol, T. Siemieniewska, INTERNATIONAL UNION OF PURE COMMISSION ON COLLOID AND SURFACE CHEMISTRY INCLUDING CATALYSIS * REPORTING PHYSISORPTION DATA FOR GAS / SOLID SYSTEMS with Special Reference to the Determination of Surface Area and Porosity, Pure Appl. Chem. 54 (1982) 2201–2218. doi:10.1351/pac198557040603.

[166] S. Navaladian, B. Viswanathan, T.K. Varadarajan, R.P. Viswanath, A rapid synthesis of oriented palladium nanoparticles by UV irradiation, Nanoscale Res. Lett. 4 (2009) 181–186. doi:10.1007/s11671-008-9223-4.

[167] W.A. Rigdon, X. Huang, Carbon monoxide tolerant platinum electrocatalysts on niobium doped titania and carbon nanotube composite supports, J. Power Sources. 272 (2014) 845–859. doi:10.1016/j.jpowsour.2014.09.054.

[168] L. Ouyang, P.F. Tian, G.J. Da, X.C. Xu, C. Ao, T.Y. Chen, R. Si, J. Xu, Y.F. Han, The origin of active sites for direct synthesis of H_2O_2 on Pd/TiO_2 catalysts: Interfaces of Pd and PdO domains, J. Catal. 321 (2015) 70–80. doi:10.1016/j.jcat.2014.10.003.

[169] M. Shibuya, M. Miyauchi, Site-selective deposition of metal nanoparticles on aligned WO_3 nanotrees for super-hydrophilic thin films, Adv. Mater. 21 (2009) 1373–1376. doi:10.1002/adma.200802918.

[170] D. Zhang, Visible light-induced photocatalysis through surface plasmon excitation of platinum-metallized titania for photocatalytic bleaching of rhodamine B, Monatshefte Fur Chemie. 143 (2012) 729–738. doi:10.1007/s00706-011-0631-2.

[171] R. Konta, T. Ishii, H. Kato, A. Kudo, Photocatalytic Activities of Noble Metal Ion Doped $SrTiO_3$ under Visible Light Irradiation, J. Phys. Chem. 108 (2004) 8992–8995. doi:10.1021/jp049556p.

[172] J.F. Reber, K. Meier, Photochemical Production of Hydrogen with Zinc-Sulfide Suspensions, J. Phys. Chem. 88 (1984) 5903–5913. doi:10.1021/j150668a032.

[173] R.J. Candal, W. Estrada, El fotocatalizador : síntesis, propiedades y limitaciones, in: Tecnol. Solares Para La Desinfección Y Descontaminación Del Agua, 2005: pp. 129–145. https://www.psa.es/webesp/projects/solarsafewater/curso.php.

[174] Y. Sakai, A. Shimanaka, M. Shioi, S. Kato, S. Satokawa, T. Kojima, A. Yamasaki, Fabrication of high-sensitivity palladium loaded tungsten trioxide photocatalyst by photodeposite method, Catal. Today. 241 (2015) 2–7. doi:10.1016/j.cattod.2014.07.044.

[175] D. Sánchez Martínez, A. Martínez-De La Cruz, E. López Cuéllar, Photocatalytic properties of WO_3 nanoparticles obtained by precipitation in presence of urea as complexing agent, Appl. Catal. A Gen. 398 (2011) 179–186. doi:10.1016/j.apcata.2011.03.034.

[176] T. Nguyen Thi Thu, N. Nguyen Thi, V. Tran Quang, K. Nguyen Hong, T. Nguyen Minh, N. Le Thi Hoai, Synthesis, characterisation, and effect of pH on degradation of dyes of copper-doped TiO_2, J. Exp. Nanosci. 11 (2016) 226–238. doi:10.1080/17458080.2015.1053541.

[177] L. Clarizia, I. Di Somma, R. Marotta, P. Minutolo, R. Villamaina, R. Andreozzi, Photocatalytic reforming of formic acid for hydrogen production in aqueous solutions containing cupric ions and TiO_2 suspended nanoparticles under UV-simulated solar radiation, Appl. Catal. A Gen. 518 (2016) 181–188. doi:10.1016/j.apcata.2015.09.020.

[178] G.R. Bamwenda, S. Tsubota, T. Nakamura, M. Haruta, Photoassisted Hydrogen-Production from a water-ethanol solution - A Comparison of activities of Au-TiO_2 and Pt-TiO_2, J. Photochem. Photobiol. A-Chemistry. 89 (1995) 177–189. doi:10.1016/1010-6030(95)04039-I.

[179] S.Y. Toledo Camacho, A. Rey, M.D. Hernández-Alonso, J. Llorca, F. Medina, S. Contreras, Pd/TiO_2-WO_3 photocatalysts for hydrogen generation from water-methanol mixtures, Appl. Surf. Sci. 455 (2018) 570–580. doi:10.1016/j.apsusc.2018.05.122.

[180] H.J. Choi, M. Kang, Hydrogen production from methanol/water decomposition in a liquid photosystem using the anatase structure of Cu loaded TiO_2, Int. J. Hydrogen Energy. 32 (2007) 3841–3848. doi:10.1016/j.ijhydene.2007.05.011.

[181] T. Chen, Z. Feng, G. Wu, J. Shi, G. Ma, P. Ying, C. Li, Mechanistic studies of photocatalytic reaction of methanol for hydrogen production on Pt/TiO_2 by in situ fourier transform IR and time-resolved IR spectroscopy, J. Phys. Chem. C. 111 (2007) 8005–8014. doi:10.1021/jp071022b.

[182] J.F. Gomes, G. Tremiliosi-Filho, Spectroscopic Studies of the Glycerol Electro-Oxidation on Polycrystalline Au and Pt Surfaces in Acidic and Alkaline Media, Electrocatalysis. 2 (2011) 96–105. doi:10.1007/s12678-011-0039-0.

[183] A.J. Maira, J.M. Coronado, V. Augugliaro, K.L. Yeung, J.C. Conesa, J. Soria, Fourier transform infrared study of the performance of nanostructured TiO_2 particles for the photocatalytic oxidation of gaseous toluene, J. Catal. 202 (2001) 413–420. doi:10.1006/jcat.2001.3301.

[184] M. Setvin, X. Shi, J. Hulva, T. Simschitz, G.S. Parkinson, M. Schmid, C. Di Valentin, A. Selloni, U. Diebold, Methanol on anatase TiO_2 (101): Mechanistic insights into photocatalysis, ACS Catal. (2017) acscatal.7b02003. doi:10.1021/acscatal.7b02003.

[185] R. Sánchez De Armas, J. Oviedo, M.A. San Miguel, J.F. Sanz, Methanol adsorption and dissociation on TiO_2(110) from first principles calculations, J. Phys. Chem. C. 111 (2007) 10023–10028. doi:10.1021/jp0717701.

[186] G. Halasi, G. Schubert, F. Solymosi, Comparative study on the photocatalytic decomposition of methanol on TiO_2 modified by N and promoted by metals, J. Catal. 294 (2012) 199–206. doi:10.1016/j.jcat.2012.07.020.

[187] N.L. Wu, M.S. Lee, Enhanced TiO_2 photocatalysis by Cu in hydrogen production from aqueous methanol solution, Int. J. Hydrogen Energy. 29 (2004) 1601–1605. doi:10.1016/j.ijhydene.2004.02.013.

[188] M. Canterino, I. Di Somma, R. Marotta, R. Andreozzi, Kinetic investigation of Cu(II) ions photoreduction in presence of titanium dioxide and formic acid, Water Res. 42 (2008) 4498–4506. doi:10.1016/j.watres.2008.07.035.

[189] S. Xu, J. Ng, A.J. Du, J. Liu, D.D. Sun, Highly efficient TiO_2 nanotube photocatalyst for simultaneous

hydrogen production and copper removal from water, Int. J. Hydrogen Energy. 36 (2011) 6538–6545. doi:10.1016/j.ijhydene.2011.03.047.

[190] T. Montini, V. Gombac, L. Sordelli, J.J. Delgado, X. Chen, G. Adami, P. Fornasiero, Nanostructured Cu/TiO_2 photocatalysts for H_2 production from ethanol and glycerol aqueous solutions, ChemCatChem. 3 (2011) 574–577. doi:10.1002/cctc.201000289.

[191] V. Jovic, H. Idriss, G.I.N. Waterhouse, D. Sun-Waterhouse, W.-T. Chen, The role of CuO in promoting photocatalytic hydrogen production over TiO_2, Int. J. Hydrogen Energy. 38 (2013) 15036–15048. doi:10.1016/j.ijhydene.2013.09.101.

[192] J. Yu, Y. Hai, M. Jaroniec, Photocatalytic hydrogen production over CuO-modified titania, J. Colloid Interface Sci. 357 (2011) 223–228. doi:10.1016/j.jcis.2011.01.101.

[193] S.S. Lee, H. Bai, Z. Liu, D.D. Sun, Novel-structured electrospun TiO_2/CuO composite nanofibers for high efficient photocatalytic cogeneration of clean water and energy from dye wastewater, Water Res. 47 (2013) 4059–4073. doi:10.1016/j.watres.2012.12.044.

[194] T. Sreethawong, S. Yoshikawa, Comparative investigation on photocatalytic hydrogen evolution over Cu-, Pd-, and Au-loaded mesoporous TiO_2 photocatalysts, Catal. Commun. 6 (2005) 661–668. doi:10.1016/j.catcom.2005.06.004.

[195] W. Sun, S. Zhang, C. Wang, Z. Liu, Z. Mao, Effects of cocatalyst and calcination temperature on photocatalytic hydrogen evolution over $BaTi_4O_9$ powder synthesized by the polymerized complex method, Catal. Letters. 123 (2008) 282–288. doi:10.1007/s10562-008-9420-x.

[196] W. Jones, D.J. Martin, A. Caravaca, A.M. Beale, M. Bowker, T. Maschmeyer, G. Hartley, A. Masters, A comparison of photocatalytic reforming reactions of methanol and triethanolamine with Pd supported on titania and graphitic carbon nitride., Appl. Catal. B Environ. (2017) 1–7. doi:10.1016/j.apcatb.2017.01.042.

[197] B.S. Kwak, J. Chae, J. Kim, M. Kang, Enhanced Hydrogen Production from Methanol / Water Photo-Splitting in TiO_2 Including Pd Component, Bull. Korean Chem. Soc. 30 (2009). doi:0253-2964.